

# Copper Bipyridyl Redox Mediators for High Performance Dye-Sensitized Solar Cells

Thèse N° 9221

Présentée le 18 janvier 2019

à la Faculté des sciences de base  
Laboratoire des sciences photomoléculaires  
Programme doctoral en chimie et génie chimique

pour l'obtention du grade de Docteur ès Sciences

par

**YASEMIN SAYGILI**

Acceptée sur proposition du jury

Prof. M. Chergui, président du jury  
Prof. U. A. Hagfeldt, directeur de thèse  
Prof. L. Kloo, rapporteur  
Prof. E. C. Constable, rapporteur  
Prof. M. K. Nazeeruddin, rapporteur

2019



To my father Salman Saygılı ...



# Abstract

Photovoltaic (PV) technologies attract a lot of attention as a result of the increasing energy demand and environmental concerns stemming from the conventional energy resources. Accordingly, the power conversion efficiency (PCE) values of various solar energy harvesting units continue to increase, targeting the Shockley-Queisser limit. However, the commercialization and integration of these photovoltaic devices in various applications depend on several criteria such as cost, ease of fabrication and reliability of the materials employed. Regarding their cost-effective and multifarious manufacturing possibilities, and short energy-payback times we can foresee dye-sensitized solar cells (DSCs) as proper candidates to become widespread power-supply devices.

In a DSC system, the open circuit potential ( $V_{OC}$ ) is determined as the difference between the quasi-Fermi level of the semiconductor and redox potential of the electrolyte. By employing redox mediators with more positive redox potentials, the dye regeneration overpotentials can be reduced and  $V_{OC}$  outputs can be increased. During the course of this PhD study, we investigated Cu(II)/Cu(I) coordination complexes with bipyridine ligands holding methyl groups on the 6,6 positions as redox mediators in DSCs. As revealed by DFT calculations, steric hindrance of the methyl groups provided proper geometries (tetrahedral for Cu(I) and distorted tetragonal for Cu(II)) for minimizing the reorganization energy for electron transfer. Thus, successful dye regeneration even with 0.1 eV driving force became feasible without compromising photocurrent densities. We achieved high photovoltages of over 1.0 V and PCEs over 10%, using the organic Y123 dye under  $1000 \text{ Wm}^{-2}$  AM1.5G illumination by the series of copper complexes.

After this initial study, we concentrated on the complications associated with the soft nature and the instability of the coordination sphere of copper species. Firstly, we showed that the Cu(II) species synthesized via  $\text{CuCl}_2$  precursor exhibit different electrochemical behaviors in comparison to Cu(I) counterparts. Hence, we proposed three procedures that lead to neat Cu(II) species: chemical oxidation of Cu(I), electrochemical oxidation and changing our precursor to  $\text{Cu}(\text{TFSI})_2$ . Secondly, we studied the effect of the 4-tertbutyl pyridine and similar base additives in the electrolyte medium. With bases, the coordination sphere and the geometry of the complexes were different in comparison to the ones presumed without a base. We studied the effects of this occurrence to the dye regeneration and charge recombination reaction rates in detail in reference to the Marcus Theory.

We demonstrated  $[\text{Cu}(\text{tmby})_2]^{2+/1+}$  (tmby = 4,4',6,6'-tetramethyl-2,2'-bipyridine), as an effective hole transport material (HTM) in solid-state DSCs (ssDSCs). With this HTM, we circumvent the pore filling problems occurring in conventional ssDSCs. Therefore, we could use thicker  $\text{TiO}_2$  films to achieve better light harvesting efficiencies. Furthermore, for the same redox mediator we demonstrated that the DSCs show remarkable PCE values at ambient lighting. Under illumination from a fluorescent light tube (1000 lux) we achieved PCE values of 28.9%.

All our findings indicate that the DSCs employing copper complexes can be utilized as power sources for low capacity electronics (such as portable devices and wireless sensor networks) and open up a new industrialization path for this scientifically well-established technology.

## Keywords

Dye sensitized solar cell, copper redox mediators, copper complexes, charge recombination, dye regeneration, copper electrolyte

# Résumé

Les technologies photovoltaïques attirent beaucoup d'attention en raison de la forte augmentation de la consommation énergétique mondiale mais aussi à cause des conséquences inhérentes liées à l'utilisation des sources conventionnelles d'énergies. De ce fait, l'efficacité énergétique (EE) de ces diverses technologies photovoltaïques ne cesse de s'améliorer avec pour but d'atteindre la limite théorique de Shockley-Queisser. Cependant, la commercialisation et l'intégration de ces unités photovoltaïques dans domaines divers et variées de la vie de tous les jours, dépend de plusieurs facteurs tels que les coûts de fabrication, la facilité de production et la durabilité des matières premières. La technologie des cellules solaires à colorants (CSCs) se présente comme une sérieuse candidate à la conversion généralisée d'énergie solaire en énergie électrique notamment grâce à leurs faibles coûts de production ainsi qu'à la facilité de fabrication.

Dans une CSC, la tension à circuit ouvert ( $V_{CO}$ ) va dépendre de la différence entre le quasi niveau de Fermi du semi-conducteur ainsi que du potentiel d'oxydoréduction de couple redox présent dans l'électrolyte. Ainsi, en utilisant des couples redox ayant un potentiel d'oxydoréduction très positif, il est possible de réduire la force motrice pour la régénération du colorant et par conséquent augmenter la tension à circuit ouvert. Dans cette thèse, nous avons étudié des complexes de coordinations basés sur le couple Cu(II)/Cu(I) ayant pour ligand deux pyridines connectées aux positions 2,2' et possédant aussi deux groupes méthyl aux positions 6,6'. Ces complexes organométalliques ont été utilisés en tant que couple redox dans les CSCs à électrolyte liquide. La théorie de la fonctionnelle de la densité a permis de prouver l'important rôle que jouaient les groupes méthyls. Ces derniers arrivent en effet à stabiliser les complexes de cuivres par effets stériques ce qui fournit une géométrie de coordination adéquat pour les atomes de cuivre : tétraèdre pour le Cu(I) et tétragone déformée pour le Cu(II). L'optimisation de ces géométries permet à ces complexes de cuivre de posséder des énergies de réorganisation pour le transfert d'électron selon Marcus minimales. En effet, il est possible de régénérer efficacement le colorant avec une force motrice de 0.1 eV seulement, sans affecter les densités de courants produites. Nous avons ainsi pu fabriqué des cellules solaires ayant une EE supérieur à 10% en utilisant le colorant organique Y123 sous une illumination de  $1000 \text{ W}\cdot\text{m}^{-2}$ .

Ensuite, nous nous sommes concentrés sur les complications liées à la nature des complexes de coordinations à base de cuivre. Nous avons dans un premier temps montré que les complexes de Cu(II) synthétisés à partir de  $\text{CuCl}_2$  avaient différents comportements électrochimiques comparé à leurs analogues de Cu(I). De ce fait nous avons développé trois procédures permettant de produire des complexes de Cu(II) : l'oxydation chimique de complexes de coordination de Cu(I), l'oxydation électrochimique de complexes de coordination de Cu(I) et finalement la synthèse chimique en utilisant un le précurseur  $\text{Cu}(\text{TFSI})_2$ . Nous avons ensuite étudié l'effet de l'additif basique 4-tertbutyl pyridine ainsi que d'autres composées similaires sur les performances des CSCs. Nous avons observé que l'ajout d'une de ces bases, modifie la géométrie de coordination des complexes et affect

de ce fait la régénération du colorant ainsi que la vitesse de recombinaison des charges selon la théorie de Marcus.

Nous avons aussi découvert que les complexes  $[\text{Cu}(\text{tmby})_2]^{2+/1+}$  (tmby = 4,4',6,6'-tetraméthyl-2,2'-bipyridine), pouvaient servir de couche de transport de trou dans les cellules solaires à colorant à électrolyte solide. Grâce à ces matériaux, nous avons pu résoudre les problèmes causés par les remplissages des pores qu'il y avait dans les cellules solaires à colorant à électrolyte solide conventionnelles. Ceci nous a ainsi permis d'utiliser des films de  $\text{TiO}_2$  plus épais et ainsi nous avons pu améliorer les EE. De plus en utilisant le même couple de complexes de cuivre dans des CSCs à électrolyte liquide, nous avons pu atteindre une EE de 28.9% en illumination avec une source de 1000 lux.

## Mots-clés

Cellule solaire à colorant, couple redox de cuivre, complexes de coordination de cuivre, recombinaison de charge, régénération du colorant, électrolyte à base de cuivre.



# Abbreviations

ACN	Acetonitrile
AM	Air Mass
bpy	bipyridyl
bpy-pz	6-(1H-pyrazol-1-yl)-2,2'-bipyridine
bpyPY4	6,6'-bis(1,1-di(pyridin-2-yl)ethyl)-2,2'-bipyridine
BTBP	2,6-bis- <i>tert</i> -butylpyridine
CR	Charge Recombination
CB	Conduction Band
CE	Counter Electrode
CPE	Constant Phase Element
D5	3-(5-(4-(diphenylamino)styryl)thiophen-2-yl)-2-cyanoacrylic acid
D35	(E)-3-(5-(4-(bis(2',4'-dibutoxy-[1,1'-biphenyl]-4-yl)amino)phenyl)thiophen-2-yl)-2-cyanoacrylic acid
D45	(E)-3-(5-(4-(bis(2',4'-dimethoxy-[1,1'-biphenyl]-4-yl)amino)phenyl)thiophen-2-yl)-2-cyanoacrylic acid
DFT	Density Functional Theory
dmby	6,6'-dimethyl - 2,2'-bipyridine
dmp	bis(2,9-dimethyl-1,10-phenanthroline)
dpphen	dpphen = 2,9-diphenyl-1,10-phenanthroline
DR	Dye Regeneration
DSC	Dye-sensitized Solar Cell
EIS	Electrochemical Impedance Spectroscopy
eto	4-ethoxy-6,6'-dimethyl-2,2'-bipyridine
FF	Fill Factor
FTO	Fluorine-doped tin oxide
GW	Gigawatt
HOMO	Highest Occupied Molecular Orbital
HTM	Hole Transport Material
IoT	Internet of Things

IPCE	Incident-Photon-to-Current-conversion Efficiency
I-V	Current-Voltage
J-V	Current density-Voltage
LED	Light Emitting Diode
LEG4	3-{6-[4-[bis(2',4'-dibutyloxybiphenyl-4-yl)amino-]phenyl]-4,4-dihexyl-cyclopenta-[2,1-b:3,4-b']dithiophene-2-yl}-2-cyanoacrylic acid
LHE	Light-Harvesting Efficiency
LiTFSI	Lithium bis(trifluoromethylsulfonyl)imide)
LS	Low Spin
LUMO	Lowest Unoccupied Molecular Orbital
MCU	Microcontroller Units
MLCT	Metal to Ligand Charge Transfer
MOP	4-methoxypyridine
NOBF <sub>4</sub>	Nitrosonium tetrafluoroborate
NOP	4-(5-nonyl)pyridine
OTf	trifluoromethanesulfonate
PCE	Power Conversion Efficiency
PEDOT	poly(3,4-ethylenedioxythiophene)
PDTO	1,8-bis(2'-pyridyl)-3,6-dithiaoctane
phen	1,10-phenanthroline
PIA	Photoinduced Absorption Spectroscopy
PN	Propionitrile
PV	Photovoltaic
SEM	Scanning electron microscope
SHE	Standard hydrogen electrode
spiro-MeOTAD	2,2',7,7'-tetrakis(N,N-di-p-methoxyphenylamine)-9,9'-spirobifluorene
ssDSC	Solid-state Dye-sensitized Solar Cell
TAS	Transient Absorption Spectroscopy
TBP	4-tert-butylpyridine
TCO	Transparent Conductive Oxide
TC-SPC	Time-Correlated Single-Photon Counting
TFSI	bis(trifluoromethylsulfonyl)imide)
tmby	4,4',6,6' – tetramethyl - 2,2' - bipyridine

TW	Terawatt
UV	Ultraviolet
UNFCCC	United Nations Framework Convention on Climate Change
WSN	Wireless Sensor Networks
XRD	X-ray Diffraction
XY1	(E)-3-(4-(6-(7-(4-(bis(2',4'-bis((2-ethylhexyl)oxy)-[1,1'-biphenyl]-4-yl)amino)phenyl)benzo[c][1,2,5]thiadiazol-4-yl)-4,4-bis(2-ethylhexyl)-4H-cyclopenta[2,1-b:3,4-b']dithiophen-2-yl)phenyl)-2-cyanoacrylic acid
Y123	3-{6-{4-[bis(2',4'-dihexyloxybiphenyl-4-yl)amino-]phenyl}-4,4-dihexyl-cyclopenta-[2,1-b:3,4-b']dithiophene-2-yl}-2-cyanoacrylic



# Symbols

A	Absorbance
C	Capacitance
C	Concentration
$D$	Diffusion Coefficient
$D_{X1}$	Extended Circuit Element
e	Elementary Charge
$E^0$	Formal Redox Potential
$E_{CB}$	Conduction Band Edge Potential
eV	Elektronvolt
F	Faraday Constant
f	Oscillator Strength
$H_{AB}$	Electronic Coupling
$j_0$	Exchange Current Density
$J_{max}$	Current density at maximum power
$J_{sc}$	Short Circuit Current Density
k	Rate constants
$k_B$	Boltzmann Constant
$n_{CB}$	Density of electrons in the conduction band
$N_{CB}$	Density of states in the conduction band
$P_{in}$	Input Power
$P_{max}$	Maximum Power Output
q	Elementary charge
$Q_{oc}$	Extracted charge
R	Gas Constant
$R_s$	Resistance
r	Spatial separation of the donor and acceptor states
T	Temperature

$V_{\max}$	Potential at maximum power
$V_{\text{OC}}$	Open Circuit Potential
$\beta$	Measure of barrier height
$\delta_{\text{cc}}$	Center-to center distance
$\Delta E_{\text{exc}}$	First vertical excitation energies
$\Delta G^0$	Reaction free energy
$\Delta G^\#$	Free energy of activation
$\eta$	Solar cell efficiency
$\lambda$	Reorganization energy
$\lambda$	Wavelength
$\varphi_{\text{inj}}$	Injection quantum efficiency
$\Phi_{\text{cc}}$	Charge collection efficiency
$\Phi_{\text{reg}}$	Regeneration efficiency
$\Phi$	Photon flux
$\tau_e$	Electron lifetime
$\tau_{\text{tr}}$	Electron transport time
$\omega$	Frequency

# Contents

<b>Abstract</b> .....	<b>v</b>
<b>Keywords</b> .....	<b>vi</b>
<b>Résumé</b> .....	<b>vii</b>
<b>Mots-clés</b> .....	<b>viii</b>
<b>Abbreviations</b> .....	<b>ix</b>
<b>Symbols</b> .....	<b>xiii</b>
<b>List of Figures</b> .....	<b>xix</b>
<b>List of Tables</b> .....	<b>xxv</b>
<b>List of Equations</b> .....	<b>xxvii</b>
<b>Chapter 1 Introduction</b> .....	<b>1</b>
<b>1.1 Rise in Energy Demand</b> .....	<b>1</b>
<b>1.2 Sunlight as an Energy Source</b> .....	<b>1</b>
<b>1.3 Dye Sensitized Solar Cells</b> .....	<b>3</b>
1.3.1 Components of DSC and Working Principles.....	4
1.3.2 Processes in Dye Sensitized Solar Cells.....	5
<b>1.4 Marcus Theory</b> .....	<b>7</b>
<b>1.5 DSC Redox Mediators</b> .....	<b>8</b>
1.5.1 Advantages and Disadvantages of iodide-triiodide.....	9
1.5.2 Advantages and Disadvantages of Cobalt Redox Mediators.....	9
<b>1.6 Copper Redox Mediators for DSC Applications</b> .....	<b>10</b>
<b>1.7 Main Characterization Techniques</b> .....	<b>13</b>
1.7.1 Current Density-Voltage Characteristics.....	13
1.7.2 Incident-Photon-to-Current-conversion Efficiency (IPCE).....	14
1.7.3 Electrochemical Impedance Spectroscopy.....	16
<b>1.8 Motivation and organization of the study</b> .....	<b>17</b>
<b>Chapter 2 Copper Bipyridyl Redox Mediators for Dye-Sensitized Solar Cells with High Photovoltage</b> .....	<b>19</b>
<b>2.1 Introduction</b> .....	<b>19</b>
<b>2.2 Results and Discussion</b> .....	<b>21</b>
2.2.1 Electrochemical and Spectroscopic Data.....	21
2.2.2 Density Functional Theory Calculations (DFT).....	25
2.2.3 Photovoltaic Performance of Dye-sensitized Solar Cells with Copper Complexes.....	27

2.2.4	Electron Lifetime Measurements .....	28
2.2.5	Dye regeneration .....	30
2.2.6	Transient Absorption Spectroscopy .....	31
<b>2.3</b>	<b>Conclusion .....</b>	<b>32</b>
<b>2.4</b>	<b>Experimental .....</b>	<b>32</b>
<b>Chapter 3</b>	<b>Methods for producing electrochemically clean Cu(II)-bipyridine complexes.....</b>	<b>37</b>
<b>3.1</b>	<b>Introduction.....</b>	<b>37</b>
<b>3.2</b>	<b>Results and Discussion .....</b>	<b>38</b>
3.2.1	Cu(II)-bipyridine complexes from the chemical oxidation of Cu(I) species .....	38
3.2.2	Preparation of electrochemically clean Cu(II)-bipyridine complexes .....	39
3.2.3	Synthesis of electrochemically and optically clean Cu(tmby) <sub>2</sub> TFSI <sub>2</sub> .....	40
<b>3.3</b>	<b>Conclusion .....</b>	<b>42</b>
<b>3.4</b>	<b>Methods .....</b>	<b>43</b>
<b>Chapter 4</b>	<b>Effect of Pyridine-derivative Bases in Dye-Sensitized Solar Cells Employing Copper Redox Mediator</b>	<b>45</b>
<b>4.1</b>	<b>Introduction.....</b>	<b>45</b>
<b>4.2</b>	<b>Results and Discussion .....</b>	<b>47</b>
4.2.1	Effect of TBP on copper redox mediators .....	47
4.2.2	Effect of other pyridine bases .....	50
4.2.3	Solar cells performance.....	55
4.2.4	Electron Lifetime and Charge Extraction Measurements .....	56
4.2.5	Stability of DSC devices .....	57
<b>4.3</b>	<b>Conclusion .....</b>	<b>58</b>
<b>4.4</b>	<b>Experimental Section.....</b>	<b>59</b>
<b>Chapter 5</b>	<b>The Effect of Coordination Sphere of Copper Redox Mediators on Regeneration and Recombination Behavior in Dye-sensitized Solar Cell Applications.....</b>	<b>61</b>
<b>5.1</b>	<b>Introduction.....</b>	<b>62</b>
<b>5.2</b>	<b>Results and Discussion .....</b>	<b>63</b>
5.2.1	Electrochemical and Spectroscopic Data of Novel Cu(I)(eto) <sub>2</sub> and Cu(II)(eto) <sub>2</sub> .....	63
5.2.2	Photovoltaic Performance.....	64
5.2.3	Photoinduced Absorption Spectroscopy.....	66
5.2.4	Transient Absorption Spectroscopy.....	67
5.2.5	Electron lifetime and charge extraction measurements .....	69
5.2.6	Electrochemical Impedance Spectroscopy.....	70
5.2.7	Rest Potential Measurements.....	71
5.2.8	Density functional theory calculations.....	72
<b>5.3</b>	<b>Conclusion .....</b>	<b>77</b>
<b>5.4</b>	<b>Methods .....</b>	<b>78</b>
<b>Chapter 6</b>	<b>Solid-State Dye-Sensitized Solar Cells with Copper (II/I) Hole Transport Materials .....</b>	<b>81</b>
<b>6.1</b>	<b>Introduction.....</b>	<b>81</b>
<b>6.2</b>	<b>Results and Discussion .....</b>	<b>82</b>
6.2.1	Cu(II/I) complexes for ssDSCs .....	82



6.2.2	Rapid hole transport in solid Cu(II/I) HTM.....	85
6.2.3	Crystallinity of solid Cu(II/I) HTM.....	86
6.2.4	Interfacial charge transport dynamics in Cu(II/I) based ssDSC.....	88
6.2.5	Cu(II/I) HTM for record efficiency ssDSC.....	90
<b>6.3</b>	<b>Conclusion</b> .....	<b>91</b>
<b>6.4</b>	<b>Methods</b> .....	<b>91</b>
<b>Chapter 7</b>	<b>Performance of Dye-Sensitized Solar Cells under Ambient Lighting</b> .....	<b>95</b>
<b>7.1</b>	<b>Introduction</b> .....	<b>95</b>
<b>7.2</b>	<b>Results and Discussion</b> .....	<b>97</b>
7.2.1	Photovoltaic performance of co-sensitized DSCs with [Cu(tmby) <sub>2</sub> ] <sup>+2/+1</sup> as redox shuttle.....	97
7.2.2	Transient absorption and steady-state absorption spectroscopy.....	101
7.2.3	DSCs performance under indoor-light conditions.....	102
<b>7.3</b>	<b>Conclusions</b> .....	<b>106</b>
<b>7.4</b>	<b>Methods</b> .....	<b>106</b>
<b>Conclusion</b>	.....	<b>109</b>
	Achieved results.....	109
	Future development.....	109
<b>Chapter 8</b>	<b>Appendix</b> .....	<b>111</b>
<b>8.1</b>	<b>Appendix to Chapter 2</b> .....	<b>111</b>
8.1.1	Methods and computational details.....	111
8.1.2	Synthesis of copper 2,2'-dimethyl phenanthroline (Cu <sup>(III)</sup> (dmp) <sub>2</sub> TFSI <sub>1/2</sub> ).....	112
8.1.3	Synthesis of copper complexes: 6,6'-dimethyl-2,2'-bipyridine (Cu <sup>(III)</sup> (dmby) <sub>2</sub> TFSI <sub>1/2</sub> ) (3,4) and 4,4',6,6'-tetramethyl-2,2'-bipyridine.....	113
<b>8.2</b>	<b>Appendix to Chapter 5</b> .....	<b>114</b>
8.2.1	Synthetic procedures.....	114
<b>8.3</b>	<b>Appendix to chapter 6</b> .....	<b>118</b>
<b>References</b>	.....	<b>123</b>
<b>Acknowledgements</b>	.....	<b>133</b>
<b>Curriculum Vitae</b>	.....	<b>135</b>



# List of Figures

Figure 1-1 Spectral irradiance of AM 0, AM 1.5Global and AM 1.5Direct Spectrums (ASTM G173-03).	2
Figure 1-2 Schematic diagram of a DSC.	5
Figure 1-3 Main processes in a DSC device.	5
Figure 1-4 a) Parabolic potential energy curves for reactant and product encounter pairs and b) Representation of Marcus normal and inverted domains.	8
Figure 1-5 Some of the reported ligands for copper redox mediators in DSC applications and the redox potentials of the corresponding complexes.	13
Figure 1-6 A typical JV curve under illumination and dark conditions.	14
Figure 1-7 Typical IPCE (left) and integrated current density (right) curves for a DSC.	15
Figure 1-8 Equivalent circuit models for a DSC for a) high b) intermediate and c) low potentials and Nyquist plots of a D45-sensitized device employing cobalt redox mediator at different applied potential biases d) high (900 mV) e) intermediate (563 mV) and f) low (169 mV).	17
Figure 2-1 a) Schematic representation of energy levels in dye-sensitized solar cells. Molecular structures of the b) Y123 dye c) $\text{Cu}(\text{dmp})_2^{2+/1+}$ d) $[\text{Cu}(\text{dmby})_2]^{2+/1+}$ and e) $[\text{Cu}(\text{tmby})_2]^{2+/1+}$ complexes.	21
Figure 2-2 Cyclic voltammograms of 5 mM solutions of (a) $[\text{Cu}(\text{dmp})_2][\text{TFSI}]$ (red curves) and $[\text{Cu}(\text{dmp})_2][\text{TFSI}]_2$ (blue curves), (b) $[\text{Cu}(\text{dmby})_2][\text{TFSI}]$ (red curves) and $[\text{Cu}(\text{dmby})_2][\text{TFSI}]_2$ (blue curves) (c) $[\text{Cu}(\text{tmby})_2][\text{TFSI}]$ (red curves) and $[\text{Cu}(\text{tmby})_2][\text{TFSI}]_2$ (blue curves) in 0.1 M LiTFSI/acetonitrile. Scan rate 10 mV/s. Dashed lines are voltammograms of the same species but after adding 4-tert-butylpyridine (12.5 mM concentration). Potentials are referenced to the Ag/AgCl (sat'd LiCl in ethanol) reference electrode. A standard ferrocene couple was 0.469 V vs. Ag/AgCl (with no significant influence of TBP addition).	23
Figure 2-3 Right chart: Cyclic voltammograms of 5 mM solutions of $[\text{Cu}(\text{tmby})_2][\text{TFSI}]_2$ (red curves) and the same complex after addition of 0.5 or 1 equivalents of ferrocene (blue or black curves, respectively) in 0.1 M LiTFSI/acetonitrile. Left chart: product of chemical oxidation of $[\text{Cu}(\text{tmby})_2][\text{TFSI}]_2$ by ascorbic acid (blue curve is for the same solution after adding ferrocene). Scan rate 10 mV/s.	23
Figure 2-4 UV-Vis spectra of $\text{CuL}_2\text{TFSI}_{1/2}$ (L= ligand) in acetonitrile solution, concentration 50 $\mu\text{M}$ (blue curves), 0.5 mM (red curves) and 5 mM (black curves). Optical cell thickness 2 mm.	24
Figure 2-5 UV-Vis spectrum of the actual electrolyte solution (diluted 1000 x with acetonitrile). For comparison, the spectra of individual components are shown too. The actual working electrolyte solutions prepared without TBP is displayed by the blue curve. Optical cell thickness 2 mm.	25
Figure 2-6 Cu(I) $\text{L}_2$ minimum-energy structures, L is dmp (a), dmby (b) and tmby (c).	26
Figure 2-7 Cu(II) $\text{L}_2$ minimum-energy structures, L is dmp (a), dmby (b) and tmby (c).	26
Figure 2-8 Photocurrent density vs voltage (J-V) curves measured under standard AM 1.5G illumination and in the dark for solar cells sensitized with Y123 dye and employing copper complexes.	27
Figure 2-9 IPCE spectra of DSC devices sensitized with Y123 dye	28
Figure 2-10 Electron lifetimes for the three copper complexes.	29
Figure 2-11 Charge extraction data obtained for devices with different electrolytes ( $E_{F,\text{TiO}_2} = E_{F,\text{redox}} - V_{oc}$ )	30
Figure 2-12 Light intensity dependence of (A) short-circuit current and (B) photovoltage for DSC devices based on the three different copper electrolytes.	30
Figure 2-13 PIA spectra of Y123 sensitized $\text{TiO}_2$ with an inert electrolyte and with electrolytes prepared with the three different copper complexes.	31
Figure 2-14 Transient absorption spectroscopy measurements of Y123 sensitized $\text{TiO}_2$ films with inert, $[\text{Cu}(\text{dmby})_2]^{2+/1+}$ , $[\text{Cu}(\text{tmby})_2]^{2+/1+}$ and $[\text{Cu}(\text{dmp})_2]^{2+/1+}$ electrolytes.	32

Figure 3-1 Cyclic voltammograms of  $[\text{Cu}(\text{tmby})_2][\text{TFSI}]$  and the products of its chemical oxidation by NOBF<sub>4</sub>. Scan rate 10 mV/s. Curve 'start' (red): cyclic voltammogram of the starting 5 mM solution of  $[\text{Cu}(\text{tmby})][\text{TFSI}]_2$  in 0.1 M LiTFSI + acetonitrile. The other voltammograms are for the products obtained upon addition of the given amount of NOBF<sub>4</sub> and/or equilibration by aging (see annotation in the graph). 39

Figure 3-2 Cyclic voltammograms of the products and intermediates of preparative electrolysis of  $[\text{Cu}(\text{tmby})_2][\text{TFSI}]$  on Pt electrode. Scan rate 10 mV/s. Curve 'start' (red): cyclic voltammogram of the initial 5 mM solution of  $[\text{Cu}(\text{tmby})_2][\text{TFSI}]$  in 0.1 M LiTFSI + acetonitrile. Voltammograms E1-E5 are for the same solution after potentiostatic oxidation at 1.1-1.4 V under stirring in divided cell. The passed charge (in equivalents of the starting amount of the Cu(I) complex) corresponds to: 0.19 eq (E1), 0.40 eq (E2), 0.60 eq (E3), 0.80 eq (E4) and 0.92 eq (E5). Right chart compares the voltammograms of the starting (start) and final (E5) complexes with the voltammogram (as rec.) of the  $[\text{Cu}(\text{tmby})_2][\text{TFSI}]_2$  species grown by the standard preparative protocol. 40

Figure 3-3 UV-Vis absorption spectrum of a solution (6.44 mg/mL in acetonitrile) of typical CuYS product prepared by our new synthetic protocol (black curve). Red dashed curve is the spectrum of a 0.5 mM solution of pure  $\text{Cu}(\text{tmby})_2\text{TFSI}$ . Blue dashed curve is the spectrum of 5 mM solution of pure  $\text{Cu}(\text{tmby})_2\text{TFSI}_2$  obtained by preparative electrolysis. Inset shows the cyclic voltammogram of the same CuYS in 0.1 M LiTFSI + acetonitrile (6.50 mg CuYS/mL) on a Pt electrode, scan rate 10 mV/s (black curve). Inset further shows the control cyclic voltammograms of pure complexes, i.e.  $\text{Cu}(\text{tmby})_2\text{TFSI}$  (red dashed curve) and  $\text{Cu}(\text{tmby})_2\text{TFSI}_2$  (blue dashed curve), both in 5 mM solutions in acetonitrile + 0.1 M LiTFSI. 41

Figure 4-1 Molecular structures of a) 4-*tert* butylpyridine, b) 2,6-bis-*tert*-butylpyridine, c) 4-methoxy pyridine, d) 4-(5-nonyl)pyridine. 46

Figure 4-2 Electrochemical activity of FTO supported thin film of PEDOT tested on symmetrical dummy cells. Top charts: Electrolyte solution:  $\text{Co}(\text{bpy})_3^{3+/2+} \text{TFSI}_{3/2}$  in propionitrile with (blue curves) or without (red curves) the addition of 4-*tert*-butylpyridine. Bottom charts: Electrolyte solution  $\text{Cu}(\text{dmp})_2^{2+/+} \text{TFSI}_{2/1}$  in propionitrile with (blue curves) or without (red curves) the addition of 4-*tert*-butylpyridine. Left charts: Cyclic voltammograms, scan rate 10 mV/s. Right charts: Nyquist plots of electrochemical impedance spectra measured at 0 V from 100 kHz to 0.1 Hz. (Markers are experimental points, dashed lines are simulated fits to the equivalent circuit). 47

Figure 4-3 Cyclic voltammetry at a Pt-electrode in 0.1 M LiTFSI, scan rate 20 mV/s.  $\text{Co}(\text{bpy})_3\text{TFSI}_2$  (red) and  $\text{Co}(\text{bpy})_3\text{TFSI}_3$  (blue); concentration 2.5 mM. Dashed lines after addition of 0.5 M (TBP). These Co-complexes exhibit the expected voltammograms in both oxidation states, i.e. identical formal potentials and only shifted currents. The found formal potential is identical to the literature value<sup>54</sup> and the influence of TBP addition is negligible. 48

Figure 4-4 Cyclic voltammograms of 5 mM  $\text{Cu}(\text{tmby})_2\text{TFSI}$  in 0.1 M LiTFSI + acetonitrile, scan rate 10 mV/s. Dashed curves show the voltammograms in absence of any bases. Full curves show the same voltammograms upon addition of the corresponding bases in 15 mM concentration. 50

Figure 4-5 Differential pulse voltammograms of 5 mM  $\text{Cu}(\text{tmby})_2\text{TFSI}$  in 0.1 M LiTFSI + acetonitrile. Dashed curve shows the voltammogram in absence of any bases. Full curves show the same voltammograms upon addition of the respective bases in 15 mM concentration. 51

Figure 4-6 Electrochemical tests of PEDOT/PEDOT symmetrical dummy cells with  $\text{Cu}(\text{tmby})_2\text{TFSI}_{2/1}$  electrolyte solution containing various pyridine bases. Chart (a): Cyclic voltammograms, scan rate 50 mV/s. The voltammograms are offset for clarity, but the current scales are identical for all plots. Chart (b): Nyquist plots of electrochemical impedance spectra measured at 0 V; markers are experimental points, dashed lines are fits to the equivalent circuit which is shown in inset. For clarity of presentation, impedance spectra (except for the spectrum labeled MOP) are offset in the  $Z'$  scale to avoid crossing of curves. The respective values of offsets applied on the bottom axis in Fig. 4b are as follows: NOP (2.6  $\Omega\text{cm}^2$ ), TBP (4.1  $\Omega\text{cm}^2$ ), no base (4.2  $\Omega\text{cm}^2$ ), BTBP (4.6  $\Omega\text{cm}^2$ ). 52

Figure 4-7 a) Cyclic voltammograms (scan rate of 50 mV/s) of PEDOT/PEDOT symmetrical dummy cells in  $\text{Co}(\text{bpy})_3\text{TFSI}_{3/2}$  electrolyte solution containing various pyridine bases. The voltammograms are offset for clarity, but the current scale is identical for all plots. b) Nyquist plots of electrochemical impedance spectra of PEDOT/PEDOT symmetrical dummy cells. Electrolyte solution  $\text{Co}(\text{bpy})_3\text{TFSI}_{3/2}$  containing various pyridine bases, measured at 0 V. Markers are experimental points, dashed lines are fits to the equivalent circuit which

is shown in the main text. For clarity of presentation, some impedance spectra are offset in the $Z'$ scale as follows: BTBP ( $0.1 \Omega\text{cm}^2$ ), TBP ( $1 \Omega\text{cm}^2$ ), MOP ( $2 \Omega\text{cm}^2$ ), No base ( $3 \Omega\text{cm}^2$ ). .....	52
Figure 4-8 Empirical correlation of formal rate constant of charge transfer ( $k_0$ ), diffusion resistance ( $R_w$ ) and overall cell resistance ( $R_{CV}$ ) with $\text{pK}_a$ values of the corresponding bases which were added to the electrolyte solution (BTBP, TBP, NOP and MOP). Data from EIS on PEDOT/PEDOT symmetrical cells for Co-mediated systems (left chart) and Cu-mediated systems (right chart). .....	54
Figure 4-9 Electrochemical impedance spectrum of a complete solar cell with Y123-sensitized $\text{TiO}_2$ photoanode and PEDOT counterelectrode measured in dark at the applied forward bias of $-1.2 \text{ V}$ . Open circles are experimental points, dashed curve is a fitted spectrum. The equivalent circuit used for spectra fitting is shown in inset to the left chart. Electrolyte solution: $0.2 \text{ M Cu(tmby)}_2\text{TFSI} + 0.06 \text{ M Cu(tmby)}_2\text{TFSI}_2 + 0.1 \text{ M LITFSI}$ in acetonitrile + $0.6 \text{ M TBP}$ (left chart) or NOP (right chart). .....	54
Figure 4-10 a) Photocurrent density vs. voltage curves measured under standard AM1.5G illumination. DSC devices employed Y123 dye, $\text{Cu(tmby)}_2^{2+/+}$ redox mediator and four different pyridine bases as labeled in the annotation b) IPCE spectra of DSC devices sensitized with Y123 dye. ....	55
Figure 4-11 a) Electron lifetimes for the DSC devices Y123 dye, $[\text{Cu(tmby)}_2]^{2+/+}$ redox mediator and the three different pyridine bases as labeled in the annotation. b) Charge extraction data for the DSC devices with Y123 dye, $[\text{Cu(tmby)}_2]^{2+/+}$ redox mediator and the three different pyridine bases as labeled in the annotation. ....	56
Figure 4-12 Evaluation of durability over 300 h at 0.5 sun illumination. The tested DSCs devices employ $[\text{Cu(tmby)}_2]^{2+/+}$ electrolyte solution with three different pyridine bases as labeled in the annotation. a) Electrical output power ( $\approx 0.5 \text{ PCE}$ ), b) Short circuit photocurrent, c) Open circuit voltage and d) Fill factor. ....	58
Figure 5-1 Molecular structures of and a) D5 b) D45 c) D35 dyes and d) $[\text{Cu(tmby)}_2]^{2+/1+}$ e) $[\text{Cu(eto)}_2]^{2+/1+}$ f) $[\text{Cu(dmp)}_2]^{2+/1+}$ g) $[\text{Cu(dmby)}_2]^{2+/1+}$ complexes. ....	63
Figure 5-2 a) Cyclic Voltammogram of $[\text{Cu(eto)}_2]^{1+}$ complex. b) Molecular extinction coefficients of $[\text{Cu(eto)}_2]^{1+}$ and $[\text{Cu(eto)}_2]^{2+}$ complexes. ....	64
Figure 5-3 a) HOMO levels of D5, D35 and D45 dyes and formal redox potentials of the Cu(I) species. b-d) Current density versus applied potential curves under dark and $100 \text{ W/cm}^2$ AM1.5G illumination for DSCs devices measured with a mask aperture of $0.158 \text{ cm}^2$ . ( $[\text{Cu(dmby)}_2]^{2+/1+}$ (Blue), $[\text{Cu(tmby)}_2]^{2+/1+}$ (Red), $[\text{Cu(eto)}_2]^{2+/1+}$ (Purple), $[\text{Cu(dmp)}_2]^{2+/1+}$ (Green), and $[\text{Co(bpy)}_3]^{3+/2+}$ (Black)). ....	65
Figure 5-4 IPCE spectra of D35 and D5 sensitized DSC devices employing the three copper complex electrolytes. ....	66
Figure 5-5 Photoinduced absorption spectroscopy spectra of D5 and D35 sensitized $\text{TiO}_2$ films with the inert and the three copper complex electrolytes. ....	67
Figure 5-6 Transient absorption spectroscopy measurements of a) D5 b) D35 and c) D45 sensitized $\text{TiO}_2$ films with inert, $[\text{Cu(dmby)}_2]^{2+/1+}$ , $[\text{Cu(tmby)}_2]^{2+/1+}$ , $[\text{Cu(eto)}_2]^{2+/1+}$ and $[\text{Cu(dmp)}_2]^{2+/1+}$ electrolytes. ....	68
Figure 5-7 Electron lifetime versus Charge extraction data obtained from the Toolbox measurements for a) D35 b) D45 and c) D5 sensitized $\text{TiO}_2$ films. $[\text{Cu(dmby)}_2]^{2+/1+}$ (blue squares), $[\text{Cu(tmby)}_2]^{2+/1+}$ (red triangles), and $[\text{Cu(dmp)}_2]^{2+/1+}$ (green circles), and $[\text{Co(bpy)}_3]^{3+/2+}$ (yellow diamonds). ....	69
Figure 5-8 Dark currents, Recombination Resistance and Capacitance values obtained from the Electrical Impedance Spectroscopy measurements. $[\text{Cu(dmby)}_2]^{2+/1+}$ (Blue squares), $[\text{Cu(tmby)}_2]^{2+/1+}$ (Red triangles), $[\text{Cu(eto)}_2]^{2+/1+}$ (Purple stars), $[\text{Cu(dmp)}_2]^{2+/1+}$ (Green circles), and $[\text{Co(bpy)}_3]^{3+/2+}$ (Yellow diamonds). ....	71
Figure 5-9 a) $[\text{Cu(tmby)}_2]^{1+}$ (left) and $[\text{Cu(tmby)}_2]^{2+}$ (right) b) $[\text{Cu(eto)}_2]^{1+}$ (left) $[\text{Cu(eto)}_2]^{2+}$ (right) minimum-energy structures without and with TBP (top and bottom, respectively) calculated at the DFT-B3LYP-D3BJ level of theory in acetonitrile (PCM). ....	73
Figure 5-10 a) $[\text{Cu(dmp)}_2]^{1+}$ (left) and $[\text{Cu(dmp)}_2]^{2+}$ (right) b) $[\text{Cu(dmby)}_2]^{1+}$ (left) and $[\text{Cu(dmby)}_2]^{2+}$ (right) minimum-energy structures without and with TBP (top and bottom, respectively) calculated at the DFT-B3LYP-D3BJ level of theory in acetonitrile (PCM). ....	73
Figure 6-1 DSCs with the Cu(II/I) hole conductor and Y123 sensitizer. a) Schematic structures of the hole conductors based on $[\text{Cu(tmby)}_2](\text{TFSI})_2$ and $[\text{Cu(tmby)}_2](\text{TFSI})$ , and the dye molecule Y123. b) Evolution of	

- the PCE of unsealed DSCs. c) Evolution of the  $J_{sc}$  of unsealed DSCs. d) Evolution of the  $V_{oc}$  of unsealed DSCs. e) Evolution of the FF of the unsealed DSCs. The unsealed DSCs were stored in ambient air in the dark. The photovoltaic parameters of solar cells were measured under standard AM1.5G conditions. The red symbols and error bars indicate the sealed DSCs based on the volatile electrolyte. The royal blue symbols and error bars indicate unsealed DSCs. The average (symbols) and standard deviation (error bars) were calculated from samples of between four and 22 solar cells..... 83
- Figure 6-2 a) A SEM image of an electrode of FTO/TiO<sub>2</sub>/Y123 with a poor contact with Cu(II/I) HTM. Scar bar: 2  $\mu\text{m}$ . The unsealed DSC with the liquid electrolyte was kept under a lower pressure to accelerate the evaporation of solvents in the electrolyte. After drying, the PEDOT counter electrode was removed to obtain the FTO/TiO<sub>2</sub>/Y123/HTM sample for SEM measurement. b) XRD of the sample prepared in (a), featuring reflection peaks from the HTM..... 84
- Figure 6-3 Solid Cu(II/I) hole conductor in ssDSC. a) Cross-sectional SEM of a ssDSC without the counter electrode. Moving from the bottom to the top, layers of FTO (cyan), 3.5  $\mu\text{m}$ -thick transparent mesoscopic TiO<sub>2</sub> + 3.0  $\mu\text{m}$ -thick light scattering TiO<sub>2</sub> (red), and 2.0  $\mu\text{m}$ -thick solid Cu(II/I) hole conductor overlayer (red) are visible. b) Photovoltage-dependent conductivity in the solid hole conductor and the volatile electrolyte of solar cells as obtained from the EIS analysis. The solar cells were measured under illumination with an intensity of 1,000 W/m<sup>2</sup> from a white light-emitting diode. The average (symbols) and standard deviation (error bars) were calculated from solar cell numbers between four and six. .... 84
- Figure 6-4 a) Cross sectional image of the Y123-sensitized TiO<sub>2</sub> film infiltrated with the Cu(II/I) HTM. b) Energy dispersive spectroscopy indicating various elements. Elementary mapping of c) Sn, d) O, e) Ti and f) Cu ..... 85
- Figure 6-5 J-V curves of a DSC with a tris-(bipyridine) cobalt(II/III) redox mediator electrolyte under AM1.5G conditions. The solid curve is J-V of the DSC with the liquid electrolyte (PCE = 9.8%,  $J_{sc}$  = 14.16 mA/cm<sup>2</sup>,  $V_{oc}$  = 950 mV and FF = 0.732). The dash curve is J-V of the unsealed DSC by releasing solvents in the electrolyte for 150 min through an unsealed hole on a counter electrode (PCE = 0.1%,  $J_{sc}$  = 0.21 mA/cm<sup>2</sup>,  $V_{oc}$  = 933 mV and FF = 0.552). The solar cell is composed of Y123-sensitized TiO<sub>2</sub> film (3.5  $\mu\text{m}$  + 3  $\mu\text{m}$ ), a graphene based counter electrode<sup>3</sup>, and a liquid electrolyte. The composition of electrolyte is 0.25 M [Co(BPY)<sub>3</sub>](BCN<sub>4</sub>)<sub>2</sub> (BPY = bipyridyl), 0.06 M [Co(BPY)<sub>3</sub>](BCN<sub>4</sub>)<sub>3</sub>, 0.1 M LiTFSI and 0.6 M TBP in acetonitrile..... 86
- Figure 6-6 Comparison of amorphous and crystalline Cu(II/I) hole conductor. a) Incident light intensity ( $P_{in}$ )-dependent  $J_{sc}$  of ssDSCs with amorphous and crystalline hole conductors. The red lines are linear fits of the data. b) XRD of amorphous and crystalline Cu(II/I) hole conductors in conjunction with Y123-sensitized TiO<sub>2</sub> film on FTO glass substrate. c) Absorption spectra for the amorphous and crystalline Cu(II/I) hole conductors. d) Photoluminescence decay dynamics of amorphous Cu(II/I) hole conductor. e) Photoluminescence decay dynamics of crystalline Cu(II/I) hole conductor. The traces were collected at 670 nm with photoluminescence maximum following nanosecond laser pulsed excitation at 408 nm. The black dot symbols are instrument response function. The red lines are bi-exponential fits of the data. .... 87
- Figure 6-7 Steady-state photoluminescence spectra of [Cu(tmby)<sub>2</sub>](TFSI) and [Cu(tmby)<sub>2</sub>](TFSI)<sub>2</sub> drop-casted on glass substrates from acetonitrile solution containing 0.1 M LiTFSI and 0.6 M TBP. .... 88
- Figure 6-8 Time resolved laser spectroscopy of interfacial electron transfer involving Y123 dye molecules. a) Transient absorption traces were probed at 650 nm following femtosecond laser pulsed excitation at 550 nm. b) Transient absorption traces were probed at 715 nm following nanosecond laser pulsed excitation at 532 nm. Samples: Al<sub>2</sub>O<sub>3</sub>/Y123/inert electrolyte (gray); TiO<sub>2</sub>/Y123/inert electrolyte (olive); TiO<sub>2</sub>/Y123/Cu(II/I) HTM (royal blue). The inert electrolyte contains 0.1 M LiTFSI and 0.6 M TBP in acetonitrile. The red lines are mono exponential fits of the data..... 89
- Figure 6-9 Performance of ssDSC with Cu(II/I) HTM. a) Histogram of PCE of our ssDSCs based on [Cu(tmby)<sub>2</sub>]<sup>2+/+</sup> as a hole conductor, compared to the reported PCEs of efficient ssDSCs using CuSCN, Cu, [Co(bpyPY<sub>4</sub>)]<sup>3+/2+</sup>, PEDOT, spiro-MeOTAD, Cs<sub>2</sub>SnI<sub>6</sub> or [Cu(dmp)<sub>2</sub>]<sup>2+/+</sup> as hole conductors. b) The J-V curves of a champion ssDSCs under standard AM1.5G with irradiation intensities of 1,000 (royal blue), 500 (red) and 100 W/m<sup>2</sup> (olive). c) IPCE spectrum and  $J_{sc}$  calculated from the overlap integral of the IPCE with the standard AM1.5G emission spectrum (ASTM G173-03). d) Evolution of normalized  $P_{max}$ ,  $J_{max}$  and  $V_{max}$  of our ssDSC operating at output maximum power under irradiation of 500 W/m<sup>2</sup>. .... 90

Figure 7-1 a) Schematic representation of the energy levels of the sensitizers XY1 and D35 and possible electron-transfer processes and molecular structures of b) XY1 and c) D35. ....	96
Figure 7-2 UV-Vis spectra of the dyes D35 (orange solid line) and XY1 (purple dashed line).....	97
Figure 7-3 Photovoltaic characteristics of D35/XY1 co-sensitized systems with Cu(tmby) <sub>2</sub> as redox mediator. a) measured J-V curves of at 12 mWcm <sup>-2</sup> (10% sun) b) 100mWcm <sup>-2</sup> (100% sun) for (a) D35, (b) 10:1 D35:XY1, (c) 4:1 D35:XY1, (d) 1:1 D35:XY1, (e) 1:4 D35:XY1, (f) 1:10 D35:XY1, to (g) pure XY1, c) of the champion solar cell at the ratio of 4:1 (D35:XY1) at 100 %, 50% and 10% sun (solid lines) and the corresponding dark currents (dashed line) d) dependence of the photo-current dynamics on the solar light intensity for the champion solar cell.....	99
Figure 7-4 IPCE spectra of DSCs co-sensitized at various dye ratios. (a) D35, (b) 10:1 D35:XY1, (c) 4:1 D35:XY1, (d) 1:1 D35:XY1, (e) 1:4 D35:XY1, (f) 1:10 D35:XY1, to (g) pure XY1 .....	100
Figure 7-5 Extracted charge at open circuit voltage (V <sub>oc</sub> ) and electron lifetime as function of V <sub>oc</sub> . Left panel: Extracted charge at open circuit voltage (V <sub>oc</sub> ) and right panel: electron lifetime as function of V <sub>oc</sub> for DSCs employing pure (a) D35, (b) 10:1 D35:XY1, (c) 4:1 D35:XY1, (d) 1:1 D35:XY1, (e) 1:4 D35:XY1, (f) 1:10 D35:XY1, to (g) XY1 .....	101
Figure 7-6 Absorption Spectroscopy and time resolved laser spectroscopy of interfacial electron transfer involving the D35 and XY1 sensitizers. a) Photoinduced Absorption (PIA) spectra of dye-sensitized TiO <sub>2</sub> electrodes with different dye solution ratios of D35 and XY1 organic dyes, from pure (a) D35, (b) 10:1 D35:XY1, (c) 4:1 D35:XY1, (d) 1:1 D35:XY1, (e) 1:4 D35:XY1, (f) 1:10 D35:XY1, to (g) pure XY1. b) UV-Vis absorption spectra of the corresponding sensitized TiO <sub>2</sub> substrates. Transient absorption decays of the a-g sensitized TiO <sub>2</sub> films following 532 nm excitation with c) inert and d) Cu(tmby) <sup>2+/1+</sup> based electrolyte. The black solid line in both transient absorption decays represents the fit of the signal at the 4:1 D35:XY1 dye ratio. The curves of transient absorption decays have an offset of 0.3 for better visualization.....	102
Figure 7-7 Normalized power spectra of various indoor light sources. For this study OSRAM Warm White 827 (orange, solid line) and OSRAM Warm White 930 (blue, solid line) were used. ....	103
Figure 7-8 Normalized power spectra of various indoor light sources with estimated integrated currents of TiO <sub>2</sub> photoanodes. For this study OSRAM Warm White 827 (orange, solid line) and OSRAM Warm White 930 (blue, solid line) were used. ....	103
Figure 7-9 Photovoltaic characteristics of co-sensitized DSCs measured under indoor light conditions. J-V curves at 200 lux and 1000 lux of DSCs with the co-sensitized dyes, D35:XY1 (4:1), with Cu(tmby) <sub>2</sub> acetonitrile (solid line) and propionitrile (dashed line) based electrolyte.....	105
Figure 8-1 Frontier molecular orbitals (HOMO and LUMO) for Cu(I)(dmp) <sub>2</sub> .....	111
Figure 8-2 Synthetic procedure for Cu <sup>(III)</sup> (dmp) <sub>2</sub> TFSI <sub>1/2</sub> .....	113
Figure 8-3 Synthetic procedure for Cu <sup>(III)</sup> (dmby) <sub>2</sub> TFSI <sub>1/2</sub> ) (3,4) and (Cu <sup>(III)</sup> (tmby) <sub>2</sub> TFSI <sub>1/2</sub> ) (5,6)....	114
Figure 8-4 Synthetic procedure of eto= <sup>2</sup> 4-ethoxy-6,6'-dimethyl-2,2'-bipyridine' ligand. Conditions: (i): 1 eq. mCPBA 75% wt, CHCl <sub>3</sub> , 0°C to RT, o.n., 62%; (ii): 3 eq. KNO <sub>3</sub> , H <sub>2</sub> SO <sub>4</sub> 98%, 120°C, o.n., 57%; (iii): 4 eq. NaH 50% wt, EtOH, 100°C, o.n., 49%; (iv) 3 eq. PBr <sub>3</sub> 1M, CHCl <sub>3</sub> , 60°C, o.n., 81%. ....	114
Figure 8-5 Synthetic procedure for [Cu(eto)2][TFSI] and [Cu(eto)2][TFSI] <sub>2</sub> .....	117
Figure 8-6 (a) Equivalent circuit model to analyze EIS of DSCs based on the volatile electrolyte and the amorphous conductor. At intermediate and higher forward biases, electron transport resistance in TiO <sub>2</sub> is much lower than recombination resistance (R <sub>rec</sub> ). A simplified equivalent circuit <sup>2</sup> , where the transmission line element is replaced by a parallel R <sub>rec</sub> C <sub>μ</sub> circuit, is used to fit the impedance spectra. For liquid DSCs, the equivalent circuit model is composed of a parallel R <sub>rec</sub> C <sub>μ</sub> in series with an RC element for the counter electrode and a Warburg diffusion resistance for the ionic transport in the electrolyte. For ssDSCs, we used a similar equivalent circuit model, where a R <sub>hole</sub> C <sub>hole</sub> element replaces the Warburg impedance. (b) A typical spectroscopy of a DSC measured by EIS. The data can be best fitted by using the equivalent circuit models in (a). The arrow indicates frequency-dependent semi-circle (from high to low frequency) corresponding to the interface of PEDOT/Cu(II/I), the interface of TiO <sub>2</sub> /Y123/Cu(II/I), and the Cu(II/I) transport material in DSCs. (c) Photocurrent-dependent conductivity of the amorphous transport and the volatile electrolyte. The solar cells were measured under irradiation intensity of 1,000 W/m <sup>2</sup> provided by a white light-emitting diode (LED). The conductivity was calculated by L/(A x R), where L (around 9 μm) is the thickness of the hole	

conductor or electrolyte between the two FTO glasses,  $A$  ( $0.286 \text{ cm}^2$ ) is the photoactive area of DSCs and  $R$  is resistance obtained by EIS measurements. The average (symbols) and standard deviation (error bars) were calculated from solar cell number between four and six. .... 118

Figure 8-7 Picosecond time resolved transient absorbance of (a)  $\text{Al}_2\text{O}_3/\text{Y123}/\text{inert}$  electrolyte and (b)  $\text{TiO}_2/\text{Y123}/\text{inert}$  electrolyte. The inert electrolyte contains 0.1 M LiTFSI and 0.6 M TBP in acetonitrile. 119

Figure 8-8 Histogram of (a)  $V_{oc}$ , (b)  $J_{sc}$  and (c) FF of ssDSCs based on the Cu(II/I) HTM..... 120

Figure 8-9 Hysteresis test for an efficient ssDSC based on the Cu(II/I) HTM at different scanning rates. 120



## List of Tables

Table 2-1 Electrochemical and absorption data for Cu(I) and Cu(II) species .....	22
Table 2-2 Free energy differences for the Cu(I) => Cu(II) process ( $\Delta G_{ox}$ ) and corresponding inner-sphere reorganization energy ( $\lambda_{in}$ ).....	26
Table 2-3 J-V characteristics for the $[Cu(dmp)_2]^{2+/1+}$ , $[Cu(dmby)_2]^{2+/1+}$ and $[Cu(tmby)_2]^{2+/1+}$ complexes	27
Table 3-1 Electrochemical parameters of the PEDOT/PEDOT symmetrical dummy cells obtained from fitting of impedance spectra for Cu(tmby) <sub>2</sub> electrolyte in acetonitrile.....	42
Table 4-1 Electrochemical parameters of the PEDOT/PEDOT symmetrical dummy cells obtained from fitting of impedance spectra for Cu(dmp) <sub>2</sub> and Co(bpy) <sub>3</sub> electrolytes in propionitrile.....	49
Table 4-2 Electrochemical parameters of the studied electrolyte solutions with different added bases. Data from PEDOT/PEDOT symmetrical dummy cells obtained from cyclic voltammetry or from fitting of impedance spectra. (Notes: a) Limiting current poorly distinguished, approximate values. b) For comparison, the corresponding $R_{CT}$ and $j_0$ values from EIS on complete solar cells).....	53
Table 4-3 Electrochemical parameters in $[Co(bpy)_3]^{3+/2+}$ electrolyte solutions containing various bases. Results from electrochemical impedance spectra of PEDOT/PEDOT symmetrical dummy cells.....	53
Table 4-4 Characteristics for the studied Cu-mediated DSCs with different bases and Y123 as sensitizer. Illumination intensity 1sun (AM1.5G). .....	55
Table 5-1 J-V Characteristics for D5, D35 and D45 sensitized DSC devices employing $[Cu(tmby)_2]^{2+/1+}$ , $[Cu(eto)_2]^{2+/1+}$ , $[Cu(dmby)_2]^{2+/1+}$ , $[Cu(dmp)_2]^{2+/1+}$ and $[Co(bpy)_3]^{3+/2+}$ electrolytes (all electrolytes have the same concentration of additives 0.1 M LiTFSI and 0.6M TBP). .....	66
Table 5-2 Transient absorption spectroscopy measurements data (halftime/ regeneration efficiency) for the TiO <sub>2</sub> films sensitized with D5, D35 and D45 dyes employing $[Cu(tmby)_2]^{2+/1+}$ , $[Cu(dmby)_2]^{2+/1+}$ , $[Cu(dmp)_2]^{2+/1+}$ and $[Cu(eto)_2]^{2+/1+}$ .....	69
Table 5-3 Rest potentials of $[Cu(tmby)_2]^{2+/1+}$ , $[Cu(dmp)_2]^{2+/1+}$ and $[Co(bpy)_3]^{3+/2+}$ electrolytes and Formal redox potentials of Cu(I) species and $[Co(bpy)_3]^{+2}$ .....	72
Table 5-4 Binding Free Energies ( $\Delta G_{bind}$ ) of TBP on $[CuL_2]^{1+}$ and $[CuL_2]^{2+}$ .....	74
Table 5-5 Free Energy Differences ( $\Delta G_{OX} Cu^I/Cu^{II}$ ) for the Cu(I) → Cu(II) process for complexes without TBP ( $[CuL_2]^{1+}/[CuL_2]^{2+}$ ), with both $[CuL_2]^{1+}$ and $[CuL_2]^{2+}$ coordinated with TBP ( $[CuL_2-TBP]^{1+}/[CuL_2-TBP]^{2+}$ ) and with only $[CuL_2]^{2+}$ coordinated by TBP ( $[CuL_2]^{1+}/[CuL_2-TBP]^{2+}$ ).....	74
Table 5-6 Reorganization energies ( $\lambda$ ) for the Cu(I) → Cu(II) process for complexes without TBP ( $[CuL_2]^{1+}/[CuL_2]^{2+}$ ), with both $[CuL_2]^{1+}$ and $[CuL_2]^{2+}$ coordinated with TBP ( $[CuL_2-TBP]^{1+}/[CuL_2-TBP]^{2+}$ ) and with only $[CuL_2]^{2+}$ coordinated by TBP ( $[CuL_2]^{1+}/[CuL_2-TBP]^{2+}$ ). $\lambda$ for dye regeneration (DR) and charge recombination (CR) indicated .....	75
Table 5-7 Computed electronic properties of D5 and D45 dyes: absorption maximum ( $\lambda_{max}$ ) with corresponding oscillator strength in parenthesis; Energy difference between S <sub>1</sub> and S <sub>0</sub> minima ( $E_{0-0}$ ), internal ( $\lambda_{int}$ ) an external ( $\lambda_{ext}$ ) reorganization energies are computed for the dye regeneration process (D <sup>+</sup> → D). .....	76
Table 5-8 Marcus parameters (Equation 1-9) for dye regeneration. $\Delta G_0$ values are derived from experiments, reorganization energies are from DFT calculations, all the values are in eV.....	76
Table 5-9 Marcus parameter (Equation 1-9) for the charge recombination (CR) process from the CB of the TiO <sub>2</sub> (approximated at -4 eV <sup>130</sup> ) to the electrolyte in the absence of TBP. All values are in eV.....	77
Table 7-1 J-V characteristics of DSCs using co-sensitized photoanodes with D35 and XY1 dye at 12 and 100mWcm <sup>-2</sup> simulated solar light intensity, letters in the first column refer to labels of sensitizing solutions, which contain: a) 0.1mM D35, b) 0.1mM D35 and 0.01mM XY1 c) 0.08mM D35 and 0.02mM XY1, d) 0.05 mM D35 and 0.05 mM XY1, e) 0.02 mM D35 and 0.08 mM XY1, f) 0.01mM D35 and 0.1 mM XY1(1:10), g) 0.1 mM XY1.....	98

Table 7-2 Photovoltaic metrics for DSCs and GaAs solar cells for indoor light sources at 200 lux and 1000 lux. $P_{in}$ and $P_{out}$ express the incoming power of the light and the power out by the solar cell. DSC <sup>a</sup> employs an acetonitrile based electrolyte and DSC <sup>b</sup> employs a propionitrile based electrolyte. The PCEs for the solar cells are determined from Equation 1-10. Flexi-GaAs solar cells are from Alta Devices measured at Gcell Ltd (Newport, South Wales) with configuration: 6 cells of 8.33cm <sup>2</sup> area in parallel and series connected to a mini-module of 50 cm <sup>2</sup> size.....	104
Table 8-1 TD-DFT results: first vertical excitation energies ( $\Delta E_{exc}$ ) and corresponding oscillator strength (f) in acetonitrile solution.....	112
Table 8-2 Geometrical features of the minimum-energy structures for CuL <sub>2</sub> (L=dmp, dmpy, tmby) complexes in acetonitrile solution.....	112
Table 8-3 Photovoltaic parameters of ssDSCs based on Cu(II/I) HTM with different thickness of mesoscopic TiO <sub>2</sub> films. The solar cells were measured under standard AM1.5G conditions.....	121

## List of Equations

Equation 1-1 – Expression of open-circuit potential in a DSC.....	4
Equation 1-2 – Nernst potetial a redox mediator.....	4
Equation 1-3 – Expression of fermi level in a semiconductor.....	4
Equation 1-4 – Quantum injection efficiency.....	5
Equation 1-5 – Regeneration efficiency.....	6
Equation 1-6 – Charge collection efficiency.....	6
Equation 1-7 – Rate equation by Marcus .....	6
Equation 1-8 – Electronic coupling.....	6
Equation 1-9 – Free energy of activation .....	7
Equation 1-10 – Efficiency of a DSC.....	14
Equation 1-11 – Fill Factor.....	14
Equation 1-12 – IPCE Equation.....	15
Equation 1-13 – Integrated current density.....	15
Equation 1-14 – Expression for IPCE .....	15
Equation 1-15 – Light harvesting efficiency.....	15
Equation 3-1 – Chemical oxidation with NOBF <sub>4</sub> .....	37
Equation 3-2 – Impedance of CPE.....	40
Equation 3-3– Exchange current density.....	40
Equation 3-4 – Diffusion impedance .....	41
Equation 4-2 – Dahms-Ruff Equation.....	47
Equation 7-1 – Monoexponential function.....	99



# Chapter 1 Introduction

The section on '1.6. Copper Redox Mediators for DSC applications' is adopted from the following article:

Postprint version of the submitted review paper: 'Metal coordination complexes as redox mediators in regenerative dye-sensitized solar cells' by Yasemin Saygili, Marko Stojanovic, Natalie Flores-Diaz, Shaik M. Zakeeruddin, Nick Vlachopoulos, Michael Gratzel, and Anders Hagfeldt. (Submitted to Inorganics)

My contribution: Writing the section related to copper redox mediators for DSC applications

## 1.1 Rise in Energy Demand

The growth in earth population and economy brings about a drastic increase in energy demand. According to U.S. Energy Information Administration the world energy consumption is expected to rise 28% between 2015 and 2040.<sup>1</sup> Similarly, the energy consumption rate at 2050 is predicted to be 27.6 TW considering the moderate projections on global population, globally averaged domestic product per capita and globally averaged energy intensity values.<sup>2</sup> Until now the greater part of the energy sources were carbon based fossil fuels.<sup>3</sup> Unfortunately, the energy production via these carbon-based materials brings about problems of environmental pollution and carbon dioxide (CO<sub>2</sub>) emission. In particular, increase in the atmospheric CO<sub>2</sub> concentration severely affects average mean global temperature and climates. The consequent global warming appears as a common concern of human-kind, which irreversibly threatens all ecosystems and biodiversity.

In order to satisfy the future energy demand without damaging the environment, non-CO<sub>2</sub> emitting and carbon neutral energy technologies should be advanced and adopted. Sustainable lifestyles/consumption patterns should be supported and a public awareness should be raised together with the technologic progress and technology based enforcements. According to the Paris Agreement<sup>4</sup>, (which was adopted under the United Nations Framework Convention on Climate Change (UNFCCC)), the global temperature rise should be limited below 2 °C. Thus, the delegate countries are responsible to take effective measures until 2020.

In 2017, 8.4% of the global electricity production was sustained by renewable energy sources including the energy obtained by wind, geothermal, solar, biomass and waste conversion. It was reported that the share of power generation by renewables have been raised 6.1% since 2007.<sup>5</sup> Considering the rising awareness on the urgent threat of climate change, policy and regulation ameliorations, the share of renewable energy on global energy production is expected to rise further.

## 1.2 Sunlight as an Energy Source

Our sun has an enormous potential to fulfill the global energy demand. Only in one-hour the sun provides more energy to earth in comparison to the energy consumed globally in a year. The sun can be considered as a blackbody at a temperature around 5800 K, which emits light with a range of

frequencies. However, this irradiation is highly affected by absorption by the molecules in Earth's atmosphere (mainly  $O_3$ ,  $H_2O$  and  $CO_2$ ), scattering effects and the optical path length through the Earth's atmosphere. The properties of the radiation striking to earth's surface depends on its own optical length. Therefore, the spectral irradiance is defined with an air mass coefficient, that takes into account the path length of light. The air mass can be estimated by  $1/\cos(\theta)$  where  $\theta$  is the zenith angle. Air Mass 0 (AM 0) corresponds to the solar spectrum outside of the atmosphere. Air Mass 1 (AM 1) corresponds to the spectrum of the sunlight that travels through the atmosphere till the sea level when the sun is at zenith. In this spectrum, the absorption of  $O_3$ ,  $H_2O$  and  $CO_2$  causes dips at certain wavelengths. Air Mass 1.5 (AM 1.5) is the solar irradiance when  $\theta$  is equal to  $48.2^\circ$ . This spectrum represents an overall yearly average radiation for mid-latitudes when the optical path is equal to 1.5 times of the atmosphere thickness. AM 1.5 Global (AM 1.5G) is the standard spectrum used for photovoltaic device characterization. The AM 1.5G spectrum includes the diffuse light components arising from scattering, whereas the AM1.5 Direct (AM 1.5D) does not. Integration of AM 1.5G over wavelength gives the energy received from the sun per unit area and per unit time as  $1000 \text{ W m}^{-2}$ . The spectral irradiance of AM 0, AM 1.5G and AM 1.5D are given in Figure 1-1.

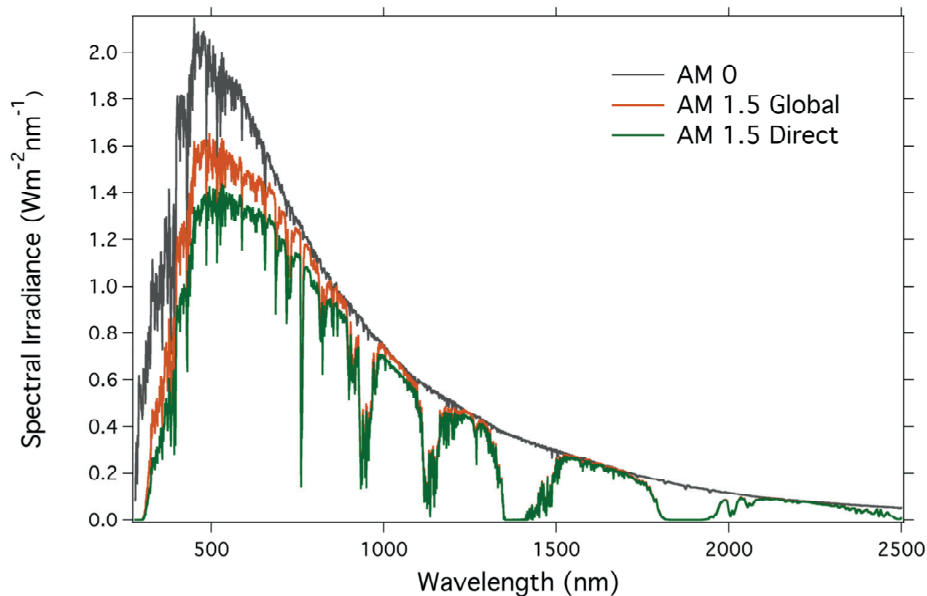


Figure 1-1 Spectral irradiance of AM 0, AM 1.5Global and AM 1.5Direct Spectrums (ASTM G173-03).

In theory, 60 TW of power can be generated by installing solar farms with 10% efficiency in view of the input energy flux through earth's atmosphere.<sup>6</sup> Thanks to the rising awareness on the harmful effects of fossil fuels and governmental subsidies, the solar-to-energy implementations are increasing. According to the International Energy Agency, during 2017, the PV(photovoltaic) market has grown 29%. This constitutes a 98 GW installed and grid-connected capacity globally for 2017 and thereby the total installed capacity became 402.5 GW by the end of 2017.<sup>7</sup> The further exten-

sion of solar energy will depend on the availability of efficient and low-cost PV technologies and effective energy storage technologies in terms of batteries and hydrogen.<sup>8</sup>

Currently, 90% of the PV market is constituted by the silicon monocrystalline and polycrystalline modules.<sup>9</sup> Based upon the historical generation and maturity, the silicon wafer technology is referred as the first generation of solar cells (together with GaAs cells). Second generation of solar cells consists of thin-film technologies such as amorphous silicon, CdTe, CIGS cells that constitute the rest of the PV market. Each of these technologies have several advantages, however, certain disadvantages such as high-cost and the scarcity of the employed materials makes PV market in the quest for new technologies. Third generation solar cells target to achieve cheaper solar cells either by lower material consumption or by employing inexpensive and simpler materials. Third generation solar cells include novel or advanced thin film technologies such as organic, quantum dot solar cells, multi junction cells, hot-carrier collection, thermo-photovoltaics, and dye-sensitized solar cells.<sup>9</sup>

### 1.3 Dye Sensitized Solar Cells

The dye-sensitized solar cell (DSC) technology has attracted a lot of interest in the last 30 years for conversion of solar energy to electrical energy. Originally, this technology was based on the concept of sensitization of semiconductors in the interest of silver halide photography and electrophotography. In photographic science, photoelectric experiments in liquid state devices and theoretical studies on the corresponding processes were carried out by Becquerel<sup>10</sup> and Gurney&Mott<sup>11</sup>, respectively. Following Vogel's<sup>12</sup> research on sensitization of silver halide emulsions for the photography field, Moser<sup>13</sup> applied the sensitization concept on photochemical cells by using the erythro-sine dye on silver halide electrodes to achieve light to electrical conversion. Similar sensitization studies in the 1960's were carried out by Gerischer and several researches on ZnO crystals.<sup>14-17</sup> In these periods, importantly, the mechanism of the initial step that is following the light absorption unveiled to be an electron transfer process rather than an energy transfer.<sup>18</sup> It was recognized that for maximum efficiency, dye molecules should be packed closely as a monolayer.<sup>19</sup> In order to increase light harvesting efficiencies, the efforts were later concentrated on the development of high surface area oxides and sensitizers with better anchoring abilities.<sup>20,21</sup> Moser and Grätzel<sup>22</sup> investigated the sensitization of colloidal TiO<sub>2</sub> by adsorbed eosin molecules in terms of electron injection and electron recombination kinetics. In this study they demonstrated that the injection rate of electrons from the photo-excited dye is orders of magnitude faster than the recombination of the oxidized dye and TiO<sub>2</sub> conduction band electrons. Eventually, Brian O'Regan and Michael Graetzel<sup>23</sup> demonstrated DSCs employing high surface area mesoporous titania film and a trimeric ruthenium complex sensitizer. This embodiment reached power conversion efficiency (PCE) values above 7%. Since this achievement, the DSC technology draws attention due to its potential for being commercialized as a low cost photovoltaic system and therefore component development and integration studies are carried out worldwide. These studies mainly concentrate on developing dye, working electrode, and electrolyte materials providing high efficiency values and long term stability for DSCs.

### 1.3.1 Components of DSC and Working Principles

Dye-sensitized solar cells are photo-electrochemical devices that are eligible for direct sunlight-to-electricity conversion. The main DSC components can be classified as a photoanode, a counter electrode and an electrolyte/redox system for a liquid-state device. The photoanode consists of a mesoporous semiconductor material (typically  $\text{TiO}_2$ ), and dye molecules that are attached to this mesoporous material. Upon light absorption, the dye molecules get photoexcited and inject electrons to the conduction band of the semiconductor. The oxidized dye molecules are regenerated by the electrolyte while the electrons follow an external circuit. The cycle is completed by the reduction of oxidized redox species at a catalyst loaded counter electrode surface. A schematic of a DSC is given in Figure 1-2.

In the dark, the quasi-Fermi level of  $\text{TiO}_2$  and the redox potential of the electrolyte are equal and therefore, no net current flows. Upon illumination, the electron concentration in the  $\text{TiO}_2$  increases and the quasi-Fermi level of  $\text{TiO}_2$  shifts up. The open circuit potential ( $V_{OC}$ ) of a DSC is determined by the difference of potential between the quasi-Fermi level of electrons in  $\text{TiO}_2$  and the Nernst potential of the redox mediator under illumination, according to Equation 1-1. The Nernst potential of the redox mediator is given in Equation 1-2, where  $E^0$  is the formal redox potential of the redox couple,  $R$  is the gas constant,  $T$  is temperature,  $n$  is the number of electrons transferred in the reaction and  $C$  is the concentration of oxidized and reduced species. The quasi-Fermi level of electrons in  $\text{TiO}_2$  can be expressed by Equation 1-3, where  $E_{CB}$  is the conduction band edge potential of  $\text{TiO}_2$ ,  $k_B$  is the Boltzmann constant,  $q$  is the elementary charge,  $n_{CB}$  is the density of electrons in the conduction band, and  $N_{CB}$  is density of states in the conduction band of  $\text{TiO}_2$ . The main parameters that are determining the photocurrent of a DSC can be listed as light harvesting efficiency, charge injection efficiency and charge collection efficiency.

$$V_{OC} = E_{F,TiO_2} - E_{F,redox} \quad (1:1)$$

$$E_{F,redox} = E^0 - \frac{RT}{nF} \ln\left(\frac{C_{ox}}{C_{red}}\right) \quad (1:2)$$

$$E_{F,TiO_2} = E_{CB} - \frac{k_B T}{q} \ln\left(\frac{n_{CB}}{N_{CB}}\right) \quad (1:3)$$



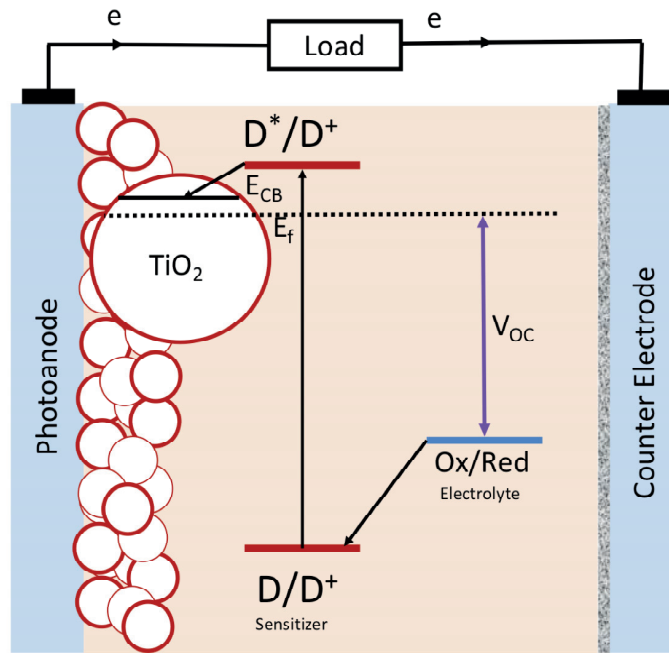


Figure 1-2 Schematic diagram of a DSC.

### 1.3.2 Processes in Dye Sensitized Solar Cells

The working principle of a DSC is based on the electron transfer processes occurring mainly on the oxide/dye/electrolyte interfaces. In order to obtain higher photovoltaic performance, all the processes should be optimized in terms of the kinetics and the energy levels (driving forces). The main processes involved in a DSC system can be simply illustrated as in Figure 1-3.

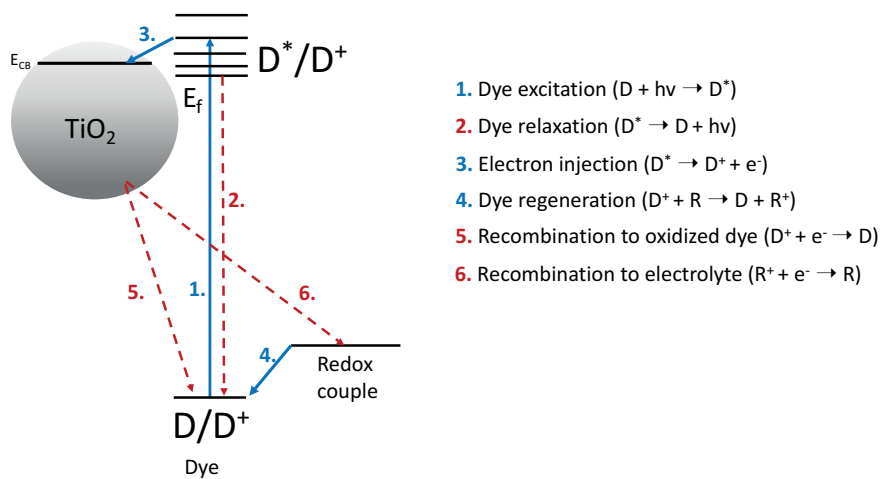


Figure 1-3 Main processes in a DSC device.

Under illumination, the dye molecules (D) absorb photons and become photoexcited (D\*) (process 1). In other words, the electron energy in the sensitizer becomes excited from the HOMO (highest occupied molecular orbital) level to the LUMO (lowest unoccupied molecular orbital) level. Following this process, the photoexcited dye molecules either inject electrons to the conduction band of TiO<sub>2</sub> (process 3) or relax back to the ground state (process 2). The injection quantum efficiency ( $\phi_{inj}$ ) is an important parameter, which affects device performance, as calculated by Equation 1-4, where  $k_{inj}$  and  $k_{decay}$  are the rate constants for electron injection and decay of the excited dye, respectively. Several groups reported electron injection timescales in femtosecond to picosecond range for the dye-coated films in an inert solvent.<sup>24-27</sup> According to these studies, the electron injection process is orders of magnitude faster than the radiative/non-radiative decay of the excited dye (which occurs in a nanosecond time scale). Therefore, competition of electron injection and dye relaxation is normally not considered as a limiting factor in terms of achieving better photovoltaic performance. However, the measurements carried out in the presence of electrolyte additives (ex. 4-tert-butylpyridine (TBP), Li<sup>+</sup>) resulted in slower electron injection halftimes due to conduction band shifts of TiO<sub>2</sub>.<sup>28</sup> Consequently, the competition of electron injection and back decay becomes a factor that is limiting the DSC photovoltaic conversion efficiencies.

$$\phi_{inj} = \frac{k_{inj}}{k_{inj} + k_{decay}} \quad (1:4)$$

Photoinduced electron injection follows the regeneration of the oxidized dye molecules by a redox mediator (process 4). The regeneration efficiency ( $\Phi_{reg}$ ) can be described as in Equation 1-5, where  $k_{reg}$  and  $k_{rec}$  are the rate constants for dye regeneration and pseudo-first order rate constant for the recombination of electron in TiO<sub>2</sub> and oxidized dye (process 5), respectively. The dye regeneration with iodide occurs in  $\mu$ s timescale<sup>29</sup> with regeneration efficiency values reaching unity.<sup>6</sup> For several one-electron cobalt complexes the regeneration is reported to occur in  $\mu$ s timescale.<sup>30</sup> The regeneration efficiency depends on the driving force for regeneration (difference between redox potential and oxidation potential of the dye), the re-organization energy of the molecules upon redox reaction and mass transfer limitations arising from slow diffusion.

$$\Phi_{reg} = \frac{k_{reg}}{k_{reg} + k_{rec}} \quad (1:5)$$

Recombination of the conduction band electrons with the oxidized dye molecules (process 5) and redox species (process 6) are the particular unwanted processes that occurs in a DSC system. The recombination process depends on the electron density in the conduction band and accordingly the light intensity. Electron lifetime ( $\tau_e$ ) is described as the time for recombination of TiO<sub>2</sub> electrons and electrolyte, whereas electron transport time ( $\tau_{tr}$ ) is defined as the time interval for electrons to transport through the TiO<sub>2</sub> layer. The charge collection efficiency ( $\Phi_{cc}$ ) shows the competition between the electron transport and electron recombination, as calculated by Equation 1-6.

$$\Phi_{cc} = \frac{1}{1 + \frac{\tau_{tr}}{\tau_e}} \quad (1:6)$$

The mesoporous TiO<sub>2</sub> film consists of nanoscale crystalline particles. Owing to the small size of these particles, a built-in electric field throughout the TiO<sub>2</sub> network is not possible. Therefore, the electron transport cannot be sustained by an electrical potential gradient (drift), instead it is expected to be dominated by diffusion.<sup>31</sup> Electron transport in the mesoporous network becomes faster with increasing incident light intensities.<sup>32</sup> This behavior is explained by the multiple trapping model.<sup>32-35</sup> According to this model, the electrons are mostly trapped in localized states below the conduction band. However, with thermal activation they become free to move. With higher light intensities, the electron concentration and Fermi level increase and in the same way the driving force for diffusion is also increased.

#### 1.4 Marcus Theory

The simple electron transfer reactions (where no chemical bonds are broken or formed), in a surrounding solvent, between molecules can be analyzed with Marcus Theory<sup>36-38</sup>. The basic equation of Marcus Theory can be given as in Equation 1-7

$$k_{et} = \frac{H_{AB}^2}{\sqrt{4\pi\lambda k_B T}} \exp\left(-\frac{(\Delta G^0 + \lambda)^2}{4\lambda k_B T}\right) \quad (1:7)$$

where  $H_{AB}^2$  is the electronic coupling,  $\lambda$  is the total reorganization energy (including changes in bond lengths and angles as well as solvent reorganization) and  $\Delta G^0$  is the reaction free energy. The electronic coupling term can be expressed as;

$$H_{AB}^2 = H_o^2 \exp^{-\beta r} \quad (1:8)$$

where  $r$  is the spatial separation of the donor and acceptor states and  $\beta$  is a measure of barrier height.

According to this theory, electron transfer rates are highly dependent on the electronic coupling between the donor and acceptor (i.e. the overlap of the populated orbitals of the donor and empty orbitals of the acceptor), reorganization energies and reaction free energy. Figure 1-4a represents the potential energy-nuclear configuration curves of the reactant encounter pair and product encounter pair. The free energy of activation  $\Delta G^\ddagger$  is given in Equation 1-9. Marcus Theory predicts that the free energy of activation decreases (rate of electron transfer increases) with increasing driving forces if  $\Delta G^0 < \lambda$ . However, if  $\Delta G^0 > \lambda$ , the rates decrease with increased driving forces for reaction and this domain is called Marcus inverted regime. The response of the rate constant in relation to reaction free energy and reorganization energy is shown in Figure 1-4b.

$$\Delta G^\ddagger = \frac{(\Delta G^0 + \lambda)^2}{4\lambda} \quad (1:9)$$

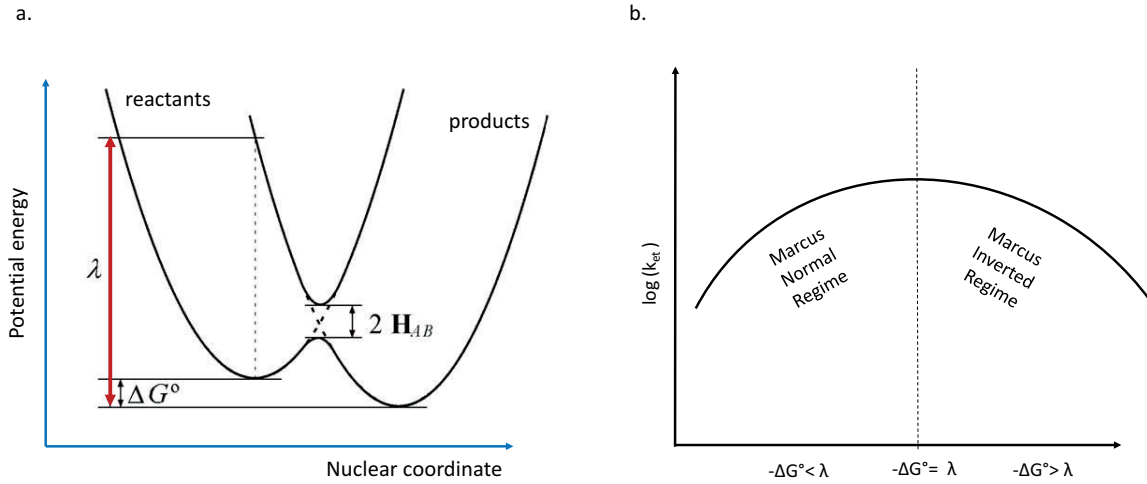


Figure 1-4 a) Parabolic potential energy curves for reactant and product encounter pairs and b) Representation of Marcus normal and inverted domains.

## 1.5 DSC Redox Mediators

In accordance with the discussed working principles of a DSC system and electron transfer theory, we can state that the redox mediators have a significant impact on the ongoing processes in DSCs. More specifically, the redox mediators have vital importance to the DSC device performance in terms of regeneration of the oxidized dye molecules, charge transfer between the electrodes and catalytic activity at the counter electrode surface. Consequently, the  $J_{sc}$ ,  $V_{OC}$  and FF values are directly affected by the redox mediator and electrolyte properties. The main requirements of being a good redox mediator can be summarized as below:

If electron injection is not a limiting process in a DSC, better  $J_{sc}$  values depend on the continuous regeneration of the oxidized dye molecules. The dye regeneration process should not be limited by the mass transport problems. The solubility of the redox species in electrolyte solvent should be enough to satisfy a continuous process. Besides, parasitic absorption of the redox mediator should be negligible in comparison to the absorbance of dye molecules. The oxidized form of the redox couple should efficiently accept electrons at the counter electrode, whereas the opposite should be the case at the photoanode.

In DSCs, the difference between the quasi-Fermi level of  $TiO_2$  and the redox potential of the electrolyte determines the  $V_{OC}$  of the system. In order to have better  $V_{OC}$  values, the redox potential of the electrolyte should be as positive as possible, though sustaining fast enough electron transfer kinetics for dye regeneration to efficiently compete with the back decay of electrons in the  $TiO_2$  to the oxidized dye. This is also reflected as resulting in a low current.

From the perspective of a whole device fabrication, operation and durability, the redox mediator should ensure good photo-electrochemical stability and compatibility with additives and other materials employed in the device.

As can be seen in the literature, the main DSC studies were concentrated on the development of sensitizers. The emphasis on the importance of the choice of redox mediator has been insufficient.

Consequently, iodide/tri-iodide and cobalt redox mediators became the mostly accepted and popular redox shuttles in the DSC field. The advantages and disadvantages of these redox couples are presented in the following sub-chapters.

### 1.5.1 Advantages and Disadvantages of iodide-triiodide

After the discovery of DSCs, iodide/tri-iodide redox couple was used as the conventional redox mediator since it had the highest efficiency values with different types of sensitizers in comparison to other redox mediators. So far, the best certified PCE value for a  $\Gamma/I_3^-$  based device is reported as 11.7% under full sun illumination ( $V_{OC}=0.758V$ ,  $J_{sc}=19.78mAcm^{-2}$ )<sup>39</sup>. The main advantage of this electrolyte was suppressed recombination of injected electrons with tri-iodide, which provided higher photovoltages and currents. Additionally, the  $\Gamma/I_3^-$  was considered to be advantageous in terms of having good solubility in a wide range of solvents and exhibiting fast diffusion rates. On the other hand, being a two-electron redox couple, this electrolyte causes large internal losses in devices. Oxidation of  $\Gamma^-$  to  $I_3^-$  is a kinetically complex process, which includes several coupled electrochemical and chemical steps<sup>40-42</sup>. This complexity makes the internal losses inevitable. The energy level difference between the  $\Gamma/I_3^-$  and HOMO level of dye stays by around 0.5 V or more by taking into account that the standard potential of this electrolyte is around 0.35 V vs SHE. This high overpotentials for dye regeneration, limits the photovoltage outputs and accordingly the efficiency values.

Another drawback of using this electrolyte is the absorption of tri-iodide in the visible part of the solar spectrum. The parasitic absorption of the tri-iodide has a detrimental effect on the light harvesting efficiency values of the working electrode.<sup>43,44</sup> In addition, the corrosiveness of  $\Gamma/I_3^-$  toward several metals is another problem of this redox mediator in terms of long term durability. It is reported that  $\Gamma/I_3^-$  causes corrosion with some DSC components such as some electrocatalysts, conductive supports and distribution grids employed for large area electrodes.<sup>45-47</sup>

### 1.5.2 Advantages and Disadvantages of Cobalt Redox Mediators

Most of the aforementioned problems of  $\Gamma/I_3^-$  redox mediator were overcome with one-electron transfer cobalt complexes. With these transition complexes, different ligand substitutions allow the tuning of the physical and chemical properties, redox potentials, and electron transfer kinetics of the corresponding redox mediator. By ligand modifications, the stability of the redox shuttle can also be controlled.<sup>48</sup> In addition, these outer-sphere complexes exhibit faster electron exchange processes since cleavage or reformation of chemical bonds, or the formation of intermediate species (as in the case of  $\Gamma/I_3^-$ ) is not observed.

With ligand engineering, the redox potentials of the coordination complexes can be kept as positive as possible in order to achieve high  $V_{OC}$  values. Owing to their more positive redox potentials, cobalt redox mediators provide improved photovoltage values and accordingly higher efficiencies in comparison to the  $\Gamma/I_3^-$  system.<sup>49-51</sup> (So far, a record efficiency value of 14% (not certified) has been achieved for liquid state DSCs with cobalt redox mediator  $[Co(bpy)_3]^{3+/2+}$  (bpy=bipyridyl) and co-sensitized working electrode.<sup>52</sup>) However, the dye regeneration rates decrease and recombination rates increase when the redox potential of the electrolyte becomes more positive.<sup>30</sup> The limitation on dye regeneration occurs due to the large internal reorganization energy requirement between  $d^7$

(high spin) and  $d^6$  (low spin) states for cobalt complexes<sup>53</sup>. For example, in order to achieve a 93% regeneration yield with a triphenylamine-based organic dye<sup>54</sup>, 230 mV dye regeneration overpotential is necessary. This necessity of driving force still appears as a substantial potential loss.<sup>30,55</sup>

Another major disadvantage of cobalt redox mediators is reported as the high recombination rate of the electrons in the  $\text{TiO}_2$  conduction band to the redox species in the electrolyte. This factor limits photovoltage and photocurrent and brings about poor overall performance.<sup>56</sup> By using sterically insulating ligands, the recombination rates can be decreased.<sup>48</sup> However with this approach, bulky complex structures are formed. This situation can be problematic in terms of mass transport limitations in the mesoporous layer.<sup>57-59</sup> Therefore, in order to reduce the recombination reaction, surface passivation<sup>58,60</sup> techniques or modification of dye structures via attachment of bulky electron rich substituents<sup>49,50,61-64</sup> is preferred. (The latter method can also be problematic in terms of dye loading).

Stability issues and toxicity appear as other important limitations for cobalt complexes in terms of their potential for industrialization and mass production.<sup>65,66</sup>

## 1.6 Copper Redox Mediators for DSC Applications

Copper is a first row transition metal; therefore, its ions are likely to form coordination complexes adopting different geometries. As a  $d^{10}$  system, Cu(I) generally favors adopting a four-coordinate complex in tetrahedral geometry<sup>67</sup>. On the other hand, as a  $d^9$  system, Cu(II) complexes can exhibit different stereochemistry such as six-coordinate tetragonal (distorted octahedral) or five-coordinate (square pyramidal or trigonal bi-pyramidal) geometries<sup>68</sup>. As a result of the different geometry preferences of Cu(I) and Cu(II) species, the electron transfer reactions in unconstrained Cu(II/I) systems are expected to require significant reorganizational energies concerning the internal changes in bond lengths and angles as well as the surrounding matrix. Nevertheless, with steric constraints the coordination number and the preferred geometry of copper species could be altered. Accordingly, the activation energy barrier for electron transfer reactions can be modified.<sup>69</sup> For instance, "blue-copper"<sup>70</sup> proteins which are involved in many chemical and biochemical catalytic systems in nature showed appropriate redox potentials and electron transfer kinetics owing to their ligand environment<sup>71-73</sup>.

Copper complexes were studied both as dye-sensitizers and redox mediators for DSC applications. Sauvage and coworkers<sup>74</sup> designed copper dyes with 2,2'-bipyridine or 1,10-phenanthroline ligands that hold carboxylate anchoring groups and substituents in the positions next to the nitrogen coordination sites. These substituents hinder the oxidation to Cu(II). Constable, Housecroft and coworkers investigated homoleptic and heteroleptic Cu(I) dyes for DSC applications.<sup>75,76</sup>

We were inspired by some of the preceding studies on copper redox mediators for DSC applications. The ligands used in these former studies and the redox potentials of the corresponding complexes are given in Figure 1-5. A brief summary of the related literature is provided below.

Copper coordination compounds were utilized as DSC redox mediators for the first time by Yanagida and coworkers<sup>77</sup>. In this pioneering work, they emphasized the significant features of copper species to be employed as a redox couple in DSC applications. According to the Franck-Condon

principle as clarified by Marcus<sup>37</sup>, in order to achieve fast electron transfer and minimize the required energy for transition between oxidized and reduced species, the geometry of the copper complexes should be adjusted. Yanagida and coworkers<sup>77</sup> employed [(-)-sparteine-N,N'](maleonitriledithiolato-S,S') copper ([Cu(SP)(mmt)]), as a blue copper model complex, which closely mimics the spectral and redox behavior of the blue copper proteins involved in the photosynthetic chain in nature. With this redox couple, by achieving a distorted tetragonal geometry, the difference in bond lengths and geometries between copper(I) and copper(II) is cleverly minimized and therefore the copper site is optimized for fast electron transfer and better dye regeneration. Additionally, they studied bis(2,9-dimethyl-1,10-phenanthroline)copper ([Cu(dmp)<sub>2</sub>](CF<sub>3</sub>SO<sub>3</sub>)<sub>2</sub>), which also exhibits distorted tetragonal geometry due to the steric hindrance effects of methyl groups in the 2,9 positions of the phenanthroline ligand. They reported a comparison of the blue copper model complex and [Cu(dmp)<sub>2</sub>] to [Cu(phen)<sub>2</sub>](CF<sub>3</sub>SO<sub>3</sub>)<sub>2</sub> (phen) 1,10-phenanthroline), in which the four N-donor atoms are expected to be nearly coplanar. It was shown that the electron self-exchange rate constant increases in the order: [Cu(phen)<sub>2</sub>]<sup>2+/+</sup> < [Cu(SP)(mmt)]<sup>0/-</sup> < [Cu(dmp)<sub>2</sub>]<sup>2+/+</sup>. With [Cu(dmp)<sub>2</sub>]<sup>2+/+</sup>, the structural change between the copper(II) and copper(I) complexes was minimized due to the distorted tetragonal geometry. Additionally, they emphasize the importance of choosing electron mediators with high redox potentials, in order to obtain high energy conversion efficiencies with high photovoltage outputs. By employing the N719 dye, the power conversion efficiency values were reported as 1.4%, 1.3% and 0.12% for [Cu(dmp)<sub>2</sub>]<sup>2+/+</sup>, [Cu(SP)(mmt)]<sup>1-/0</sup> and [Cu(phen)<sub>2</sub>]<sup>2+/1+</sup> complexes, respectively, under full-sun illumination. With [Cu(dmp)<sub>2</sub>]<sup>2+/1+</sup>, the V<sub>OC</sub> (0.79 V) is reported to be higher than the other two complexes as well as I<sup>-</sup>/I<sub>3</sub><sup>-</sup> in accordance with the formal redox potentials of these complexes. (For [Cu(dmp)<sub>2</sub>]<sup>2+/1+</sup>, the redox potential was reported as 0.66 V vs Fc<sup>+</sup>/Fc.) (Pavlishchuk et al. reported Fc<sup>+</sup>/Fc versus SHE value as +0.624 V for acetonitrile solutions<sup>78</sup>)

By following a different strategy, Bignozzi and co-workers<sup>79</sup> also developed new copper complexes ([Cu(bpy-(COOEt)<sub>2</sub>)<sub>2</sub>]<sup>2+/1+</sup>, [Cu(bpy-(COOnbut)<sub>2</sub>)<sub>2</sub>]<sup>2+/1+</sup>, [Cu(bpy-(COOTbut)<sub>2</sub>)<sub>2</sub>]<sup>2+/1+</sup>, [Cu(PQ)<sub>2</sub>]<sup>2+/1+</sup>, [Cu(MeTBPQ)<sub>2</sub>]<sup>2+/1+</sup>, [Cu(BQ)<sub>2</sub>]<sup>2+/1+</sup>) and investigated them as redox mediators in conjunction with Z907 sensitized DSC devices. In order to minimize the back electron transfer rates, i.e. recombination of injected electrons with the oxidized redox species, they preferred copper complexes having high reorganization energies. Considering the relevant nuclear re-arrangement occurring in tetrahedral Cu(I) oxidation to octahedral or trigonal-bipyramidal Cu(II) species (and vice versa), sluggish electron recombination rates were expected. However, this strategy resulted in a slow dye regeneration processes. With this set of molecules, the IPCE maxima values lied around 35-40%. Among other complexes, [Cu(BQ)<sub>2</sub>]<sup>2+/1+</sup> reported to have a higher formal redox potential, and therefore smaller driving force for dye regeneration. This complex did not however, perform well with the Z907 dye. It was also shown that 4,4' di-substituted bipyridine complexes exhibit very slow electron transfer kinetics, and the bulky substituents in the same position are not advantageous in terms of suppressing the recombination. Moreover, both the dye regeneration and the electrochemical response of the counter electrode were negatively affected.

Wang and co-workers<sup>80</sup> re-examined the [Cu(dmp)<sub>2</sub>]<sup>2+/1+</sup> redox shuttle in combination with the C218 dye. By employing the C218 dye, a 7% photon-to-electrical-conversion efficiency was reported (V<sub>OC</sub> = 0.932V, J<sub>sc</sub> = 11.3mA/cm<sup>2</sup>, FF=0.66). In this work low electron transfer rates on sev-

eral counter electrode materials such as noble metals, carbon black and conductive oxides, was reported resulting in poor fill factors. The same complex  $[\text{Cu}(\text{dmp})_2]^{2+/1+}$ , was studied by Freitag et al.<sup>81</sup> with an organic dye (LEG4) and a PEDOT (poly(3,4-ethylenedioxythiophene)-coated counter electrode (CE). In this work, the use of a  $[\text{Cu}(\text{dmp})_2]^{2+/1+}$  electrolyte led to a higher photovoltaic performance, with a PCE of 8.3% for LEG4-sensitized  $\text{TiO}_2$  solar cells, with a remarkably high open-circuit voltage of above 1.0 V at  $1000 \text{ W m}^{-2}$  under full sun conditions ( $J_{\text{sc}} = 12.6 \text{ mA/cm}^2$ ,  $\text{FF} = 0.62$ ). In comparison, the efficiency obtained in the same study was 7.3% with the  $[\text{Co}(\text{bpy})_3]^{3+/2+}$  mediator ( $V_{\text{OC}} = 0.88 \text{ V}$ ,  $J_{\text{sc}} = 7.33 \text{ mA/cm}^2$ ). Additionally, it was unveiled that a small driving force for dye regeneration of only 0.2 eV is sufficient to obtain a virtually unit yield in dye regeneration. By means of electrochemical analysis, it was shown that the copper complexes have higher diffusion coefficients compared to the Co-based alternatives. Therefore, copper-based systems exhibited less mass transport limitations compared to Co-based electrolytes. A drawback of the Cu-complex was observed due to quenching of the dye excited state by the mediator. According to steady-state emission and time-correlated single-photon counting (TC-SPC) measurements, the authors reported bimolecular reductive quenching of the excited LEG4 dye by the  $[\text{Cu}(\text{dmp})_2]^{2+}$  complex through a dynamic mechanism. Quenching of the reduced dye molecules by the  $[\text{Cu}(\text{dmp})_2]^{2+}$  complex competes with electron injection and results in a lower photocurrent. It was reported that the quenching of excited LEG4 by the  $[\text{Cu}(\text{dmp})_2]^{1+}$ ,  $[\text{Co}(\text{bpy})_3]^{2+}$ , and  $[\text{Co}(\text{bpy})_3]^{3+}$  complexes followed a static mechanism, however, only for the  $[\text{Cu}(\text{dmp})_2]^{2+}$  complex, a dynamic quenching mechanism is engendered from purely collisional encounters between the excited dye and the  $[\text{Cu}(\text{dmp})_2]^{2+}$  complex. They suggested structural modifications in dye and redox molecules in order to inhibit unwanted quenching processes and hence achieve higher photovoltaic conversion efficiencies.

Hoffeditz et al.<sup>82</sup> developed a copper redox shuttle obtained from the 1,8-bis(2'-pyridyl)-3,6-dithiaoctane (PDTO) ligand and the common DSC additive TBP in acetonitrile (ACN). In this work they showed that, upon oxidation, copper ions replace the PDTO ligand with TBP and accept four or more TBP ligands. Thus, in the electrolyte Cu(I) and Cu(II) species exist with different ligand coordinations i.e.  $\text{Cu}(\text{PDTO})^+$  and  $\text{Cu}(\text{TBP})_{4+x}(\text{ACN})_y^{2+}$ . These species are reported to be interconvertible based on transfer of a single electron. The variance of the coordination spheres of Cu(I) and Cu(II) species results in widely differing Cu(II/I) formal potentials and reactivities for the forward as compared to the reverse electron transfer. It is reported that various factors such as charge transfer resistance, dark current suppression and redox couple potential, and, as a result, the photovoltaic performance of the devices, are highly dependent on the TBP concentration. With increasing TBP concentration both  $V_{\text{OC}}$  and  $J_{\text{sc}}$  values are increased, however, fill factor values are decreased ( $V_{\text{OC}} = 0.88 \text{ V}$ ,  $J_{\text{sc}} = 4 \text{ mAcm}^{-2}$ ,  $\text{FF} = 0.52$ ).



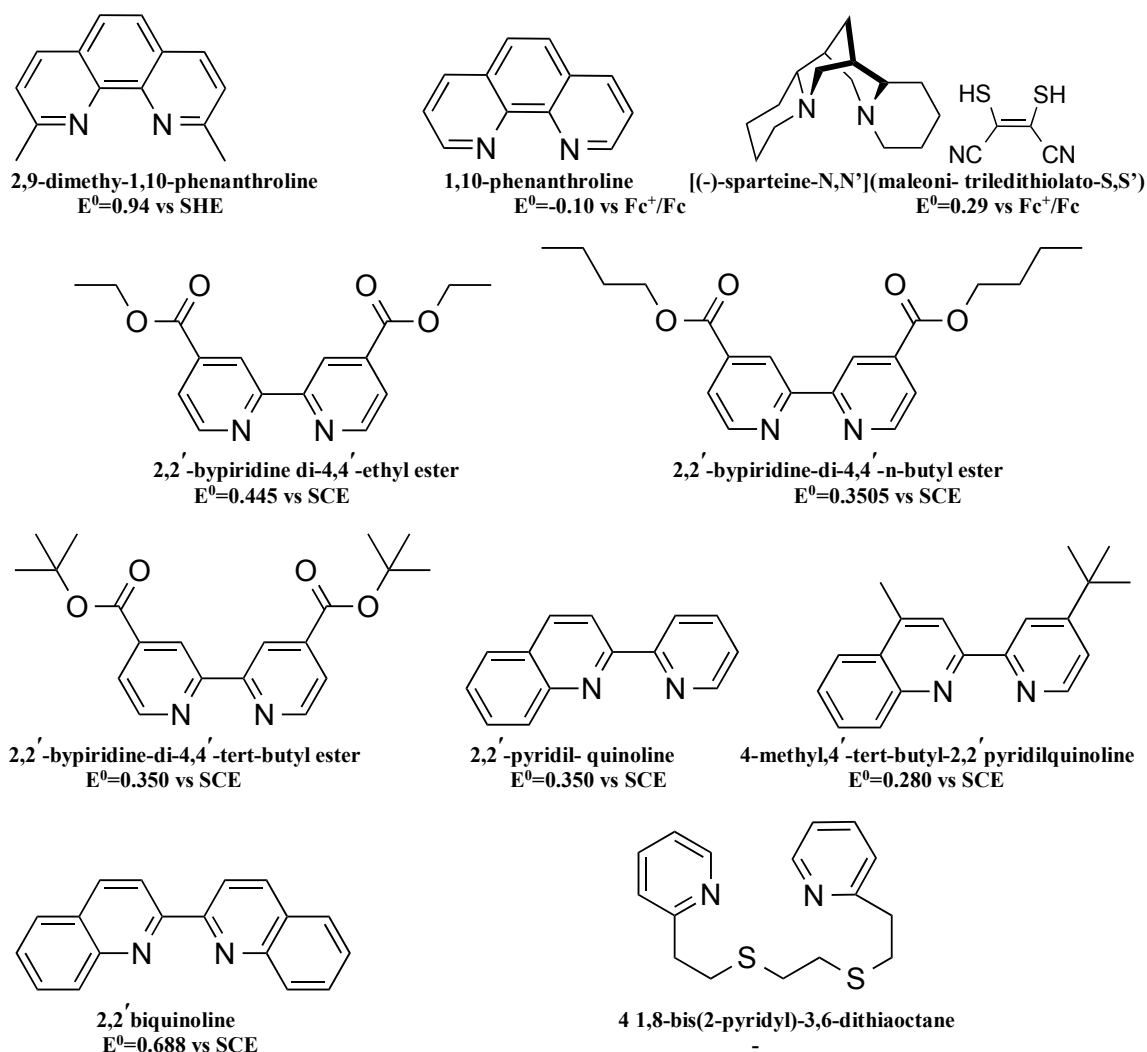


Figure 1-5 Some of the reported ligands for copper redox mediators in DSC applications and the redox potentials of the corresponding complexes.

## 1.7 Main Characterization Techniques

The main device characterization techniques that are used during this thesis are given in the following subchapters. These techniques enable the performance assessment of each device as well as the analysis of the effects and interaction of the materials employed, ongoing competitive processes, and their effects on the power conversion efficiencies. (The characterization of the components are provided in the related main chapters when necessary).

### 1.7.1 Current Density-Voltage Characteristics

The power conversion efficiency of a DSC can be measured by means of current density-voltage (J-V) characteristics. The current-voltage (I-V) data are collected by a voltage scan from open circuit

conditions (infinite load) to short-circuit conditions (zero load). The maximum power density output can be calculated at the point where the multiplication of current density and potential is maximum. The solar cell efficiency ( $\eta$ ) can be obtained with the ratio of the obtained maximum power output ( $P_{max}$ ) to the input power ( $P_{in}$ ) from the irradiation as in Equation 1-10, where FF denotes the fill factor. FF is defined by the ratio of maximum power density to the multiplication of open circuit voltage and short circuit current density ( $J_{sc}$ ) as in Equation 1-11. This parameter includes the effects of several loss mechanisms such as recombination of electrons, leaking current and series resistances.

$$\eta = \frac{P_{max}}{P_{in}} = \frac{J_{sc}V_{oc}FF}{P_{in}} \quad (1:10)$$

$$FF = \frac{J_{max}V_{max}}{J_{sc}V_{oc}} \quad (1:11)$$

The J-V characteristics carried out in the dark shows the recombination behavior of the electrons in the photoelectrode to the oxidized redox species. A typical J-V curve is illustrated in Figure 1-6.

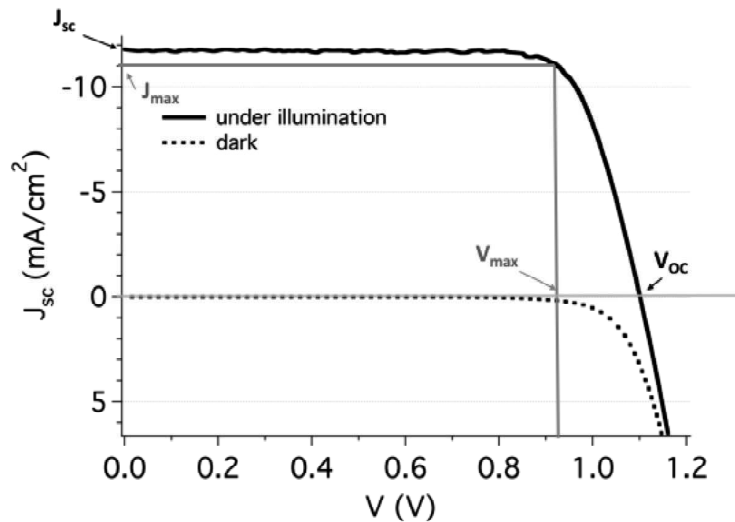


Figure 1-6 A typical JV curve under illumination and dark conditions.

### 1.7.2 Incident-Photon-to-Current-conversion Efficiency (IPCE)

Incident Photon-to-Current-conversion Efficiency (IPCE) indicates how efficiently the absorbed photons are converted into electrons as given in Equation 1-12, where  $e$  is the elementary charge and  $\Phi(\lambda)$  is the photon flux as a function of wavelength ( $\lambda$ ). IPCE is measured under monochro-

matic illumination under short circuit conditions. By means of this measurement the spectral response of a device at a certain wavelength can be obtained.

$$IPCE = \frac{J_{sc}(\lambda)}{e\Phi(\lambda)} = 1240 \frac{J_{sc}(\lambda)[Acm^{-2}]}{\lambda P_{in}(\lambda)[W cm^{-2}]} \quad (1:12)$$

The integration of the produced photocurrent density over the illumination wavelength results in a short-circuit current density as given in Equation 1-13: A typical IPCE data and the integrated current density of a DSC device is given in Figure 1-7.

$$J_{sc} = \int IPCE(\lambda) e \Phi(\lambda) d\lambda \quad (1:13)$$

The IPCE can also be expressed as:

$$IPCE = LHE \Phi_{inj} \Phi_{reg} \Phi_{coll} \quad (1:14)$$

where LHE is light-harvesting efficiency (Equation 1-15),  $\Phi_{inj}$  is the quantum yield of electron injection,  $\Phi_{reg}$  is the dye regeneration efficiency and  $\Phi_{coll}$  photo-generated charge collection efficiency. The light harvesting efficiency can be calculated by knowing the absorbance of the film(A) as:

$$LHE = 1 - 10^{-A} \quad (1:15)$$

Equation 1-14 is quite useful in terms of estimating the performance limiting processes in a DSC system.

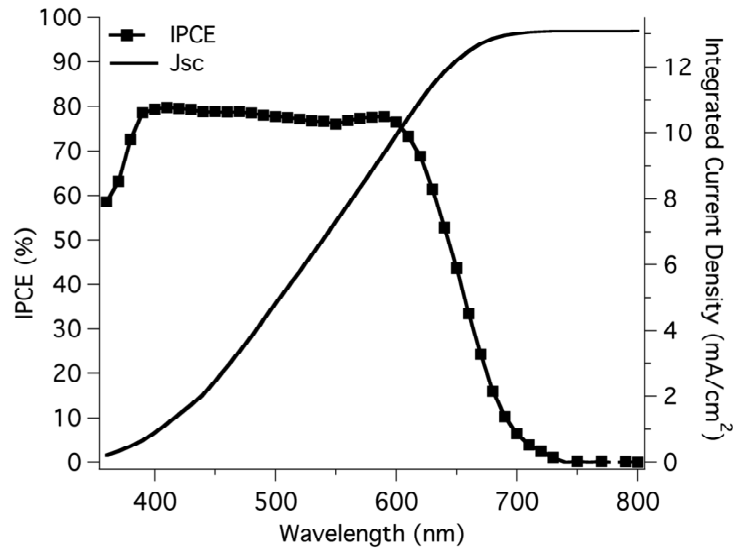


Figure 1-7 Typical IPCE (left) and integrated current density (right) curves for a DSC.

### 1.7.3 Electrochemical Impedance Spectroscopy

Electrochemical Impedance Spectroscopy (EIS) is a well-established method to investigate the interfacial charge transfer between a solid (working electrode) and electrolyte. This method is also developed as an important tool for DSC since it provides an analysis of the electrochemical processes occurring in a DSC system. A DSC can be modeled with basic electrical elements by using Transmission Line- equivalent circuits<sup>83</sup>. Within the certain range of potentials, some DSC processes become negligible and some of them much dominant. For that reason, different equivalent circuit models are viable for different range of potentials. The analogous electrical circuits of a DSC for high, intermediate and low potential regions are represented in Figure 1-8 (a, b and c), respectively. The circuit elements can be summarized as below:

$R_{series}$  is the series resistance, which represents the transport resistance of the transparent conductive oxide (TCO).

$R_{CE}$  is the charge transfer resistance at the counter electrode/electrolyte interface.

$CP_{CE}$  is the interfacial capacitance at the counter electrode/electrolyte interface.

$R_{FTO}$  represents the charge transfer resistance for electron recombination at the FTO (Fluorine-doped tin oxide)/electrolyte interface (becomes dominant at low forward voltage biases).

$CP_{FTO}$  is the capacitance at the TCO/TiO<sub>2</sub>/electrolyte interface.

$W_s$  is the Warburg element related to the diffusion of redox species in the electrolyte.

$D_{X1}$  is the extended element for complete equivalent circuit of diffusion-recombination transmission line.

Figure 1-8 (d, e and f) shows the Nyquist plots at high, intermediate and low potentials, respectively for a DSC sensitized with D45 dye and employing a cobalt redox shuttle. At a high potential bias Figure 1-8 (d), the first semicircle in the high frequency region indicates the resistance at the counter electrode/electrolyte interface. The second and third semicircles represent the charge recombination and diffusion resistances, respectively. At intermediate potentials Figure 1-8 (e), the characteristic transmission line is observed (the transport resistance line), and the following semicircle accounts for the electron chemical capacitance with the charge transfer resistance. For low potentials (Figure 1-8 (f)) the large arc represents the charge recombination and the capacitance at the FTO/electrolyte interface, as the dominating elements of impedance. For low potentials, diffusion related to the electrolyte is not observed.

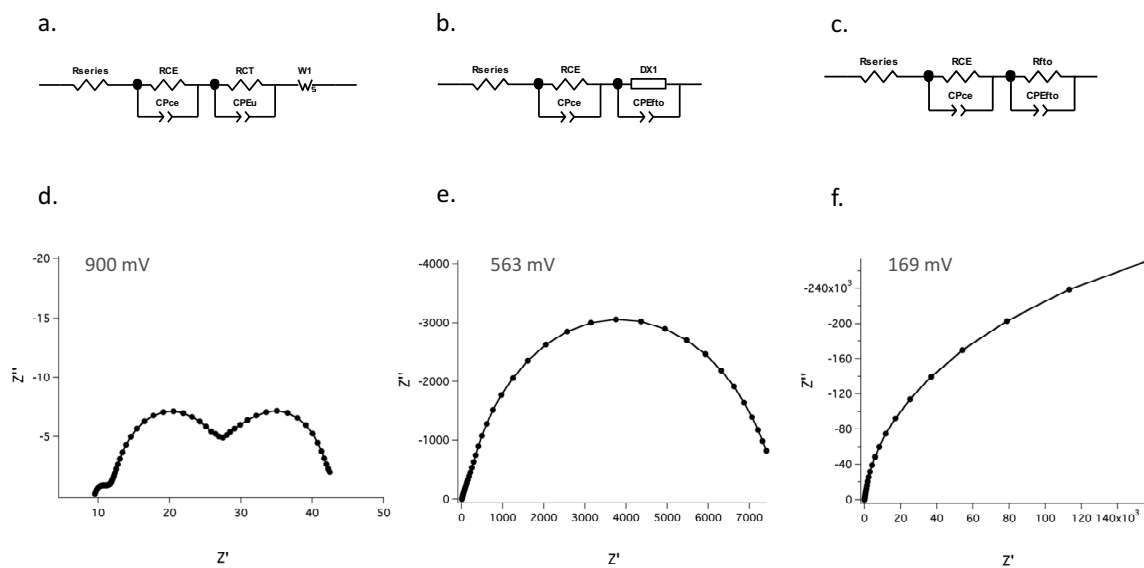


Figure 1-8 Equivalent circuit models for a DSC for a) high b) intermediate and c) low potentials and Nyquist plots of a D45-sensitized device employing cobalt redox mediator at different applied potential biases d) high (900 mV) e) intermediate (563 mV) and f) low (169 mV).

## 1.8 Motivation and organization of the study

The general goals of this thesis were to design new redox mediators and investigate them via in-situ and ex-situ techniques prior to DSC optimization studies in order to provide higher performance with long-term stability in DSC applications. In order to increase photovoltage outputs, firstly, we concentrate on decreasing the overpotential for dye regeneration. Considering the promising studies appeared in literature (Chapter 1.6), we concentrated on the development of new copper redox mediators.

Accordingly, in Chapter 2, we introduced two copper bipyridyl complexes as new redox couples for DSCs. We showed that with these redox couples, oxidized dye molecules can be regenerated sufficiently even with driving forces as low as 0.1V. This can be achieved as a result of the small reorganization energy between Cu(I) and Cu(II) species. By keeping a low driving force for dye regeneration, high photovoltages of over 1.0 V were attainable without compromising photocurrent densities.

In Chapter 3 and Chapter 4, in order to gain further understanding on copper redox mediators we performed further electrochemistry experiments. We showed that the coordination spheres of these complexes are highly dependent on the precursor materials used in the synthesis and the electrolyte additives (more specifically TBP). In Chapter 4, we studied four pyridine bases (4-*tert*-butylpyridine, 2,6-bis-*tert*-butylpyridine, 4-methoxypyridine and 4-(5-nonyl)pyridine) and evaluated these bases as electrolyte additives. We observed that base-specific electrochemical properties also affects the device performance.

In Chapter 5, we studied the effect of coordination sphere on copper redox mediators on dye regeneration and electron recombination processes both experimentally and theoretically. We showed that the dye regeneration occurs in the Marcus normal regime. The electron recombination occurs, however, in the Marcus normal regime in the presence of TBP.

In Chapter 6, we used copper complexes as a hole transport material, (HTM), for a solid state DSC(ssDSC). We showed that copper complex-HTM completely infiltrated the 6.5 $\mu$ m mesoscopic TiO<sub>2</sub> scaffold, and efficiently conduct holes by rapid hopping.

Finally, in Chapter 7, we demonstrate a DSC system, which achieves very high power conversion efficiencies under ambient light conditions. We showed that PCE values can be as high as 28.9% under fluorescence light tube illumination.

# Chapter 2 Copper Bipyridyl Redox Mediators for Dye-Sensitized Solar Cells with High Photovoltage

*This chapter is adopted from the following article with the permission of the journal:*

*Postprint version of the publication: 'Copper Bipyridyl Redox Mediators for Dye Sensitized Solar Cells with High Photovoltage. Journal of the American Chemical Society.,2016, 138, 45, 15087-15096.DOI: 10.1021/jacs.6b10721' by Yasemin Saygili, Magnus Söderberg, Norman Pellet, Fabrizio Giordano, Yiming Cao, Ana Belen Muñoz-García, Shaik M. Zakeeruddin, Nick Vlachopoulos, Michele Pavone, Gerrit Boschloo, Ladislav Kavan, Jacques-E. Moser, Michael Grätzel, Anders Hagfeldt and Marina Freitag*

*My contribution: Synthesis and characterization of the copper complexes, device preparation and characterization, analysis of the data, writing the manuscript.*

In this chapter we introduce two copper complexes as promising redox mediators in DSCs. With these new copper complexes, we reduced the driving force for dye regeneration with the redox mediator (as low as 0.1 V). We demonstrate high photovoltages of over 1.0 V and power conversion efficiencies over 10% by using the organic Y123 dye under 1000 W m<sup>-2</sup> AM1.5G illumination.

## 2.1 Introduction

Since the discovery of DSCs, the iodide/tri-iodide redox couple has been conventionally used as the redox mediator, which has shown the highest efficiency values together with excellent stability data with different types of sensitizers in comparison to other redox mediators.<sup>6</sup> The main advantage of this redox couple is the suppressed recombination of injected electrons with tri-iodide providing high photo-currents. On the other hand, being a two-electron redox couple, I<sup>-</sup>/I<sub>3</sub><sup>-</sup> electrolytes cause large internal potential losses for oxidized dye regeneration. In addition, there may be problems of corrosiveness and competitive visible light absorption.<sup>43,44</sup> These disadvantages were overcome with one-electron transfer cobalt complexes with more positive redox potentials, which resulted in an improved photovoltage and with overall higher efficiencies compared to the I<sup>-</sup>/I<sub>3</sub><sup>-</sup> system.<sup>49-51</sup> In these complexes, different ligand substitutions to the cobalt metal center enable the tuning of the redox potentials and electron transfer kinetics. However, the large internal reorganization energy requirement between d<sup>7</sup> (high spin) and d<sup>6</sup> (low spin) states for cobalt complexes turns out to be a disadvantage by limiting the driving force available for dye regeneration.<sup>53</sup> With a coordination number of six (octahedral), the ligands linked to a cobalt metal center form bulky structures, leading to mass transport limitations in the mesoporous layer.<sup>57-59</sup>

As alternative redox mediators, copper complexes (Cu(I)/Cu(II)) have been studied both as redox mediators<sup>77,79,80,84</sup> and hole transport materials (HTMs)<sup>85</sup> in DSCs. First, Hattori et al. obtained a maximum photon-to-electrical-conversion efficiency (PCE) of 1.4% with bis(2,9-dimethyl-1,10-phenanthroline)copper(I)/(II)  $[\text{Cu}(\text{dmp})_2]^{2+/1+}$ , which has a distorted tetragonal shape providing a relatively low reorganization energy.<sup>77</sup> The results were further improved by Bai et al., who reached 7% PCE<sup>80</sup> with the organic C218 dye, and recently Freitag et al. attained 8.3% PCE by having remarkably high open circuit voltages ( $V_{\text{oc}}$ ) above 1.0 V with the organic D- $\pi$ -A LEG4 dye.<sup>81</sup> Further, it was reported that the  $[\text{Cu}(\text{dmp})_2]^{2+/1+}$  complex with a redox potential of 0.93 V vs SHE, is able to sufficiently regenerate the oxidized dye molecules with a small driving force (0.2 eV), minimizing internal energy losses.

In this chapter, we report two new copper bipyridine complexes 6,6'-dimethyl - 2,2'-bipyridine ( $\text{Cu}^{\text{(II/I)}}(\text{dmby})_2\text{TFSI}_{2/1}$ ) and 4,4',6,6' - tetramethyl - 2,2' - bipyridine ( $\text{Cu}^{\text{(II/I)}}(\text{tmby})_2\text{TFSI}_{2/1}$ ), which we examined in comparison to the reference  $[\text{Cu}(\text{dmp})_2]^{2+/1+}$  complex in DSCs sensitized with the 3-{6-{4-[bis(2',4'-dihexyloxybiphenyl-4-yl)amino-]phenyl}-4,4-dihexyl-cyclopenta-[2,1-b:3,4-b']dithiophene-2-yl}-2-cyanoacrylic (Y123) dye.<sup>54,64</sup> We tuned the formal redox potentials of copper complexes relative to  $[\text{Cu}(\text{dmp})_2]^{2+/1+}$  and investigated this change with respect to regeneration kinetics and device performance. By maintaining the coordination geometry around the copper metal center during the change of the Cu oxidation state from I to II, internal reorganization energies can be minimized, allowing the regeneration to proceed rapidly at low driving force. For Cu(I) bis-phenanthroline complexes, the non-hydrogen groups at 2,9 positions of phenanthroline ligand had already been reported to provide small changes in ligand-copper distances upon oxidation.<sup>86-88</sup>

Since  $\text{Cu}(\text{dmp})_2$  is already proven to be successful as a redox mediator for DSCs, the  $\text{Cu}(\text{dmby})_2$  complex is similar designed by keeping the methyl groups adjacent to the nitrogen groups and replacing the phenanthroline with bipyridine to tune the redox potential and other properties. The structure of the  $\text{Cu}(\text{tmby})_2$  complex has two additional methyl groups at each ligand. The electron donating effect of a methyl group (4,6 positions) shifts the redox potential by 100mV towards the negative. A schematic representation of the energy levels in DSC devices, and molecular structures of the Y123 dye and the copper complexes are given in Figure 2-1.



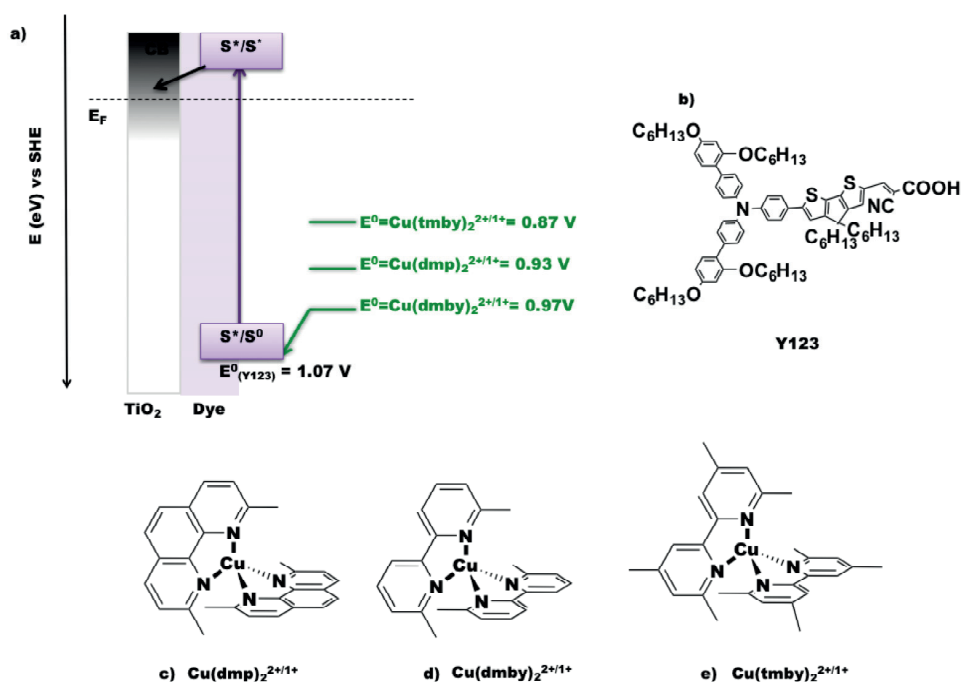


Figure 2-1 a) Schematic representation of energy levels in dye-sensitized solar cells. Molecular structures of the b) Y123 dye c)  $\text{Cu}(\text{dmp})_2^{2+/1+}$  d)  $[\text{Cu}(\text{dmby})_2]^{2+/1+}$  and e)  $[\text{Cu}(\text{tmby})_2]^{2+/1+}$  complexes.

## 2.2 Results and Discussion

### 2.2.1 Electrochemical and Spectroscopic Data

The formal redox potentials, extinction coefficients and diffusion coefficients of the investigated complexes, are tabulated in Table 2-1. The formal redox potentials of the  $[\text{Cu}(\text{dmby})_2]^{2+/1+}$  and  $[\text{Cu}(\text{tmby})_2]^{2+/1+}$  complexes are determined by cyclic voltammetry using a three electrode setup with a glassy carbon working electrode.

From the obtained reversible voltammograms (with equal anodic and cathodic peak currents after repeated cycles) of Cu(I) species, the formal (conditional) redox potentials for  $[\text{Cu}(\text{dmby})_2]^{2+/1+}$  and  $[\text{Cu}(\text{tmby})_2]^{2+/1+}$  are determined. If we omit the difference in activity coefficients, the potentials can be approximated to the standard electrochemical potential, with 0.97 V and 0.87 V vs the standard hydrogen electrode (SHE) for  $[\text{Cu}(\text{dmby})_2]^{2+/1+}$  and  $[\text{Cu}(\text{tmby})_2]^{2+/1+}$ , respectively. The redox potentials were referenced to SHE by addition of 0.624 V with respect to the formal potential of the reference ferrocene/ferrocenium redox couple, see Figure 2-4.

Table 2-1 Electrochemical and absorption data for Cu(I) and Cu(II) species

	$\epsilon$ ( $M^{-1}cm^{-1}$ )	$\lambda_{max}$ (nm)	$D$ ( $10^{-6} cm^2 s^{-1}$ )	$E^{0'}$ (V vs SHE)
Cu(I)(dmp) <sub>2</sub> TFSI	7300	457	12.6	0.93
Cu(II)(dmp) <sub>2</sub> (TFSI) <sub>2</sub>	850	360	14.4	
Cu(I)(dmby) <sub>2</sub> TFSI	6900	455	11.7	0.97 <sup>a</sup>
Cu(II)(dmby) <sub>2</sub> TFSI/Cl	1300	360	33.3	
Cu(I)(tmby) <sub>2</sub> TFSI	5300	451	11.2	0.87 <sup>a</sup>
Cu(II)(tmby) <sub>2</sub> TFSI/Cl	1400	360	22.0	

( $\epsilon$  : extinction coefficient,  $\lambda_{max}$ =absorption peak wavelength, D: diffusion coefficient,  $E^{0'}$ : formal redox potential)

Note<sup>a</sup> These formal potentials are determined from the voltammogram of Cu(I)-species only.

The substitutions of the bipyridine ligands have an explicit influence on the redox potential of the complexes. The dimethyl substitution of the bipyridine ligands provides a higher redox potential for  $[Cu(dmby)_2]^{2+/1+}$ , whereas the additional two methyl groups giving the electron donation function, lower the redox potential for  $[Cu(tmby)_2]^{2+/1+}$ . The redox potential of  $[Cu(dmp)_2]^{2+/1+}$  has been reported to be 0.94 V vs SHE.<sup>89</sup>

In case of  $[Cu(tmby)_2]^{2+}$  and  $[Cu(dmby)_2]^{2+}$  species, we observe more complex voltammograms with negative shifts against the redox wave of  $[Cu(tmby)_2]^{1+}$  and  $[Cu(dmby)_2]^{1+}$ . Solely in the case of phenanthroline complex, the formal redox potentials of Cu(II) and Cu(I) species were matching. To address this issue further, an additional study was carried out, in which the  $Cu(dmby)^{2+}$  and  $Cu(tmby)^{2+}$  were reduced chemically, either by ferrocene or by ascorbic acid. In all cases simple voltammograms of Cu(I) species were obtained, which points out issues with the purity of the Cu(II) complexes (Figure 2-3). The reduction of  $Cu(tmby)^{2+}$  by ferrocene caused precipitation in the electrolyte solution, so the voltammogram cannot be considered quantitative, but an upshift of the redox waves of the reduction product is obvious (Figure 2-3a). A more elegant way of reducing  $Cu(tmby)^{2+}$  to  $Cu(tmby)^+$  is the use of ascorbic acid (Figure 2-3b). The electrochemical data shows that the reaction of  $CuCl_2$  with the corresponding ligand provides more complex products than it is originally assumed. In this stage of the study, it was presumed that the TFSI anion is coordinating to Cu(II) center, leading to the two species deferring in redox potentials. In contrast the chemical oxidation of  $Cu(dmp)^+$  by  $NOBF_4$  provided a single species as shown in Figure 2-2a.

In a more recent work by J. Hupp and coworkers,  $TiO_2$  conduction band edge shifts were attributed to the result of the coordination changes of the copper species due to excess TBP<sup>82</sup>. In addition to standard electrochemical potential determinations, cyclic voltammetry experiments were also performed in excess TBP conditions (2.5 times higher molar excess of TBP referenced to Cu(I), similar to the electrolyte solution). In the case of excess TBP, significant negative shifts (about 20 mV) in the redox potentials were observed for the three investigated complexes, which also enhance the dye regeneration efficiencies by the increased driving forces (Figure 2-2).

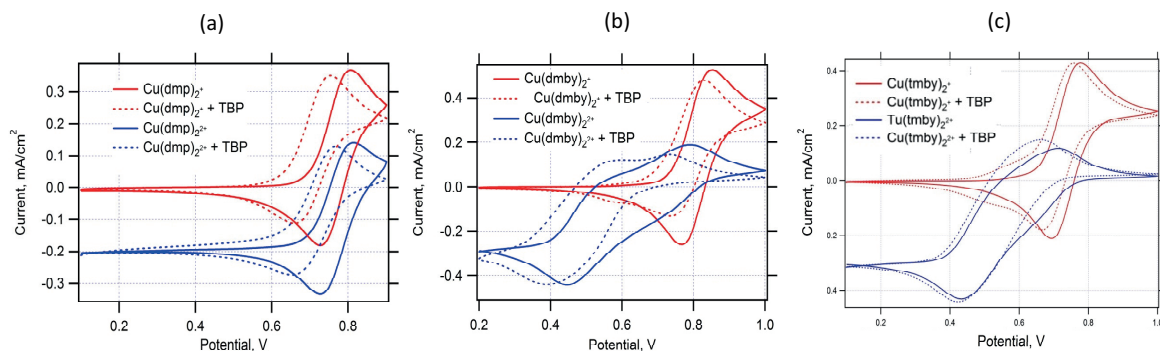


Figure 2-2 Cyclic voltammograms of 5 mM solutions of (a)  $[\text{Cu}(\text{dmp})_2][\text{TFSI}]$  (red curves) and  $[\text{Cu}(\text{dmp})_2][\text{TFSI}]_2$  (blue curves), (b)  $[\text{Cu}(\text{dmby})_2][\text{TFSI}]$  (red curves) and  $[\text{Cu}(\text{dmby})_2][\text{TFSI}]_2$  (blue curves) (c)  $[\text{Cu}(\text{tmby})_2][\text{TFSI}]$  (red curves) and  $[\text{Cu}(\text{tmby})_2][\text{TFSI}]_2$  (blue curves) in 0.1 M LiTFSI/acetonitrile. Scan rate 10 mV/s. Dashed lines are voltammograms of the same species but after adding 4-tert-butylpyridine (12.5 mM concentration). Potentials are referenced to the Ag/AgCl (sat'd LiCl in ethanol) reference electrode. A standard ferrocene couple was 0.469 V vs. Ag/AgCl (with no significant influence of TBP addition).

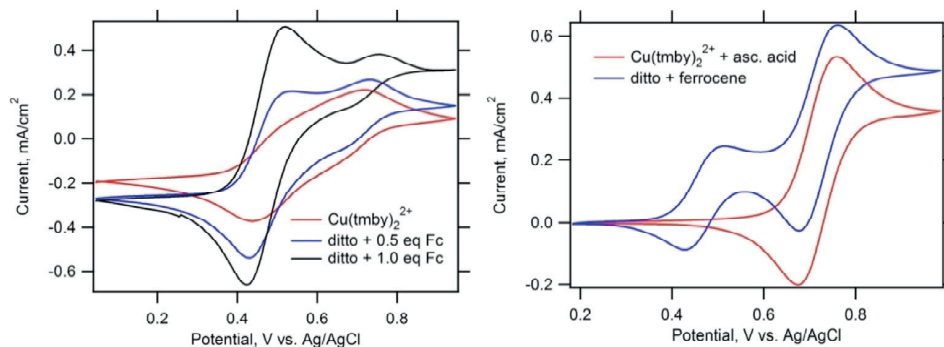


Figure 2-3 Right chart: Cyclic voltammograms of 5 mM solutions of  $[\text{Cu}(\text{tmby})_2][\text{TFSI}]_2$  (red curves) and the same complex after addition of 0.5 or 1 equivalents of ferrocene (blue or black curves, respectively) in 0.1 M LiTFSI/acetonitrile. Left chart: product of chemical oxidation of  $[\text{Cu}(\text{tmby})_2][\text{TFSI}]_2$  by ascorbic acid (blue curve is for the same solution after adding ferrocene). Scan rate 10 mV/s.

The absorption spectra of  $\text{Cu}(\text{I})(\text{tmby})_2$ ,  $\text{Cu}(\text{I})(\text{dmby})_2$  and  $\text{Cu}(\text{I})(\text{dmp})_2$  show absorption maxima at  $\lambda_{\text{max}} = 450\text{--}460$  nm in acetonitrile, which is attributed to the metal-to-ligand charge transfer (MLCT) transitions (Figure 2-4 and Figure 2-5). For  $\text{Cu}(\text{II})$  species, the absorption peaks are observed in the UV region assigned to  $\pi \rightarrow \pi^*$  transitions (see, Figure 2-4).

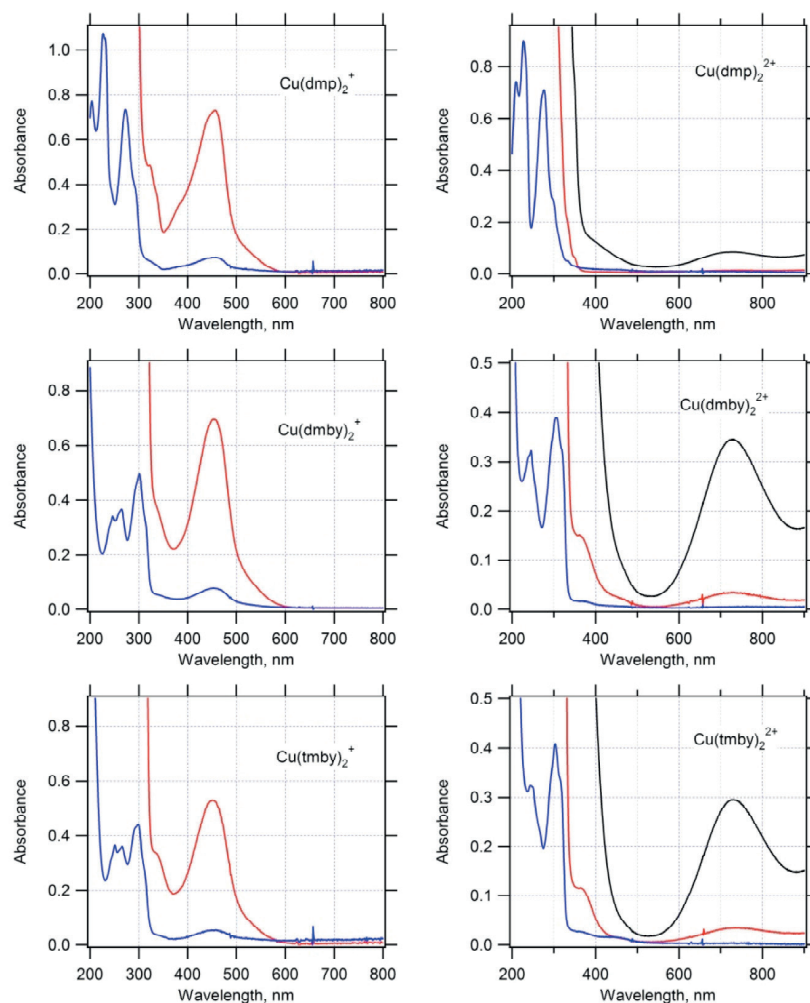


Figure 2-4 UV-Vis spectra of  $\text{CuL}_2\text{TFSI}_{1/2}$  ( $L = \text{ligand}$ ) in acetonitrile solution, concentration  $50 \mu\text{M}$  (blue curves),  $0.5 \text{ mM}$  (red curves) and  $5 \text{ mM}$  (black curves). Optical cell thickness  $2 \text{ mm}$ .

To compare the diffusion coefficients of the copper complexes, rotating disk electrode measurements were carried out. The results were analyzed with the use of the Koutecky-Levich equation. It is observed that copper complexes have higher diffusion coefficients in comparison to a cobalt tris-bipyridine complex. Each copper atom (with coordination number 4) is chelated with 2 ligands, whereas cobalt complexes (coordination number of 6) require 3 ligands. The copper complexes have smaller molecular sizes and therefore higher diffusion coefficients. It can easily diffuse in the mesoporous structure. (The diffusion coefficients for  $\text{Co(III)(bpy)}_3(\text{TFSI})_3$  and  $\text{Co(II)(bpy)}_3(\text{TFSI})_2$  were determined to be  $7.2 \times 10^{-6} \text{ cm}^2 \text{ s}^{-1}$  and  $6.1 \times 10^{-6} \text{ cm}^2 \text{ s}^{-1}$ , respectively, under the same experimental conditions.)

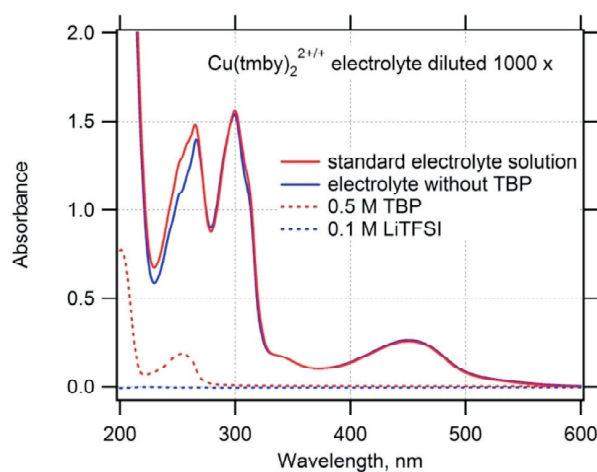


Figure 2-5 UV-Vis spectrum of the actual electrolyte solution (diluted 1000 x with acetonitrile). For comparison, the spectra of individual components are shown too. The actual working electrolyte solutions prepared without TBP is displayed by the blue curve. Optical cell thickness 2 mm.

### 2.2.2 Density Functional Theory Calculations (DFT)

In order to estimate the reaction free energies and internal reorganization energies for the three copper complexes, we performed DFT calculations with the Gaussian 09 suite of programs<sup>90</sup> at the PBE0 level of theory<sup>91</sup> with SDD ECP as basis set for Cu and TZVP basis set for other atoms. Structural optimizations, molecular frequencies and thermochemistry data were obtained in solution with the polarizable continuum model (PCM) for acetonitrile.<sup>92,93</sup> Vertical excitation energies have been computed with time-dependent DFT (TD-DFT) at the same level of theory.<sup>94</sup>

For the three copper(I) complexes, HOMO and LUMO are both doubly degenerate. For  $[\text{Cu}(\text{dmp})_2]^{1+}$ , the computed first electronic transition ( $\Delta E_{\text{exc}}$ ) at 466 nm (Table 8-1) corresponds to the HOMO-LUMO transition and has a clear metal-to-ligand charge transfer character, Figure 8-1. The molecular orbitals for  $[\text{Cu}(\text{tmby})_2]^{1+}$  and  $[\text{Cu}(\text{dmby})_2]^{1+}$  present similar qualitative features.

According to the computations, copper(I) ligands stay in a perpendicular configuration (Figure 2-6), providing a tetrahedral coordination sphere for copper. Upon oxidation, the perpendicular alignment decays to a distorted tetragonal structure (Figure 2-7 and Table 8-2): the most favored square-planar Cu(II) coordination is prevented by the steric hindrance effects of the methyl groups in the 2,9 positions of the ligands. The free energy difference ( $\Delta G_{\text{ox}}$ ) for oxidation of copper species and the internal reorganization energies ( $\lambda_{\text{in}}$ ) have been calculated for such configurations and the results are listed in Table 2-2. These free-energy values are qualitatively consistent with the observed trend in experimental oxidation potentials. For the three copper complexes, the predicted inner-sphere reorganization energies are very low, about 0.3 eV, in comparison with these of cobalt species: for  $\text{Co}(\text{bpy})_3$  and related complexes, the  $\lambda_{\text{in}}$  values, computed with the same approach, lie in the range of 0.52-0.63 eV (considering Co(II) low spin) and 1.39-1.78 eV (for Co(II) high spin).<sup>95</sup> We have only addressed the internal (inner-sphere) reorganization energy because recent works from other groups<sup>95,96</sup> have proven that this parameter ( $\lambda_{\text{in}}$ ) is the key feature limiting the overall dye regeneration process by Co-based redox mediators.

It is found that these low reorganization energy values for the copper complexes originate from very small changes in ligand-copper distances upon oxidation, which are only  $\sim 2\%$  for Cu-ligand (against  $\sim 10\%$  for Co-ligand complexes).<sup>95</sup> Moreover, the Cu(I) ion in its spherically symmetric  $3d^{10}$  electronic configuration is less sensitive than Co(II) to structural distortions in the ligand coordination sphere. For copper complexes, with the smaller re-organization energies, the driving force for dye regeneration can be kept small to obtain improved photovoltages.

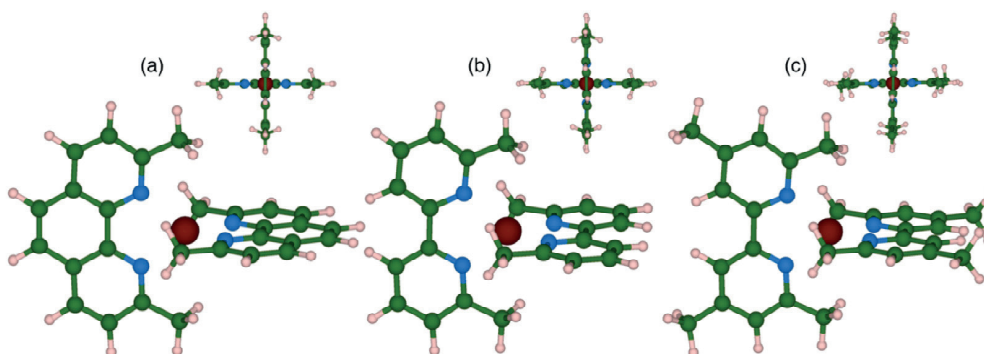


Figure 2-6 Cu(I)  $L_2$  minimum-energy structures, L is dmp (a), dmby (b) and tmby (c).

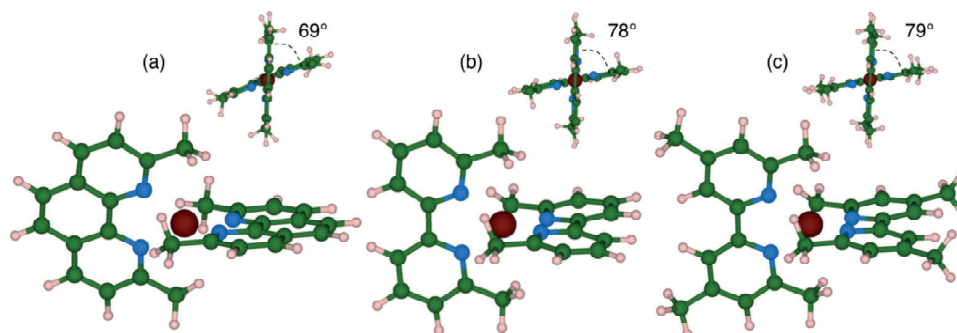


Figure 2-7 Cu(II)  $L_2$  minimum-energy structures, L is dmp (a), dmby (b) and tmby (c).

Table 2-2 Free energy differences for the Cu(I)  $\Rightarrow$  Cu(II) process ( $\Delta G_{\text{ox}}$ ) and corresponding inner-sphere reorganization energy ( $\lambda_{\text{in}}$ )

	$\Delta G_{\text{ox}}$ (eV)	$\lambda_{\text{in}}$ (eV)
$[\text{Cu}(\text{dmp})_2]^{1+/2+}$	4.68	<b>0.281</b>
$[\text{Cu}(\text{dmby})_2]^{1+/2+}$	4.64	<b>0.301</b>
$[\text{Cu}(\text{tmby})_2]^{1+/2+}$	4.47	<b>0.294</b>
$[\text{Co}(\text{bpy})_2]^{2+/3+}$ (low-spin) <sup>95</sup>	5.00	<b>0.613</b>

### 2.2.3 Photovoltaic Performance of Dye-sensitized Solar Cells with Copper Complexes

The photocurrent-voltage data of solar cells containing the three different copper redox mediators and Y123 sensitized TiO<sub>2</sub> films are given in Figure 2-8.

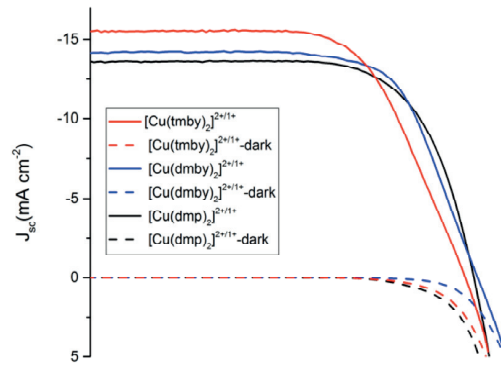


Figure 2-8 Photocurrent density vs voltage (J-V) curves measured under standard AM 1.5G illumination and in the dark for solar cells sensitized with Y123 dye and employing copper complexes.

The photocurrent densities, open circuit voltages, fill factors and power conversion efficiencies of the DSC devices employing the [Cu(tmby)<sub>2</sub>]<sup>2+/1+</sup>, [Cu(dmby)<sub>2</sub>]<sup>2+/1+</sup> and [Cu(dmp)<sub>2</sub>]<sup>2+/1+</sup> complexes are summarized in Table 2-3. The power conversion efficiency is calculated using Equation 1-10. For all complexes, PCEs above 10% at AM 1.5 G illumination were reached. This was the highest PCEs reported for DSCs based on Cu complexes as redox mediators when we carried out this study. The three redox couples show remarkably high open circuit voltage values of more than 1.0 V at full sunlight illumination. Evidently, a regular trend between the formal redox potentials (Table 2-3) and the V<sub>oc</sub> values was observed. Though the trend between V<sub>oc</sub> and E<sup>0</sup> is proportional, there are other effects to be taken into account in the discussion of the open circuit voltages of the DSCs. This will be further discussed below in relation to recombination and conduction band edge shifts with electron lifetimes and charge extraction measurements, respectively. The short-circuit current density is observed to be highest for the [Cu(tmby)<sub>2</sub>]<sup>2+/1+</sup> electrolyte as a result of the highest driving force available for dye regeneration. Having the highest extinction coefficients for Cu(I), the [Cu(dmp)<sub>2</sub>]<sup>1+/2+</sup> complex shows the lowest short-circuit current density due to the competitive light absorbance.

Table 2-3 J-V characteristics for the [Cu(dmp)<sub>2</sub>]<sup>2+/1+</sup>, [Cu(dmby)<sub>2</sub>]<sup>2+/1+</sup> and [Cu(tmby)<sub>2</sub>]<sup>2+/1+</sup> complexes

Redox couple	V <sub>oc</sub> (V)	J <sub>sc</sub> (mA cm <sup>-2</sup> )	FF	PCE (%)
[Cu(tmby) <sub>2</sub> ] <sup>2+/1+</sup>	1.04	15.53	0.640	10.3
[Cu(dmby) <sub>2</sub> ] <sup>2+/1+</sup>	1.07	14.15	0.687	10.0
[Cu(dmp) <sub>2</sub> ] <sup>2+/1+</sup>	1.06	13.61	0.692	10.3

The IPCE spectra for the DSC devices employing the three different redox couples are given in Figure 2-9. For  $[\text{Cu}(\text{tmby})_2]^{2+/1+}$  based electrolyte, the maximum IPCE is found to be 92% at 520 nm. For  $[\text{Cu}(\text{dmp})_2]^{2+/1+}$  and  $[\text{Cu}(\text{dmby})_2]^{2+/1+}$  the maxima are 85% and 75%, respectively, around 500nm. The drop of IPCE at 360nm and 450nm is ascribed to the absorption of Cu(I) and Cu(II) species in these regions. For further analysis, IPCE can be expressed as in Equation 1-14, by considering the effects of light-harvesting efficiency, quantum yield of electron injection, and photo-generated charge collection efficiency. By assuming similar light-harvesting efficiency and quantum yield of electron injection values (same dye and same working electrode parameters), the charge collection efficiency values can be compared for the copper complexes under study. The  $[\text{Cu}(\text{tmby})_2]^{2+/1+}$  electrolyte showed the best charge collection efficiencies due to the increased driving force for dye regeneration and presumably reduced recombination as indicated from electron lifetime measurements (electron lifetimes are measured under open circuit conditions). The broader IPCE spectrum for the  $[\text{Cu}(\text{tmby})_2]^{2+/1+}$  complex is attributed both to the electron collection yield due to longer electron lifetimes in the  $\text{TiO}_2$ , and lower extinction coefficient of this complex. The slightly blue shifted IPCE of  $[\text{Cu}(\text{dmp})_2]^{2+/1+}$  indicates higher competitive light absorption for this complex.

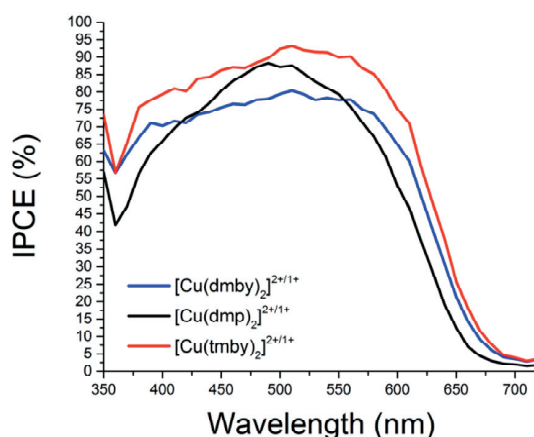


Figure 2-9 IPCE spectra of DSC devices sensitized with Y123 dye

#### 2.2.4 Electron Lifetime Measurements

To understand the recombination reaction between the oxidized form of the redox species and injected electrons in  $\text{TiO}_2$ , electron lifetime and charge extraction measurements were carried out. Semi-logarithmic plots of the measured electron lifetimes with respect to the quasi-Fermi level of the electrons in the  $\text{TiO}_2$  electrode of the complete devices are given in Figure 2-10. At the same Fermi level (-0.05V vs SHE) the electron lifetimes were measured as 0.036, 0.021 and 0.006 s for the  $[\text{Cu}(\text{tmby})_2]^{2+/1+}$ ,  $[\text{Cu}(\text{dmp})_2]^{2+/1+}$  and  $[\text{Cu}(\text{dmby})_2]^{2+/1+}$ , respectively. The electron lifetime values indicate that the recombination reaction is driving force dependent, corresponding to the Marcus normal-region. The effect of steric properties of the ligands on the copper complexes is calculated to be similar for the recombination reaction due to similar re-organization energy values (Table 2-2) and therefore neglected. Electron lifetimes followed a coherent trend with respect to the driving force for recombination reaction. Since the driving force for recombination is the lowest in case of  $[\text{Cu}(\text{tmby})_2]^{2+/1+}$  complex, the electron lifetime showed higher values in comparison to the other



complexes. By having the most positive formal redox potential, the  $[\text{Cu}(\text{dmby})_2]^{2+/1+}$  complex resulted in lower electron lifetimes. The changes in the slopes of the electron lifetime data (see Figure 2-10) of the copper complexes are attributed to the recombination of electrons with FTO substrates at low currents. Preventing recombination at low currents can be achieved by better blocking layer processing and sensitizers with blocking properties.<sup>97</sup>

The fact that the  $V_{\text{OC}}$  values from the different Cu-complexes are close to each other, above 1.0 V, although the redox potentials differ by about 0.1 V, can be explained together by the differences in electron lifetimes and conduction band shifts. The  $V_{\text{OC}}$  value will be a compromise between driving force and recombination. For a larger driving force there will be a bigger internal potential drop between the redox potential of the electrolyte and the oxidation potential of the dye, leading to relatively lower  $V_{\text{OC}}$ . At the same time dye regeneration will be faster and more efficient (see below). Faster dye regeneration will intercept the recombination reaction between electrons in the  $\text{TiO}_2$  and oxidized dye and lead to longer electron lifetime. This is an indication of higher electron concentration in the  $\text{TiO}_2$ , which means a higher quasi-Fermi level of the electrons and a relatively higher  $V_{\text{OC}}$ . Even if the  $[\text{Cu}(\text{tmby})_2]^{2+/1+}$  complex has a lower redox potential, 0.1V lower compared to  $[\text{Cu}(\text{dmby})_2]^{2+/1+}$ , the  $V_{\text{OC}}$  values are similar due to longer electron lifetimes for  $[\text{Cu}(\text{tmby})_2]^{2+/1+}$ . The contribution of conduction band positions on  $V_{\text{OC}}$  can be observed via the charge extraction data. For the studied complexes, the charge extraction values normalized to Fermi level of the  $\text{TiO}_2$  are given in Figure 2-11. At a certain value of extracted charge, the conduction band positions appeared to be most negative for  $[\text{Cu}(\text{dmp})_2]^{2+/1+}$ , which is followed by  $[\text{Cu}(\text{tmby})_2]^{2+/1+}$  and  $[\text{Cu}(\text{dmby})_2]^{2+/1+}$ . By having the most negative conduction band position and longer electron lifetimes,  $[\text{Cu}(\text{dmp})_2]^{2+/1+}$  could reach  $V_{\text{OC}}$  values similar to the values of  $[\text{Cu}(\text{dmby})_2]^{2+/1+}$  although the redox potential is lower. The differences in conduction band edges are attributed to the ligand coordination changes due to TFSI and TBP especially for the  $[\text{Cu}(\text{tmby})_2]^{2+}$  and  $[\text{Cu}(\text{dmby})_2]^{2+}$ , in which the effect of coordination differences are clearly observable via cyclic voltammograms (Figure 2-2).

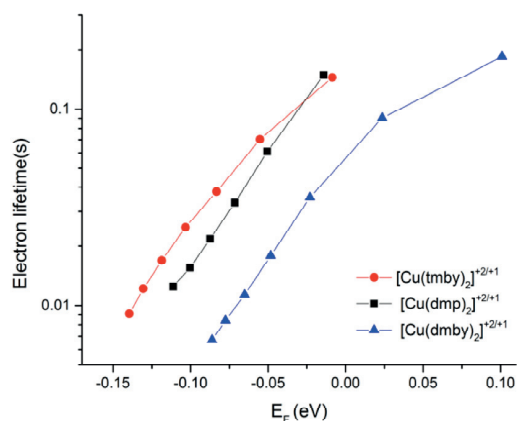


Figure 2-10 Electron lifetimes for the three copper complexes.

The light intensity dependence of the short circuit current density and photovoltage are given in Figure 2-12. The  $J_{\text{SC}}$  values showed a linear dependence for the  $[\text{Cu}(\text{tmby})_2]^{2+/1+}$  complex. For the  $[\text{Cu}(\text{dmp})_2]^{2+/1+}$  and  $[\text{Cu}(\text{dmby})_2]^{2+/1+}$  complexes the photocurrent deviates from linearity with in-

creasing light intensities. This effect can be explained with mass transport limitations of the copper complexes. Under higher light intensities diffusion problems gives rise to a higher internal series resistance. This will result in a non-linear behavior of the photocurrent with light intensity as well as limitations of the fill factor in the DSC device. The high photovoltage stays nearly independent of illumination intensity above 0.2 sun, being higher than 1.0 V at 0.2 sun for the  $[\text{Cu}(\text{tmby})_2]^{2+/1+}$  and  $[\text{Cu}(\text{dmp})_2]^{2+/1+}$  complexes. This feature gives copper complexes an intriguing potential for use in devices for diffuse light and indoor applications (see Chapter 7).

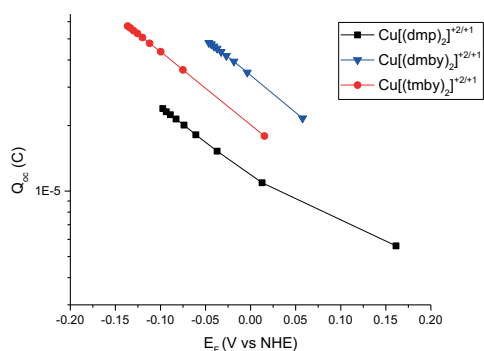


Figure 2-11 Charge extraction data obtained for devices with different electrolytes ( $E_{F,\text{TiO}_2} = E_{F,\text{redox}} - V_{oc}$ )

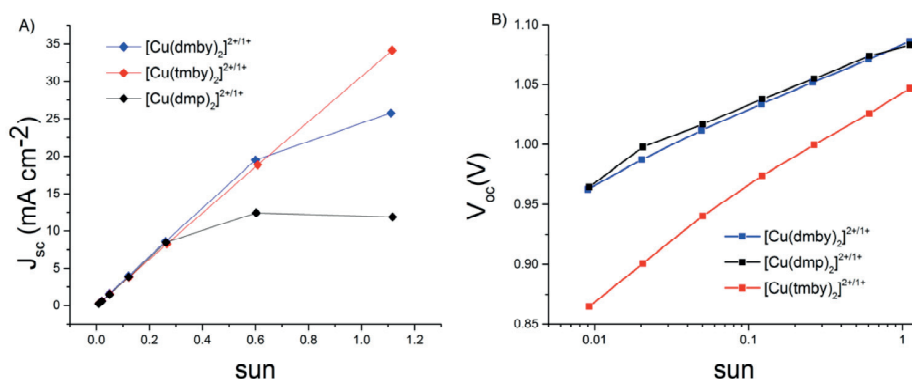


Figure 2-12 Light intensity dependence of (A) short-circuit current and (B) photovoltage for DSC devices based on the three different copper electrolytes

### 2.2.5 Dye regeneration

The regeneration kinetics of the Y123 chromophore by the three copper complexes were investigated with Photoinduced Absorption Spectroscopy (PIA). The PIA spectra for the inert electrolyte solution together with the  $[\text{Cu}(\text{dmp})_2]^{2+/1+}$ ,  $[\text{Cu}(\text{dmby})_2]^{2+/1+}$  and  $[\text{Cu}(\text{tmby})_2]^{2+/1+}$  electrolytes are given in Figure 2-13. Without the redox couple in the electrolyte, a bleach was observed at 540 nm due to the ground-state bleach of the dye upon oxidation and Stark shift, i.e. absorption change of the dye as a result of changes in the electrical field across the dye molecules by the photoinjected elec-

trons.<sup>98,99</sup> We also observe absorption peaks of the oxidized dye appearing at 680 nm and 800 nm in the absence of the copper complexes. In the spectra of copper complexes, the bleach persisted around 520 nm as a result of the Stark effect, whereas the absorption peaks of the oxidized dye disappear due to efficient regeneration of the oxidized dye molecules with the redox species. The positive signal remaining in the PIA spectra higher than 650 nm is attributed to the absorption of electrons that are accumulated in TiO<sub>2</sub>. From the results of the PIA measurements it can be concluded that the copper complexes can effectively regenerate the oxidized dye species.

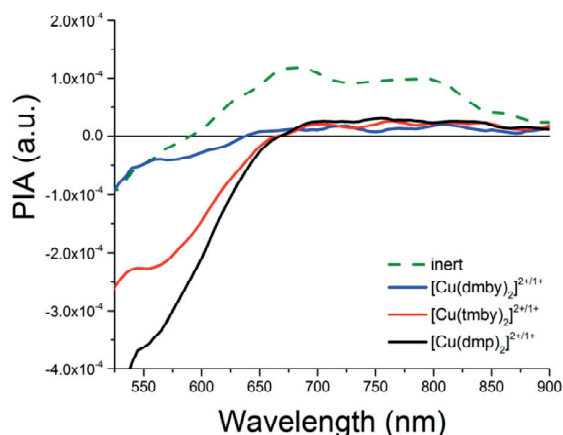


Figure 2-13 PIA spectra of Y123 sensitized TiO<sub>2</sub> with an inert electrolyte and with electrolytes prepared with the three different copper complexes.

## 2.2.6 Transient Absorption Spectroscopy

Dye regeneration kinetics with the copper complexes were further investigated with nanosecond transient absorption spectroscopy (TAS) measurements, Figure 2-14. With an inert electrolyte (0.1 M Lithium bis(trifluoromethylsulfonyl)imide)(LiTFSI) and 0.6M TBP in acetonitrile), the recombination of injected electrons in the TiO<sub>2</sub> and oxidized dye molecules showed an absorbance decay signal with a 10 ms half-time( $\tau_{1/2}$ ). This is significantly slower than previously reported value for this dye, which can be explained by the lower laser light intensity used in this work (1.27  $\mu\text{J}/\text{cm}^2$ ) with respect to the reference study (20  $\mu\text{J}/\text{cm}^2$ ).<sup>54</sup> In the presence of copper-complexes, the absorbance signal show an accelerated decay by the faster regeneration of oxidized dye molecules with Cu<sup>1+</sup> species. The regeneration halftimes of [Cu(tmby)<sub>2</sub>]<sup>2+/1+</sup>, [Cu(dmp)<sub>2</sub>]<sup>2+/1+</sup> and [Cu(dmby)<sub>2</sub>]<sup>2+/1+</sup> are 1.8 $\mu\text{s}$ , 2.8 $\mu\text{s}$  and 4.8 $\mu\text{s}$ , respectively, under the same conditions, showing a direct relation to the driving forces for dye regeneration. The regeneration efficiencies ( $\Phi_{\text{reg}}$ ) for the copper complexes are calculated using Equation 1-5. For all the copper electrolytes the  $\Phi_{\text{reg}}$  values found are close to 100%. For the Y123 dye, the regeneration efficiencies of cobalt ([Co(bpy-pz)<sub>2</sub>]<sup>3+/2+</sup>) (0.86V vs SHE) and iodide/tri-iodide (0.37V vs SHE) electrolytes were previously reported to be 0.93 and 0.98, respectively based on 1.1ms half-time for the oxidized dye signal decay.<sup>54</sup> We can conclude that with a relatively low driving force for dye regeneration, the Cu-complexes investigated in this study provide faster kinetics compared to previously reported systems. The comparison of regeneration efficiencies with previously reported values for cobalt and iodide/tri-iodide indicates a better dye regeneration for copper complexes.

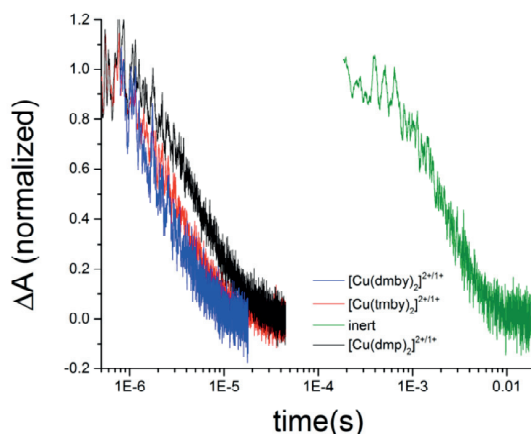


Figure 2-14 Transient absorption spectroscopy measurements of Y123 sensitized  $\text{TiO}_2$  films with inert,  $[\text{Cu}(\text{dmby})_2]^{2+/1+}$ ,  $[\text{Cu}(\text{tmby})_2]^{2+/1+}$  and  $[\text{Cu}(\text{dmp})_2]^{2+/1+}$  electrolytes.

### 2.3 Conclusion

In this chapter, the conventional iodide/tri-iodide or cobalt based electrolytes for DSCs have very successfully been replaced with  $\text{Cu}^{(\text{II/I})}(\text{dmby})_2\text{TFSI}_{2/1}$  (0.97 V vs SHE) and  $\text{Cu}^{(\text{II/I})}(\text{tmby})_2\text{TFSI}_{2/1}$  (0.87 V vs SHE) complexes. These copper complexes were compared to the previously reported  $[\text{Cu}(\text{dmp})_2]^{2+/1+}$  complex by using the Y123 dye. Because of the high redox potentials of the copper electrolytes, the potential used for dye regeneration is minimized. With the given ligand structures providing small reorganization energies, the copper electrolytes are able to regenerate oxidized dye molecules with values close to unit yield even with relatively low driving forces. With the optimized devices 10.2%, 10.1 % and 10.3% overall solar-to-electrical power efficiencies were recorded for  $[\text{Cu}(\text{tmby})_2]^{2+/1+}$ ,  $[\text{Cu}(\text{dmby})_2]^{2+/1+}$  and  $[\text{Cu}(\text{dmp})_2]^{2+/1+}$  based electrolytes, respectively, under  $1000 \text{ W m}^{-2}$  AM1.5G illumination. The photocurrent voltages are recorded to be higher than 1000mV indicating reduced potential losses in the devices. The efficient regeneration at minimized driving forces open up possibilities for increasing DSC record efficiencies. Since the photovoltage remain high, above 1V down to 0.2 sun light intensity, we anticipate these Cu-complex based DSCs to be particularly attractive for indoor applications (as shown in Chapter 7). It is also clear that with an improved fill factor through a better counter electrode material, the PCE values could be improved further.

### 2.4 Experimental

*Chemicals and Reagents.* All chemicals and solvents were purchased from Sigma-Aldrich, HetCat and TCI Chemicals, if not otherwise stated, and were used without further purification.

*Synthesis of copper complexes.* The synthesis of copper complexes was performed as previously reported.<sup>89</sup> For  $(\text{Cu}(\text{dmp})_2\text{TFSI})$  (Figure 8-2), one equivalent of CuI was mixed with four equivalents of neocuproine hydrate in ethanol, under nitrogen atmosphere, at room temperature for 2 hours. The stirred solution was filtered and washed with water and diethyl ether. The resulting complex was collected as an intense red crystalline powder.

The  $\text{Cu}(\text{dmp})_2\text{TFSI}_2$  complex was produced by the oxidation of Cu(I) species with an addition of  $\text{NOBF}_4$ . Briefly,  $\text{Cu}(\text{dmp})_2\text{TFSI}$  was dissolved in acetonitrile and one equivalent of  $\text{NOBF}_4$ , followed by five equivalents of  $\text{LiTFSI}$  being added after 30 min.

The solution was further stirred for 2 hours at room temperature and nitrogen atmosphere. The solvent was removed by rotatory evaporation and the crude redissolved in minimum amount of dichloromethane (DCM).  $\text{Cu}(\text{dmp})_2\text{TFSI}_2$  was collected by filtration after precipitation from diethyl ether and washed with diethyl ether. The product was a bright violet powder.

For complexation of  $\text{Cu}(\text{dmby})_2\text{TFSI}$  and  $\text{Cu}(\text{tmby})_2\text{TFSI}$  one equivalent of  $\text{CuI}$  was mixed with three equivalents of  $\text{dmby}$  or  $\text{tmby}$ , respectively, in 20 ml ethanol, under nitrogen atmosphere, at room temperature for 2 hours (Figure 8-3). The resulting Cu(I) complexes were obtained as intense red, crystalline powders. The Cu(I) products were filtered and redissolved by addition of 5 ml of deionized water followed by an addition of five equivalents of  $\text{LiTFSI}$ . The solutions were further stirred for 2 hours at room temperature under nitrogen atmosphere resulting in red precipitations. The complexes were collected by filtration and washed with water as bright red powders.

For  $\text{Cu}(\text{dmby})_2\text{TFSI}_2$  and  $\text{Cu}(\text{tmby})_2\text{TFSI}_2$  one equivalent of  $\text{CuCl}_2$  was mixed with 3 equivalents of  $\text{dmby}$  or  $\text{tmby}$ , respectively, in 20 ml ethanol, under nitrogen atmosphere, at room temperature for 2 hours. The resulting complexes were obtained as green powders. The product Cu(II) species were filtered and redissolved by addition of 5 ml of deionized water followed by an addition of five equivalents of  $\text{LiTFSI}$ . The solution was further stirred for 2 hours at room temperature and under nitrogen atmosphere. The complexes were collected by filtration as green powders and washed with water.

*Electrochemical characterization.* Three electrode cyclic voltammetry measurements were performed using a Autolab Pgstat-30 potentiostat with  $\text{Ag}/\text{AgCl}/\text{saturated LiCl}$  (ethanol) as reference electrode and glassy carbon or platinum working electrodes under argon. Copper complexes were dissolved in acetonitrile, with  $\text{LiTFSI}$  (0.1M) as supporting electrolyte. Redox potentials were primarily referenced versus ferrocene, which was added *in-situ* as voltammetric standard. The formal potential of  $\text{Fc}/\text{Fc}^+$  couple was between 0.468 and 0.471 V vs, our  $\text{Ag}/\text{AgCl}$  reference electrode.

Diffusion coefficient measurements were performed via rotating disk electrode voltammetry. A Bio Logic SP300 potentiostat with a quasi-reference platinum electrode and glassy carbon rotating disk electrode (2.9 mm, Radiometer Analytical-CVJ) were used in a solution of 0.1 M  $\text{LiTFSI}$  and 0.5 M 4-tert-butylpyridine in acetonitrile under argon atmosphere. The rotor speed was controlled by a speed control unit (Radiometer Analytical-CTV101). The cell temperature was kept constant at 25 °C by a circulating water bath (HAAKE GH).

UV/Vis absorption data was gathered by a Hewlett-Packard 8453 diode array spectrometers and the extinction coefficients were calculated using the Lambert-Beer Law.

*Device fabrication.* Preparation of the working electrodes: The photoanodes with a mesoporous  $\text{TiO}_2$  layer, counter electrodes and electrolyte were prepared separately and then assembled in a solar cell device. For photoanodes a glass pretreatment procedure was followed to remove the contaminations that can affect the preparation of the compact underlayer and thus the cell performance.

FTO glasses (NSG-10, Nippon Sheet Glass) were first cleaned with a detergent solution (Deconex) in ultrasonic bath (45 min) and rinsed with water and ethanol. This initial step was followed by a 15 min UV/O<sub>3</sub> treatment (Model no.256-220, Jelight Company, Inc.). Then the substrates were immersed into a 53mM TiCl<sub>4</sub> solution and kept at 70 °C in an oven for 30 min to allow the formation of thin and compact TiO<sub>2</sub> underlayer. After 30 minutes the substrates were rinsed with water and ethanol. The TiCl<sub>4</sub> treatment was followed by 2 hours annealing process at 250 °C. Two layers of mesoporous TiO<sub>2</sub> layers were prepared on top of the underlayer; the first layer was screen printed using a paste consisting of 30 nm in diameter sized TiO<sub>2</sub> particles (Dyesol) and the second one with 400 nm sized particles (scattering layer). The substrates were sintered on a hot plate with a ramped temperature profile, keeping the temperature at 125, 250, 325, 450 and 500 °C for 5, 5, 5, 15 and 15 minutes, respectively, with 5 minutes ramp duration between each temperature. The resulting TiO<sub>2</sub> film thickness was 10 μm (5 μm + 5 μm). To increase the surface area of the TiO<sub>2</sub> particles, a TiCl<sub>4</sub> post-treatment was performed, which was followed by another sintering process at 500 °C for 30 min. Before dipping the TiO<sub>2</sub> electrodes into dye solutions, they were annealed with a heat gun for 30 minutes at 500°C. After cooling down to 80 °C, they were put into the dye solution.

Dye solutions: 0.1mM Y123 dye (Dyename AB) solutions were prepared in tert-butanol/acetonitrile (1:1 v:v) mixture. 0.4 mM chenodeoxycholic acid was used in the dye solutions as an additive to prevent aggregation. Working electrodes were dipped for 16 hours in these solutions.

Preparation of counter electrodes: FTO glass (TEC 6, Pilkington) as substrate for the counter electrodes was cleaned with Deconex (2 % wt in water), acetone and ethanol with 30 minutes duration for each, and coated with PEDOT via electrodeposition.<sup>100</sup>

The working electrodes and counter electrodes were assembled in a dry box with 25μm Surlyn (Dupont), which provides the spacing between the two electrodes as well as sealing for the electrolyte. The electrolyte was introduced into the device through a predrilled hole in the counter electrode under vacuum. The electrolytes consisted of 0.2 M Cu(I) and 0.04 M Cu(II) complexes with 0.1M LiTFSI and 0.6 M TBP in acetonitrile.

*Solar Cell Characterization.* The device current-voltage characteristics were obtained by using a 450W xenon light source (Oriel, U.S.A). A Keithley model 2400 digital source meter (Keithley, U.S.A) was used to apply an external potential bias to the devices and measure the resulting current.

*Incident-Photon-to-Current-Conversion Efficiency.* IPCE data were acquired using a modulated light intensity with a frequency of 1 Hz. The light, from a 300 W xenon light source (ILC Technology, U.S.A), was focused through a monochromator (JobinYvon Ltd., U.K) and directed to the device under test. A white light bias was used to have similar light intensity conditions as during normal operation.

*Electron Lifetime Measurements.* Electron lifetime measurements were performed using a white LED (Luxeon Star 1W) as light source. Voltage traces were recorded with a 16-bit resolution digital acquisition board (National Instruments) and lifetimes were determined by monitoring photovoltage transients at different light intensities upon applying a small square wave modulation to the base light intensity. The photovoltage responses were fitted using first-order kinetics to obtain time constants.

*Photoinduced Absorption Spectroscopy.* The photo-induced absorption spectra of the various cells were recorded over a wave-length range of 450–1000 nm following an (on/off) photo-modulation using a 36 Hz square wave emanating from a blue laser (406 nm) filter through a notch (Balzers 405). White probe light from a halogen lamp (20 W) was used as an illumination source. The light was focused into a monochromator (Horiba, Gemini) and detected using a Si photodiode with a gain of 10, connected to a lock-in amplifier (Stanford Research Systems model SR830).

*Transient Absorption Spectra.* The photo-induced kinetics was measured with an Ekspla NT-342 Q-switched Nd:YAG laser using 532 nm as excitation wavelength. The pulse width was 4-5 ns (FWHM) and the repetition rate was 20 Hz. The probe light source was a halogen lamp and the probe wavelength at 715 nm was chosen using a monochromator. The film was positioned at approximately 45 degree angle with respect to the incoming laser pulse, for front illumination. The signal was detected using the photomultiplier tube R9110 from Hamamatsu and recorded using the oscilloscope DPO 7254 from Tektronix. The radiant output of the laser was attenuated using grey optical density filters to  $46 \mu\text{J}/\text{cm}^2$  for the measurements of the samples containing redox mediators, and  $1.27 \mu\text{J}/\text{cm}^2$  for the electrolytically inert samples. Low light intensity value was deliberately chosen in order to ensure that the data could be fitted to single exponential functions from which the lifetimes could be obtained. An acquisition was averaged over 3000 laser shots.





# Chapter 3 Methods for producing electrochemically clean Cu(II)-bipyridine complexes

This chapter is adopted from the following articles with the permission of the journals:

Postprint version of the publication: 'Electrochemical Properties of Cu(II/I)-Based Redox Mediators for Dye-Sensitized Solar Cells, *Electrochimica Acta* 2017, 227, 194-207. doi:10.1016/j.electacta.2016.12.185' by Ladislav Kavan, Yasemin Saygili, Marina Freitag, Shaik M. Zakeeruddin, Anders Hagfeldt and Michael Grätzel

and

Postprint version of the publication: 'Alternative Bases to 4-tert-butylpyridine for Dye-Sensitized Solar Cells Employing Copper Redox Mediator, *Electrochimica Acta* 2018, 265, 194-201. doi:10.1016/j.electacta.2018.01.142' by Parnian Ferdowsi\*, Yasemin Saygili\*, Shaik M. Zakeeruddin, Javad Mokhtari, Michael Grätzel, Anders Hagfeldt, and Ladislav Kavan. (\* denotes shared first co-authors)

My contribution for the 1<sup>st</sup> paper: Synthesis of the complexes, preparation of the electrodes, device fabrication and characterization, writing the corresponding parts in the manuscript.

My contribution for the 2<sup>nd</sup> paper: Reformulation of the synthetic method of Cu(II) species, synthesis of the complexes, preparation of the electrodes, device characterization, impedance analysis (partly), analysis of the characterization data, writing the corresponding parts in the manuscript.

In the previous chapter, we showed that the  $[\text{Cu}(\text{tmby})_2]^{2+}$  and  $[\text{Cu}(\text{dmby})_2]^{2+}$  species did not behave electrochemically like the corresponding Cu(I) counterparts, interestingly, however, the  $[\text{Cu}(\text{dmp})_2]^{2+}$  complex did. More specifically, the Cu(II)-bipyridine complexes exhibited unexpected two-waves voltammograms with downshifted formal potentials, clearly pointing to impurity issues from the synthetic procedure of these complexes, but the problem remained open. In this chapter we demonstrate three methods for producing electrochemically and optically a clean  $[\text{Cu}(\text{tmby})_2]^{2+}$  complex.

## 3.1 Introduction

One of the non-trivial problems associated with the  $[\text{Cu}(\text{tmby})_2]^{2+/+}$ -mediator is the low stability of the coordination sphere of the Cu(II) counterpart of the redox couple, which follows from strong

preference of Cu(II), but not Cu(I), for less-polarizable and more Lewis-basic ligands<sup>82,101</sup>. Consequently, in the previous chapter<sup>102</sup>, as well as the succeeding breakthrough contributions,<sup>103,104</sup> the standard-purity Cu(tmby)<sub>2</sub><sup>+</sup> complex was used, but the corresponding Cu(II)-counterpart was of debatable quality. More specifically, the used Cu(II)-complex exhibited a complicated cyclic voltammogram, different from that of Cu(tmby)<sub>2</sub><sup>+</sup><sup>101,102</sup>. Obviously, the originally used synthetic protocol, based on the reaction of CuCl<sub>2</sub> with 1.5 excess of a free ligand (tmby) and 2.5 excess of LiTFSI<sup>102</sup>, did not lead to a simple product, i.e. Cu(tmby)<sub>2</sub>TFSI<sub>2</sub>. To address this issue, we found that chemical oxidation of Cu(tmby)<sub>2</sub>TFSI provided the desired electrochemically clean Cu(tmby)<sub>2</sub>TFSI<sub>2</sub><sup>101</sup>. Furthermore, we showed an electrochemical method towards electrochemically clean Cu(II) species. However, the preparative electrolysis requires special equipment. Lastly, we provide a novel facile synthetic protocol to prepare electrochemically and optically clean Cu(tmby)<sub>2</sub>TFSI and Cu(tmby)<sub>2</sub>TFSI<sub>2</sub> in a mixture (tmby = 4,4,6,6-tetramethyl-2,2-bipyridine; TFSI = trifluoromethylsufonylimide). This pure Cu(II/I) redox mediator exhibits improved charge-transfer rate at the counter-electrode (PEDOT) and faster diffusion transport in the solution.

## 3.2 Results and Discussion

### 3.2.1 Cu(II)-bipyridine complexes from the chemical oxidation of Cu(I) species

In order to address the peculiarity of Cu(II)-bipyridine voltammograms (Figure 2-2), we first recall the fact that ‘neat’ Cu(II)-dmp species is synthesized from the parent Cu(I)-dmp by chemical oxidation with NOBF<sub>4</sub>, while the ‘un-neat’ Cu(II)-bipyridine is made by direct synthesis from CuCl<sub>2</sub> and the corresponding ligand. This outlines a logical strategy to test the chemical oxidation of Cu(I)-bipyridine as well. Figure 3-1 shows that, indeed, the chemical oxidation of [Cu(tmby)<sub>2</sub>]<sup>+</sup> successfully provided the electrochemically clean Cu(II)-bipyridine. The oxidized species exhibited the expected voltammogram with identical formal potentials and only with a cathodically shifted plateau of diffusion currents. Hence, the reactions which are schematically depicted as follows:



is readily applicable for the bipyridine complexes as well as for the phenanthroline complexes. However, closer inspection of Figure 3-1 reveals that the reactions (3:1) are by far not stoichiometric, i.e. more than 1 equivalent of the oxidant is needed to complete the oxidation. Furthermore, the reaction proceeds quite slowly (progressing during 10 hours of aging the reaction mixture) and is accompanied by partial oxidative destruction of the starting substance, which manifests itself by decreasing voltammetric currents at the final stages of the reaction. Owing to these drawbacks, we developed other methods as described in the following sections.

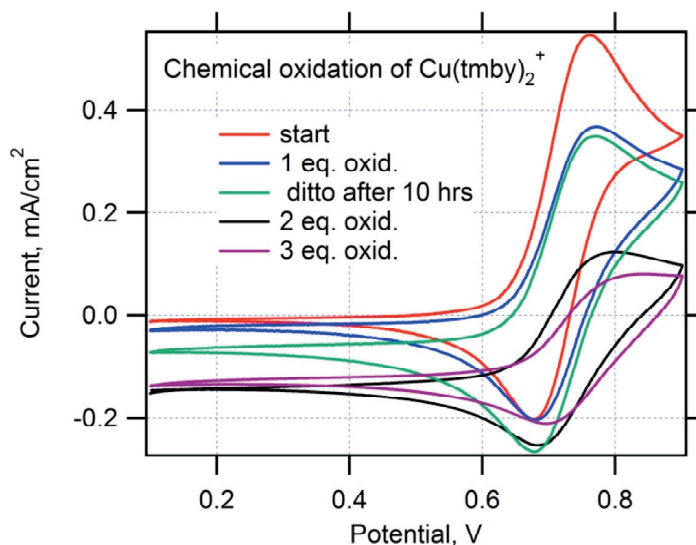


Figure 3-1 Cyclic voltammograms of  $[\text{Cu}(\text{tmby})_2][\text{TFSI}]$  and the products of its chemical oxidation by  $\text{NOBF}_4$ . Scan rate 10 mV/s. Curve 'start' (red): cyclic voltammogram of the starting 5 mM solution of  $[\text{Cu}(\text{tmby})][\text{TFSI}]_2$  in 0.1 M LiTFSI + acetonitrile. The other voltammograms are for the products obtained upon addition of the given amount of  $\text{NOBF}_4$  and/or equilibration by aging (see annotation in the graph). Potentials are referenced to the Ag/AgCl (saturated LiCl in ethanol) reference electrode.

### 3.2.2 Preparation of electrochemically clean Cu(II)-bipyridine complexes

The problems observed in oxidation with  $\text{NOBF}_4$ , are elegantly avoided if the oxidation is carried out electrochemically instead of chemically. A preparative electrolysis of Cu(I)-bipyridine in a divided electrochemical cell and potentiostatic mode leads to clean Cu(II)-bipyridine products in stoichiometric yield and free from any oxidative destruction. Figure 3-2 shows the relevant data for  $[\text{Cu}(\text{tmby})_2]^+$  oxidation. Obviously, each portion of the passed charge (E1-E5) caused the relevant oxidative transformation. The speed of preparative electrolysis depends on the stirring rate, electrode area and the applied potential, but the reaction is generally faster than chemical oxidation and does not require any harmful reactants ( $\text{NOBF}_4$ ).

To illustrate the differences between our product of preparative electrolysis and the product of standard chemical synthesis of  $[\text{Cu}(\text{tmby})_2]^{2+}$  by  $\text{CuCl}_2$  (as presented in the previous chapter) we compare the relevant voltammograms in the right chart of Figure 3-2. The dashed black line shows the cyclic voltammogram of the latter species highlighting its complicated electrochemistry. This is obviously due to changes in the coordination sphere of Cu(II)-bipyridine complexes during their direct synthesis from  $\text{Cu}^{2+}$  and the corresponding ligand. On the other hand, the preparative electrolysis through anodic oxidation of Cu(I)-bipyridine species is an ideal protocol towards electrochemically clean Cu(II)-bipyridine counterparts of the redox couple, at least for small scale applications.

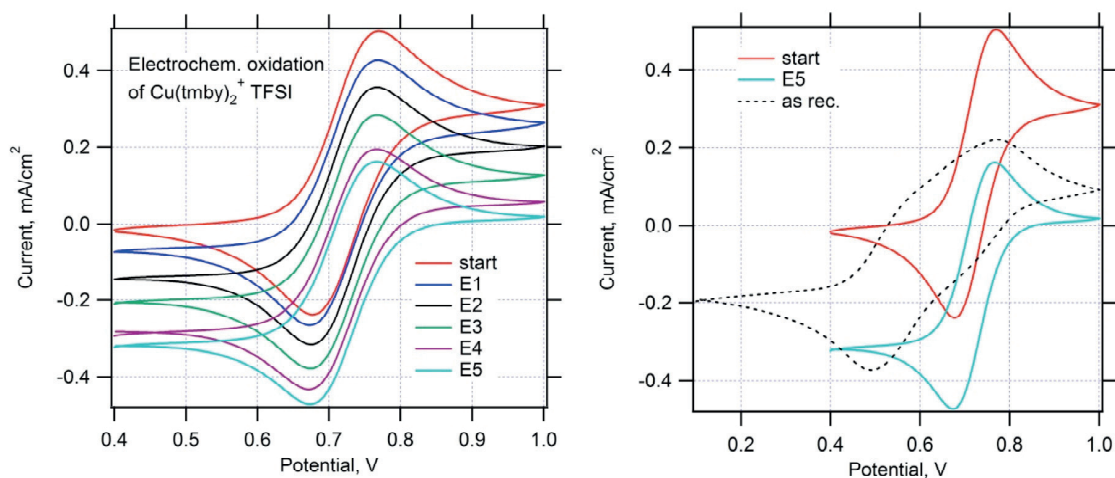


Figure 3-2 Cyclic voltammograms of the products and intermediates of preparative electrolysis of  $[\text{Cu}(\text{tmby})_2][\text{TFSI}]$  on Pt electrode. Scan rate 10 mV/s. Curve 'start' (red): cyclic voltammogram of the initial 5 mM solution of  $[\text{Cu}(\text{tmby})_2][\text{TFSI}]$  in 0.1 M LiTFSI + acetonitrile. Voltammograms E1-E5 are for the same solution after potentiostatic oxidation at 1.1-1.4 V under stirring in divided cell. The passed charge (in equivalents of the starting amount of the Cu(I) complex) corresponds to: 0.19 eq (E1), 0.40 eq (E2), 0.60 eq (E3), 0.80 eq (E4) and 0.92 eq (E5). Right chart compares the voltammograms of the starting (start) and final (E5) complexes with the voltammogram (as rec.) of the  $[\text{Cu}(\text{tmby})_2][\text{TFSI}]_2$  species grown by the standard preparative protocol. Potentials are referenced to the Ag/AgCl (saturated LiCl in ethanol) reference electrode.

### 3.2.3 Synthesis of electrochemically and optically clean $\text{Cu}(\text{tmby})_2\text{TFSI}_2$

In this section, we have reconsidered the problems regarding the Cu(II) synthesis, and developed an alternative synthetic protocol to get a good-quality  $\text{Cu}(\text{tmby})_2\text{TFSI}_2$ , but avoiding the preparative electrolysis and chemical oxidation. Our product (CuYS) was prepared by a simple synthetic pathway as detailed in Experimental Section by using  $\text{Cu}(\text{II})\text{TFSI}_2$  as the starting material. Nevertheless, CuYS is not a simple product, either, because it contains - in addition to the desired  $\text{Cu}(\text{tmby})_2\text{TFSI}_2$  - also some amount of  $\text{Cu}(\text{tmby})_2\text{TFSI}$ . The proportion of both components was varying (between ca 57 to 82 mol% of Cu(II) species for different batches of CuYS). This is illustrated by optical spectra and cyclic voltammograms of a typical synthetic product shown in Figure 3-3. (The actual product shown in Figure 3-3 contained 75 mol% of Cu(II) species.)

Obviously, the 100%-pure  $\text{Cu}(\text{tmby})_2\text{TFSI}$  can be safely prepared only by preparative electrolysis<sup>101</sup>. Its optical spectrum is shown by the blue dashed line in Figure 3-3, providing an extinction coefficient  $\epsilon_{730} = 170 \text{ M}^{-1}\text{cm}^{-1}$ . The corresponding extinction coefficient of  $\text{Cu}(\text{tmby})_2\text{TFSI}_2$  is  $\epsilon_{451} = 5300 \text{ M}^{-1}\text{cm}^{-1}$ <sup>102</sup>. Thanks to these two diagnostic optical absorptions, the analysis of CuYS is straightforward. As there is no other impurity in our CuYS, beyond the  $\text{Cu}(\text{tmby})_2\text{TFSI}$  component (which is anyway added to the final electrolyte solution), we can prepare the high-quality electrolyte solution simply from CuYS and from the pure  $\text{Cu}(\text{tmby})_2\text{TFSI}$ . The amounts of both materials need to be adjusted according to the actual composition of the used CuYS. In this work, we systematically employed this approach. Hence, we report here, for the first time, the  $\text{Cu}(\text{tmby})_2^{2+/+}$ -mediated DSCs using the redox couple with electrochemically clean Cu(II)-species.

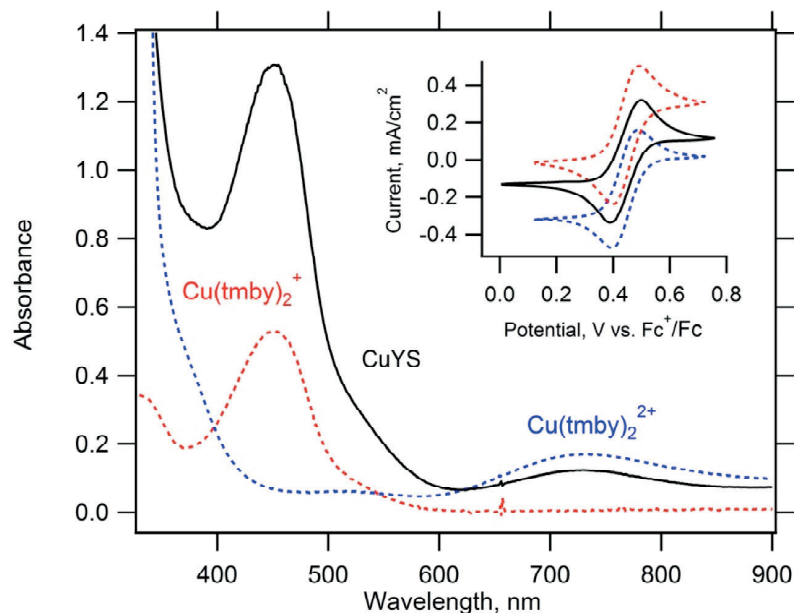


Figure 3-3 UV-Vis absorption spectrum of a solution (6.44 mg/mL in acetonitrile) of typical CuYS product prepared by our new synthetic protocol (black curve). Red dashed curve is the spectrum of a 0.5 mM solution of pure  $\text{Cu}(\text{tmby})_2\text{TFSI}$ . Blue dashed curve is the spectrum of 5 mM solution of pure  $\text{Cu}(\text{tmby})_2\text{TFSI}_2$  obtained by preparative electrolysis. Inset shows the cyclic voltammogram of the same CuYS in 0.1 M LiTFSI + acetonitrile (6.50 mg CuYS/mL) on a Pt electrode, scan rate 10 mV/s (black curve). Inset further shows the control cyclic voltammograms of pure complexes, i.e.  $\text{Cu}(\text{tmby})_2\text{TFSI}$  (red dashed curve) and  $\text{Cu}(\text{tmby})_2\text{TFSI}_2$  (blue dashed curve), both in 5 mM solutions in acetonitrile + 0.1 M LiTFSI.

Two different  $\text{Cu}(\text{tmby})_2^{2+/+}$  electrolytes (obtained via  $\text{CuCl}_2$  and  $\text{Cu}(\text{TFSI})_2$ ) were studied on symmetrical PEDOT/PEDOT dummy cells. The fitting of the spectra provide the following parameters:  $R_s$  is the ohmic serial resistance,  $R_{CT}$  is the charge-transfer resistance, and CPE (constant phase element) is used to account for the roughness of our PEDOT-electrode<sup>101,105,106</sup>. The impedance of CPE equals:

$$Z_{CE} = B^{-1} \cdot (i\omega)^{-\beta} \quad (3:2)$$

where  $\omega$  is the frequency and  $B$ ,  $\beta$  are the frequency-independent parameters of the CPE ( $0 \leq \beta \leq 1$ ; the corresponding parameters are 'CPE-T' =  $B$  and 'CPE-P' =  $\beta$ ). The fitted  $R_{CT}$  values scale inversely with the exchange current density,  $j_0$ , at the cathode<sup>106</sup>:

$$j_0 = \frac{RT}{nFR_{CT}} = Fk_0(c_{ox}^{1-\alpha} \cdot c_{red}^{\alpha}) \quad (3:3)$$

$R$  is the gas constant,  $T$  is temperature,  $k_0$  is the formal (conditional) rate constant of the electrode reaction,  $c_{ox}$  and  $c_{red}$  are the concentrations of oxidized and reduced mediator, respectively and  $\alpha$  is

the charge-transfer coefficient ( $\alpha \approx 0.5$ ). The low-frequency part of the spectrum is modeled by a finite-length Warburg element  $W_s$  with the parameters ' $W_s-R$ '= $R_w$ , ' $W_s-T$ '= $T_w$  and ' $W_s-P$ ' = 0.5<sup>107,108</sup>. The diffusion impedance equals:

$$Z_w = \frac{R_w}{\sqrt{iT_w\omega}} \tanh\sqrt{iT_w\omega} \quad ; T_w = \frac{\delta^2}{D} \quad (3:4)$$

The electrochemical parameters obtained from the impedance fittings of the dummy cells are given in Table 3-1. We can clearly see that the copper complexes that are produced with the  $\text{Cu}(\text{TFSI})_2$  precursor provides better charge transfer at the counter electrode and mass transport properties in comparison to the one synthesized by  $\text{CuCl}_2$ .

Table 3-1 Electrochemical parameters of the PEDOT/PEDOT symmetrical dummy cells obtained from fitting of impedance spectra for  $\text{Cu}(\text{tmby})_2$  electrolyte in acetonitrile.

Cu(II) precursor	$R_s$ ( $\Omega \cdot \text{cm}^2$ )	$R_{CT}$ ( $\Omega \cdot \text{cm}^2$ )	$R_w$ ( $\Omega \cdot \text{cm}^2 \cdot \text{s}^{-1/2}$ )	CPE:B ( $\text{S} \cdot \text{s}^\beta$ )	CPE: $\beta$
$\text{CuCl}_2$	2.4	3.0	22.7	$3.6 \cdot 10^{-4}$	0.94
$\text{Cu}(\text{TFSI})_2$	1.6	0.35	4.2	$2.7 \cdot 10^{-4}$	0.92

### 3.3 Conclusion

The instability of the coordination sphere of the Cu(II)-species manifest itself by the complications during their synthesis from  $\text{CuCl}_2$  and the corresponding ligand. In this chapter we demonstrate methods for preparing clean  $\text{Cu}(\text{tmby})_2\text{TFSI}_2$  by chemical ( $\text{NOBF}_4$ ) or electrochemical oxidation of the parent Cu(I) species and  $[\text{Cu}(\text{tmby})_2][\text{TFSI}]/[\text{Cu}(\text{tmby})_2][\text{TFSI}]_2$  redox mediators in a mixture (CuYS) by changing our synthetic precursor. We showed that the chemical oxidation is poorly controlled and complicated by a partial destruction of the product whereas the electrochemical route provides electrochemically clean Cu(II)-species rapidly, in stoichiometric yield and without using harmful chemical oxidants (but presumed to necessitate special electrodes for large scale applications). Fortunately, the production of CuYS allows the formulation of high-quality electrolyte solution for Cu-mediated DSCs without compromising on the quality of the Cu(II)-species (which was an issue in Chapter 2). Electrochemical data and optical spectra confirm the purity of both components in CuYS. Our improved Cu-mediator provides faster charge-transfer at the PEDOT counter electrode as well as faster diffusion transport in the solution as compared to 'unclean' systems reported previously.

### 3.4 Methods

*Chemicals.* All the chemical obtained from Aldrich, Merck, Dyenamo and HetCat, and used as received from the supplier.

*Synthesis of copper complexes.* Here we describe, for the first time, a simple chemical synthesis to get a clean  $[\text{Cu}(\text{tmby})_2]^{2+/+}$  redox mediator. Besides an unprecedented product's purity, the main advantage of our new recipe is that it avoids the awkward preparative electrolysis.  $[\text{Cu}(\text{tmby})_2]\text{TFSI}$  was synthesized by the reaction of CuI with tmby as detailed in the previous chapter. The Cu(II) counterpart of the complex,  $[\text{Cu}(\text{tmby})_2]\text{TFSI}_2$  was prepared by a newly developed protocol as follows: 1 equivalent of  $\text{CuTFSI}_2$  (194 mg, 0.31 mmol; Solvionics) was mixed with 3 equivalents of tmby (200 mg, 0.93 mmol) in 30 mL of ethanol/water (1/1, v/v). The reaction mixture was stirred for 3 hours at room temperature. The solution was filtered and the product was washed with water and diethyl ether. The resulting crystalline solid ( $\approx 280$  mg yield) varied its color depending on the content of Cu(I) impurity in the product. The color changed from brown (for higher Cu(I) content) to purple (for lower Cu(I)-content). This material is further abbreviated as CuYS.

*Fabrication of dummy cells.* The symmetrical dummy cell was fabricated from two identical FTO-supported electrodes which were separated by Surlyn (DuPont) tape as a seal and spacer. The PEDOT-coated FTO electrodes were fabricated by an electrochemical deposition from EDOT as detailed in Chapter 2.<sup>100</sup> The sheet edges of FTO were coated by ultrasonic soldering (Cerasolzer alloy 246, MBR Electronics GmbH) to improve electrical contacts. The distance between electrodes was measured by a digital micrometer. The cell was filled with an electrolyte through two holes in one FTO support which was finally closed either by Kapton foil or by a Surlyn seal. Electrolyte solution consists (L is the corresponding ligand): 0.2 M  $\text{CuL}_2\text{TFSI}$  + 0.04 M  $\text{CuL}_2\text{TFSI}_2$  + 0.1 M  $\text{LiTFSI}$  + 0.5 M TBP.

*Methods.* Electrochemical measurements were carried out using Autolab PGstat-30 equipped with the FRA module (Ecochemie). A standard Ar-purged one-compartment three-electrode cell was used for cyclic voltammetry in solution. Preparative electrolysis was carried out potentiostatically at platinized FTO electrode using a divided cell, in which the counterelectrode was separated by two frits from the working-electrode. Electrochemical impedance data were processed using Zplot/Zview software. The impedance spectra were acquired in the frequency range from 100 kHz to 0.1 Hz, at 0 V bias voltage, the modulation amplitude was 10 mV. Ag/AgCl/saturated LiCl (ethanol) served as reference electrode and glassy carbon or platinum were the working electrodes. The optical spectra were measured by the Perkin Elmer Lambda 1050 spectrometer with integrating sphere in transmission mode. The reference spectrum was air.





# Chapter 4 Effect of Pyridine-derivative Bases in Dye-Sensitized Solar Cells Employing Copper Redox Mediator

This chapter is adopted from the following articles with the permission of the journal:

Postprint version of the publication: ‘Electrochemical Properties of Cu(II/I)-Based Redox Mediators for Dye-Sensitized Solar Cells, *Electrochimica Acta* 2017, 227, 194-207. doi:10.1016/j.electacta.2016.12.185’ by Ladislav Kavan, Yasemin Saygili, Marina Freitag, Shaik M. Zakeeruddin, Anders Hagfeldt and Michael Grätzel

and

Postprint version of the publication: ‘Alternative Bases to 4-*tert*-butylpyridine for Dye-Sensitized Solar Cells Employing Copper Redox Mediator, *Electrochimica Acta* 2018, 265, 194-201. doi:10.1016/j.electacta.2018.01.142’ by Parnian Ferdowsi\*, Yasemin Saygili\*, Shaik M. Zakeeruddin, Javad Mokhtari, Michael Grätzel, Anders Hagfeldt, and Ladislav Kavan. (\* shared first co-authors)

My contribution for the 1<sup>st</sup> paper: Synthesis of the complexes, preparation of the electrodes, device fabrication and characterization, writing the corresponding parts in the manuscript.

My contribution for the 2<sup>nd</sup> paper: Reformulation of the synthetic method of Cu(II) species, synthesis of the complexes, preparation of the electrodes, device characterization, impedance analysis (partly), analysis of the characterization data, writing the corresponding parts in the manuscript.

In this chapter, we addressed the ‘TBP-effect’ in more detail, and found a strikingly strong influence of TBP on the mass-transport and charge transfer kinetic at the counter electrode. While TBP has almost no effect on  $[\text{Co}(\text{bpy})_3]^{3+/2+}$  mediators, significant slowdown of electrode kinetics and diffusion rate is observed in the case of Cu-mediators. Additionally, we tested and evaluated four pyridine derivatives: 4-*tert*-butylpyridine, 2,6-bis-*tert*-butylpyridine, 4-methoxypyridine and 4-(5-nonyl)pyridine as electrolyte additives.

## 4.1 Introduction

The 4-*tert*-butylpyridine is commonly used for the desired Fermi level upshift, for preventing the electron recombination and thus for  $V_{\text{OC}}$  enhancement<sup>101,107,109</sup>. (The same effect, albeit less pronounced, is achievable through the crystal-face engineering in titania photoanode<sup>110,111</sup>). Consequently, TBP is used in almost every electrolyte solution for liquid-junction DSCs as a standard

additive<sup>112</sup>. Furthermore, nitrogen-containing heterocyclic compounds are essential for ionic-liquid based electrolytes, while TBP is sometimes used even in these ionic-liquid formulations<sup>113</sup>.

In the I-mediated and Co-mediated systems, the TBP addition does not practically influence the cathode's charge-transfer and ionic diffusion in electrolyte solution. However, TBP has significant negative effect in Cu-mediated systems<sup>102</sup>. One of the fundamental problems associated with the tetra-coordinated tetrahedral Cu-complexes is the soft nature of their coordination sphere and its significant dependence on the oxidation state of Cu. An example study was conducted by Hoffeditz et al.<sup>82</sup> using the tetradentate ligand, 1,8-bis(2,2'-pyridyl)-3,6-dithiaoctane (PDTO). Their Cu(II)(PDTO) was very sensitive to substitution reactions with TBP. In acetonitrile (ACN) solution, various 4-, 5- and 6-coordinated complexes,  $[\text{Cu}(\text{TBP})_x(\text{ACN})_y]^{2+}$ , were detected and even the counterion ( $\text{CF}_3\text{SO}_3^-$ ; triflate) was found to enter the coordination sphere in a  $[\text{Cu}(\text{TBP})_4(\text{triflate})_2]$  complex<sup>82</sup>. The complicated coordination chemistry was implicitly mentioned also with the state-of-art DSCs using  $\text{Cu}(\text{dmbpy})_2^{2+}$  and  $\text{Cu}(\text{tmby})_2^{2+}$  mediators in Chapter 2: cyclic voltammograms were dependent on the TBP addition, and the Cu(II) complexes had significantly different cyclic voltammograms compared to the Cu(I) complexes<sup>102</sup> (Figure 2-2).

In this chapter, firstly we investigate the effect of TBP on DSC systems employing copper redox mediators and then we report on different bases, viz: 2,6-bis-*tert*-butylpyridine (BTBP), 4-methoxypyridine (MOP) and 4-(5-nonyl)pyridine (NOP) for  $[\text{Cu}(\text{tmby})_2]^{2+/+}$  complexes, which we examined in comparison to the reference TBP base. The pyridine bases with different functional groups are expected to show different interaction with the  $\text{TiO}_2$  surface and the Cu(II/I)-complexes, while the bases with lower  $\text{pK}_a$  can also improve the dye anchoring. The  $\text{TiO}_2$  photoanode was sensitized by the Y123 dye. The molecular structures of the used bases are shown in Figure 4-1.

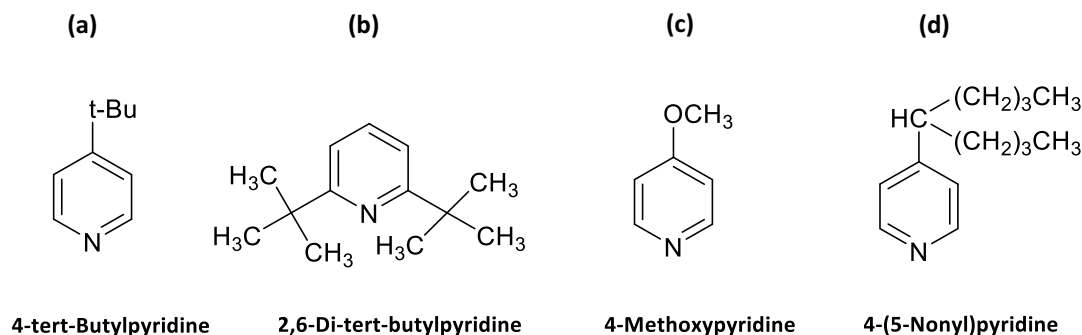


Figure 4-1 Molecular structures of a) 4-*tert* butylpyridine, b) 2,6-bis-*tert*-butylpyridine, c) 4-methoxypyridine, d) 4-(5-nonyl)pyridine.

## 4.2 Results and Discussion

### 4.2.1 Effect of TBP on copper redox mediators

The electrocatalytic activity of DSCs' cathodes and mass transport in the electrolyte solution are conveniently studied using symmetrical dummy cells<sup>106</sup>. Figure 4-2 (top charts) presents cyclic voltammograms and electrochemical impedance spectra of symmetrical dummy cells with the copper redox mediator. In these cells, the electrolyte solution with  $[\text{Cu}(\text{dmp})_2]^{2+/+}$  is sandwiched between two identical FTO-supported PEDOT electrodes. For comparison, the bottom charts display the corresponding data for the  $[\text{Co}(\text{bpy})_3]^{3+/2+}$  couple in analogous dummy cells. The most striking difference between Cu- and Co-based mediators is the influence of TBP addition. While the electrochemical behavior of  $[\text{Co}(\text{bpy})_3]^{3+/2+}$  is invariant with the TBP addition, the  $[\text{Cu}(\text{dmp})_2]^{2+/+}$  is not. For  $[\text{Co}(\text{bpy})_3]^{3+/2+}$ , this is further illustrated by standard cyclic voltammograms, measured on a Pt-electrode in the conventional three-electrode set-up. Figure 4-3 shows that the voltammograms of Co(III) and Co(II) occur at the same formal potential, independent of TBP, solely the diffusion currents are shifted in accord with the presence of the particular diffusion-limiting species. In contrast, the same experiment with  $[\text{Cu}(\text{dmp})_2]^{2+/+}$  reported in Figure 2-2 indicated the same formal potentials for the Cu(I)-dmp and Cu(II)-dmp counterparts (with expectedly shifted diffusion currents), but there was considerable downshift of the formal potentials for both Cu(I) and Cu(II) species caused by the addition of TBP.

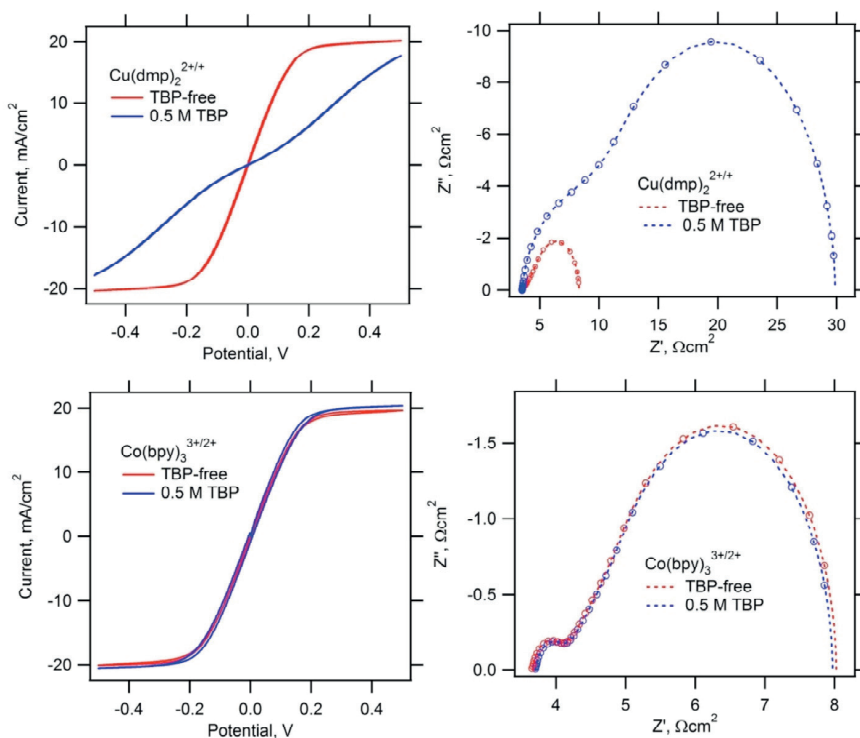


Figure 4-2 Electrochemical activity of FTO supported thin film of PEDOT tested on symmetrical dummy cells. Top charts: Electrolyte solution:  $[\text{Co}(\text{bpy})_3]^{3+/2+}$  TFSI<sub>3/2</sub> in propionitrile with (blue curves) or without (red curves) the addition of 4-tert-butylpyridine. Bottom charts: Electrolyte solution  $[\text{Cu}(\text{dmp})_2]^{2+/+}$  TFSI<sub>2/1</sub> in propionitrile with (blue curves) or without (red curves) the addition of 4-tert-butylpyridine. Left charts: Cyclic voltammograms, scan rate 10 mV/s. Right charts: Nyquist plots of electrochemical impedance spectra measured at 0 V from 100 kHz to 0.1 Hz. (Markers are experimental points, dashed lines are simulated fits to the equivalent circuit).

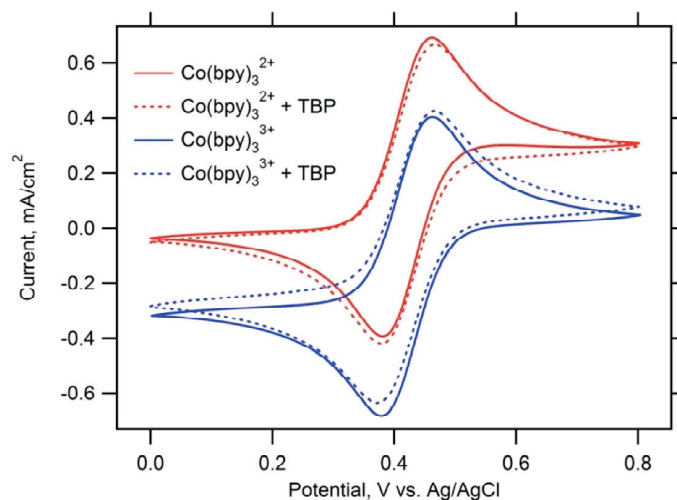


Figure 4-3 Cyclic voltammetry at a Pt-electrode in 0.1 M LiTFSI, scan rate 20 mV/s.  $\text{Co}(\text{bpy})_3\text{TFSI}_2$  (red) and  $\text{Co}(\text{bpy})_3\text{TFSI}_3$  (blue); concentration 2.5 mM. Dashed lines after addition of 0.5 M (TBP). These Co-complexes exhibit the expected voltammograms in both oxidation states, i.e. identical formal potentials and only shifted currents. The found formal potential is identical to the literature value<sup>54</sup> and the influence of TBP addition is negligible.

Cyclic voltammogram in the TBP-free electrolyte solution confirms that the charge transfer and diffusion are quite fast (Figure 4-2). The inverse slope of a voltammogram at the potential of 0 V characterizes the catalytic activity of an electrode; it actually reflects the overall cell resistance ( $R_{CV}$ ) that can be attained at low current densities<sup>114</sup>. The found  $R_{CV}$  is ca.  $9 \Omega \cdot \text{cm}^2$  both for the Cu- and Co-based mediators. Also the limiting diffusion currents,  $j_L$  are comparable ( $\approx 20 \text{ mA/cm}^2$ ) though they are also dependent on the dummy cell spacing ( $\delta$ ):

$$j_L = \frac{2nFcD}{\delta} \quad (4:1)$$

( $n = 1$  is the number of electrons,  $F$  is the Faraday constant,  $c$  is the concentration of diffusion-limited species ( $[\text{Cu}(\text{dmp})_2]^{2+}$  or  $[\text{Co}(\text{bpy})_3]^{3+}$ ) and  $D$  is the diffusion coefficient. Assuming the spacing  $\delta \approx 30 \mu\text{m}$  (by the Surlyn foil) then the  $D$  equals ca.  $6 \cdot 10^{-6} \text{ cm}^2/\text{s}$  or  $3 \cdot 10^{-6} \text{ cm}^2/\text{s}$  for the  $[\text{Cu}(\text{dmp})_2]^{2+}$  or  $[\text{Co}(\text{bpy})_3]^{3+}$ , respectively in the TBP-free propionitrile solutions. While the found diffusion coefficient for the Co-mediator is comparable to the literature values for similar systems<sup>49,81,114–116</sup>, the coefficient of  $[\text{Cu}(\text{dmp})_2]^{2+}$  is somewhat smaller than the value reported from rotating-disc experiments in Chapter 2 ( $25 \cdot 10^{-6} \text{ cm}^2/\text{s}$ <sup>81</sup> or  $14.4 \cdot 10^{-6} \text{ cm}^2/\text{s}$ <sup>102</sup>). Nevertheless, the previous works<sup>81,102</sup> found that the diffusion coefficient of  $[\text{Cu}(\text{dmp})_2]^{2+}$  was larger than that of  $[\text{Co}(\text{bpy})_3]^{3+}$  by a factor of ca. 2, which is consistent with this new data.

The faster diffusion of  $[\text{Cu}(\text{dmp})_2]^{2+}$  was ascribed to a smaller size of this ion<sup>81</sup> but in view of the instability of the coordination sphere<sup>82</sup>, this argument should be used with care. We can also speculate that the very fast electron self-exchange rate constant ( $k_{ex} = 23 \text{ M}^{-1}\text{s}^{-1}$ , which is 1000 times larger than that of the homologue phenanthroline complex,  $[\text{Cu}(\text{phen})_2]^{2+}$ )<sup>77</sup> could contribute to charge transfer by electron-hopping between redox molecules. For the center-to-center distance  $\delta_{cc}$ , the charge percolation occurs by hopping without physical motion in the electrolyte solution

(Dahms-Ruff mechanism<sup>117,118</sup>). According to this model, the observed diffusion coefficient corresponds to the sum of the mass transport by physical displacement of molecules,  $D_{mass}$  and the electron-hopping contribution:

$$D = D_{mass} + \frac{k_{ex} c \delta_{cc}^2}{6} \quad (4:2)$$

We can estimate  $\delta_{cc} \approx 2$  nm from the used  $[\text{Cu}(\text{dmp})_2]^{2+/+}$  concentration, from which the hopping contribution to the diffusion coefficient is of the order of  $10^{-13}$   $\text{cm}^2/\text{s}$ , i.e. negligible for these Cu-complexes at the concentrations employed in the redox electrolytes. However, if we consider ligand exchange and/or formation of larger aggregates, then the  $k_{ex}$  can be significantly higher. For instance, the redox reaction  $[\text{Cu}(\text{dmp})_2(\text{ACN})]^{2+}/[\text{Cu}(\text{dmp})_2]^+$  has  $k_{ex} = 10^3$   $\text{M}^{-1}\text{s}^{-1}$  and values of ca.  $10^5$ - $10^6$   $\text{M}^{-1}\text{s}^{-1}$  were found for Cu complexes with certain proteins<sup>119</sup>.

The fast charge-transfer on PEDOT electrode is confirmed by a very small value of  $R_{CT}$  of 0.07  $\Omega\cdot\text{cm}^2$ , which is even better than that of the control Co-system (0.20  $\Omega\cdot\text{cm}^2$ ). (Electrochemical impedance spectra of symmetrical dummy cells are analyzed as described in the Chapter3, through the Equations (3:2)-(3:4)). Also the Warburg diffusion resistance,  $R_W$  is small: 4.6  $\Omega\cdot\text{cm}^2$  and it is comparable to 4.0  $\Omega\cdot\text{cm}^2$  found for Co-bipy@PEDOT, the latter being reasonably similar to the literature value (2.9  $\Omega\cdot\text{cm}^2$ ) for an analogous Co-mediated system<sup>120</sup>. (See Table 4-1)

Unfortunately, these promising properties of  $[\text{Cu}(\text{dmp})_2]^{2+/+}$  are strongly impaired by TBP, while with TBP-containing Co-bipy solutions unperturbed charge transfer and diffusion are still observed in the control devices. The  $R_{CT}$  and  $R_W$  values in the TBP-containing solutions of  $[\text{Cu}(\text{dmp})_2]^{2+/+}$  increase ca. 10 and 5 times, respectively (Table 4-1). The fact that both the catalytic activity and diffusion rate are deteriorated by TBP is reminiscent of the findings by Kim et al.<sup>107</sup> in the traditional system, i.e.  $\Gamma/\text{I}_3^-$  in the Pt@FTO/Pt@FTO dummy cells. In this case the enhancement of TBP concentration from 0.5 M to 2.5 M caused  $R_{CT}$  and  $R_W$  to increase by a factor of 3 and 2, respectively, which was attributed to the adsorption of TBP on Pt (impairing access of redox molecules to the catalytic surface) and enhanced viscosity of the solution (impairing diffusion)<sup>107</sup>. In the case of the  $[\text{Cu}(\text{dmp})_2]^{2+/+}$  mediator, we need to consider also qualitatively different effects than adsorption and viscosity (though viscosity is also at play, as seen from the  $R_W$  values for our PN solutions in Table 4-1).

Table 4-1 Electrochemical parameters of the PEDOT/PEDOT symmetrical dummy cells obtained from fitting of impedance spectra for  $\text{Cu}(\text{dmp})_2$  and  $\text{Co}(\text{bpy})_3$  electrolytes in propionitrile.

	$R_s$ ( $\Omega\cdot\text{cm}^2$ )	$R_{CT}$ ( $\Omega\cdot\text{cm}^2$ )	$R_W$ ( $\Omega\cdot\text{cm}^2\cdot\text{s}^{-1/2}$ )	CPE:B ( $\text{S}\cdot\text{s}^\beta$ )	CPE: $\beta$
$\text{Cu}(\text{dmp})_2$ without TBP	1.8	0.07	4.6	$3.7\cdot 10^{-3}$	0.77
$\text{Cu}(\text{dmp})_2$ with TBP	1.7	1.8	22.2	$6.1\cdot 10^{-4}$	0.97
$\text{Co}(\text{bpy})_3$ without TBP	1.8	0.20	4.0	$1.1\cdot 10^{-3}$	0.83
$\text{Co}(\text{bpy})_3$ with TBP	1.8	0.19	3.9	$1.0\cdot 10^{-3}$	0.83

This hypothesis is supported by the fact that (a) the Cu(II) species is in low-concentration-, i.e. the diffusion-controlling ion in the system and (b) the same Cu(II) species is prone to changes of its coordination sphere. These changes include three different effects: (b<sub>1</sub>) variations of coordination geometry, (b<sub>2</sub>) increase of coordination number (from 4 to 6) and (b<sub>3</sub>) ligand substitution by TBP, solvent and/or counterions<sup>89</sup>. The Cu(II) species in solution likely becomes more bulky and hydrophobic due to these changes, which accounts for the sluggish diffusion and charge-transfer. Nevertheless, the final  $R_{CT}$  and  $R_w$  values in TBP-containing solutions are still not critical for the use in solar cells, i.e. the DSCs using these solutions still exhibit the short circuit photocurrent of ca. 14 mA/cm<sup>2</sup> and efficiency of ca. 10% at 1 sun illumination<sup>81</sup>. From the Equation (3:3), the current of 14 mA/cm<sup>2</sup> translates into the ‘ideal’ value of  $R_{CT}$  of <1.8 Ω·cm<sup>2</sup>, which is quite near the observed  $R_{CT}$  values in the actual electrolyte solutions used in solar cells (Table 4-1). Nevertheless, this analysis highlights a strong need for replacing TBP by another additives in Cu-mediated DSCs, which do not decrease the charge transfer and mass transport rates.

#### 4.2.2 Effect of other pyridine bases

Figure 4-4 shows cyclic voltammograms of Cu(tmby)<sub>2</sub>TFSI in the presence of four different bases investigated. In accord with Figure 2-2<sup>102</sup> we detect some downshift of the formal redox potential upon addition of TBP as well as suppression of the cathodic wave of Cu<sup>II</sup>-reduction. This effect is base-specific, i.e. it is very significant for MOP, and less significant for NOP (Figure 4-4). On the other hand, BTBP has the smallest influence on the electrochemistry of Cu(tmby)<sub>2</sub><sup>2+/+</sup>; the redox potential is even slightly upshifted against the reference base-free solution. This qualitative difference (to the other used bases) is also confirmed by differential pulse voltammetry (Figure 4-5) and is attributed to steric hindrance of BTBP-coordination.

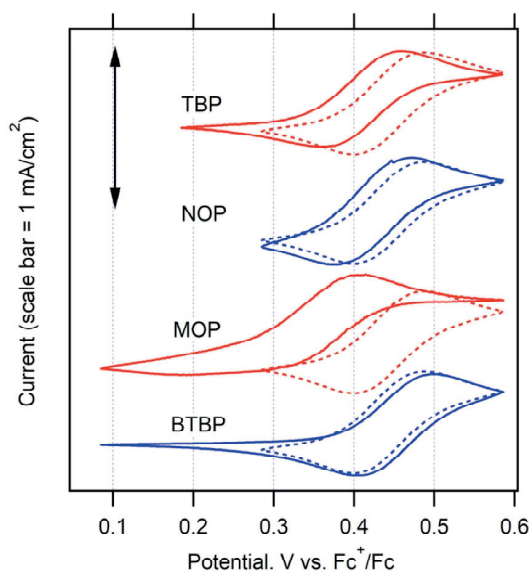


Figure 4-4 Cyclic voltammograms of 5 mM Cu(tmby)<sub>2</sub>TFSI in 0.1 M LiTFSI + acetonitrile, scan rate 10 mV/s. Dashed curves show the voltammograms in absence of any bases. Full curves show the same voltammograms upon addition of the corresponding bases in 15 mM concentration.

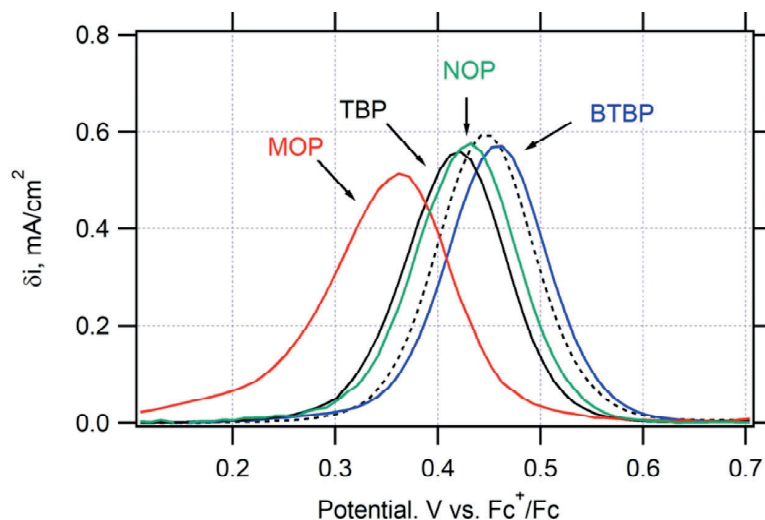


Figure 4-5 Differential pulse voltammograms of 5 mM  $\text{Cu}(\text{tmby})_2\text{TFSI}$  in 0.1 M  $\text{LiTFSI}$  + acetonitrile. Dashed curve shows the voltammogram in absence of any bases. Full curves show the same voltammograms upon addition of the respective bases in 15 mM concentration.

The effect of different bases was further investigated using symmetrical (PEDOT/PEDOT) dummy cells<sup>106</sup>. Figure 4-6 shows cyclic voltammograms (chart a) and electrochemical impedance spectra (chart b) of these cells. The parameters determined from these studies are summarized in Table 4-4. The found diffusion coefficients (via Equation (4-1)) are near the value reported in Chapter 2 from rotating-disc experiments ( $2.2 \cdot 10^{-5} \text{ cm}^2/\text{s}$ ) or similar PEDOT/PEDOT cells investigated ( $1.2 \cdot 10^{-5} \text{ cm}^2/\text{s}$ )<sup>105</sup>.

Interestingly, the base-specific slowdown of charge transfer rate and ionic transport occur exclusively for Cu-mediated electrolyte solutions. Figure 4-7 and Table 4-2 confirm that these effects are practically absent in Co-mediated electrolyte solutions. This finding was first disclosed in the previous chapter, and here we extend this information also for other bases investigated in the current work. In base-free electrolyte solutions, the formal rate constant,  $k_0$  equals ca. 0.022 cm/s (for Co-mediated systems) and 0.027 cm/s (for Cu-mediated systems). The  $k_0$  values are nearly invariant with base addition in Co-systems. On the other hand, they decrease significantly for Cu-systems containing TBP, NOP and MOP, but not BTBP.

On the other hand, our corresponding data for the Co(III/II) couple (Table 4-3) are reasonably comparable to earlier literature values, which were obtained on similar (but not identical) systems<sup>81,101</sup>. There even exists an empirical correlation of the charge-transfer and diffusion transport rates with acidity constants ( $\text{pK}_a$ ) of the corresponding pyridine bases (Figure 4-8). While there is a clear  $\text{pK}_a$ -dependence for the Cu-mediated systems, no such dependence is found for the Co-mediated systems.

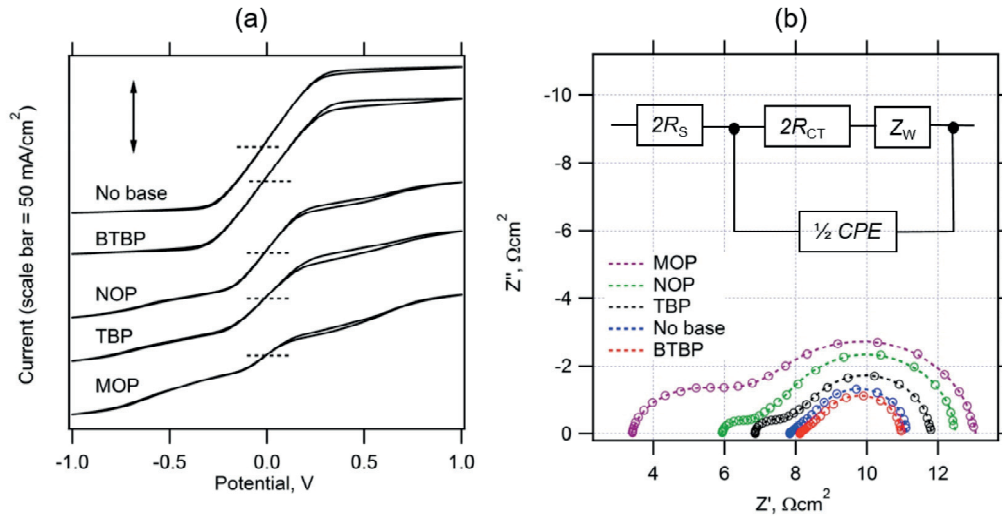


Figure 4-6 Electrochemical tests of PEDOT/PEDOT symmetrical dummy cells with  $\text{Cu}(\text{tmby})_2\text{TFSI}_{2/1}$  electrolyte solution containing various pyridine bases. Chart (a): Cyclic voltammograms, scan rate 50 mV/s. The voltammograms are offset for clarity, but the current scales are identical for all plots. Chart (b): Nyquist plots of electrochemical impedance spectra measured at 0 V; markers are experimental points, dashed lines are fits to the equivalent circuit which is shown in inset. For clarity of presentation, impedance spectra (except for the spectrum labeled MOP) are offset in the  $Z'$  scale to avoid crossing of curves. The respective values of offsets applied on the bottom axis in Fig. 4b are as follows: NOP ( $2.6 \Omega\text{cm}^2$ ), TBP ( $4.1 \Omega\text{cm}^2$ ), no base ( $4.2 \Omega\text{cm}^2$ ), BTBP ( $4.6 \Omega\text{cm}^2$ ).

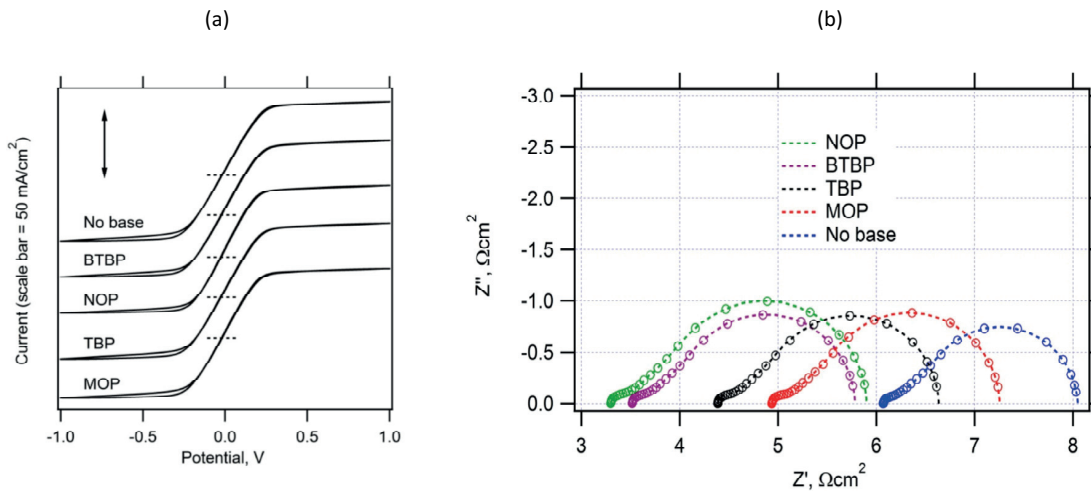


Figure 4-7 a) Cyclic voltammograms (scan rate of 50 mV/s) of PEDOT/PEDOT symmetrical dummy cells in  $\text{Co}(\text{bpy})_3\text{TFSI}_{3/2}$  electrolyte solution containing various pyridine bases. The voltammograms are offset for clarity, but the current scale is identical for all plots. b) Nyquist plots of electrochemical impedance spectra of PEDOT/PEDOT symmetrical dummy cells. Electrolyte solution  $\text{Co}(\text{bpy})_3\text{TFSI}_{3/2}$  containing various pyridine bases, measured at 0 V. Markers are experimental points, dashed lines are fits to the equivalent circuit which is shown in the main text. For clarity of presentation, some impedance spectra are offset in the  $Z'$  scale as follows: BTBP ( $0.1 \Omega\text{cm}^2$ ), TBP ( $1 \Omega\text{cm}^2$ ), MOP ( $2 \Omega\text{cm}^2$ ), No base ( $3 \Omega\text{cm}^2$ ).



Table 4-2 Electrochemical parameters of the studied electrolyte solutions with different added bases. Data from PEDOT/PEDOT symmetrical dummy cells obtained from cyclic voltammetry or from fitting of impedance spectra. (Notes: a) Limiting current poorly distinguished, approximate values. b) For comparison, the corresponding  $R_{CT}$  and  $j_0$  values from EIS on complete solar cells)

Parameter (Units)	BTBP	NOP	TBP	MOP	No base
$R_{CV} (\Omega \cdot \text{cm}^2)$	5.8	6.3	7.7	10.5	5.4
$j_L (\text{mA}/\text{cm}^2)$	52	$\approx^a 47$	$\approx^a 45$	$\approx^a 40$	49
$D (\text{cm}^2/\text{s})$ from $j_L$	$1.1 \cdot 10^{-5}$	$\approx^a 1 \cdot 10^{-5}$	$\approx^a 1 \cdot 10^{-5}$	$\approx^a 0.9 \cdot 10^{-5}$	$1.4 \cdot 10^{-5}$
$R_s (\Omega \cdot \text{cm}^2)$	1.8	1.7	1.6	1.7	1.7
$R_{CT} (\Omega \cdot \text{cm}^2)$	0.10	0.36	0.35	1.4	0.09
$R_w (\Omega \cdot \text{cm}^2 \cdot \text{s}^{-1/2})$	2.8	5.7	4.2	6.9	3.1
$\text{CPE:B} (\Omega^{-1} \cdot \text{cm}^2 \cdot \text{s}^b)$	$2.3 \cdot 10^{-4}$	$1.9 \cdot 10^{-4}$	$2.7 \cdot 10^{-4}$	$5.2 \cdot 10^{-4}$	$7.0 \cdot 10^{-4}$
$\text{CPE: } \beta$	0.99	0.90	0.92	085	0.99
$D (\text{cm}^2/\text{s})$ from EIS	$1.4 \cdot 10^{-5}$	$2.9 \cdot 10^{-5}$	$2.6 \cdot 10^{-5}$	$3.0 \cdot 10^{-5}$	$3.5 \cdot 10^{-5}$
$j_0 (\text{mA}/\text{cm}^2)$	257	71	73	18	285
$k_0 (\text{cm}/\text{s})$	$2.4 \cdot 10^{-2}$	$6.7 \cdot 10^{-3}$	$6.9 \cdot 10^{-3}$	$1.7 \cdot 10^{-3}$	$2.7 \cdot 10^{-2}$

Table 4-3 Electrochemical parameters in  $[\text{Co}(\text{bpy})_3]^{3+/2+}$  electrolyte solutions containing various bases. Results from electrochemical impedance spectra of PEDOT/PEDOT symmetrical dummy cells.

Parameter (Unit)	BTBP	NOP	TBP	MOP	No base
$R_{CV} (\Omega \cdot \text{cm}^2)$	4.8	4.8	4.8	4.8	4.8
$j_L (\text{mA}/\text{cm}^2)$	49	46	49	46	50
$D (\text{cm}^2/\text{s})$ from $j_L$	$6.4 \cdot 10^{-6}$	$6.0 \cdot 10^{-6}$	$6.3 \cdot 10^{-6}$	$6.0 \cdot 10^{-6}$	$6.5 \cdot 10^{-6}$
$R_s (\Omega \cdot \text{cm}^2)$	1.8	1.7	1.6	1.7	1.7
$R_{CT} (\Omega \cdot \text{cm}^2)$	0.07	0.08	0.07	0.07	0.07
$R_w (\Omega \cdot \text{cm}^2 \cdot \text{s}^{-1/2})$	2.2	2.6	2.2	2.1	1.9
$\text{CPE:B} (\Omega^{-1} \cdot \text{cm}^2 \cdot \text{s}^b)$	$6.8 \cdot 10^{-4}$	$6.9 \cdot 10^{-4}$	$7.3 \cdot 10^{-4}$	$5.5 \cdot 10^{-4}$	$7.9 \cdot 10^{-4}$
$\text{CPE: } \beta$	0.92	0.94	0.95	0.94	0.94
$D (\text{cm}^2/\text{s})$ from EIS	$3.9 \cdot 10^{-6}$	$2.2 \cdot 10^{-6}$	$4.3 \cdot 10^{-6}$	$2.8 \cdot 10^{-6}$	$4.3 \cdot 10^{-6}$
$j_0 (\text{mA}/\text{cm}^2)$	370	320	370	370	370
$k_0 (\text{cm}/\text{s})$	$2.2 \cdot 10^{-2}$	$1.9 \cdot 10^{-2}$	$2.2 \cdot 10^{-2}$	$2.2 \cdot 10^{-2}$	$2.2 \cdot 10^{-2}$

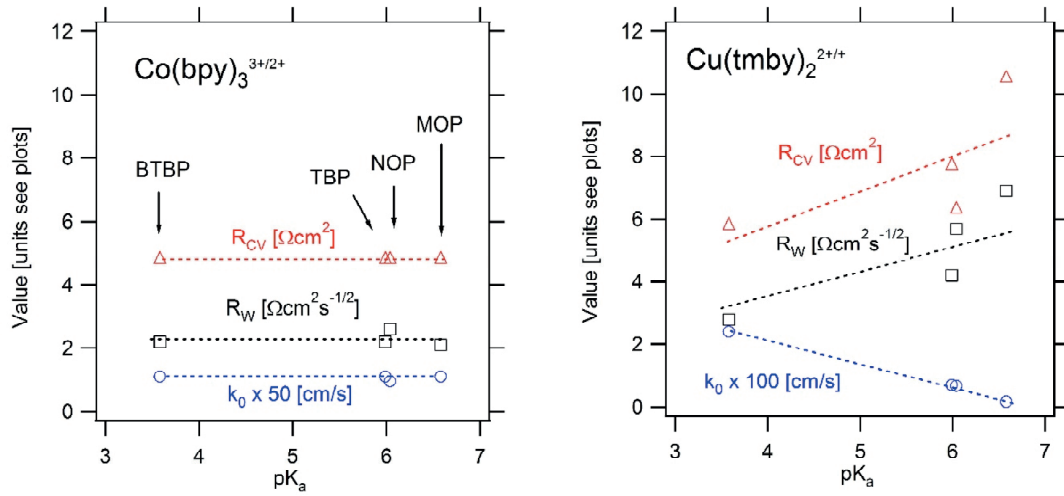


Figure 4-8 Empirical correlation of formal rate constant of charge transfer ( $k_0$ ), diffusion resistance ( $R_W$ ) and overall cell resistance ( $R_{CV}$ ) with  $\text{pK}_a$  values of the corresponding bases which were added to the electrolyte solution (BTBP, TBP, NOP and MOP). Data from EIS on PEDOT/PEDOT symmetrical cells for Co-mediated systems (left chart) and Cu-mediated systems (right chart).

The charge transfer at the counter electrode can be alternatively evaluated from the high-frequency part of impedance spectra of complete DSC devices in dark at high applied forward bias (near  $V_{oc}$ ) when the transport resistance in  $\text{TiO}_2$  becomes negligible<sup>6,101,115</sup>. Figure 4-9 shows examples of impedance spectra of solar cells with TBP- and NOP-containing electrolyte solutions. The fitted  $R_{CT}$  values are 0.98 and 0.87  $\Omega\text{cm}^2$  for TBP and NOP, respectively. We can assume that very similar  $\text{pK}_a$  values contributes to these similar  $R_{CT}$  values.

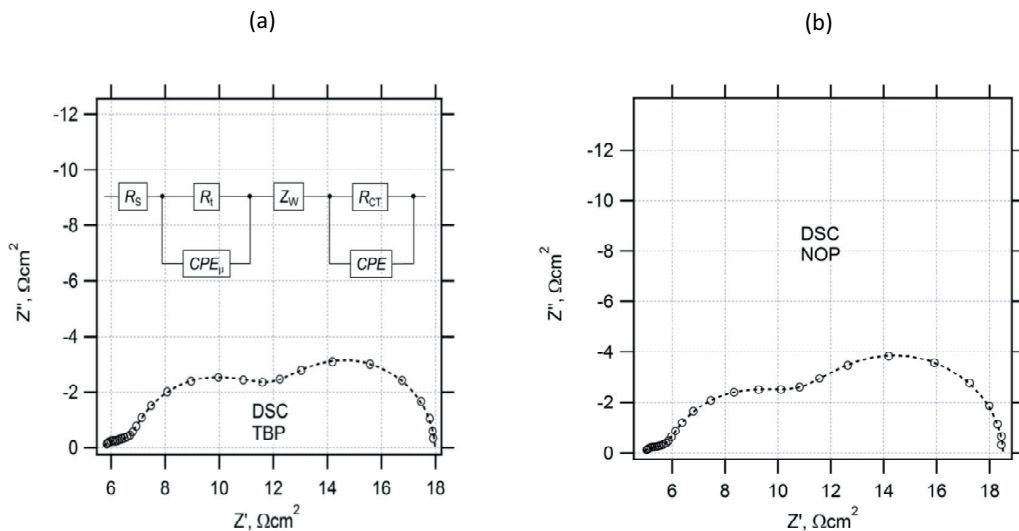


Figure 4-9 Electrochemical impedance spectrum of a complete solar cell with Y123-sensitized  $\text{TiO}_2$  photoanode and PEDOT counterelectrode measured in dark at the applied forward bias of -1.2 V. Open circles are experimental points, dashed curve is a fitted spectrum. The equivalent circuit used for spectra fitting is shown in inset to the left chart. Electrolyte solution: 0.2 M  $\text{Cu}(\text{tmby})_2\text{TFSI}$  + 0.06 M  $\text{Cu}(\text{tmby})_2\text{TFSI}_2$  + 0.1 M LITFSI in acetonitrile + 0.6 M TBP (left chart) or NOP (right chart).

### 4.2.3 Solar cells performance

Figure 4-10a presents the current-voltage (J-V) curves of DSCs based on the  $[\text{Cu}(\text{tmby})_2]^{2+/+}$  mediator, Y123 dye and different pyridine bases used as electrolyte additive. The open-circuit voltages, photocurrent densities, fill factors and power conversion efficiencies at 1 sun illumination are listed in Table 4-4. The  $J_{\text{SC}}$  in NOP-containing electrolyte solution was significantly higher than that for MOP- or BTBP-solutions, consistent with the highest IPCE peak of NOP at around 80% (Figure 4-10b). All bases show high  $V_{\text{OC}}$ s exceeding 1 V, except for BTBP (0.846 V). The lower  $V_{\text{OC}}$  for BTBP is attributed to a steric effect, which prevents attachment to the  $\text{TiO}_2$  surface. This causes higher rates of electron recombination. Eventually, NOP showed 9.4% efficiency at 1sun, which is higher than the values obtained with TBP, BTBP and MOP, respectively. (The performance metrics of our control device (TBP-containing) is similar or better compared to analogous DSCs using ‘unclean’ Cu(II)-complex<sup>102,104,105</sup> or electrochemically-made  $\text{Cu}(\text{tmby})_2^{2+}$ <sup>101</sup>; the most significant improvement concerns the fill factor. For instance, our FF value (0.76) is markedly better than the previously reported value in Chapter 2 (0.66 at 1 sun illumination)<sup>101,102,104,105</sup>.)

Table 4-4 Characteristics for the studied Cu-mediated DSCs with different bases and Y123 as sensitizer. Illumination intensity 1sun (AM1.5G).

Base	$V_{\text{OC}}$ (V)	$J_{\text{SC}}$ ( $\text{mA cm}^{-2}$ )	FF	PCE (%)
TBP	1.080	11.23	0.76	9.3
BTBP	0.846	8.77	0.67	5.1
MOP	1.079	10.61	0.74	8.6
NOP	1.075	12.01	0.71	9.4

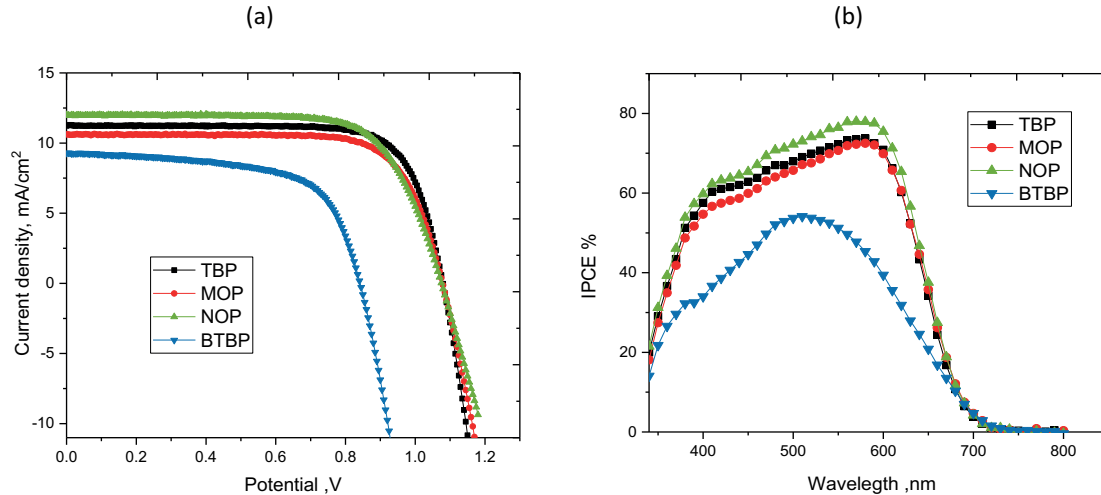


Figure 4-10 a) Photocurrent density vs. voltage curves measured under standard AM1.5G illumination. DSC devices employed Y123 dye,  $\text{Cu}(\text{tmby})_2^{2+/+}$  redox mediator and four different pyridine bases as labeled in the annotation b) IPCE spectra of DSC devices sensitized with Y123 dye.

Figure 4-10b shows the corresponding IPCE spectra for our DSCs. The maximum IPCE value is around 80% with the electrolyte with NOP base. For TBP and MOP, the IPCE maxima were approximately 75%. BTBP showed the lowest IPCE compared to other bases, reaching a maximum 50% IPCE. For all the devices the IPCE drop between 360 and 450 nm is attributed to the competitive light absorption of Cu(I) and Cu(II) species. Assuming the same light harvesting and electron injection efficiencies for all the devices, the differences in DSCs' performance are attributed to the different dye regeneration and electron recombination rates. As discussed previously, the basicity ( $pK_a$  values) and steric effects of pyridine bases influence the coordination spheres of Cu(II/I) and cause different formal redox potentials. For TBP, MOP and NOP, the coordination of pyridine base results in similar redox potential for the copper species, and accordingly similar driving forces for dye regeneration and electron recombination. For BTBP, the methyl units hinder the coordination to copper center resulting in a lower driving force for dye regeneration, and additionally these units possibly prevent attachment of BTBP to the  $TiO_2$  surface, which causes higher rates of electron recombination. (Due to the poor photovoltaic performance of BTBP, this base is excluded for the following electron lifetime and stability measurements.)

#### 4.2.4 Electron Lifetime and Charge Extraction Measurements

Electron lifetime and charge extraction measurements were used to analyze the effect of different bases (NOP, MOP and TBP) to the recombination of injected electron and oxidized redox species. Figure 4-11a shows the plot of electron lifetimes with respect to the quasi-Fermi level of electrons in  $TiO_2$ . At same quasi-Fermi level, the higher electron lifetime is observed with MOP, which has a slightly lower driving force for recombination reaction. For the devices employing NOP and TBP, electron lifetimes are similar and lower compared to the MOP-device. Figure 4-11b shows the corresponding charge extraction data for our DSCs. At each selected value of extracted charge, the MOP-device exhibits a down-shifted Fermi level, i.e. a more positive conduction band edge (in electrochemical scale). This is attributed to the smaller basicity of MOP (larger  $pK_a$ ), which provides lower surface charge for conduction band shifts.

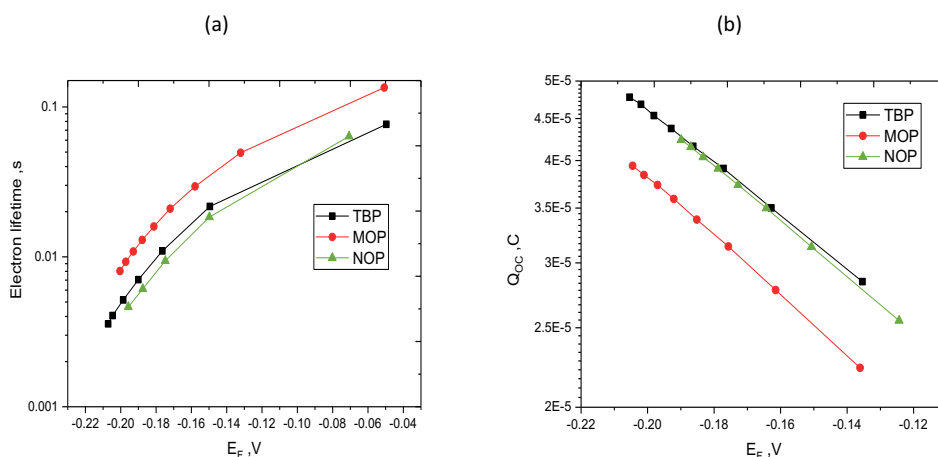


Figure 4-11 a) Electron lifetimes for the DSC devices Y123 dye,  $[Cu(tmby)_2]^{2+/+}$  redox mediator and the three different pyridine bases as labeled in the annotation. b) Charge extraction data for the DSC devices with Y123 dye,  $[Cu(tmby)_2]^{2+/+}$  redox mediator and the three different pyridine bases as labeled in the annotation.

#### 4.2.5 Stability of DSC devices

The stability of our DSC devices was tested during 300 hours under 0.5 sun illumination at room temperature. These experimental conditions were chosen to comply with prospective applications, which favor the Cu-mediated DSCs at low light intensity.<sup>103</sup> Figure 4-12(a-d) shows the variation of the main photovoltaic parameters, i.e. output power, short-circuit photocurrent, open-circuit voltage and fill factor of three devices using TBP, MOP and NOP bases, respectively. The output power in Figure 4-12a is actually a measure of solar power conversion efficiency (PCE) if we normalize the output power to the used illumination intensity ( $50 \text{ mW/cm}^2$ ). No additional encapsulation of testing devices was made, i.e. the solar cells were assembled solely with the standard Surlyn seal as detailed in Experimental Section. Hence, the observed effects are assignable to various aging phenomena, such as light-soaking, which improves the  $\text{TiO}_2$ /dye interaction and downshifts the  $\text{TiO}_2$  conduction band<sup>6</sup>. Specific for Cu-mediated devices is the effect of electrolyte evaporation through imperfect sealing, which transforms the electrolyte into a solid hole-conductor.<sup>89,101,104</sup>

Figure 4-12a confirms that NOP-device shows the smallest overall decrease of PCE (ca. 10%) mainly resulting from the  $V_{\text{OC}}$  drop (Figure 4-12c). For the TBP and MOP devices, the efficiency initially decreased and then remained nearly constant. The variation of  $J_{\text{SC}}$  exhibited a similar trend except for TBP where the current decreased monotonically (Figure 4-12b). For our TBP-device, all the parameters showed roughly similar trend as reported in Cao et al.<sup>104</sup> for non-encapsulated TBP-devices with non-optimized Cu mediator. The marked initial PCE drop of the TBP-device is followed by a slow recovery during ca. 100 hours of light-soaking. Interestingly, the fill factor of the TBP-device exhibit quite similar trend. The observed enhancements of FF and PCE are reminiscent of the evaporation-induced transformation to solid hole-conductor, which occurs at roughly similar timescale<sup>104</sup>. Our results confirm that the NOP base is beneficial not only for the best solar conversion efficiency of the corresponding DSC, but also for long-term stability.

Optimization of pyridine derivatives for Cu-mediated DSCs represents an interplay of basicity and coordination ability, which in turn allows for tuning the charge transfer rate at the DSC cathode, and the mass transport in the electrolyte solution. The NOP-containing DSC-device is outperforming all the remaining ones in solar power conversion efficiency, which makes NOP suitable as a replacement for the standard TBP base in these solar cells. Nevertheless, an ‘ideal base’ which would selectively improve the  $\text{TiO}_2$ /electrolyte interface without impairing the mass transport and the counter-electrode/electrolyte interface in Cu-mediated DSCs was not yet found (if it exists).

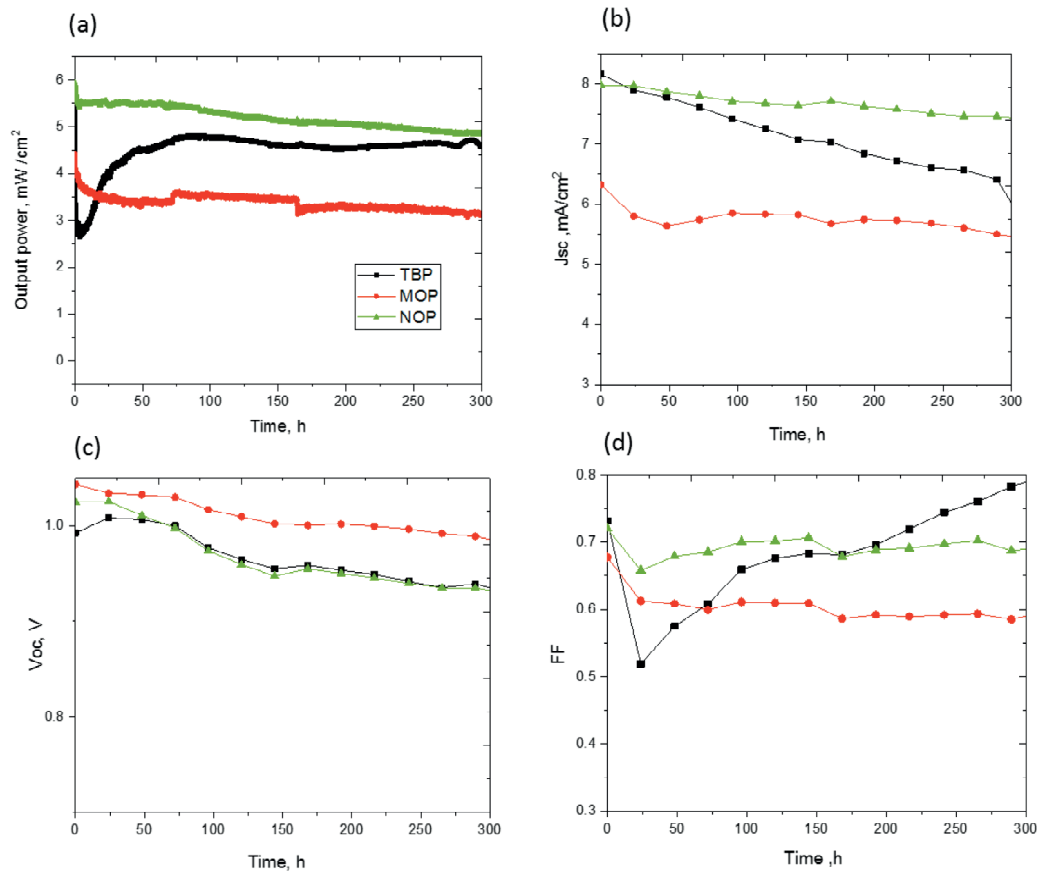


Figure 4-12 Evaluation of durability over 300 h at 0.5 sun illumination. The tested DSCs devices employ  $[\text{Cu}(\text{tmby})_2]^{2+/+}$  electrolyte solution with three different pyridine bases as labeled in the annotation. a) Electrical output power ( $\approx 0.5$  PCE), b) Short circuit photocurrent, c) Open circuit voltage and d) Fill factor.

### 4.3 Conclusion

Four pyridine bases, viz. 4-*tert*-butylpyridine (TBP) 2,6-bis-*tert*-butylpyridine (BTBP), 4-methoxypyridine (MOP) and 4-(5-nonyl)pyridine (NOP) were evaluated as electrolyte additives for optimization of these solar cells. While the control experiments with  $\text{Co}(\text{bpy})_3^{3+/2+}$ -mediator confirmed negligible effects of the bases on the electrochemical properties of  $\text{Co}(\text{III/II})$  couple, significant influence of the bases was found for the  $\text{Cu}(\text{tmby})_2^{2+/+}$ -mediator. Solely BTBP had small effect on charge-transfer rates at the  $\text{Cu}(\text{tmby})_2^{2+/+}$ /PEDOT interface and ionic diffusion in the electrolyte solution. However, BTBP was also ineffective for  $V_{\text{OC}}$  enhancement through a  $\text{TiO}_2$  conduction band upshift. Both effects are understood in terms of steric hindrance of coordination of BTBP to either the Cu central atom or to the  $\text{TiO}_2$  surface. All tested bases further exhibit simple correlation of their basicity ( $\text{pK}_a$ ) with charge transfer rate at the PEDOT surface and diffusion resistances in electrolyte solutions. The NOP-containing DSC-device is outperforming all the remaining ones in solar conversion metrics.

## 4.4 Experimental Section

*Chemicals and Reagents.* All chemicals were purchased from Aldrich, TCI or Merck, and used as received.

*Synthesis of copper complexes.* The detailed description for the synthesis of copper complexes are given in Chapter 2 and Chapter 3.

*Electrode materials and fabrication of devices.* The electrode materials and device fabrication techniques are provided in Chapter 2.

*Fabrication of dummy cells.* The symmetrical dummy cells were fabricated with two identical PEDOT electrodes, which were separated by 30  $\mu\text{m}$  Surlyn (DuPont). The cells were filled with an electrolyte solution, which was identical to that used for DSC devices (see above). The cells were filled through a predrilled hole in one FTO support, and closed by a Surlyn seal. The sheet edges of FTO were coated by ultrasonic soldering. The cell spacing was measured by digital micrometer and found to be from 22 to 29  $\mu\text{m}$ . To account for casual fluctuations in cell spacing, the measured volt-ammetric currents on dummy cells were normalized for constant spacing of 25  $\mu\text{m}$ .

*Methods.* UV-Vis optical spectra were measured by a Hewlett-Packard 8453 diode array spectrometer. Electrochemical measurements were carried out using Autolab PGstat-30 equipped with the FRA module (Metrohm) or BioLogic SP300 potentiostats. The ZView software (Scribner Associates) was used to analyze the spectra of DSCs according to transmission line method<sup>121</sup>. The impedance spectra of dummy cells were acquired in the frequency range from 100 kHz to 0.1 Hz, at 0 V bias voltage, the modulation amplitude was 10 mV. Current–voltage characteristics, Incident-photon-to-current-conversion efficiency, electron lifetime and charge extraction measurements were carried out as detailed in Chapter 2.

Stability measurements were performed with a Biologic MPG2 potentiostat under continuous illumination from a white LED lamp (Lumileds LXM3-PW51) with 0.5-sun intensity. The ageing procedure consisted of measuring IV curves every 24 h (at 100  $\text{mV s}^{-1}$ ) followed by the long period of maximum power point tracking (MPPT). The maximum power point (MPP) was updated every second by a standard perturb and observe method. The temperature of the devices was about 35  $^{\circ}\text{C}$ ; the atmosphere was ambient air.





# Chapter 5 The Effect of Coordination Sphere of Copper Redox Mediators on Regeneration and Recombination Behavior in Dye-sensitized Solar Cell Applications

This chapter is adopted from the following article with the permission of the journal:

Postprint version of the publication: 'The Effect of Coordination Sphere Geometry of Copper Redox Mediators on Regeneration and Recombination Behavior in Dye-sensitized Solar Cell Applications. ACS Applied Energy Materials., 2018, 1(9),4950-4962. DOI: 10.1021/acsaem.8b00957' by Yasemin Saygili, Marko Stojanovic, Hannes Michaels, Jan Tiepelt, Joel Teuscher, Arianna Massaro, Michele Pavone, Fabrizio Giordano, Shaik M. Zakeeruddin, Gerrit Boschloo, Jacques-E. Moser, Michael Grätzel, Ana B. Muñoz-García, Anders Hagfeldt and Marina Freitag

My contribution: Synthesis of the complexes, characterization of the complexes, device preparation and characterization, analysis of the data, writing the manuscript.

In the previous chapter, we investigated the effect of TBP and other bases on the copper redox mediators in detail. In this chapter we take a closer look on the dye regeneration and charge recombination behaviors in the absence and presence of TBP. We investigate four copper complexes,  $[\text{Cu}(\text{dmby})_2]^{2+/1+}$  (dmby = 6,6'-dimethyl-2,2'-bipyridine),  $[\text{Cu}(\text{tmby})_2]^{2+/1+}$  (tmby = 4,4',6,6'-tetramethyl-2,2'-bipyridine),  $[\text{Cu}(\text{eto})_2]^{2+/1+}$  (eto=4-ethoxy-6,6'-dimethyl-2,2'-bipyridine) and  $[\text{Cu}(\text{dmp})_2]^{2+/1+}$  (dmp=bis(2,9-dimethyl-1,10-phenantroline) in conjunction with the D5, D35 and D45 sensitizers, having various degrees of blocking moieties. We show that, for Cu(II) species, the presence of 4-tert-butylpyridine (TBP) in the electrolyte medium, results in penta-coordinated complexes with altered charge recombination kinetics ( $\lambda = 1.23\text{-}1.40$  eV). These higher reorganization energies lead to charge recombination in the Marcus normal regime instead of the Marcus inverted regime that could have been expected from the large driving force for electrons in the conduction band of  $\text{TiO}_2$  to react with Cu(II). Additionally, we show that the recombination resistance and electron lifetime values were higher for the copper redox species compared to the reference cobalt redox mediator. The DSC devices employing D35 dye with  $[\text{Cu}(\text{dmp})_2]^{2+/1+}$  reached a record value for the open circuit voltage of 1.14 V without compromising the short circuit current density value. Even with the D5 dye, which lacks recombination preventing steric units, we reached 7.5 % efficiency by employing  $[\text{Cu}(\text{dmp})_2]^{2+/1+}$  and  $[\text{Cu}(\text{dmby})_2]^{2+/1+}$  at AM 1.5G full sun illumination with open circuit voltage values as high as 1.13V.

## 5.1 Introduction

Despite reaching high PCE values with copper complexes based DSCs, various electron transfer processes were insufficiently investigated and understood in the previous chapters. In this chapter, we studied the recombination and regeneration behaviors of the  $[\text{Cu}(\text{dmby})_2]^{2+/1+}$ ,  $[\text{Cu}(\text{tmby})_2]^{2+/1+}$ ,  $[\text{Cu}(\text{eto})_2]^{2+/1+}$  (eto=4-ethoxy-6,6'-dimethyl-2,2'-bipyridine) and  $[\text{Cu}(\text{dmp})_2]^{2+/1+}$  together with sensitizers, having various degrees of blocking side chains. We introduce a new copper complex,  $[\text{Cu}(\text{eto})_2]^{2+/1+}$ , in order to have similar redox potential as  $[\text{Cu}(\text{tmby})_2]^{2+/1+}$  to understand solely the effect of ligand structure on dye regeneration and charge recombination by comparing the data of  $[\text{Cu}(\text{eto})_2]^{2+/1+}$  and  $[\text{Cu}(\text{tmby})_2]^{2+/1+}$ . The chemical structures of copper complexes and D5, D45 and D35 dyes are given in Figure 5-1. The D5, D35 and D45 dyes consist of a triphenylamine electron donor, thiophene chain extending  $\pi$ -conjugation and cyanoacrylic acid as the anchoring group. The D5 dye has no bulky substituents to prevent electron recombination, but D35 and D45 dyes include bulky alkoxy electron donating substituents. Employing these three sensitizers, the dye regeneration kinetics were investigated via Transient Absorption Spectroscopy and Photoinduced Absorption Spectroscopy experiments. To further investigate the recombination behavior of the injected electrons in  $\text{TiO}_2$  and electrolyte, we performed Electrical Impedance Spectroscopy measurements and small amplitude light-modulation technique (Toolbox) measurements. In addition, a detailed density functional theory analysis was provided to understand the effect of molecular configuration on electron transfer processes.

According to Transient Absorption Spectroscopy, the oxidized dye molecules are regenerated close to unity yields (in the micro-second range) with very low driving forces (i.e. 0.1 eV) by employing the four copper redox mediators. The calculated activation energy values for the regeneration of the oxidized D5 and D45 dyes, were found to be similar to the values of  $[\text{Co}(\text{bpy})_3]^{3+/2+}$ . This finding explains the reason of having similar current density values with  $[\text{Co}(\text{bpy})_3]^{3+/2+}$  and copper redox couples.

Contrary to Cu(I) species, the Cu(II) counterparts tend to be penta-coordinated by accepting 4-tert-butylpyridine (TBP) (or alternatively some counter ions) as the 3<sup>rd</sup> ligand.<sup>82,101,102,122–124</sup> By means of density functional theory calculations, we proved that TBP coordinated Cu(II) species have higher reorganization energies in comparison to Cu(I) counterparts. In the presence of TBP, the formal Cu(II)/Cu(I) redox potential shifts negatively by several tens of millivolts.<sup>102</sup> These findings show that the charge recombination stays in the Marcus normal regime. The experimentally derived electron lifetimes, extracted charge values and recombination resistances were compared to  $[\text{Co}(\text{bpy})_3]^{3+/2+}$ . In accordance with calculated parameters, it is shown that even though the driving force for recombination in copper redox mediators is higher compared to cobalt electrolyte, the copper electrolytes give higher recombination resistance and higher electron lifetimes in most of the cases. Due to the higher resistance for recombination, the effect of dye structure becomes less significant for the copper complexes, which can be clearly observed for the devices sensitized with the D5 dye. It is also shown that in the absence of TBP, the calculated reorganization energy values suggest a Marcus inverted regime for recombination.

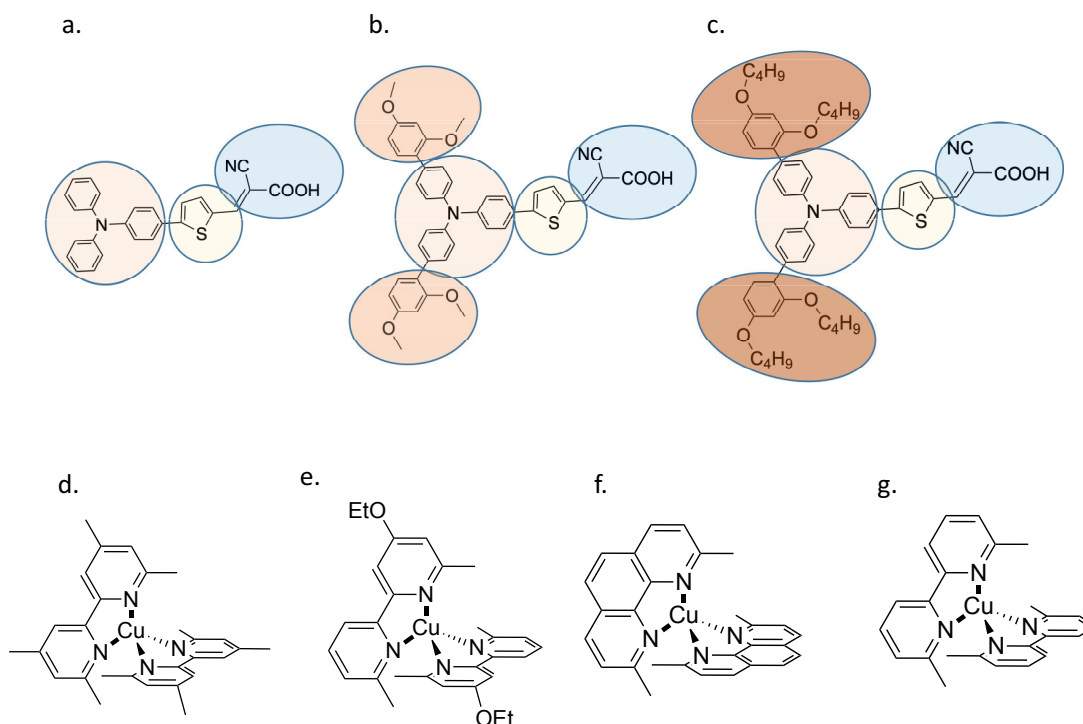


Figure 5-1 Molecular structures of and a) D5 b) D45 c) D35 dyes and d)  $[\text{Cu}(\text{tmby})_2]^{2+/1+}$  e)  $[\text{Cu}(\text{eto})_2]^{2+/1+}$  f)  $[\text{Cu}(\text{dmp})_2]^{2+/1+}$  g)  $[\text{Cu}(\text{dmby})_2]^{2+/1+}$  complexes.

## 5.2 Results and Discussion

### 5.2.1 Electrochemical and Spectroscopic Data of Novel $\text{Cu}(\text{I})(\text{eto})_2$ and $\text{Cu}(\text{II})(\text{eto})_2$ .

The formal redox potential of the novel  $[\text{Cu}(\text{eto})_2]^{2+/1+}$  complex was determined by three-electrode cyclic voltammetry measurement. By omitting the activity coefficient differences, the redox potential of this complex can be approximated as 0.86 V vs SHE (Figure 5-2a). The absorption spectra of the  $[\text{Cu}(\text{eto})_2]^{1+}$  and  $[\text{Cu}(\text{eto})_2]^{2+}$  are given in (Figure 5-2b). For  $[\text{Cu}(\text{eto})_2]^{1+}$ , the extinction coefficient is found to be  $1750 \text{ M}^{-1}\text{cm}^{-1}$  at 450 nm, suggesting a metal-to-ligand charge transfer (MLCT) transition. For  $[\text{Cu}(\text{eto})_2]^{2+}$ , the absorption peaks are observed in the UV region, attributed to the  $\pi \rightarrow \pi^*$  transitions, with an extinction coefficient value of  $1400 \text{ M}^{-1}\text{cm}^{-1}$  at 360 nm.

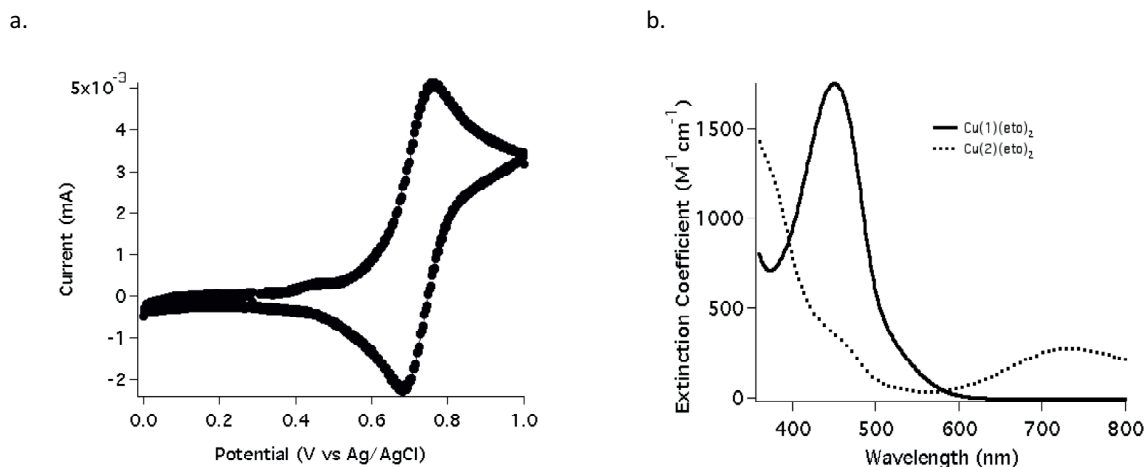


Figure 5-2 a) Cyclic Voltammogram of  $[\text{Cu}(\text{eto})_2]^{1+}$  complex. b) Molecular extinction coefficients of  $[\text{Cu}(\text{eto})_2]^{1+}$  and  $[\text{Cu}(\text{eto})_2]^{2+}$  complexes.

## 5.2.2 Photovoltaic Performance.

The energy levels of the D5, D35, D45 sensitizers,  $[\text{Cu}(\text{tmby})_2]^{1+}$ ,  $[\text{Cu}(\text{dmby})_2]^{1+}$ ,  $[\text{Cu}(\text{dmp})_2]^{1+}$ ,  $[\text{Co}(\text{bpy})_3]^{3+/2+}$  complexes, and the photocurrent-voltage characteristics of the DSC devices employing these materials are given in Figure 5-3(a) and (b-d), respectively. The power conversion efficiencies are calculated by Equation 1-10 and the photovoltaic data is provided in Table 5-1.

The DSC devices sensitized with D35 dye and employing  $[\text{Cu}(\text{tmby})_2]^{2+/1+}$  reached 9.44 % efficiency at AM 1.5G illumination. With the D35 dye, all the copper complexes showed remarkably high open circuit values above 1.0 V at full sunlight illumination. For  $[\text{Cu}(\text{dmp})_2]^{2+/1+}$ , the  $V_{\text{OC}}$  was recorded as 1.14 V and is one of the highest values to our knowledge. Although the copper complexes have lower driving force for dye regeneration with respect to  $[\text{Co}(\text{bpy})_3]^{3+/2+}$ , the  $J_{\text{sc}}$  values stayed similar. Especially in case of  $[\text{Cu}(\text{tmby})_2]^{2+/1+}$ , the  $J_{\text{sc}}$  reached up to  $12.71 \text{ mA cm}^{-2}$ .

The D5 dye with a simple diphenylaniline moiety as electron donor and a thiophene chain extending the  $\pi$ -conjugation, lacks the steric-bulky structures to prevent the recombination of electrons from the  $\text{TiO}_2$  with the electrolyte. A record efficiency for this dye of 7.5 % was achieved with both  $[\text{Cu}(\text{dmby})_2]^{2+/1+}$  and  $[\text{Cu}(\text{dmp})_2]^{2+/1+}$  electrolytes. The  $V_{\text{OC}}$  values were 1.13 V and 1.07 V for  $[\text{Cu}(\text{dmp})_2]^{2+/1+}$  and  $[\text{Cu}(\text{dmby})_2]^{2+/1+}$ , respectively. These remarkable  $V_{\text{OC}}$  values shows that the D5 dye can be effectively utilized as a co-sensitization dye for other systems. The molecular simplicity and compactness of this dye can allow better dye loading when it is applied in conjunction with bulkier dye molecules. In case of  $[\text{Cu}(\text{tmby})_2]^{2+/1+}$ , the  $J_{\text{SC}}$  value was the highest as  $10.3 \text{ mA cm}^{-2}$ , whereas the other electrolytes were above  $9 \text{ mA cm}^{-2}$ . Depending on the smaller size of the D5 dye, the fill factors obtained with this chromophore were generally better.

$[\text{Cu}(\text{tmby})_2]^{2+/1+}$  electrolyte with D45 dye<sup>125,126</sup> reached a PCE value of 8.3%. Although  $[\text{Cu}(\text{dmby})_2]^{2+/1+}$  and  $[\text{Cu}(\text{dmp})_2]^{2+/1+}$  electrolytes have limited driving force for regenerating the D45 dye, the PCE values were comparable to the one for  $[\text{Co}(\text{bpy})_3]^{3+/2+}$ . For  $[\text{Cu}(\text{dmby})_2]^{2+/1+}$  and

$[\text{Cu}(\text{dmp})_2]^{2+/1+}$  species, the recombination suppressing parts of D45 (o,p-dimethoxyphenyl units) can be considered as redundant when we compare with the D5 dye.

In general, the FF values for  $[\text{Co}(\text{bpy})_3]^{3+/2+}$  appeared to be higher than that of the copper complexes. This is attributed both to the higher charge transfer resistance of the counter electrode and diffusion resistances for copper complexes, as reported by Kavan et. al.<sup>101</sup> The reason for the higher diffusion resistances of the Cu-complexes was reported to be due to the coordination of TBP molecules to the copper complex molecular coordination sphere.

According to J-V data, the  $[\text{Cu}(\text{tmby})_2]^{2+/1+}$  and  $[\text{Cu}(\text{eto})_2]^{2+/1+}$  complexes correspond to similar current, voltage and fill factor values for all the sensitizers. This indicates that the ligand structures of these complexes do not cause a profound difference on photovoltaic performance. Instead, the driving force for dye regeneration and recombination is more important.

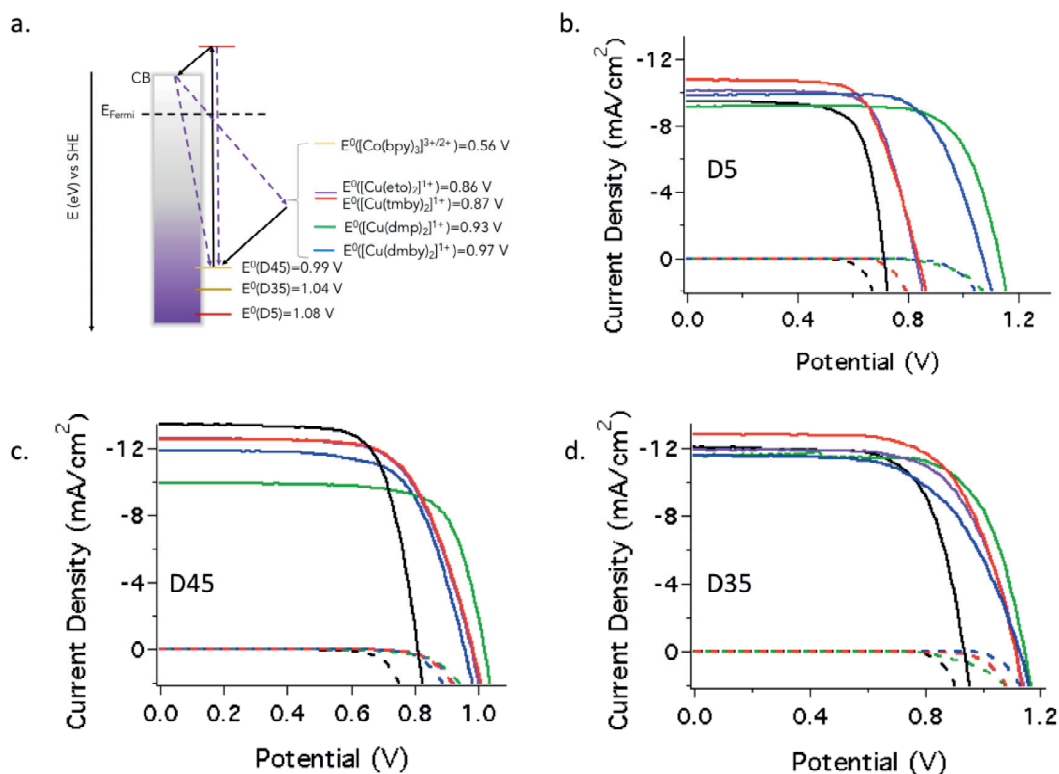


Figure 5-3 a) HOMO levels of D5, D35 and D45 dyes and formal redox potentials of the Cu(I) species. b-d) Current density versus applied potential curves under dark and 100W/cm<sup>2</sup> AM1.5G illumination for DSCs devices measured with a mask aperture of 0.158 cm<sup>2</sup>. ( $[\text{Cu}(\text{dmby})_2]^{2+/1+}$  (Blue),  $[\text{Cu}(\text{tmby})_2]^{2+/1+}$  (Red),  $[\text{Cu}(\text{eto})_2]^{2+/1+}$  (Purple),  $[\text{Cu}(\text{dmp})_2]^{2+/1+}$  (Green), and  $[\text{Co}(\text{bpy})_3]^{3+/2+}$  (Black)).

Table 5-1 J-V Characteristics for D5, D35 and D45 sensitized DSC devices employing  $[\text{Cu}(\text{tmby})_2]^{2+/1+}$ ,  $[\text{Cu}(\text{eto})_2]^{2+/1+}$ ,  $[\text{Cu}(\text{dmby})_2]^{2+/1+}$ ,  $[\text{Cu}(\text{dmp})_2]^{2+/1+}$  and  $[\text{Co}(\text{bpy})_3]^{3+/2+}$  electrolytes (all electrolytes have the same concentration of additives 0.1 M LiTFSI and 0.6M TBP).

Redox couple	D5				D45				D35			
	$V_{oc}$ (V)	$J_{sc}$ (mA $\text{cm}^{-2}$ )	FF	PCE (%)	$V_{oc}$ (V)	$J_{sc}$ (mA $\text{cm}^{-2}$ )	FF	PCE (%)	$V_{oc}$ (V)	$J_{sc}$ (mA $\text{cm}^{-2}$ )	FF	PCE (%)
$[\text{Co}(\text{bpy})_3]^{3+/2+}$	0.713	9.45	0.728	4.9	0.810	13.40	0.730	7.9	0.936	12.05	0.691	7.8
$[\text{Cu}(\text{tmby})_2]^{2+/1+}$	0.837	10.79	0.674	6.1	0.984	12.52	0.673	8.3	1.11	12.81	0.661	9.4
$[\text{Cu}(\text{eto})_2]^{2+/1+}$	0.828	10.12	0.715	6.0	0.978	12.59	0.667	8.2	1.12	11.93	0.663	8.8
$[\text{Cu}(\text{dmp})_2]^{2+/1+}$	1.13	9.02	0.736	7.5	1.02	9.90	0.741	7.5	1.14	11.40	0.706	9.2
$[\text{Cu}(\text{dmby})_2]^{2+/1+}$	1.07	9.85	0.712	7.5	0.956	11.85	0.680	7.7	1.13	11.53	0.602	7.8

The typical IPCE spectra for D35 and D5 sensitizers employing copper electrolytes are given in Figure 5-4. For D35 dye, the maximum IPCE is found to be over 70% around 550 nm, with the three copper compounds. The IPCE drop around 360 nm is attributed to the competitive light absorption of the FTO glass and the electrolyte. The slightly blue shifted IPCE spectrum of the  $[\text{Cu}(\text{dmp})_2]^{2+/1+}$  electrolyte indicates that this complex has a higher extinction coefficient compared with the other Cu-complexes. In case of D5 sensitized devices employing copper electrolytes, the maximum IPCE and the corresponding wavelength were observed to be higher than 70% (around 400 nm). The parasitic light absorption was stronger around 500 nm when D5 dye is employed, which is attributed to the absorption of Cu(I) species.

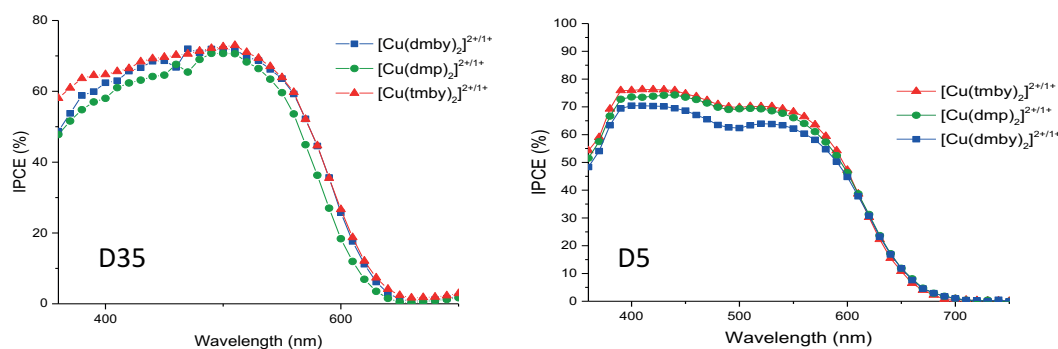


Figure 5-4 IPCE spectra of D35 and D5 sensitized DSC devices employing the three copper complex electrolytes.

### 5.2.3 Photoinduced Absorption Spectroscopy.

The regeneration kinetics of D5 and D35 chromophores employing  $[\text{Cu}(\text{tmby})_2]^{2+/1+}$ ,  $[\text{Cu}(\text{dmby})_2]^{2+/1+}$ ,  $[\text{Cu}(\text{dmp})_2]^{2+/1+}$  and inert electrolyte (0.1 M LiTFSI and 0.6 M TBP in acetonitrile) were investigated via photoinduced absorption spectroscopy measurements (See Figure 5-5). For both sensitizers, with the inert electrolyte, a bleach was observed around 460 nm indicating a ground-state bleach of the dye upon oxidation. The absorption change of the dye molecules stems

from the change of the electric field caused by photoinjected electrons, i.e., a Stark shift.<sup>98,99</sup> In the presence of copper complexes, the bleach shifted to 520 nm (for the D5 sensitizer employing  $[\text{Cu}(\text{dmp})_2]^{2+/1+}$ , the signal persisted around 460 nm due to excitation light) as a result of the Stark effect. The lack of absorption peaks of oxidized dye molecules in the photoinduced absorption spectroscopy spectra indicates that the oxidized dye molecules are efficiently regenerated by the Cu(I) complex.

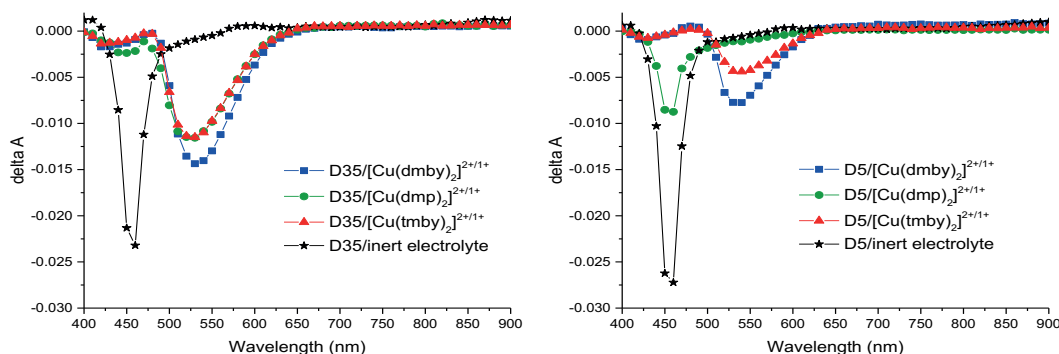


Figure 5-5 Photoinduced absorption spectroscopy spectra of D5 and D35 sensitized  $\text{TiO}_2$  films with the inert and the three copper complex electrolytes.

### 5.2.4 Transient Absorption Spectroscopy

Transient absorption spectroscopy measurements were carried out to investigate the dye regeneration kinetics and recombination of oxidized dye molecules and injected electrons in the  $\text{TiO}_2$ . The transient absorption spectroscopy figures and the corresponding data for the D5, D35 and D45 sensitized films employing  $[\text{Cu}(\text{tmby})_2]^{2+/1+}$ ,  $[\text{Cu}(\text{dmby})_2]^{2+/1+}$ ,  $[\text{Cu}(\text{dmp})_2]^{2+/1+}$ ,  $[\text{Cu}(\text{eto})_2]^{2+/1+}$  and the inert electrolyte are given in Figure 5-6 and Table 5-2, respectively. In the absence of redox couples, the recombination of injected electrons in the  $\text{TiO}_2$  and oxidized dye molecules showed absorbance decay signals of 1.1 ms, 2.3 ms and 1.9 ms half-times ( $\tau_{1/2}$ ), for D5, D35 and D45 dyes, respectively. These half-time values clearly show the effect of electron donating substituents on the chromophore. The *o,p*-dibutoxyphenyl substituent involved in the D35 dye provides the strongest barrier for recombination of injected electrons with oxidized dye molecules as observed by the highest half-time. The D5 dye shows the shortest recombination half-time since it lacks the recombination preventing bulky units. The presence of copper species accelerates the absorbance signal decay which indicates faster regeneration of the oxidized dye molecules with Cu(I) species. The regeneration efficiencies ( $\Phi_{\text{reg}}$ ) are estimated via Equation 1-5. All the copper complexes showed  $\Phi_{\text{reg}}$  values that are close to 100% with D5, D35 and D45 dyes.

For the D35 and D45 dyes, the  $\tau_{1/2}$  values can be related to the driving force for dye regeneration, suggesting a Marcus normal regime for dye regeneration for the complexes under study. This finding will be supported by the DFT calculations described in detail further below. Thus, the  $[\text{Cu}(\text{tmby})_2]^{2+/1+}$  and  $[\text{Cu}(\text{eto})_2]^{2+/1+}$  complexes showed the shortest regeneration times due to the more negative formal redox potential enabling higher driving forces for dye regeneration. In case of

the D5 dye no clear relation between regeneration half-times and driving force values was observable. The transient absorption spectroscopy measurements indicate that the copper redox mediators are able to regenerate oxidized dye molecules with faster kinetics in comparison to the Co-complexes based redox mediators.<sup>54</sup>

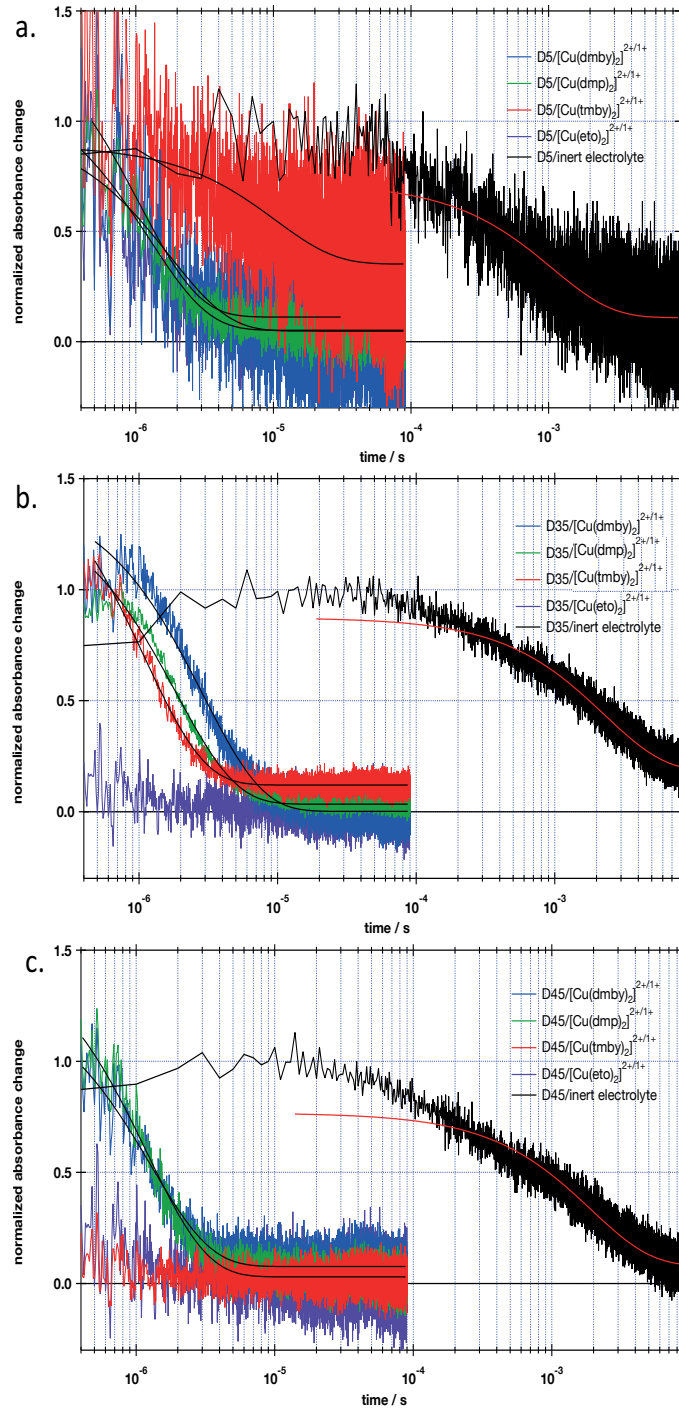


Figure 5-6 Transient absorption spectroscopy measurements of a) D5 b) D35 and c) D45 sensitized  $\text{TiO}_2$  films with inert,  $[\text{Cu}(\text{dmby})_2]^{2+/1+}$ ,  $[\text{Cu}(\text{tmby})_2]^{2+/1+}$ ,  $[\text{Cu}(\text{eto})_2]^{2+/1+}$  and  $[\text{Cu}(\text{dmp})_2]^{2+/1+}$  electrolytes.



Table 5-2 Transient absorption spectroscopy measurements data (halftime/ regeneration efficiency) for the TiO<sub>2</sub> films sensitized with D5, D35 and D45 dyes employing [Cu(tmby)<sub>2</sub>]<sup>2+/1+</sup>, [Cu(dmby)<sub>2</sub>]<sup>2+/1+</sup>, [Cu(dmp)<sub>2</sub>]<sup>2+/1+</sup> and [Cu(eto)<sub>2</sub>]<sup>2+/1+</sup>.

	Inert	[Cu(dmby) <sub>2</sub> ] <sup>2+/1+</sup>	[Cu(dmp) <sub>2</sub> ] <sup>2+/1+</sup>	[Cu(tmby) <sub>2</sub> ] <sup>2+/1+</sup>	[Cu(eto) <sub>2</sub> ] <sup>2+/1+</sup>
D5	1.1 ms	1.8 μs / 99.8%	1.2 μs / 99.9%	10.3 μs / 99.0%	1.1 μs / 99.9%
D35	2.3 ms	2.9 μs / 99.9%	1.9 μs / 99.9%	1.1 μs / 100%	< 1 μs / 99.9%
D45	1.9 ms	1.3 μs / 99.9%	1.2 μs / 99.9%	< 1 μs / 99.9%	< 1 μs / 99.9%

### 5.2.5 Electron lifetime and charge extraction measurements.

The recombination kinetics were further investigated by a small amplitude light-modulation technique in terms of electron lifetime and charge extraction measurements. For the same light intensity, the measured electron lifetimes versus extracted charge values are given in Figure 5-7. We can clearly observe that the [Co(bpy)<sub>3</sub>]<sup>3+/2+</sup> electrolyte has relatively lower lifetimes in most devices, for the same extracted charge values, i.e. the same density of conduction band electrons. Only the D35 dye, employing the [Cu(dmp)<sub>2</sub>]<sup>2+/1+</sup> electrolyte gives lower electron lifetimes compared to [Co(bpy)<sub>3</sub>]<sup>3+/2+</sup>. For [Cu(dmp)<sub>2</sub>]<sup>2+/1+</sup> electrolyte, this behavior is attributed to the bimolecular reductive quenching of the excited dye by the [Cu(dmp)<sub>2</sub>]<sup>2+</sup> species as reported by Freitag et al.<sup>81</sup> In this previous work<sup>81</sup>, it was stated that the excited dye can be intercepted with an electron from the electrolyte, resulting in the reduced state of the dye. Furthermore, quenching of the reduced dye by the electrolyte competes with electron injection and results in a lower photocurrent. Therefore, the lower lifetime and charge extraction values for D35 sensitized films, employing [Cu(dmp)<sub>2</sub>]<sup>2+/1+</sup>, can also be explained by bimolecular reductive quenching by considering the same donating group of the D35 and LEG4 dyes.

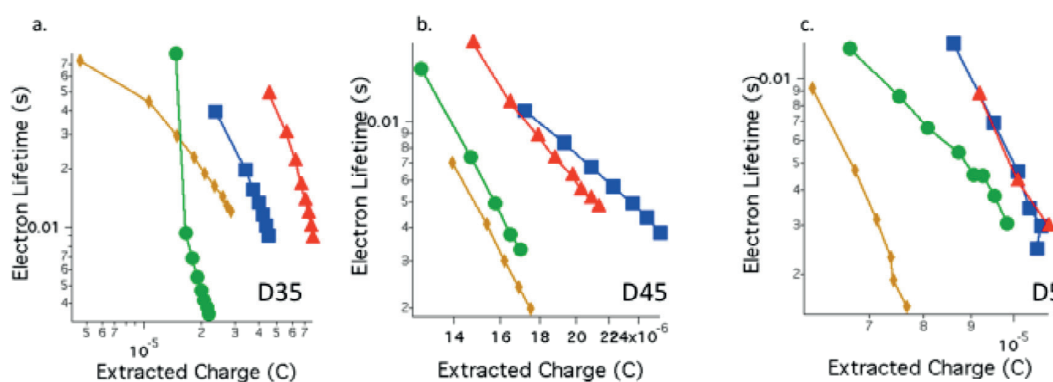


Figure 5-7 Electron lifetime versus Charge extraction data obtained from the Toolbox measurements for a) D35 b) D45 and c) D5 sensitized TiO<sub>2</sub> films. [Cu(dmby)<sub>2</sub>]<sup>2+/1+</sup> (blue squares), [Cu(tmby)<sub>2</sub>]<sup>2+/1+</sup> (red triangles), and [Cu(dmp)<sub>2</sub>]<sup>2+/1+</sup> (green circles), and [Co(bpy)<sub>3</sub>]<sup>3+/2+</sup> (yellow diamonds).

### 5.2.6 Electrochemical Impedance Spectroscopy.

In order to disregard the effects of light on the analysis of recombination kinetics, i.e. eliminating the recombination losses to unregenerated or oxidized dyes, the dark currents, dark recombination resistances and chemical capacitances are analyzed.

In

Figure 5-8, the dark currents of DSC devices are presented. As expected, with different dye and electrolyte employments, the dark current values change. These differences are related to the kinetics of electron transfer reactions at the  $\text{TiO}_2/\text{dye}/\text{electrolyte}$  interface and  $\text{TiO}_2$  conduction band changes, which are important for the recombination characteristics in the DSC devices.<sup>127</sup> The recombination resistance and chemical capacitance of  $\text{TiO}_2$  are extracted by using the transmission line model.<sup>83</sup>

For all the devices, the recombination resistance showed a decreasing trend with increasing capacitance at forward bias, as reflected in the curves of dark currents. (At low forward bias (up to 0.4 V), the recombination resistance behavior is dominated by the recombination of electrons with FTO, therefore the data obtained at higher forward bias will provide a better charge transfer analysis<sup>83</sup>). By concentrating on the higher chemical capacitance data, we can see that the recombination resistance increases according to the steric substituents of the dyes, as expected. (e.g. at a chemical capacitance of  $10^{-4}$  C, for the  $[\text{Cu}(\text{tmby})_2]^{2+/1+}$  electrolyte the recombination resistance is estimated approximately as  $10^3$ ,  $3 \times 10^3$  and  $5 \times 10^4$  Ohms for the D5, D45 and D35 dyes, respectively). For the three sensitizers, at the same capacitance the recombination resistances were the lowest, and the dark currents were the highest for  $[\text{Co}(\text{bpy})_3]^{3+/2+}$  indicating a higher rate of recombination between the electrons in  $\text{TiO}_2$  and Co(III) species.

$[\text{Cu}(\text{tmby})_2]^{2+/1+}$  and  $[\text{Cu}(\text{eto})_2]^{2+/1+}$  complexes showed almost the same recombination resistance values since they have similar formal redox potentials. This finding suggests that the structural differences with tmby and eto ligands have lower effect on reaction rates compared to differences in driving forces.

According to the Marcus model, the electron transfer rates depend on the driving force for reaction, electronic coupling, the reorganization energies and diffusion rates of reactants. The rate constant for electron transfer  $k_{\text{et}}$  can be given as in Equation 1-7. The measured electron lifetimes, extracted charge values and recombination resistances qualitatively indicate a lower recombination rate for copper complexes compared to  $[\text{Co}(\text{bpy})_3]^{3+/2+}$ . In order to understand the origin of this trend, a more detailed analysis is provided below with rest potential measurements and density functional theory calculations.

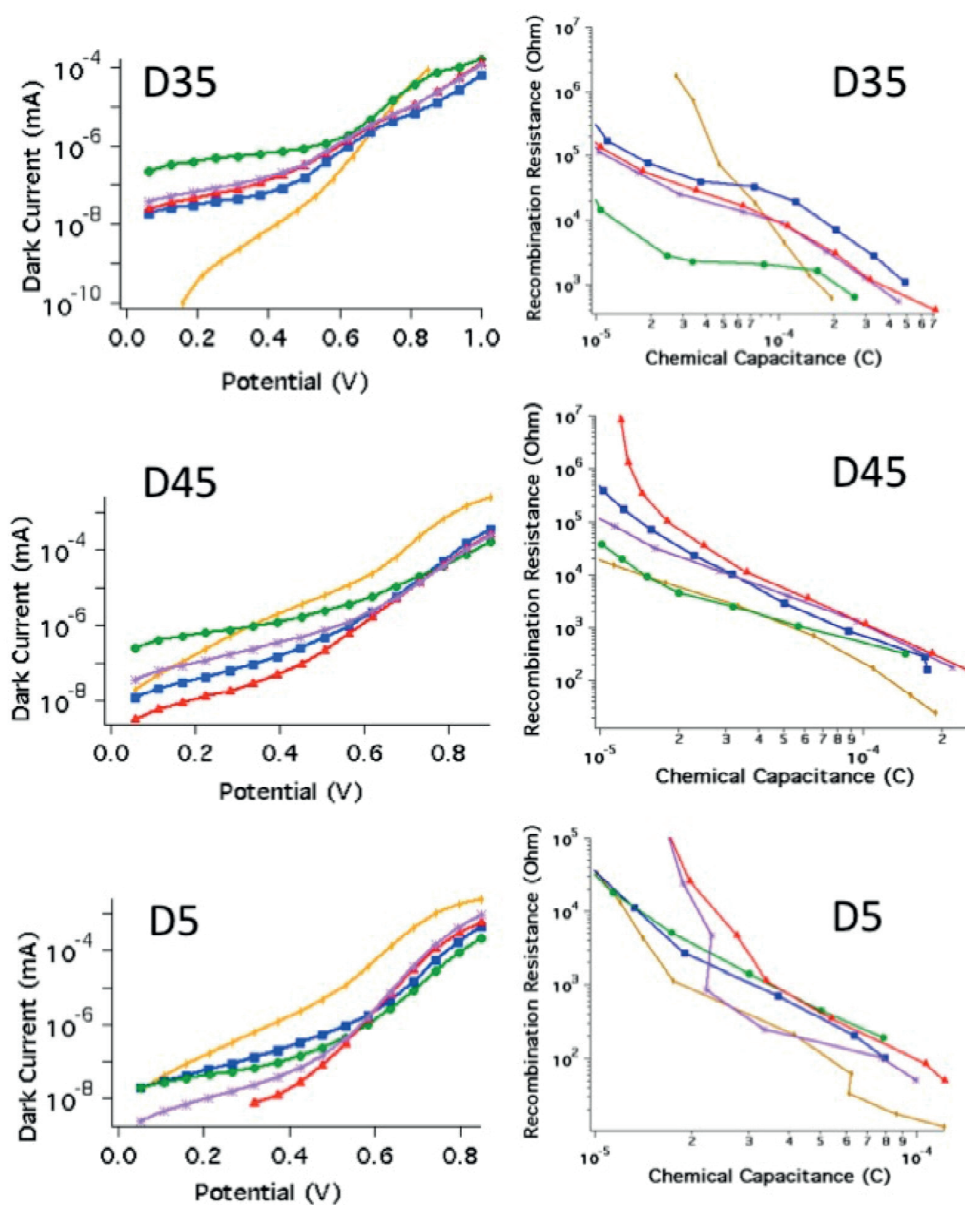


Figure 5-8 Dark currents, Recombination Resistance and Capacitance values obtained from the Electrical Impedance Spectroscopy measurements. [Cu(dmby)<sub>2</sub>]<sup>2+/1+</sup> (Blue squares), [Cu(tmby)<sub>2</sub>]<sup>2+/1+</sup> (Red triangles), [Cu(eto)<sub>2</sub>]<sup>2+/1+</sup> (Purple stars), [Cu(dmp)<sub>2</sub>]<sup>2+/1+</sup> (Green circles), and [Co(bpy)<sub>3</sub>]<sup>3+/2+</sup> (Yellow diamonds).

### 5.2.7 Rest Potential Measurements.

As discussed in previous chapters<sup>101,102</sup>, Cu(II) species exhibits more complicated cyclic voltammograms based upon counter ion coordinations or base coordinations. We also showed that these more complicated copper(II) species show more negative redox potentials.<sup>101,102,122</sup> In this study, we also carried out electrolyte rest potential measurements in order to see how Cu(II) species affects the

electrolyte redox potential. Surprisingly, there was a significant difference between the rest potentials of electrolytes and cyclic voltammetry data of only Cu(I) species, as given in

Table 5-3. With this finding we can speculate that penta-coordinated Cu(II) species shifts the electrolyte potentials to more negative values<sup>123,124</sup>. Since the driving force for the recombination reaction is determined by the difference between quasi-fermi level of the TiO<sub>2</sub> and redox potential of Cu(II) species, reaction free energies ( $\Delta G^\circ$  in Equation 1-7) for recombination is less than the values expected<sup>123</sup> (i.e. when the Cu(I) and Cu(II) species are assumed to have the same redox potentials). For [Co(bpy)<sub>3</sub>]<sup>3+/2+</sup>, the difference between cyclic voltammetry and rest potential measurements can be considered insignificant in comparison to the data obtained for the copper complexes.

Table 5-3 Rest potentials of [Cu(tmby)<sub>2</sub>]<sup>2+/1+</sup>, [Cu(dmp)<sub>2</sub>]<sup>2+/1+</sup> and [Co(bpy)<sub>3</sub>]<sup>3+/2+</sup> electrolytes and Formal redox potentials of Cu(I) species and [Co(bpy)<sub>3</sub>]<sup>+2</sup>

Redox couple	Rest Potential (V vs SHE)	Formal redox potential (V vs SHE)
[Cu(tmby) <sub>2</sub> ] <sup>2+/1+</sup>	0.644	0.87 <sup>(102)</sup>
[Cu(dmp) <sub>2</sub> ] <sup>2+/1+</sup>	0.669	0.93 <sup>(102)</sup>
[Co(bpy) <sub>3</sub> ] <sup>3+/2+</sup>	0.525	0.56 <sup>(49)</sup>

### 5.2.8 Density functional theory calculations

As discussed in Chapter 2 and 3<sup>101,102</sup>, when we use CuCl<sub>2</sub> as the starting material for Cu(II) production, the obtained Cu(II) species exhibits complicated electrochemical behaviors, unlike the electrochemically clean Cu(I) counterparts, because of counter ion coordination. We also showed that, by using Cu(TFSI)<sub>2</sub> as the starting material, electrochemically clean Cu(II) species can be produced.<sup>122</sup> However, this clean Cu(II) species tend to adopt more complicated coordination spheres in presence of TBP or other Lewis base additives and exhibit more negative redox potentials.<sup>101,102,122</sup> Following these findings, the DFT computations are carried out for ‘with TBP’ and ‘without TBP’ cases.

Firstly, in order to see the possible TBP interactions, the minimum energy structures and binding free energies are calculated. In the absence of TBP, copper(I) species prefer a tetrahedral coordination sphere for copper. Upon oxidation, the tetrahedral alignment decays to a distorted tetragonal structure, and most favoured square-planar Cu(II) coordination is prevented by the steric hindrance effects of the methyl groups adjacent to the nitrogen atoms of the ligands. The minimum energy structures of [Cu(tmby)<sub>2</sub>]<sup>2+/1+</sup> and [Cu(eto)<sub>2</sub>]<sup>2+/1+</sup>, with and without TBP, are given in Figure 5-9. Similarly, the minimum energy structures for [Cu(tmby)<sub>2</sub>]<sup>2+/1+</sup> and [Cu(dmp)<sub>2</sub>]<sup>2+/1+</sup> are provided in Figure 5-10. Although, according to our calculations, TBP remains in the vicinity of both Cu(I) and Cu(II) complexes, computed binding free energy values ( $\Delta G_{\text{bind}}$ ) of TBP (Table 5-4) are very different for Cu(I) and Cu(II) species. Negative free energies correspond to favorable binding, with a

clear indication of TBP coordination to Cu(II). On the other hand, positive values correspond to an unfavorable interaction between the Cu(I) complexes and TBP. Thus, we can conclude that TBP binds selectively to Cu(II) in the reaction media.

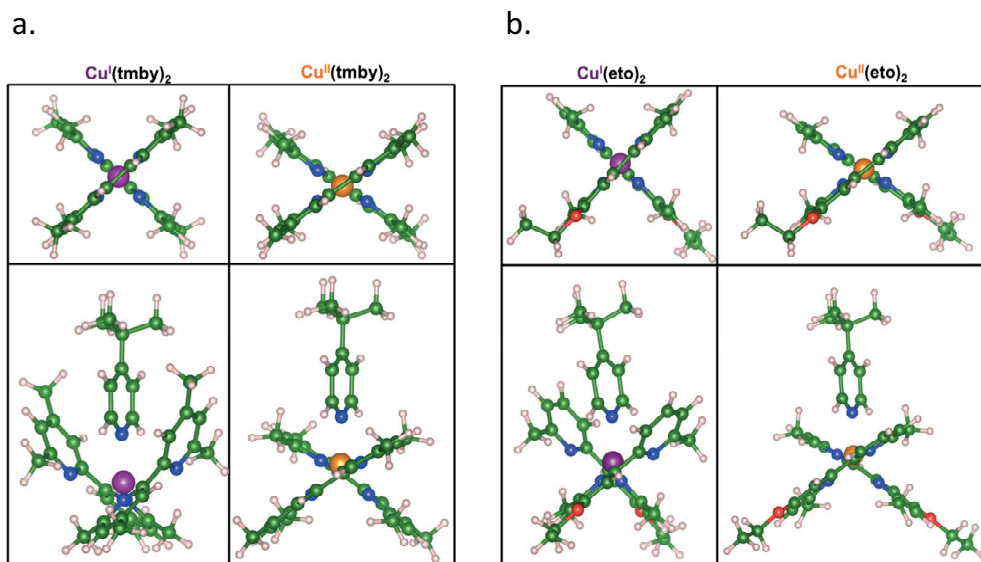


Figure 5-9 a)  $[\text{Cu}(\text{tmby})_2]^{1+}$  (left) and  $[\text{Cu}(\text{tmby})_2]^{2+}$  (right) b)  $[\text{Cu}(\text{eto})_2]^{1+}$  [Cu(eto)<sub>2</sub>]<sup>2+</sup> (right) minimum-energy structures without and with TBP (top and bottom, respectively) calculated at the DFT-B3LYP-D3BJ level of theory in acetonitrile (PCM).

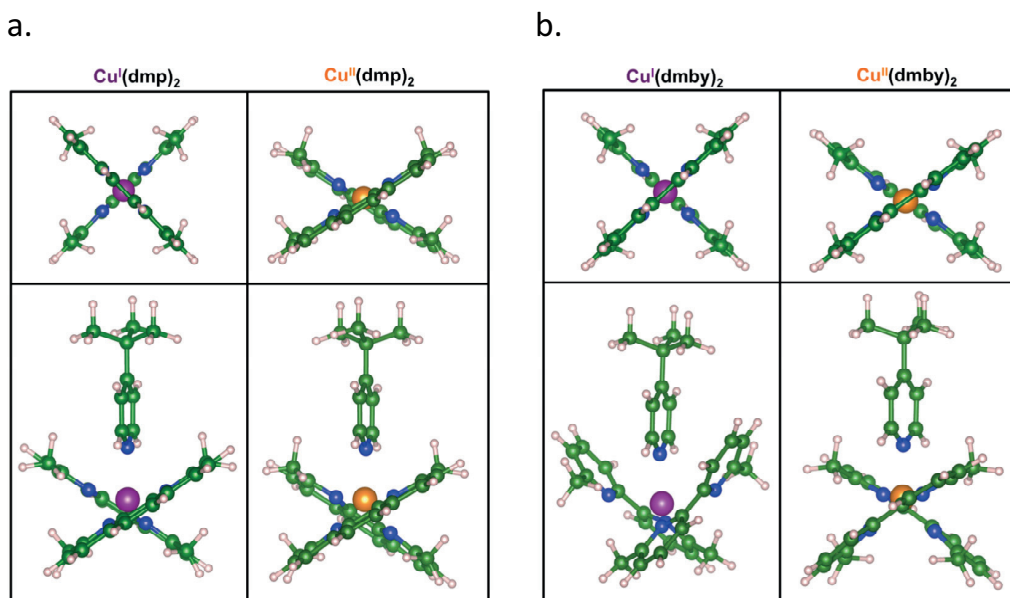


Figure 5-10 a)  $[\text{Cu}(\text{dmp})_2]^{1+}$  (left) and  $[\text{Cu}(\text{dmp})_2]^{2+}$  (right) b)  $[\text{Cu}(\text{dmby})_2]^{1+}$  and  $[\text{Cu}(\text{dmby})_2]^{2+}$  (right) minimum-energy structures without and with TBP (top and bottom, respectively) calculated at the DFT-B3LYP-D3BJ level of theory in acetonitrile (PCM).

Table 5-4 Binding Free Energies ( $\Delta G_{\text{bind}}$ ) of TBP on  $[\text{CuL}_2]^{1+}$  and  $[\text{CuL}_2]^{2+}$ .

Ligand	$\Delta G_{\text{bind}}(\text{TBP})$ (eV)	
	$\text{Cu}^{\text{I}}\text{-L}_2$	$\text{Cu}^{\text{II}}\text{-L}_2$
dmp	0.393	-0.334
dmby	0.350	-0.360
tmby	0.329	-0.265
eto	0.340	-0.268

The charge transfer process between the photo-oxidized dye ( $\text{D}^+$ ) and the electrolyte that lead to dye regeneration is in competition with the charge recombination process that occurs at the solid-liquid interface between the electron in the  $\text{TiO}_2$  conduction band and the oxidized dye. The  $\text{Cu}^{2+}/\text{Cu}^{1+}$  - and  $\text{Co}^{3+}/\text{Co}^{2+}$ - complex redox couples are involved in the second pathway of recombination of electrons in the  $\text{TiO}_2$ , *viz.* the reaction with oxidized electrolyte species. To address the energetics in play in these processes, we also computed the redox potentials and the total reorganization energies for the four copper-based complexes with dmp, dmby, tmby and eto ligands by considering the complexes without TBP ( $[\text{CuL}_2]^{2+}/[\text{CuL}_2]^{1+}$ ), with both  $[\text{CuL}_2]^{2+}$  and  $[\text{CuL}_2]^{1+}$  coordinated with TBP ( $[\text{CuL}_2\text{-TBP}]^{2+}/[\text{CuL}_2\text{-TBP}]^{1+}$ ) and with only  $[\text{CuL}_2]^{2+}$  coordinated by TBP. The trends on computed redox potentials given in Table 5-5 are in good agreement with the experimental data and the decreasing free energy values with TBP coordination also confirms our previous experimental findings.<sup>101,102,122</sup>

Table 5-5 Free Energy Differences ( $\Delta G_{\text{Ox}} \text{Cu}^{\text{I}}/\text{Cu}^{\text{II}}$ ) for the  $\text{Cu}(\text{I}) \rightarrow \text{Cu}(\text{II})$  process for complexes without TBP ( $[\text{CuL}_2]^{1+}/[\text{CuL}_2]^{2+}$ ), with both  $[\text{CuL}_2]^{1+}$  and  $[\text{CuL}_2]^{2+}$  coordinated with TBP ( $[\text{CuL}_2\text{-TBP}]^{1+}/[\text{CuL}_2\text{-TBP}]^{2+}$ ) and with only  $[\text{CuL}_2]^{2+}$  coordinated by TBP ( $[\text{CuL}_2]^{1+}/[\text{CuL}_2\text{-TBP}]^{2+}$ )

L	$\Delta G_{\text{Ox}} \text{Cu}^{\text{I}}/\text{Cu}^{\text{II}}$ (eV)		
	$[\text{CuL}_2]^{1+}/[\text{CuL}_2]^{2+}$	$[\text{CuL}_2\text{-TBP}]^{1+}/[\text{CuL}_2\text{-TBP}]^{2+}$	$[\text{CuL}_2]^{1+}/[\text{CuL}_2\text{-TBP}]^{2+}$
dmp	5.19	4.46	4.86
dmby	5.25	4.54	4.89
tmby	5.12	4.52	4.85
eto	5.10	4.49	4.83

We must note here that absolute values of computed redox potentials are 0.2 to 0.5 eV off the experimental values, as reported for similar DFT-based approaches<sup>53</sup>, due to the well-known draw-

backs of the approximated nature of the exchange-correlation term when comparing systems with a different number of electrons. Still, DFT can reliably predict reorganization energies ( $\lambda$ ), since they are calculated as energy differences between two points of the same potential energy surface. Table 5-6 reports the computed  $\lambda$  values for all the complexes in both dye regeneration (DR) and charge recombination (CR) directions, by considering the complexes without TBP, with both  $[\text{CuL}_2]^{1+}$  and  $[\text{CuL}_2]^{2+}$  coordinated with TBP, and with only  $[\text{CuL}_2]^{2+}$  coordinated by TBP. For comparison, the reorganization energies for DR and CR of  $[\text{Co}(\text{bpy})_3]^{3+/2+}$  complex are also calculated as 0.66 eV and 0.76 eV, respectively. We considered here only the low-spin case for the cobalt complex that is most convenient for the DR process even if it is not the most stable in acetonitrile solution.<sup>53</sup> Since the electro-chemical behavior of  $[\text{Co}(\text{bpy})_3]^{3+/2+}$  is invariant with the TBP addition<sup>101</sup>, the reorganization energies are calculated for solely  $\text{Co}^{2+} \rightarrow \text{Co}^{3+}$  and  $\text{Co}^{3+} \rightarrow \text{Co}^{2+}$  reactions.

Table 5-6 Reorganization energies ( $\lambda$ ) for the Cu(I)  $\rightarrow$  Cu(II) process for complexes without TBP ( $[\text{CuL}_2]^{1+}/[\text{CuL}_2]^{2+}$ ), with both  $[\text{CuL}_2]^{1+}$  and  $[\text{CuL}_2]^{2+}$  coordinated with TBP ( $[\text{CuL}_2\text{-TBP}]^{1+}/[\text{CuL}_2\text{-TBP}]^{2+}$ ) and with only  $[\text{CuL}_2]^{2+}$  coordinated by TBP ( $[\text{CuL}_2]^{1+}/[\text{CuL}_2\text{-TBP}]^{2+}$ ).  $\lambda$  for dye regeneration (DR) and charge recombination (CR) indicated.

L	$\lambda$ (eV)					
	$[\text{CuL}_2]^{1+}/[\text{CuL}_2]^{2+}$		$[\text{CuL}_2\text{-TBP}]^{1+}/[\text{CuL}_2\text{-TBP}]^{2+}$		$[\text{CuL}_2]^{1+}/[\text{CuL}_2\text{-TBP}]^{2+}$	
	DR	CR	DR	CR	DR	CR
<b>dmp</b>	0.321	0.368	0.391	0.754	0.272	1.368
<b>dmby</b>	0.313	0.334	0.523	1.269	0.369	1.253
<b>tmby</b>	0.322	0.350	0.595	1.203	0.380	1.232
<b>eto</b>	0.317	0.362	0.542	1.182	0.328	1.268

The total  $\lambda_{\text{DR}}$  values are not very different from just the internal reorganization energies<sup>102</sup>, meaning that the solvent effects on this parameter are less relevant than the internal structural rearrangements upon oxidation of the transition metal center. In the absence of TBP (Table 5-6,  $[\text{CuL}_2]^{1+}/[\text{CuL}_2]^{2+}$  entries), with the reduction of the transition metal center, the  $\lambda_{\text{CR}}$  values are similar but slightly higher than the DR counterparts. The relative magnitudes of the reorganization energies for CR among Cu complexes and  $[\text{Co}(\text{bpy})_3]^{3+/2+}$  have the same trend as for DR: in the absence of TBP, all the copper complexes have lower reorganization energies ( $\lambda_{\text{CR}}$ ) than the cobalt one. Considering coordination of TBP exclusively to Cu(II) (Table 5-6,  $[\text{CuL}_2]^{1+}/[\text{CuL}_2\text{-TBP}]^{2+}$  entries),  $\lambda_{\text{DR}}$  does not change dramatically, due to the geometry of  $\text{Cu}^{\text{II}}\text{L}_2$  species changing very little upon binding with TBP, and remain in the 0.3 eV range, but  $\lambda_{\text{CR}}$  increase for all complexes to values higher than 1.2 eV.

Considering the unfavorable binding of TBP with Cu(I), we can further analyze the dye regeneration patterns without considering TBP. Table 5-7 reports the electronic features of D5 and D45 dyes, including the internal and external reorganization energies. The predicted values on electronic properties are consistent with experimental counterparts. It is worth noting that the internal reorganization energies of the dyes are very small compared to the external one. This feature is consistent

with the significant electronic rearrangement in these push-pull dyes, which has a more pronounced effect on the solvent than in the case of the electrolytes, where the charge center does not change position and is protected by the ligands.

Table 5-7 Computed electronic properties of D5 and D45 dyes: absorption maximum ( $\lambda_{\text{max}}$ ) with corresponding oscillator strength inter parenthesis; Energy difference between  $S_1$  and  $S_0$  minima ( $E_{0-0}$ ), internal ( $\lambda_{\text{int}}$ ) an external ( $\lambda_{\text{ext}}$ ) reorganization energies are computed for the dye regeneration process ( $D^+ \rightarrow D$ ).

	Abs ( $\lambda_{\text{max}}$ ) (nm)	$E_{0-0}$ (eV)	$\lambda_{\text{int}}$ (eV)	$\lambda_{\text{ext}}$ (eV)
<b>D5</b>	497 (1.929) exp 476 <sup>128</sup>	1.866	0.071	0.661
<b>D45</b>	459 (1.532) exp 420 <sup>129</sup>	2.102	0.261	0.591

From this data, by combining the experimental redox potentials and the DFT reorganization energies, we can derive an estimate of the activation energy in the Marcus model for the dye-electrolyte charge transfer Equation 1-9. Table 5-8 lists the computed parameters.

Table 5-8 Marcus parameters (Equation 1-9) for dye regeneration.  $\Delta G_0$  values are derived from experiments, reorganization energies are from DFT calculations, all the values are in eV.

	<b>D5</b>			<b>D45</b>		
	$\Delta G_0$	$\lambda_{\text{tot}}$	$\Delta G_{\text{DR}}^{\#}$	$\Delta G_0$	$\lambda_{\text{tot}}$	$\Delta G_{\text{DR}}^{\#}$
<b>[Cu(dmp)<sub>2</sub>]<sup>1+</sup></b>	-0.15	1.054	0.19	-0.06	1.173	0.26
<b>[Cu(dmby)<sub>2</sub>]<sup>1+</sup></b>	-0.11	1.046	0.21	-0.02	1.165	0.28
<b>[Cu(tmby)<sub>2</sub>]<sup>1+</sup></b>	-0.21	1.055	0.17	-0.12	1.174	0.24
<b>[Cu(eto)<sub>2</sub>]<sup>1+</sup></b>	-0.22	1.050	0.16	-0.13	1.169	0.23
<b>[Co(bpy)<sub>3</sub>]<sup>2+</sup> (LS)</b>	-0.52	1.388	0.14	-0.43	1.508	0.19

The cobalt complex has a higher driving force for dye regeneration ( $\Delta G_0$ ) but also higher reorganization energy ( $\lambda_{\text{tot}}$ ) than the copper counterparts. The overall effect is that the activation energies ( $\Delta G_{\text{DR}}^{\#}$ ) for Cu complexes and  $[\text{Co}(\text{bpy})_3]^{3+/2+}$  are similar, the cobalt complex being only slightly favored and the  $[\text{Cu}(\text{eto})_2]^{2+/1+}$  having the lowest activation energy among the four tested ligands. Experimentally, the regeneration kinetics is slower for the  $[\text{Co}(\text{bpy})_3]^{3+/2+}$  complex ( $\tau_{1/2}$  of about 8  $\mu\text{s}$ ,<sup>128</sup>) indicating steric hindrance and/or inclusion of high-spin effects.

We focus now on the charge recombination of electrons in the  $\text{TiO}_2$  with oxidized species in the electrolyte, which undermines the photo-current generation by recombining the hole at the electrolyte (the oxidized redox species) with the injected electron from the excited dye to the electrode conduction band (CB). In order to have a qualitative description of the charge recombination ener-



getics and recalling the Marcus parameters, we consider the reduction of the  $\text{Cu}^{2+}$  (or  $\text{Co}^{3+}$ ) transition metal center by the electron that is coming from the  $\text{TiO}_2$  CB, neglecting the reorganization energy of the solid surface. Table 5-9 lists the computed results, following a similar approach as in the dye regeneration case (without TBP).

Table 5-9 Marcus parameter (Equation 1-9) for the charge recombination (CR) process from the CB of the  $\text{TiO}_2$  (approximated at  $-4 \text{ eV}^{130}$ ) to the electrolyte in the absence of TBP. All values are in eV.

	$\Delta G_0$	$\lambda_{tot}$	$\Delta G_{CR}^\#$
$[\text{Cu}(\text{dmp})_2]^{2+}$	-1.37	0.31	0.92
$[\text{Cu}(\text{dmby})_2]^{2+}$	-1.41	0.32	0.93
$[\text{Cu}(\text{tmby})_2]^{2+}$	-1.31	0.34	0.69
$[\text{Cu}(\text{eto})_2]^{2+}$	-1.30	0.33	0.73
$[\text{Co}(\text{bpy})_3]^{3+}(\text{LS})$	-1.00	0.76	0.02

These results outline a very different behavior between copper and cobalt when TBP is not considered. The copper complexes have a large driving force for CR and a small recombination energy, leading to an inverse Marcus regime ( $|\Delta G_0| \gg \lambda_{tot}$ ) and the resulting CR activation energy is two to three times larger than the DR values for all the complexes. On the contrary, a lower driving force and a higher reorganization energy for  $[\text{Co}(\text{bpy})_3]^{3+/2+}$  ( $|\Delta G_0| \sim \lambda_{tot}$ ) keeps the electron transfer recombination process kinetically favorable with a very low activation energy. Instead, if TBP interaction with Cu(II) species is considered, this results in much higher reorganization energies for the charge recombination process, and the electron transfer reaction stays in the Marcus normal regime (Table 5-9). For copper complexes, the higher reorganization energy values for charge recombination results in lower recombination rates. Moreover, considering the Cu(II) and TBP affinity, it is predicted that there will be less amount of TBP adsorbed on  $\text{TiO}_2$  films in case of copper-based electrolytes, which will shift the  $\text{TiO}_2$  conduction band position to more positive values, causing lower photovoltages. In a qualitative way, our results highlight a clear trend that is consistent and explains the observed behaviors for all the investigated electrolyte couples.

### 5.3 Conclusion

In this chapter, we showed the importance of the coordination sphere of copper redox mediators for dye regeneration and recombination processes. To minimize the dye regeneration overpotentials, the driving forces for dye regeneration are minimized. Transient Absorption Spectroscopy measurements show that the dye regeneration efficiencies stay close to unity with the D5, D35 and D45 dyes. Employing the common electrolyte additive, TBP, alter the molecular configurations especially by binding to Cu(II) species. These characteristics show some major differences for the reorganization energies and redox potentials of the corresponding Cu(II) species. Without TBP coordina-

tion, with higher driving forces for recombination, the recombination reaction rate constant becomes lower due to the lower reorganization energy values (i.e. 0.33-0.37 eV) of the complexes and the charge recombination process occurs in the Marcus inverted regime. However, with TBP coordination, the reorganization energies become higher (1.230-1.370 eV) and the driving force for recombination becomes less, and the charge recombination occurs in the Marcus normal regime. In comparison to  $[\text{Co}(\text{bpy})_3]^{3+/2+}$  electrolyte, the device recombination resistances and lifetimes are observed to be higher with the copper complexes. Moreover, the effect of dye structure observed to be less significant for the copper electrolytes. Even with the simple D5 dye, which lacks recombination preventing bulky units, remarkable  $V_{oc}$  values of e.g. 1.13V can be achieved. A record  $V_{oc}$  value of 1.14 V is achieved with the devices employing the D35 dye and  $[\text{Cu}(\text{dmp})_2]^{2+/1+}$  electrolyte. Besides the obtained remarkable photovoltaic performance, this study provides a better understanding of copper redox mediators and can motivate the future DSC research in terms of improving photovoltage outputs by employing copper complexes. New ligand structures allowing dye regeneration with smaller driving forces, and recombination in the Marcus inverted regime, could result in higher photovoltage outputs and accordingly improved device efficiencies. As another approach, TBP usage could be discarded by applying novel surface treatment techniques.

## 5.4 Methods

*Materials.* All chemicals were purchased from Sigma-Aldrich, HetCat, Dyenamo and TCI Chemicals and were used without further purification, unless otherwise stated.

*Synthesis of eto (4-ethoxy-6,6'-dimethyl-2,2'-bipyridine) ligand.* The detailed synthetic procedure for eto ligand is given in Figure 8-4.

*Synthesis of Copper Complexes.* The  $[\text{Cu}(\text{dmby})_2]^{2+/1+}$ ,  $[\text{Cu}(\text{tmby})_2]^{2+/1+}$ , and  $[\text{Cu}(\text{dmp})_2]^{2+/1+}$  were produced as previously reported in Chapter 2.<sup>89,102</sup> Detailed complexation procedures for  $[\text{Cu}(\text{eto})_2][\text{TFSI}]$  and  $[\text{Cu}(\text{eto})_2][\text{TFSI}]_2$  complexes are given Figure 8-5. For complexation of  $[\text{Cu}(\text{eto})_2][\text{TFSI}]$  one equivalent of CuI was mixed with three equivalents of eto ligand in 20 ml ethanol under inert atmosphere at room temperature. After 2 hours, five equivalents of LiTFSI were added to the solution and stirring continued for additional 2 hours. The resulting Cu(I) complexes were filtrated and collected as red powder and washed with water and diethyl ether. In order to produce  $[\text{Cu}(\text{eto})_2][\text{TFSI}/\text{Cl}]$ , one equivalent of  $\text{CuCl}_2$  was mixed with 3 equivalents of eto ligand in 20 ml ethanol under nitrogen atmosphere at room temperature. After 2 hours, five equivalents of LiTFSI and 5 ml of deionized water were added to the mixture. The solution was stirred for an additional 2 hours and the complexes were collected by filtration as green powders and washed with water and diethyl ether.

*Electrochemical Characterization.* Three-electrode cyclic voltammetry measurements were performed using Ag/AgCl/saturated LiCl (ethanol) as reference electrode and glassy carbon working electrode under nitrogen with Autolab Pgstat-30 potentiostat.  $[\text{Cu}(\text{eto})_2]^{1+}$  was dissolved in acetonitrile with 0.1M LiTFSI. Redox potentials were referenced with respect to ferrocene.

UV/vis absorption data for  $[\text{Cu}(\text{eto})_2]^{1+}$  and  $[\text{Cu}(\text{eto})_2]^{2+}$  were obtained by a Hewlett-Packard 8453 diode array spectrometer. The corresponding extinction coefficients were calculated using the Lambert-Beer Law.

*Device fabrication.* The photoanodes were prepared as previously described in Chapter 2. 0.1mM of dye solutions (Dyename AB) were prepared in tert-butanol/acetonitrile (1:1 v:v) mixture. 0.4 mM chenodeoxycholic acid was used in the dye solutions as an additive in order to prevent aggregation. Working electrodes were dipped for 16 hours in these solutions. FTO glasses (TEC 6, Pilkington) were coated with PEDOT via electrodeposition<sup>100</sup> and used as counter electrodes<sup>102</sup>. 25 $\mu$ m Surlyn spacer (Dupont) was used for assembling the working electrode and counter electrodes and electrolyte encapsulation. The electrolytes were prepared with 0.2 M Cu(I) and 0.06 M Cu(II) complexes, 0.1M LiTFSI and 0.6 M TBP in acetonitrile. A detailed device preparation description can be found in the Chapter 2.<sup>102</sup>

*Solar Cell Characterization.* The methods for the current-voltage, IPCE, electron lifetime and charge extraction measurements are provided in Chapter 2.

*Photoinduced Absorption Spectroscopy.* The photo-induced absorption spectra of the various cells were recorded using excitation from a square-wave-modulated blue LED (Luxeon Star 1 W, Royal Blue, 460 nm) and white probe light from a tungsten-halogen lamp (20 W) was used as an illumination source. The transmitted light was focused into a monochromator (Acton Research Corp. SP-150) and detected using a UV-enhanced Si photodiode, connected to a lock-in amplifier (Stanford Research Systems model SR830). LED excitation intensity was approximately 80 Wm<sup>-2</sup> and the modulation intensity was 9.33 Hz.

*Transient Absorption Spectroscopy.* Nano-microsecond laser flash photolysis was applied to samples loaded with D45, D35 for D5 dyes. The samples for Transient Absorption Spectroscopy measurement were prepared by sandwiching the TiO<sub>2</sub> films and electrolytes in between two non-conductive glasses. 4  $\mu$ m thick transparent TiO<sub>2</sub> films were screen printed on a glass substrate. In order to have smaller amounts of dye loading on TiO<sub>2</sub>, 0.01mM of D5, D35 and D45 dyes solutions were used. The TiO<sub>2</sub> electrodes were dipped into the dye solution for 16 hours. The TiO<sub>2</sub> electrodes and glass substrates were assembled with 35  $\mu$ m Surlyn (Dupont) spacer, similar to DSC fabrication. The electrolyte was injected through predrilled holes in the glass substrate. The samples were excited by 7 ns (fwhm) pulsed laser light produced at a repetition rate of 20 Hz by a frequency-doubled Qswitched Nd:YAG laser ( $\lambda_{\text{ex}}=532\text{nm}$ ). The laser fluence on the sample was kept at a low level (50  $\mu\text{J cm}^{-2}$  per pulse) to ensure that, on average, less than one electron is injected per TiO<sub>2</sub> nanoparticle per pulse. The probe light consists of a halogen lamp passed through a monochromator, focused onto the sample and collected in a second monochromator at 1200 nm. The detector is a fast InGaAs diode (SM05PD5A, Thorlabs) connected to a digital oscilloscope. Typical data are averaged over 1000 laser shots.

*Electrochemical Impedance Spectroscopy.* Impedance measurements were carried out with a Bio-Logic SP300 potentiostat. A sinusoidal potential perturbation was applied within a frequency range of 7 MHz-0.1 Hz. The bias potential was manipulated between 0 V and V<sub>OC</sub>, with 50 mV increments. The impedance data was fitted with ZView software (Scribner Associates) according to the transmission line method.<sup>83</sup>

*Rest Potential Measurements.* The electrolyte solutions were investigated with home-made paper-plug electrodes. The rest potential of the redox couple (with TBP) was measured with a Pt-wire vs

an Ag/AgCl reference electrode. A 0.1 M tetrabutylammonium hexafluorophosphate in acetonitrile solution served as supporting electrolyte. The data was calibrated with respect to ferrocene.

*Density functional theory calculations.* The dye regeneration and charge recombination processes have been investigated also by carrying out state-of-the-art density functional theory (DFT) calculations with the reliable B3LYP hybrid density functional<sup>131</sup> and the well-known polarizable continuum model (PCM) to take into account the acetonitrile solvent medium.<sup>92</sup> To account for the dispersion interaction that is neglected in standard DFT we applied the DFT-D3 approach of Grimme with the BJ damping scheme.<sup>132</sup> Molecular frequencies have been computed within the harmonic approximation and were used to obtain zero-point vibrational frequencies and other thermodynamic parameters at standard conditions.<sup>133</sup> The vertical excitation energies and the excited-state properties of D5 and D45 dyes have been computed by applying the time-dependent DFT (TD-DFT) approach with the CAM-B3LYP density functional<sup>134</sup> that provides reliable predictions for push-pull organic dyes for DSSC applications.<sup>135</sup> In all these calculations we exploited the Stuttgart/Dresden Effective Core Potential and basis set (SDD) for copper<sup>136</sup> and the 6-31++G(d,p)<sup>137</sup> for all the other atoms of ligands and TBP. Further details on the methods for computing redox potentials and reorganization energies can be found in Chapter 8.<sup>102,138</sup>

# Chapter 6 Solid-State Dye-Sensitized Solar Cells with Copper (II/I) Hole Transport Materials

This chapter is adapted from the following articles with the permission of the journal:

Postprint version of the publication '11% Efficiency Solid-State Dye-Sensitized Solar Cells with Copper (II/I) Hole Transport Materials. Nature Communications, 2017, 8:15390 | DOI: 10.1038/ncomms15390' by Yiming Cao\*, Yasemin Saygili\*, Amita Ummadisingu, Joël Teuscher, Jingshan Luo, Norman Pellet, Fabrizio Giordano, Shaik Mohammed Zakeeruddin, Jacques-E. Moser, Marina Freitag, Anders Hagfeldt and Michael Grätzel. (\* shared first co-authorship)

My contribution: Devising the experiments with other co-authors, performing and analyzing the absorption and emission spectroscopy experiments, synthesizing the copper complexes and, preparation of counter electrodes.

In this chapter, we employed a blend of  $[\text{Cu}(\text{tmby})_2](\text{TFSI})_2$  and  $[\text{Cu}(\text{tmby})_2](\text{TFSI})$  (tmby = 4,4',6,6'-tetramethyl-2,2'-bipyridine; TFSI = bis(trifluoromethylsulfonyl)imide) as a HTM for solid state DSCs. We analyse the corresponding devices in terms of photovoltaic performance and stability. Conductivity and hole transport, dispersion through the electrodes and interfacial charge separation are also discussed in detail.

## 6.1 Introduction

In conventional solid-state dye-sensitized solar cells (ssDSCs), solid hole conductors are responsible for the dye regeneration and the transport of the charges toward the counter electrode. The counter electrode is usually made up of Au, Ag or carbon based materials whereas the hole transport materials (HTM) exist in a huge variety of inorganic and organic compounds. However, for ssDSCs the most common HTM is the p-doped small-molecule 2,2',7,7'-Tetrakis(N,N-di-p-methoxyphenylamine)-9,9'-spiro-bifluorene, (spiro-OMeTAD)<sup>139,140</sup>, which has a low intrinsic conductivity. Bach *et al.*<sup>141</sup> employed doped spiro-OMeTAD in ssDSCs in order to improve the fill factors and reduce the charge-transport resistances of the solar cells.<sup>141,142</sup>

Solid-state dye-sensitized solar cells, currently suffer from issues such as poor nanopore filling, low conductivity and crystallization of HTMs infiltrated in the mesoscopic  $\text{TiO}_2$  scaffolds, leading to low performance. The spin-coating of the hole transport material results in low pore filling through the mesoscopic semiconductor. Therefore, the spin coating technique is only applicable to thinner working electrodes (For 2.5 $\mu\text{m}$ -thick films, only 60-65% of the pores can be filled<sup>143</sup>). The amor-

phous copper complexes HTM that conduct holes by rapid hopping infiltrated in a mesoscopic TiO<sub>2</sub> scaffold are crucial for achieving high power conversion efficiencies.

Considering the rapid electron self-exchange rate in rigid copper complexes, [Cu(dmp)<sub>2</sub>]<sup>2+/+</sup> molecules were recently used as a HTM for solid-state DSCs (ssDSCs)<sup>89</sup>. The so called ‘zombie’ ssDSCs were made simply by evaporating volatile solvents from the [Cu(dmp)<sub>2</sub>]<sup>2+/+</sup> redox shuttle electrolyte in ambient air. Surprisingly, the ssDSC showed a high short-circuit photocurrent ( $J_{sc}$ ) of 13.8 mA/cm<sup>2</sup>, exceeding the  $J_{sc}$  of a liquid electrolyte based DSC (9.4 mA/cm<sup>2</sup>). The PCE of the ssDSC was 8.2% under standard AM1.5G conditions, a performance superior to those of ssDSC counterparts made using CuSCN (2%)<sup>144</sup>, CuI (4.5%)<sup>145</sup>, poly(3,4-ethylenedioxythiophene (PEDOT) (7.1%)<sup>146</sup>, 2,2',7,7'-tetrakis(N,N-di-p-methoxyphenylamine)-9,9'-spirobifluorene (spiro-MeOTAD) (7.7%)<sup>147</sup>, Cs<sub>2</sub>SnI<sub>6</sub> (7.8%)<sup>148</sup> or cobalt complexes<sup>149</sup> as HTMs.

In this chapter, we report a new record PCE of 11.0% (average 10.2%) for stable ssDSC under standard AM1.5G conditions, fabricated using a blend of [Cu(tmby)<sub>2</sub>](TFSI)<sub>2</sub> and [Cu(tmby)<sub>2</sub>](TFSI) (tmby or tmbp<sup>71</sup> = 4,4',6,6'-tetramethyl-2,2'-bipyridine; TFSI = bis(trifluoromethylsulfonyl)imide) as a HTM and Y123 as a sensitizer (Figure 6-1). Substituent methyl groups at the 6,6'-positions provide a rigid framework for the Cu(II) and Cu(I) complexes<sup>71</sup> and reduce the structural changes between them to allow for rapid self-exchange electron-transfer<sup>150</sup>. We investigate the infiltration of the copper complexes in a 6.5 μm-thick mesoscopic TiO<sub>2</sub> film, the conductivity of the HTM, the influence of crystallinity of the hole conductor and the photoinduced interfacial charge transfer dynamics of Y123 dye molecules in our solid Cu(II/I) HTM based ssDSCs.

## 6.2 Results and Discussion

### 6.2.1 Cu(II/I) complexes for ssDSCs

As we showed in Chapter 2, the energetic alignment of the redox potential of [Cu(tmby)<sub>2</sub>]<sup>+</sup> with that of Y123, allows efficient dye regeneration following the initial photo-induced interfacial charge separation step. We fabricate the DSCs by adsorbing Y123 as the sensitizer on the TiO<sub>2</sub> surface, [Cu(tmby)<sub>2</sub>]<sup>2+/+</sup> as the redox shuttle in a volatile electrolyte and electrodeposited PEDOT on FTO as the counter electrode. The electrolyte contains 0.06 M [Cu(tmby)<sub>2</sub>](TFSI)<sub>2</sub>, 0.2 M [Cu(tmby)<sub>2</sub>](TFSI), 0.1 M LiTFSI and 0.6 M 4-*tert*-butylpyridine (TBP) in acetonitrile. DSCs with this electrolyte show a PCE of 9.3±0.3% ( $V_{oc}$  = 1.07±0.03 V,  $J_{sc}$  = 13.17±0.46 mA/cm<sup>2</sup> and FF = 0.66 ± 0.02) under standard AM1.5G conditions (red symbols and error bars in Figure 6-1(b-e)), a value comparable to the previous result<sup>102</sup>.

Here, our investigation focuses on ssDSCs employing the blend of [Cu(tmby)<sub>2</sub>]<sup>2+</sup> and [Cu(tmby)<sub>2</sub>]<sup>+</sup> as solid-state HTM. We produced the devices by slowly evaporating the solvents of the electrolyte in ambient air through the unsealed hole on the counter electrode. Fortunately, the methyl group substituents at the 6,6'-positions can stabilize the copper complexes against oxidation and moisture<sup>151</sup>. The evaporation of acetonitrile (ACN) induces the solidification of [Cu(tmby)<sub>2</sub>]<sup>2+/+</sup>, facilitated by the low solubility of the copper complexes in this solvent. The residual solid copper complexes contain small amounts of entrapped ACN. We note that a slow evaporation of solvents is pivotal to yield efficient solar cells, because a too fast evaporation leads to a poor contact of the

solid-state crystalline HTM with the electrodes (Figure 6-2). Figure 6-1(b-e) show the evolution of the photovoltaic performance of the unsealed DSCs. Strikingly, the average PCE of unsealed DSCs increases to over 10% after five days in ambient air due to improvements in the  $J_{sc}$ ,  $V_{oc}$  and FF.

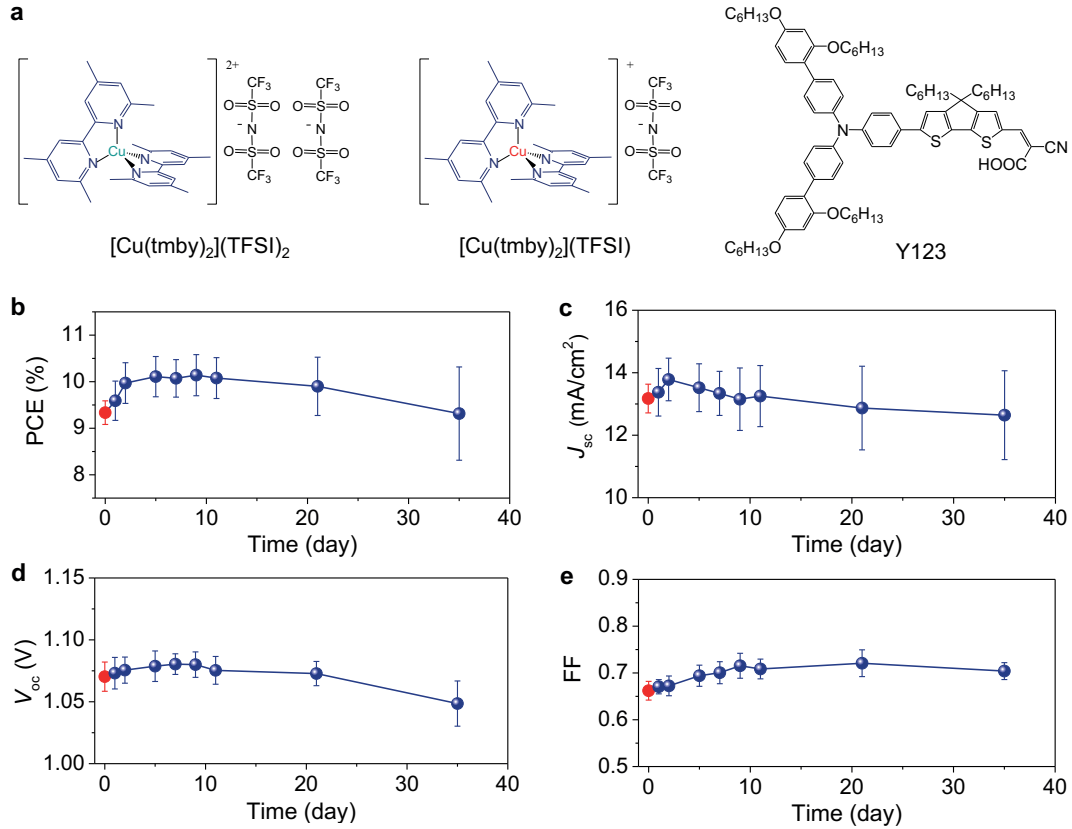


Figure 6-1 DSCs with the Cu(II/I) hole conductor and Y123 sensitizer. a) Schematic structures of the hole conductors based on  $[\text{Cu}(\text{tmby})_2](\text{TFSI})_2$  and  $[\text{Cu}(\text{tmby})_2](\text{TFSI})$ , and the dye molecule Y123. b) Evolution of the PCE of unsealed DSCs. c) Evolution of the  $J_{sc}$  of unsealed DSCs. d) Evolution of the  $V_{oc}$  of unsealed DSCs. e) Evolution of the FF of the unsealed DSCs. The unsealed DSCs were stored in ambient air in the dark. The photovoltaic parameters of solar cells were measured under standard AM1.5G conditions. The red symbols and error bars indicate the sealed DSCs based on the volatile electrolyte. The royal blue symbols and error bars indicate unsealed DSCs. The average (symbols) and standard deviation (error bars) were calculated from samples of between four and 22 solar cells.

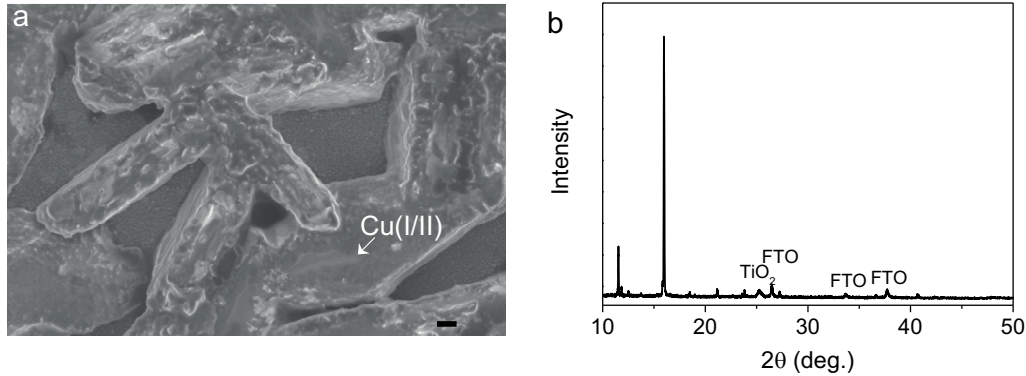


Figure 6-2 a) A SEM image of an electrode of FTO/TiO<sub>2</sub>/Y123 with a poor contact with Cu(II/I) HTM. Scar bar: 2 μm. The unsealed DSC with the liquid electrolyte was kept under a lower pressure to accelerate the evaporation of solvents in the electrolyte. After drying, the PEDOT counter electrode was removed to obtain the FTO/TiO<sub>2</sub>/Y123/HTM sample for SEM measurement. b) XRD of the sample prepared in (a), featuring reflection peaks from the HTM.

Figure 6-3a shows the cross-sectional SEM image of the mesoscopic sensitized TiO<sub>2</sub> scaffold infiltrated by the solid Cu(II/I) HTM after the five days drying period. The solid Cu(II/I) HTM layer covering the mesoscopic TiO<sub>2</sub> film has a thickness of about 2.0 μm. Apparently, rapid hole transport can occur across this layer resulting in a high FF for the device. The thickness of the overlayer can be controlled by tuning the thickness of the thermoplastic spacer between the electrodes. From energy dispersive X-ray spectroscopy analysis, we show that the solid Cu(II/I) HTM is homogeneously infiltrated in the 6.5 μm-thick sensitized-mesoporous TiO<sub>2</sub> scaffold (Figure 6-4). Unlike our HTM, using spiro-MeOTAD as HTM for ssDSCs<sup>141</sup> generally calls for thinner mesoscopic TiO<sub>2</sub> films (<3 μm) to ensure maximum filling of its mesopores<sup>143</sup>. However, the light harvesting efficiency suffers from reducing the thickness of the mesoscopic TiO<sub>2</sub> films.

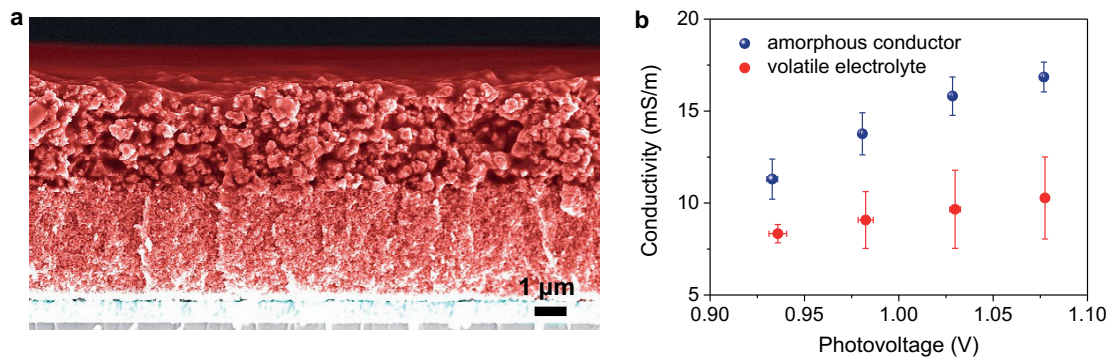


Figure 6-3 Solid Cu(II/I) hole conductor in ssDSC. a) Cross-sectional SEM of a ssDSC without the counter electrode. Moving from the bottom to the top, layers of FTO (cyan), 3.5 μm-thick transparent mesoscopic TiO<sub>2</sub> + 3.0 μm-thick light scattering TiO<sub>2</sub> (red), and 2.0 μm-thick solid Cu(I/II) hole conductor overlayer (red) are visible. b) Photovoltage-dependent conductivity in the solid hole conductor and the volatile electrolyte of solar cells as obtained from the EIS analysis. The solar cells were measured under illumination with an intensity of 1,000 W/m<sup>2</sup> from a white light-emitting diode. The average (symbols) and standard deviation (error bars) were calculated from solar cell numbers between four and six.



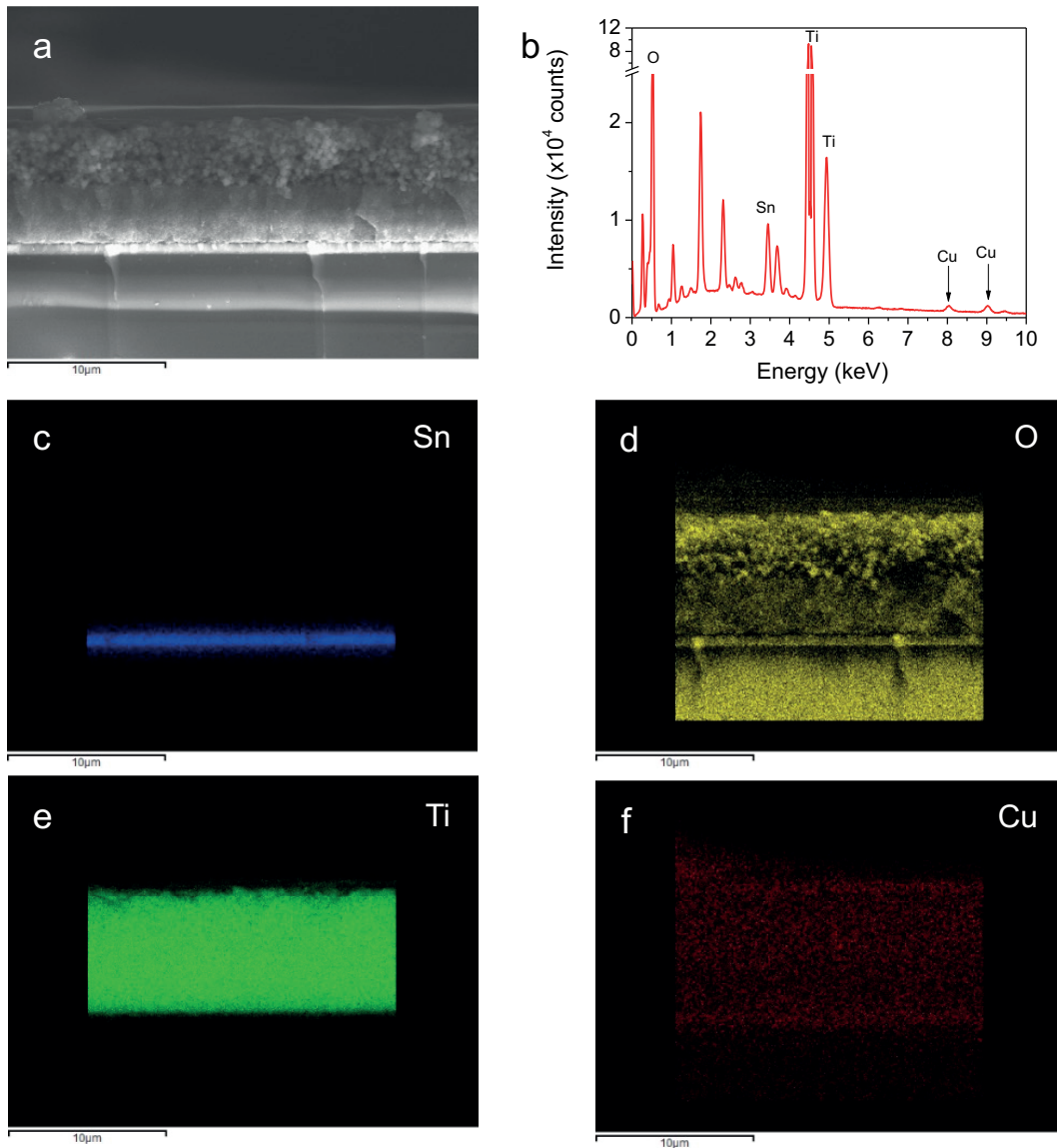


Figure 6-4 a) Cross sectional image of the Y123-sensitized TiO<sub>2</sub> film infiltrated with the Cu(II/I) HTM. b) Energy dispersive spectroscopy indicating various elements. Elementary mapping of c) Sn, d) O, e) Ti and f) Cu.

### 6.2.2 Rapid hole transport in solid Cu(II/I) HTM

We observe that the conductivity in solid Cu(II/I) HTM of the ssDSCs is higher than that in the volatile electrolyte of the DSCs under a photovoltage (Figure 6-3b) or a photocurrent (Figure 8-6), indicating a rapid hole hopping in solid Cu(II/I) HTM. Remarkably, the conductivity of our Cu(II/I) HTM is over ten times higher than that of spiro-MeOTAD in a mesoscopic TiO<sub>2</sub> film at a light intensity of 1,000 W/m<sup>2</sup> conditions<sup>152</sup>. It was shown that at high carrier densities in TiO<sub>2</sub> (>2×10<sup>17</sup> cm<sup>-3</sup>) the HTM conductivity can limit the charge transport in DSCs<sup>153</sup>. In our solar cells, the carrier density in TiO<sub>2</sub> is over 7×10<sup>17</sup> cm<sup>-3</sup> under full sun illumination determined by charge extraction

measurements<sup>109</sup>. Thereby, the increased conductivity of Cu(II/I) HTM results in an improved  $J_{sc}$  in ssDSCs.

When the solvents slowly evaporate from a volatile electrolyte containing the *tris*-(bipyridine) cobalt(III/II) complexes redox electrolyte, the PCE of the DSC drops remarkably from 9.8% to 0.1% (Figure 6-5). The reduction in  $J_{sc}$  from 14.2 to 0.2 mA/cm<sup>2</sup> is partly due to the extremely sluggish outer sphere electron self-exchange between the Co(III) and Co(II) complexes ( $0.645 \text{ M}^{-1} \text{ s}^{-1}$ )<sup>154</sup>. Although *tris*-(bipyridine) cobalt(III/II) volatile electrolytes have improved the PCE of DSCs from 6.7%<sup>49</sup> to over 13%<sup>51,52</sup>, the encapsulation of such highly efficient DSCs to prevent solvent leakage is a challenge. Recently, ssDSCs using a blend of [Co(bpyPY4)](OTf)<sub>3</sub> and [Co(bpyPY4)](OTf)<sub>2</sub> (bpyPY4 = hexadentate ligand 6,6'-bis(1,1-di(pyridin-2-yl)ethyl)-2,2'-bipyridine; OTf = trifluoromethanesulfonate) as a HTM displayed a PCE of 5.7% under standard AM1.5G<sup>149</sup>. However, this ssDSC had a lower  $J_{sc}$  (12.12 mA/cm<sup>2</sup>) and PCE than the liquid counterpart (17.2 mA/cm<sup>2</sup> and 9.6%), which is not the case when our copper complexes with a small internal reorganization energy<sup>102,150</sup> are used.

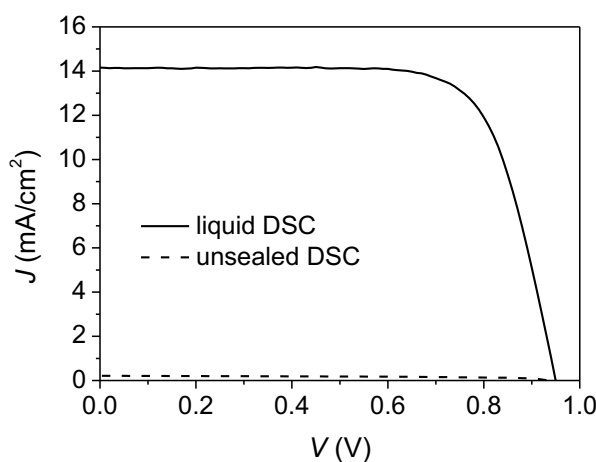


Figure 6-5 J-V curves of a DSC with a tris-(bipyridine) cobalt(II/III) redox mediator electrolyte under AM1.5G conditions. The solid curve is J-V of the DSC with the liquid electrolyte (PCE = 9.8%,  $J_{sc}$  = 14.16 mA/cm<sup>2</sup>,  $V_{oc}$  = 950 mV and FF = 0.732). The dash curve is J-V of the unsealed DSC by releasing solvents in the electrolyte for 150 min through an unsealed hole on a counter electrode (PCE = 0.1%,  $J_{sc}$  = 0.21 mA/cm<sup>2</sup>,  $V_{oc}$  = 933 mV and FF = 0.552). The solar cell is composed of Y123-sensitized TiO<sub>2</sub> film (3.5  $\mu\text{m}$  + 3  $\mu\text{m}$ ), a graphene based counter electrode<sup>3</sup>, and a liquid electrolyte. The composition of electrolyte is 0.25 M [Co(BPY)<sub>3</sub>](BCN<sub>4</sub>)<sub>2</sub> (BPY = bipyridyl), 0.06 M [Co(BPY)<sub>3</sub>](BCN<sub>4</sub>)<sub>3</sub>, 0.1 M LiTFSI and 0.6 M TBP in acetonitrile.

### 6.2.3 Crystallinity of solid Cu(II/I) HTM

Our ssDSCs stored in ambient air for over 20 days have large variations in  $J_{sc}$  as shown in Figure 6-1d, because a few solar cells display a sublinear dependence of the  $J_{sc}$  on light intensity ( $P$ ) according to the power law<sup>155</sup>,  $J_{sc} \propto P^\alpha$ , where  $\alpha$  is the slope. Such a ssDSC has an  $\alpha$  of 0.81 as shown in Figure 6-6a, while the most efficient one has an  $\alpha$  of 0.99. To probe the molecular origin of this observation, we performed XRD measurements on the samples of sensitized TiO<sub>2</sub> films combined with the Cu(II/I) HTM in both kinds of ssDSCs. Apart from reflections corresponding to FTO and TiO<sub>2</sub> in Figure 6-6b, we see reflections (at  $2\theta$  values of 16.0 and 16.6 degree) in the sample for a

ssDSC with a sublinear dependence of the  $J_{sc}$ , pointing to the presence of a crystalline phase within the Cu(II/I) HTM. The absence of these reflections in the sample for a ssDSC with a linear dependence of the  $J_{sc}$  indicates that the HTM may be amorphous in nature in this case. The holes in the crystalline HTM are likely to get trapped at crystal grain boundaries, leading to reduced hole mobility and a build-up space charge layer in the solar cells as a consequence of the difference in electron and hole mobility<sup>156</sup>.

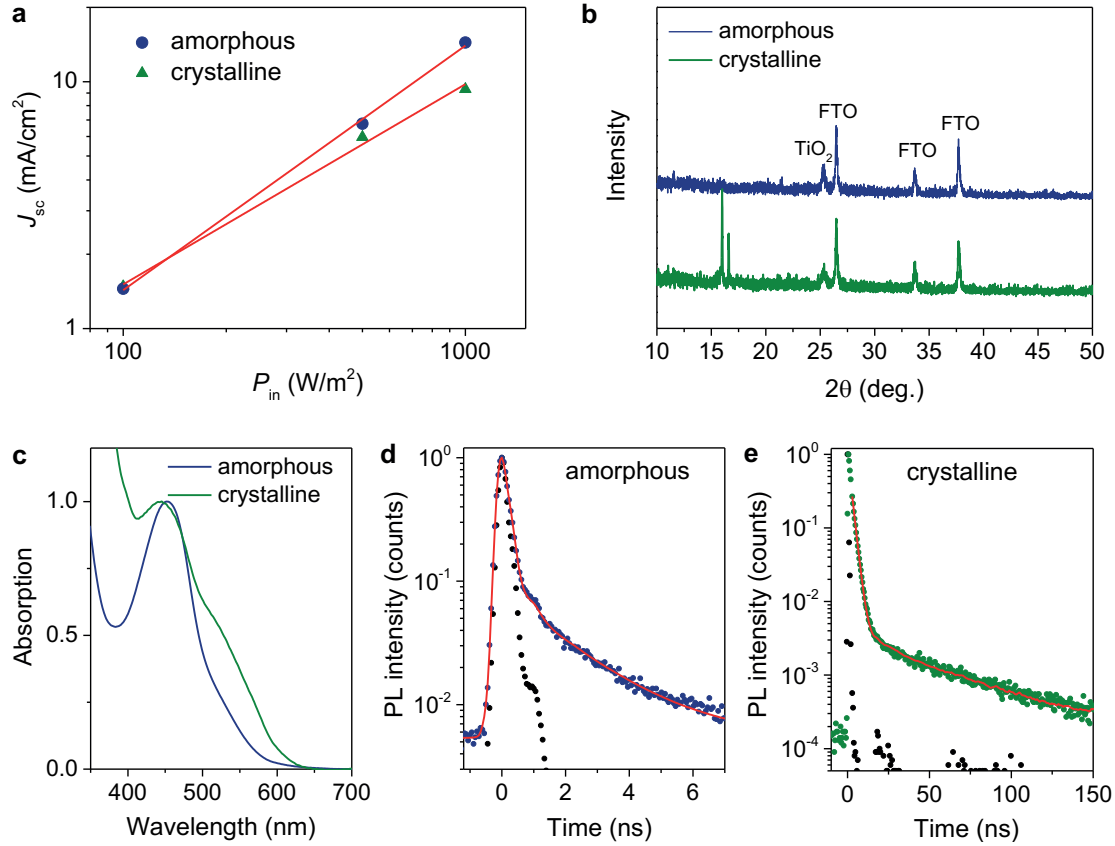


Figure 6-6 Comparison of amorphous and crystalline Cu(II/I) hole conductor. a) Incident light intensity ( $P_{in}$ )-dependent  $J_{sc}$  of ssDSCs with amorphous and crystalline hole conductors. The red lines are linear fits of the data. b) XRD of amorphous and crystalline Cu(II/I) hole conductors in conjunction with Y123-sensitized TiO<sub>2</sub> film on FTO glass substrate. c) Absorption spectra for the amorphous and crystalline Cu(II/I) hole conductors. d) Photoluminescence decay dynamics of amorphous Cu(II/I) hole conductor. e) Photoluminescence decay dynamics of crystalline Cu(II/I) hole conductor. The traces were collected at 670 nm with photoluminescence maximum following nanosecond laser pulsed excitation at 408 nm. The black dot symbols are instrument response function. The red lines are bi-exponential fits of the data.

Compared to the amorphous Cu(II/I) HTM, the crystalline one displays a slightly blue shifted peak in the absorption spectrum and enhanced absorption in the metal-to-ligand charge transfer (MLCT) transition region, as shown in Figure 6-6c. This result highlights the magnitude of structural difference between the ground and excited states. We infer that copper complexes in the crystalline HTM adopt a flattened distorted tetrahedral structure by reducing the dihedral angle between the

ligands<sup>157–159</sup>, while in the amorphous state they are less flattened. A similar flattened distorted structure that intensifies the absorption in the weak broad MLCT region was also observed in crystals of  $[\text{Cu}(\text{dpphen})_2]^+$  (dpphen = 2,9-diphenyl-1,10-phenanthroline)<sup>160</sup>.

We note that the aggregation of copper complexes by evaporation of solvents in the electrolyte enhances the photoluminescence of the HTM. The crystalline HTM has a stronger emission than the amorphous one. We posit that the photoluminescence of the HTM originates from the Cu(I), because the solid Cu(II) film shows a negligible emission at 670 nm (Figure 6-7). We performed nanosecond photoluminescence decay dynamics measurements of the amorphous and crystalline HTMs. Convolved with the instrument response function (IRF), the traces of the amorphous hole conductor in Figure 6-6d are best fitted by a bi-exponential decay function, giving photoluminescence decay time components (and pre-exponential factors) of 94 ps (0.78) and 2.0 ns (0.22), while the traces of the crystalline sample in Figure 6-6e are fitted by the bi-exponential decay function, giving 2.1 ns (0.96) and 37.9 ns (0.04). The longer photoluminescence decay times in the crystalline HTM support a flattened distorted structure of the copper complexes<sup>159–161</sup>. The crystalline phase also has influences on the molecular photochemistry<sup>162</sup>, for instance, copper complexes in the crystalline state are quite restricted by the closely packed molecules, resulting in longer photoluminescence decay times.

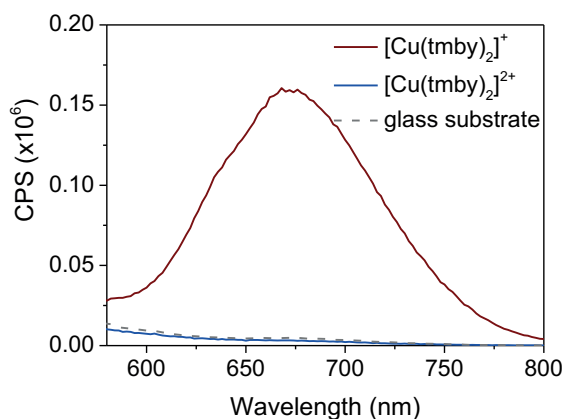


Figure 6-7 Steady-state photoluminescence spectra of  $[\text{Cu}(\text{tmby})_2]\text{TFSI}$  and  $[\text{Cu}(\text{tmby})_2](\text{TFSI})_2$  drop-casted on glass substrates from acetonitrile solution containing 0.1 M LiTFSI and 0.6 M TBP.

#### 6.2.4 Interfacial charge transport dynamics in Cu(II/I) based ssDSC

We performed picosecond time resolved transient absorption spectroscopy to investigate the electron injection dynamics of Y123. We selected 650 nm as a suitable wavelength to probe for electron injection, because we observed a transient absorbance change of the photo-excited Y123 species on an  $\text{Al}_2\text{O}_3$  film, while the absorbance of the photo-oxidized Y123 on a  $\text{TiO}_2$  film does not differ from the dye ground state absorbance at this wavelength (Figure 8-7). Moreover, exclusive monitoring of the excited dye eliminates charge accumulation effects that could arise from the 6 ms lifetime of oxidized Y123, when probed at 1kHz. However, charge accumulation certainly occurs and the experiment is likely performed at higher charge density than suggested by the fluence only.

Figure 6-8a shows two distinct dynamic events at 650 nm for the sample of  $\text{Al}_2\text{O}_3/\text{Y123}/\text{inert}$  electrolyte: an initial fast rise with a 1 ps time constant ( $\tau$ ) followed by a monoexponential decay ( $\tau$ =

337 ps). The initial fast component is likely to arise from an excited state species formed by intramolecular charge separation process forming an intramolecular radical ion pair following dye excitation<sup>163</sup>. The slow component is attributed to the lifetime of this excited species. Upon replacing Al<sub>2</sub>O<sub>3</sub> film by TiO<sub>2</sub>, the sample of TiO<sub>2</sub>/Y123/inert electrolyte shows an initial fast rise followed by a monoexponential decay with a  $\tau$  of 12 ps, attributed to the electron injection from the photo-excited Y123. Therefore, electron injection is in competition with the intramolecular process and indicating that it occurs from these different excited species. Because the signal recovers to zero at 650 nm, electron injection is unambiguously characterized and no event can occur at a longer time-scale. Upon combining TiO<sub>2</sub>/Y123 with the solid Cu(I/II) HTM, we observe a variation in the electron injection lifetime with a  $\tau$  of 25 ps, which is longer than that of TiO<sub>2</sub>/Y123 without the HTM (12 ps). This result is probably due to the effects of the environment, because a longer lifetime constant of 750 ps of photo-excited Y123 on Al<sub>2</sub>O<sub>3</sub> with the HTM is also observed. Overall we extract electron injection yields of 97% from these measurements. Our result differs from the previous time constant of 2 ps for the electron injection from Y123 in samples composed of large TiO<sub>2</sub> nanoparticles and cobalt complexes based electrolyte, measured using the diffuse reflectance spectroscopy method<sup>164</sup>.

The electron donating dynamics of Cu(I) to the photo-oxidized Y123 was resolved by nanosecond transient absorption spectroscopy. The photo-oxidized Y123 species on the TiO<sub>2</sub> surface have a strong absorption at 715 nm<sup>102</sup>, at which wavelength the transient absorption traces were collected as shown in Figure 6-8b. In the sample of TiO<sub>2</sub>/Y123/inert electrolyte, photo-oxidized Y123 species recombine with injected electrons in the TiO<sub>2</sub> film. The time constant for this process is determined to be 6.0 ms. In the sample of TiO<sub>2</sub>/Y123/solid Cu(II/I) HTM, the photo-oxidized Y123 species either recombine with injected electrons from TiO<sub>2</sub> or are regenerated by the Cu(I) in the HTM. The time constant for the decay traces of this sample is 3.2  $\mu$ s. This results indicates that the electron donation from Cu(I) to photo-oxidized Y123 outcompetes charge recombination by a factor of 938 ascertaining near quantitative regeneration of the sensitizer.

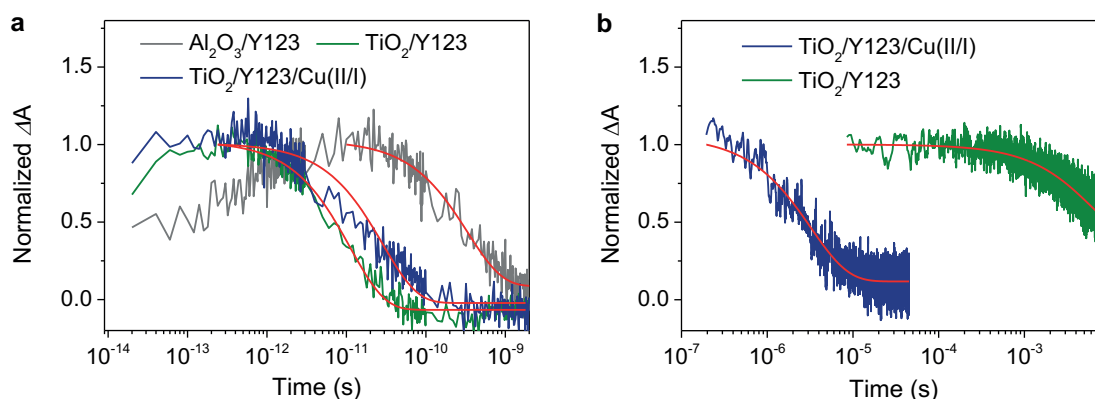


Figure 6-8 Time resolved laser spectroscopy of interfacial electron transfer involving Y123 dye molecules. a) Transient absorption traces were probed at 650 nm following femtosecond laser pulsed excitation at 550 nm. b) Transient absorption traces were probed at 715 nm following nanosecond laser pulsed excitation at 532 nm. Samples: Al<sub>2</sub>O<sub>3</sub>/Y123/inert electrolyte (gray); TiO<sub>2</sub>/Y123/inert electrolyte (olive); TiO<sub>2</sub>/Y123/Cu(II/I) HTM (royal blue). The inert electrolyte contains 0.1 M LiTFSI and 0.6 M TBP in acetonitrile. The red lines are mono exponential fits of the data.

### 6.2.5 Cu(II/I) HTM for record efficiency ssDSC

Figure 6-9a shows the histogram of PCEs for ssDSCs using the blend of  $[\text{Cu}(\text{tmby})_2]^{2+/+}$  and  $[\text{Cu}(\text{tmby})_2]^+$  as a HTM and employing the optimal mesoscopic  $\text{TiO}_2$  scaffold ( $3.5 + 3 \mu\text{m}$ -thickness, Figure 8-8) as a working electrode under standard AM1.5G conditions. We see that our ssDSCs are superior to the state-of-the-art counterparts with various HTMs<sup>144–149</sup>. The histograms of  $J_{\text{sc}}$ ,  $V_{\text{oc}}$  and FF are presented in Figure 8-8. Compared to these HTMs, the  $[\text{Cu}(\text{tmby})_2]^{2+/+}$  for ssDSCs demonstrates an average PCE of 10.2%, with average  $J_{\text{sc}}$ ,  $V_{\text{oc}}$  and FF of  $13.70 \text{ mA/cm}^2$ , 1.07 V and 0.70, respectively. The average  $V_{\text{oc}}$  of ssDSCs is the same as that of liquid DSCs. This result indicates that the HOMO of Cu(II/I) HTM is comparable to the redox potential of the Cu(II/I) measured by cyclic voltammetry<sup>102</sup>.

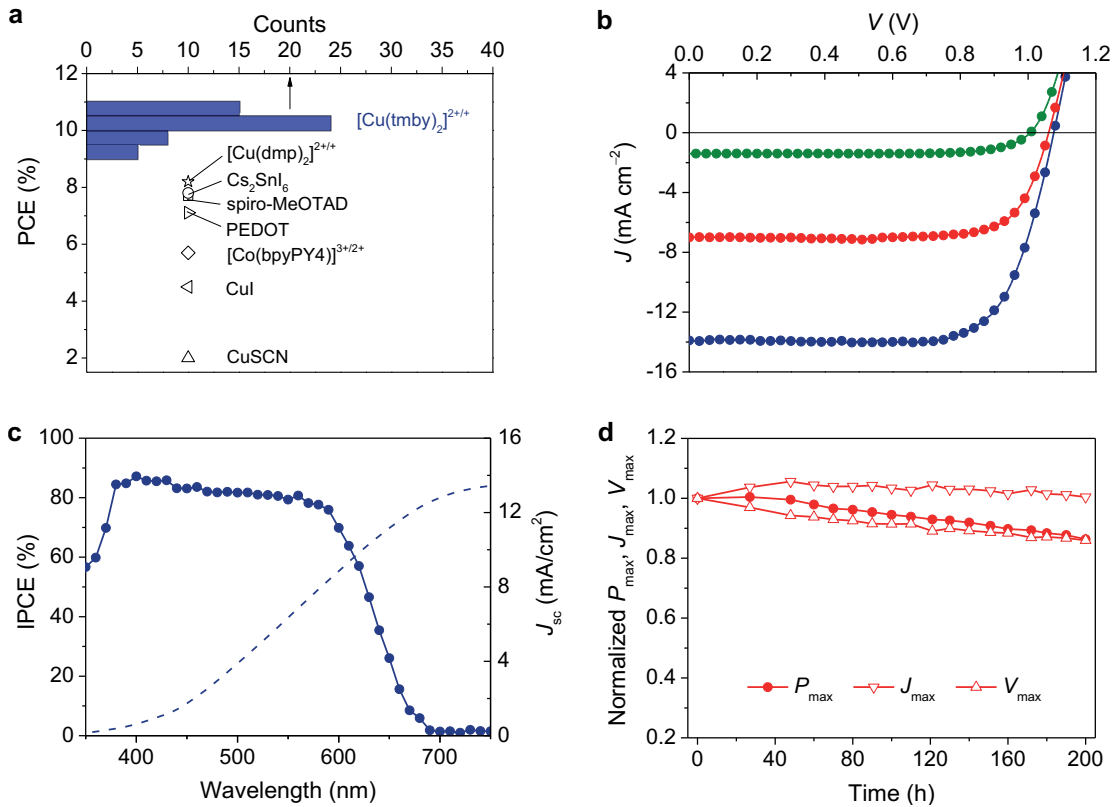


Figure 6-9 Performance of ssDSC with Cu(II/I) HTM. a) Histogram of PCE of our ssDSCs based on  $[\text{Cu}(\text{tmby})_2]^{2+/+}$  as a hole conductor, compared to the reported PCEs of efficient ssDSCs using CuSCN, CuI,  $[\text{Co}(\text{bpyPY}_4)]^{3+/2+}$ , PEDOT, spiro-MeOTAD,  $\text{Cs}_2\text{SnI}_6$  or  $[\text{Cu}(\text{dmp})_2]^{2+/+}$  as hole conductors. b) The J-V curves of a champion ssDSCs under standard AM1.5G with irradiation intensities of 1,000 (royal blue), 500 (red) and  $100 \text{ W/m}^2$  (olive). c) IPCE spectrum and  $J_{\text{sc}}$  calculated from the overlap integral of the IPCE with the standard AM1.5G emission spectrum (ASTM G173-03). d) Evolution of normalized  $P_{\text{max}}$ ,  $J_{\text{max}}$  and  $V_{\text{max}}$  of our ssDSC operating at output maximum power under irradiation of  $500 \text{ W/m}^2$ .

As shown in Figure 6-9b, our best cell reaches a record 11.0% for ssDSC under standard AM1.5G irradiation intensity of  $1,000 \text{ W/m}^2$ , with  $J_{\text{sc}} = 13.87 \text{ mA/cm}^2$ ,  $V_{\text{oc}} = 1.08 \text{ V}$  and  $\text{FF} = 0.733$ . Under  $500 \text{ W/m}^2$  intensity, the PCE achieves 11.3% with  $J_{\text{sc}} = 7.00 \text{ mA/cm}^2$ ,  $V_{\text{oc}} = 1.06 \text{ V}$  and  $\text{FF} = 0.76$  and the PCE attains 10.5% under  $100 \text{ W/m}^2$  intensity with  $J_{\text{sc}} = 1.40 \text{ mA/cm}^2$ ,  $V_{\text{oc}} = 1.01 \text{ V}$  and  $\text{FF} = 0.746$ . Our ssDSC is hysteresis free regardless of the scan rate, which ranges from 20 to 500 mV/s, as shown in Figure 8-9. Figure 6-9c presents the incident monochromatic photon-to-electron conversion efficiency (IPCE). The maxima of the IPCE is below 90% mainly due to the quenching of photo-excited dye molecules by copper complexes<sup>81</sup> in the HTM, charge recombination and optical loss. The  $J_{\text{sc}}$  calculated from the overlap integral of the IPCE with the standard AM1.5G emission spectrum (ASTM G173-03) is  $13.44 \text{ mA/cm}^2$ , a value comparable to the  $J_{\text{sc}}$  obtained under simulated AM1.5G conditions. We evaluate the photo-stability of a ssDSC operating at maximum output power for 200 hours under an irradiation intensity of  $500 \text{ W/m}^2$ , as shown in Figure 6-9d. Remarkably, the  $P_{\text{max}}$  retains over 85% of its initial value after 200 h due to slight improvement in  $J_{\text{max}}$  and a small loss in  $V_{\text{max}}$ .

### 6.3 Conclusion

In summary, we demonstrate a 11% efficiency stable ssDSC under AM1.5G standard by using a solid HTM composed of a blend of  $[\text{Cu}(\text{tmby})_2](\text{TFSI})_2$  and  $[\text{Cu}(\text{tmby})_2](\text{TFSI})$ . When this work was published, this PCE was the highest efficiency in the ssDSCs with reported HTMs till now and is achieved by simultaneously high  $J_{\text{sc}}$  of  $13.87 \text{ mA/cm}^2$  and high  $V_{\text{oc}}$  of  $1.08 \text{ V}$ . The high performance are mainly ascribed to the rapid hole hopping in amorphous copper complexes HTM infiltrated in a thick mesoscopic  $\text{TiO}_2$  scaffold ( $6.5 \mu\text{m}$ ) and favorable energetic alignment and efficient charge separation at the  $\text{TiO}_2/\text{Y123}/\text{HTM}$  interfaces. Our work will foster future developments of low-cost photovoltaics<sup>165</sup> based on solid-state metal complexes HTMs.

### 6.4 Methods

*Materials.* Acetonitrile (ABCR), tert-butanol (Sigma-Aldrich), LiTFSI (TCI) and TBP (TCI) were purchased from commercial company and used as received, unless stated otherwise. The  $[\text{Cu}(\text{tmby})_2](\text{TFSI})$  and  $[\text{Cu}(\text{tmby})_2](\text{TFSI})_2$  powders were synthesised as previously described in Chapter 2<sup>15</sup>. The  $[\text{Cu}(\text{tmby})_2](\text{TFSI})_2$  powders contain chloride anion impurity at ppm.

*Fabrication of solar cells.* The fabrication of DSCs followed the procedure in Chapter 2<sup>25</sup>. Briefly, the  $6.5 \mu\text{m}$ -thick mesoporous  $\text{TiO}_2$  films ( $3.5 \mu\text{m}$  transparent layer +  $3.0 \mu\text{m}$  light scattering layer) were immersed in  $100 \mu\text{M}$  Y123 solution in acetonitril/tert-butanol ( $v/v$ , 1/1) for 16 h to graft the dye molecules onto the  $\text{TiO}_2$  surface. The counter electrodes consisted of PEDOT films electrochemically deposited on FTO glass<sup>15</sup>. The dye-coated  $\text{TiO}_2$  working electrode and the counter electrode were assembled by using thermoplastic spacer (Surlyn, DuPont) heating at  $120^\circ\text{C}$ . Electrolytes were injected into the space between the electrodes through predrilled hole on the counter electrode. The hole was sealed by using the thermoplastic sheet and a glass cover. The ssDSCs were obtained by removing the sealing on the hole to evaporate solvents in air.

*Characterization of solar cells.* Solar cells were used without antireflection films and masked to an aperture area of  $0.158 \text{ cm}^2$  for  $J$ - $V$  and IPCE characterizations. The  $J$ - $V$  measurement details are provided in Chapter 2. IPCE spectra were measured with a lock-in amplifier (Stanford Research System SR830 DSP) under chopped monochromatic light (2 Hz) generated by white light source from a 300 W xenon lamp passing through a Gemini-180 double monochromator (Jobin Yvon Ltd). The solar cell is illuminated under a constant white light bias with intensity of  $50 \text{ W/m}^2$  supplied by an array of white light emitting diodes.

EIS measurements were performed with a BioLogic SP300 potentiostat coupled with LED light array to provide white light irradiation intensity of  $1,000 \text{ W/m}^2$  onto DSCs. To obtain the spectra, the solar cell was biased with potentials and a modulation of 15 mV in the frequency range (1 MHz to 0.1 Hz). Z-view software (v2.8b, Scribner Associates Inc.) was used to analyze the impedance spectroscopy. The equivalent circuit models for EIS analysis and the calculation of conductivity are presented in the Supplementary Information.

*SEM characterization.* Scanning electron microscopy and energy dispersive X-ray spectroscopy (EDX) were carried out on a MERLIN high resolution scanning electron microscope (Zeiss, Germany). The sample for SEM measurement was obtained by removing the PEDOT counter electrode of a ssDSC.

*XRD.* X-ray powder diffractions were recorded on an X'Pert MPD PRO (Panalytical) equipped with a ceramic tube (Cu anode,  $\lambda = 1.54060 \text{ \AA}$ ), a secondary graphite (002) monochromator and a RTMS X'Celerator (Panalytical) in an angle range of  $2\theta = 5$  to  $60^\circ$ . Samples for XRD measurements were obtained by removing the PEDOT counter electrode of ssDSCs.

*UV/Vis spectroscopy, steady-state photoluminescence spectroscopy, and TCSPC.* UV/Vis absorption data was collected by a Perkin-Elmer Lambda 950 spectrophotometer and the extinction coefficients were calculated using the Beer-Lambert law. Steady-state photoluminescence spectra were recorded by exciting the samples at 450 nm with a 450-W Xenon CW lamp. The signal was recorded with a spectrofluorometer (Fluorolog; Horiba Jobin Yvon Technology FL1065). The time-correlated single-photon counting (TCSPC) measurements were performed by exciting samples with a laser source at 408 nm (Horiba NanoLED 402-LH; pulse width  $<200 \text{ ps}$ , 11 pJ per pulse, approximately  $1 \text{ mm}^2$  in spot size) to generate a train of excitation pulses at 10 MHz. Decay curves were analyzed with the software DAS-6 and DataStation provided by Horiba Jobin Yvon.

*Pump-probe spectroscopy.* Ultrafast transient absorbance spectra were acquired using pump-probe spectroscopy. A chirped pulse amplified Ti:Sapphire laser (CPA-2001, Clark-MXR, 778 nm fundamental central wavelength, 120 fs pulse duration, 1 kHz repetition rate) was pumping a two-stage non-collinear optical parametric amplifier (NOPA) to obtain the pump beam at  $\lambda_{\text{ex}} = 550 \text{ nm}$ . The pump fluence was of  $25 \mu\text{J/cm}^2$  at the sample. The probe beam was generated in a  $\text{CaF}_2$  crystal, yielding a white light continuum across the visible splitted in a signal and a reference beams that were directed to spectrographs (Princeton Instruments, Spectra Pro 2150i) and detected pulse-to-pulse with  $512 \times 58$  pixels back-thinned CCD detectors (Hamamatsu S07030-0906). Motorized translation stage on the pump path controlled the acquisition of transient traces. The pump beam was chopped at half of the laser frequency and we typically averaged 3000 laser shots to obtain satisfactory signal-to-noise ratio.



Samples for transient absorption spectroscopy were excited at 532 nm using an Ekspla NT-342 Q-switched Nd:YAG laser (pulse width: 4–5 ns; repetition rate: 20 Hz) and probed at 715 nm using a monochromator coupled with the probe light source of halogen lamp. The sample was positioned at approximately 45° angle with respect to the incoming laser pulse. The signal was detected using the photomultiplier tube R9110 from Hamamatsu and recorded using the oscilloscope DPO 7254 from Tektronix. The output power density of the laser was attenuated using gray optical density filters to 50  $\mu\text{J}/\text{cm}^2$ . An acquisition was averaged over 3000 laser shots.



# Chapter 7 Performance of Dye-Sensitized Solar Cells under Ambient Lighting

This chapter is adapted from the following article with the permission of the journal:

Postprint version of the publication 'Dye-sensitized Solar Cells for Efficient Power Generation under Ambient Lighting', Nature Photonics, 2017, 11, DOI: 10.1038/NPHOTON.2017.60' by Marina Freitag, Joël Teuscher, Yasemin Saygili, Xiaoyu Zhang, Fabrizio Giordano, Paul Liska, Jianli Hua, Shaik M. Zakeeruddin, Jacques-E. Moser, Michael Grätzel and Anders Hagfeldt.

My contribution: Taking part in fabrication and characterization of the solar cells.

In the previous chapters, we showed that with the introduction of new copper based redox shuttles, we surpassed the 10.0% efficiency mark at 100 mW/cm<sup>2</sup> AM 1.5G light. As we know, solar cells that operate efficiently under indoor lighting are of great practical interest as they can serve as electric power sources for portable electronics and devices for wireless sensor networks (WSN) or the IoT (Internet of Things). Here, we demonstrate a dye-sensitized solar cell (DSC), which achieves very high power conversion efficiencies (PCE) under ambient light conditions with power output of 15.6 mW/cm<sup>2</sup> and 88.5 mW/cm<sup>2</sup>, at 200 lux and 1000 lux, respectively, under illumination from a model Osram 930 warm-white fluorescent light tube, which corresponds to a PCE value of 28.9%.

## 7.1 Introduction

Currently, the market for solar cells can be divided into large module installations for terrestrial power generation and smaller modules to power portable electronics.<sup>166</sup> DSCs can be used in both areas, but they have considerable promise within the second category. They show outstanding performance under indoor, artificial light source conditions in comparison to other solar cell technologies.<sup>167</sup> The unique properties of DSCs make them the best alternative to wired and battery energy sources, as DSCs are capable of maintaining high photovoltage even in diffuse light conditions.<sup>6,168–172</sup>

DSCs are known to perform well in ambient light, however, very few studies have been published regarding the performance under such conditions. In addition, the few existing reports all use iodide-based electrolytes in combination with a ruthenium-based inorganic dye.<sup>173–175</sup> However in 2005, Fukuzumi *et al.* reported that copper complexes worked well as redox mediators at reduced



## 7.2 Results and Discussion

### 7.2.1 Photovoltaic performance of co-sensitized DSCs with $[\text{Cu}(\text{tmby})_2]^{+2/+1}$ as redox shuttle

The “blend” of organic chromophores brings out the outstanding attributes of both dyes. The XY1 sensitizer, a D-A- $\pi$ -A dye, has a very high molar extinction coefficient and spectral response extending beyond 700 nm while D35 is an organic D- $\pi$ -A dye endowed with a judiciously designed arylamine donor structure, suppressing electron recapture by the Cu(II) complex from the TiO<sub>2</sub> conduction band generating a high open circuit potential.<sup>49,178</sup> The UV-Vis spectra of the D35 and XY1 dyes are given in Figure 7-2.

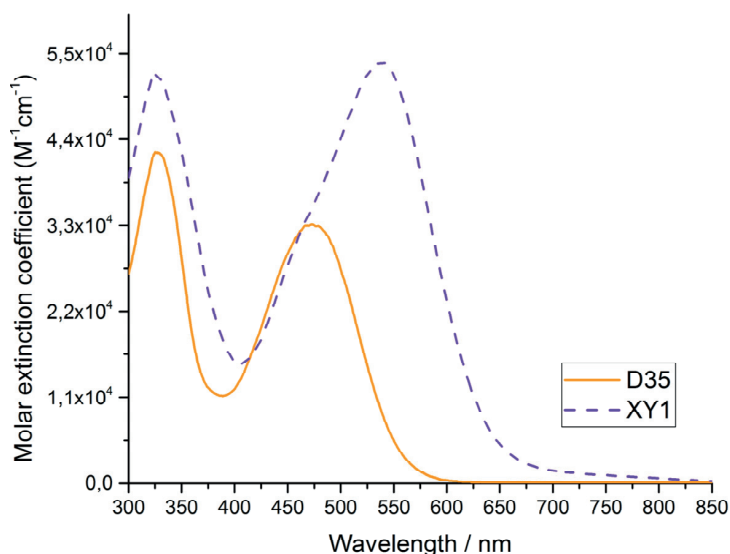


Figure 7-2 UV-Vis spectra of the dyes D35 (orange solid line) and XY1 (purple dashed line).

Table 7-1 and Figure 7-3 give an overview of the photocurrent density-voltage characteristics of the DSCs co-sensitization series between D35 and XY1. For standard full AM 1.5 sunlight we obtain the best conversion efficiency of 11.3 % at a D35:XY1 ratio of 4:1 in the staining solution, Figure 7-3 (b, c). We measured a  $J_{sc}$  of 16.2 mA/cm<sup>2</sup> and a FF of 68%.  $V_{oc}$  values over 1.0 V were reached for the whole series, the maximum being 1.1V for pure D35. At 10x lower solar light intensity of 12 mWcm<sup>-2</sup>, the maximum PCE increased to 13% for the same staining solution, which is an exceptionally high value for a solar cell system under these low light conditions (Figure 7-3 (a, c)). It is evident that both dyes complement each other in terms of PV performance, XY1 contributing to the large photocurrents due to its high molar extinction coefficient, and D35 supporting the high  $V_{oc}$  values being endowed with groups that block sterically the access of the Cu(II)(tmby)<sub>2</sub> complex to the TiO<sub>2</sub> surface. This reduces the ability of the Cu(II) complex to recapture the photo-injected electrons from the TiO<sub>2</sub> conduction band. Figure 7-3d shows the photocurrent dynamics as a function of various light intensities for the best performing DSC. The  $J_{sc}$  depends linearly on the light intensity and hence is not limited by mass transport up to full sun illumination.

Table 7-1 J-V characteristics of DSCs using co-sensitized photoanodes with D35 and XY1 dye at 12 and 100mWcm<sup>-2</sup> simulated solar light intensity, letters in the first column refer to labels of sensitizing solutions, which contain: a) 0.1mM D35, b) 0.1mM D35 and 0.01mM XY1 c) 0.08mM D35 and 0.02mM XY1, d) 0.05 mM D35 and 0.05 mM XY1, e) 0.02 mM D35 and 0.08 mM XY1, f) 0.01mM D35 and 0.1 mM XY1(1:10), g) 0.1 mM XY1.

#	Ratio of D35:XY1 (sensitizing solution)	Incident light intensity $I_0$ (mWcm <sup>-2</sup> )	$J_{sc}$ (mA cm <sup>-2</sup> )	Voc (V)	FF (%)	n (%)
<b>a</b>	01:00	12	1,63	1,01	74	9,90
<b>b</b>	10:01		1,73	0,96	78	10,6
<b>c</b>	<b>04:01</b>		<b>2,17</b>	<b>0,96</b>	<b>78</b>	<b>13,2</b>
<b>d</b>	01:01		2,07	0,96	79	12,6
<b>e</b>	01:04		2,03	0,97	78	12,3
<b>f</b>	01:10		2,00	0,95	78	11,9
<b>g</b>	00:01		1,94	0,96	78	11,8
<b>a</b>	01:00	100	12,48	1,10	72	9,90
<b>b</b>	10:01		13,26	1,05	71	9,90
<b>c</b>	<b>04:01</b>		<b>16,19</b>	<b>1,03</b>	<b>68</b>	<b>11,3</b>
<b>d</b>	01:01		15,54	1,03	68	10,8
<b>e</b>	01:04		14,66	1,03	67	10,1
<b>f</b>	01:10		15,00	1,02	66	10,1
<b>g</b>	00:01		14,56	1,02	67	10,2

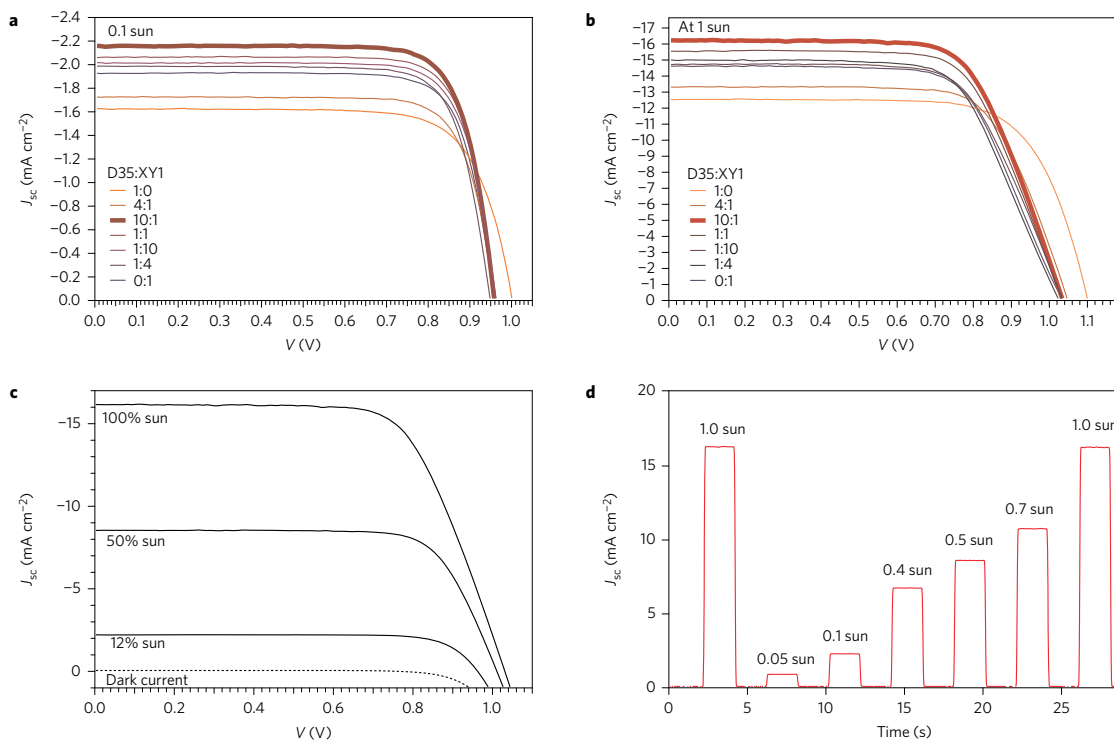


Figure 7-3 Photovoltaic characteristics of D35/XY1 co-sensitized systems with  $\text{Cu}(\text{tmby})_2$  as redox mediator. a) measured J-V curves of at  $12 \text{ mWcm}^{-2}$  (10% sun) b)  $100 \text{ mWcm}^{-2}$  (100% sun) for (a) D35, (b) 10:1 D35:XY1, (c) 4:1 D35:XY1, (d) 1:1 D35:XY1, (e) 1:4 D35:XY1, (f) 1:10 D35:XY1, to (g) pure XY1, c) of the champion solar cell at the ratio of 4:1 (D35:XY1) at 100 %, 50% and 10% sun (solid lines) and the corresponding dark currents (dashed line) d) dependence of the photo-current dynamics on the solar light intensity for the champion solar cell.

The IPCE spectra for the DSC at the various co-sensitization ratios, recorded at 10 % LED bias light intensity, are shown in Figure 7-4. For the best performing co-sensitized system (4:1, D35:XY1), the IPCE reaches its highest values of 91% at 540 nm within the series. Considering the optical loss of the FTO substrate, the internal quantum efficiency ranges between 90% and practically 100% (380 nm – 600 nm). For comparison, DSCs incorporating the single dye D35 show a lower IPCE of 80% at 540 nm and narrower spectral response of the photocurrent, which is limited to the 380 nm – 550 nm wavelength domain. DSCs with only XY1 sensitizer show larger spectral coverage up to 640 nm but slightly lower IPCE of 88% at 540 nm.

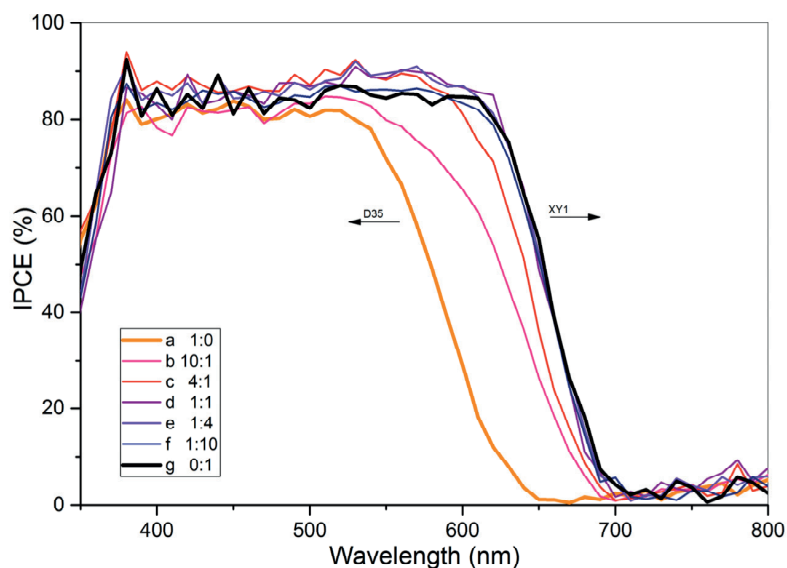


Figure 7-4 IPCE spectra of DSCs co-sensitized at various dye ratios. (a) D35, (b) 10:1 D35:XY1, (c) 4:1 D35:XY1, (d) 1:1 D35:XY1, (e) 1:4 D35:XY1, (f) 1:10 D35:XY1, to (g) pure XY1

The charge extraction measurements as function of  $V_{oc}$  presented in Figure 7-5A, show a down shift of 70 mV of the conduction band edge for the best performing co-sensitization ratio of the D35:XY1 dye (4:1). More charge is extracted at lower  $V_{oc}$  especially in comparison to the DSC with only one of the two sensitizers. This is likely related to the optimal dye coverage between the two sensitizers on the  $TiO_2$  layer. We measured electron lifetimes as a function of  $V_{oc}$  of complete DSCs for the co-sensitized series employing the copper(II/I) complex based electrolyte, which are displayed in Figure 7-5B, in a semilogarithmic plot of electron lifetime as function of  $V_{oc}$ . The electron lifetimes of DSCs made at higher ratios of D35 dye are longer than those obtained from XY1 rich staining solutions. Considering that the same electrolyte composition and redox mediators were used for all studied solar cells, this indicates a higher rate of recombination for the XY1 dye. The curved shape of the slopes can be attributed to electron recombination from the FTO substrate (with a thin  $TiO_2$  blocking layer) to the redox mediator. It is likely, that the blocking layer contains pinholes, which become more apparent at lower light intensities.<sup>180</sup>



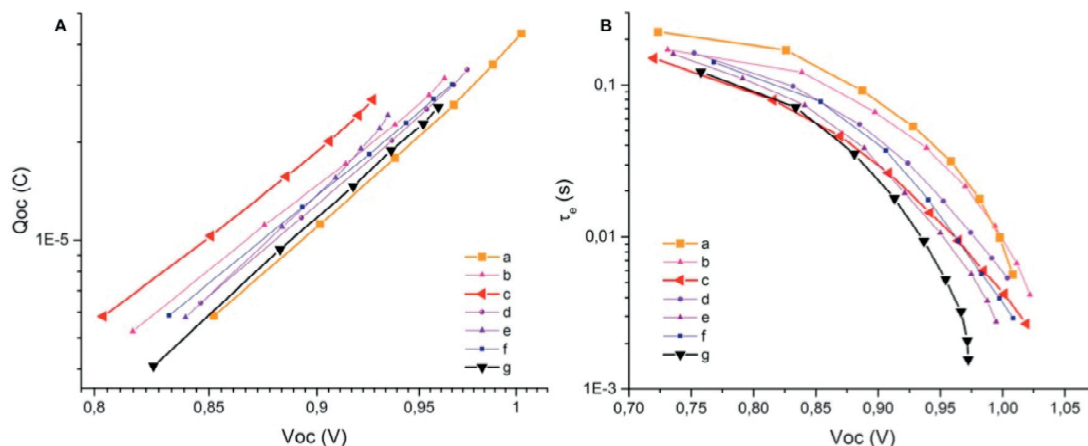


Figure 7-5 Extracted charge at open circuit voltage ( $V_{oc}$ ) and electron lifetime as function of  $V_{oc}$ . Left panel: Extracted charge at open circuit voltage ( $V_{oc}$ ) and right panel: electron lifetime as function of  $V_{oc}$  for DSCs employing pure (a) D35, (b) 10:1 D35:XY1, (c) 4:1 D35:XY1, (d) 1:1 D35:XY1, (e) 1:4 D35:XY1, (f) 1:10 D35:XY1, to (g) XY1

## 7.2.2 Transient absorption and steady-state absorption spectroscopy.

To gain better insight into the electron transfer dynamics of the D35/XY1 co-sensitized mesoscopic  $\text{TiO}_2$  films, time resolved nanosecond transient and steady-state absorbance measurements were performed. In total, we examined 7 dye-sensitized  $\text{TiO}_2$  electrodes with different D35/XY1 loading ratios of: (a) 100% D35, (b) 9% XY1, (c) 20% XY1, (d) 50% XY1, (e) 80% XY1, (f) 90% XY1, and (g) 100% XY1. The relative surface coverage by the two sensitizers will differ from their concentration ratios in the staining solution. This is confirmed by the absorption spectra of the sensitized  $\text{TiO}_2$ , Figure 7-6b. Photoinduced Absorption Spectroscopy was performed to resolve oxidized dyes spectra adsorbed on  $\text{TiO}_2$  along with bleaching of their ground states. We use this measurement to extract two wavelengths to preferentially monitor one oxidized dye or the other. Figure 7-6a shows that at 780 nm we mainly observe oxidized XY1 (oxidized D35 minimum absorbance and oxidized XY1 close to its maximum absorbance), while the 1200 nm probing will target oxidized D35 (oxidized XY1 minimum absorbance and oxidized D35 close to its maximum absorbance). In between, a smooth transition is observed, indicating that we effectively load the films with different concentration ratios. No significant lateral hole transfer takes place between both dyes as none of the two oxidized species is preferentially observed from the PIA spectra. Transient Absorption Spectroscopy (TAS) was performed at both wavelengths (780 and 1200 nm) in the micro- to millisecond timescale to follow the transient decay of the dyes oxidized species, and therefore recombination of the oxidized dyes with  $\text{TiO}_2$  electrons or regeneration by the copper-based electrolyte. The time evolution of the transient absorption at 780 nm reflecting the lifetime of oxidized XY1 does not appear to depend on the dye concentration ratio. In inert electrolyte, we observe similar lifetimes for the oxidized state of both dyes, i.e. 2.10 and 1.85 ms for D35 and XY1, respectively (Figure 7-6c). Upon addition of  $\text{Cu}(\text{tmb})_2$  containing redox electrolyte both sensitizers are efficiently regenerated. From monitoring the transient absorption at 1200 nm we infer that regeneration of D35 occurs with time constants ranging from 2 to 10.8  $\mu\text{s}$  and without any identifiable trend,

while at 780 nm we observe the regeneration of XY1 oxidized molecules with time constants ranging from 1.1 to 5.2  $\mu\text{s}$  (Figure 7-6d). Overall, dye regeneration yields are only marginally affected by these variations and are all above 99.5%, using pseudo-first-order rate constants for regeneration and first-order rate constants for recombination reactions. (The lifetimes were obtained fitting the data with a monoexponential function as in Equation 7-1)

$$\Delta A(t) = A \cdot e^{-\frac{t}{\tau}} \quad (7: 1)$$

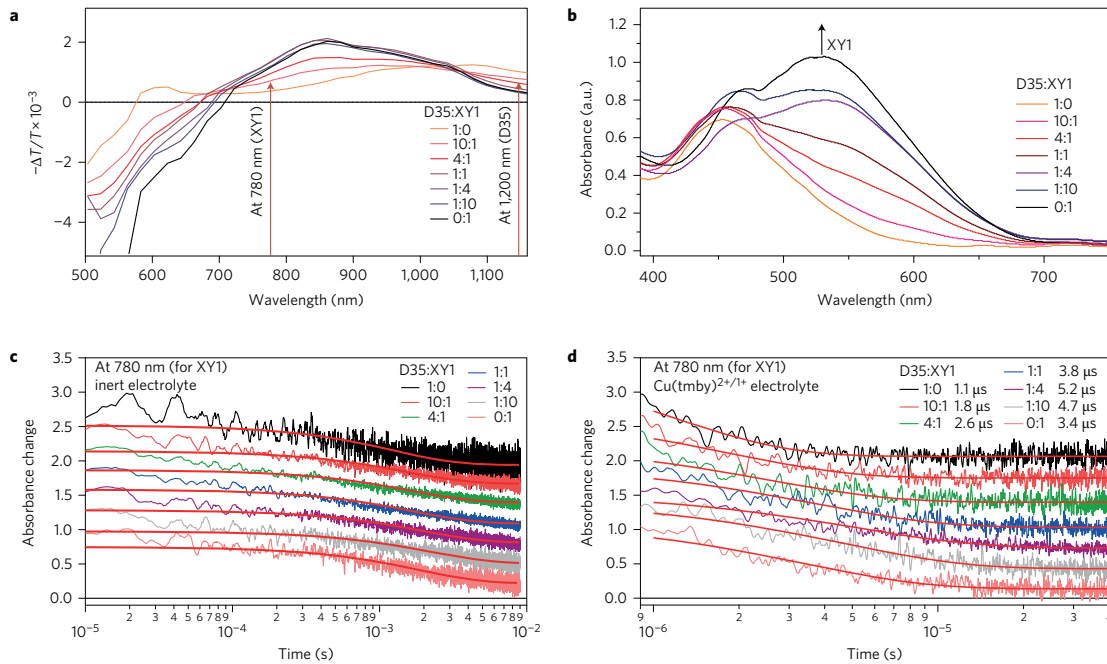


Figure 7-6 Absorption Spectroscopy and time resolved laser spectroscopy of interfacial electron transfer involving the D35 and XY1 sensitizers. a) Photoinduced Absorption (PIA) spectra of dye-sensitized  $\text{TiO}_2$  electrodes with different dye solution ratios of D35 and XY1 organic dyes, from pure (a) D35, (b) 10:1 D35:XY1, (c) 4:1 D35:XY1, (d) 1:1 D35:XY1, (e) 1:4 D35:XY1, (f) 1:10 D35:XY1, to (g) pure XY1. b) UV-Vis absorption spectra of the corresponding sensitized  $\text{TiO}_2$  substrates. Transient absorption decays of the a-g sensitized  $\text{TiO}_2$  films following 532 nm excitation with (c) inert and (d)  $\text{Cu(tmby)}^{2+/1+}$  based electrolyte. The black solid line in both transient absorption decays represents the fit of the signal at the 4:1 D35:XY1 dye ratio. The curves of transient absorption decays have an offset of 0.3 for better visualization.

### 7.2.3 DSCs performance under indoor-light conditions

Indoor light conditions are very different compared with the solar irradiance outdoors, because the light intensity is orders of magnitude lower and the spectra of the indoor light sources differs greatly from the solar emission. Standard indoor illumination has an intensity between 200–2000 lux, where lux is the unit of light illuminance. Illuminance is analogue to the irradiance ( $\text{W}/\text{m}^2$ ) that is commonly used for outdoor devices, but relates the intensity to how it is perceived by the human eye instead of the power.<sup>181</sup> As a comparison between the two units, full solar irradiation, i.e. 100

$\text{mW/cm}^2$  AM 1.5G, corresponds to about 100 000-110 000 lux. Therefore, indoor light at 1000 lux corresponds to ca 1 % of the standard AM 1.5 solar irradiation.<sup>43,182,183</sup>

Since relatively few reports exist that focus on the use of DSCs for indoor light harvesting, no standard indoor light source has been established so far. We chose a typical light tube, OSRAM Warm White 930 (representative spectrum of the light source is given in Figure 7-7 and Figure 7-8), to test the DSCs under realistic indoor conditions. We measured the light intensity striking the DSC by the use of a lux meter (TES 1334).

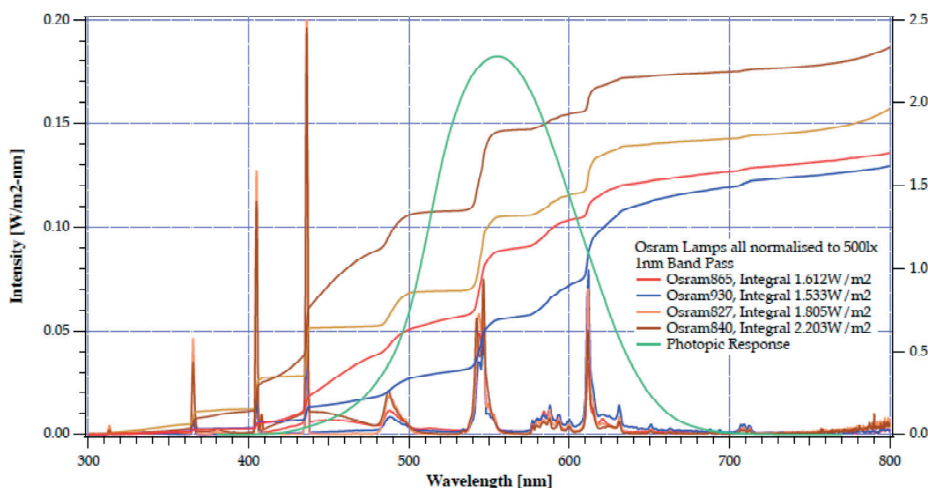


Figure 7-7 Normalized power spectra of various indoor light sources. For this study OSRAM Warm White 827 (orange, solid line) and OSRAM Warm White 930 (blue, solid line) were used.

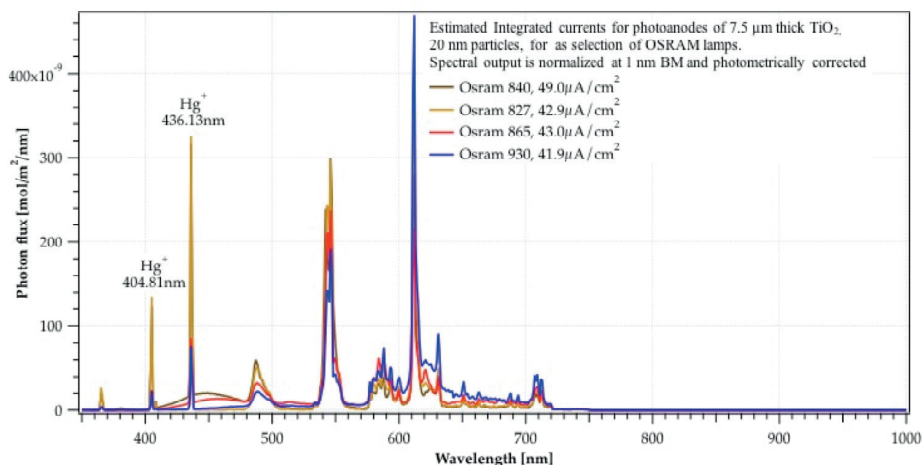


Figure 7-8 Normalized power spectra of various indoor light sources with estimated integrated currents of  $\text{TiO}_2$  photoanodes. For this study OSRAM Warm White 827 (orange, solid line) and OSRAM Warm White 930 (blue, solid line) were used.

The DSCs fabricated for the indoor light condition study have a larger area of  $2.8 \text{ cm}^2$  compared with the normally used laboratory test DSCs ( $0.22 \text{ cm}^2$ ). The purpose behind this is to have a small-

er discrepancy between “real life application” and laboratory produced solar cells, which tend to have better efficiency attributed to their smaller size. Further, the DSCs with a less volatile electrolyte solvent, propionitrile (PN) were compared with DSCs using the standard electrolyte composition, containing acetonitrile.<sup>175</sup> Otherwise, the same composition for the  $\text{Cu}^{(II/I)}$  (tmby)<sub>2</sub> was applied. The mesoscopic  $\text{TiO}_2$  films were sensitized with D35 and XY1 dyes in the staining solution containing 0.08mM D35 and 0.02mM XY1 (ratio (c) 4:1). The PV metrics and power output ( $P_{\text{out}}$ ) of the DSCs and GaAs solar cells (flexi GaAs Alta Devices), were compared under similar indoor light conditions in Table 7-2. The efficiencies of the solar cells at indoor conditions were calculated by Equation 1-10.

Table 7-2 Photovoltaic metrics for DSCs and GaAs solar cells for indoor light sources at 200 lux and 1000 lux.  $P_{\text{in}}$  and  $P_{\text{out}}$  express the incoming power of the light and the power out by the solar cell. DSC<sup>a</sup> employs an acetonitrile based electrolyte and DSC<sup>b</sup> employs a propionitrile based electrolyte. The PCEs for the solar cells are determined from Equation 1-10. Flexi-GaAs solar cells are from Alta Devices measured at Gcell Ltd (Newport, South Wales) with configuration: 6 cells of 8.33cm<sup>2</sup> area in parallel and series connected to a mini-module of 50 cm<sup>2</sup> size.

Solar Cell	Light source	Light intensity	$J_{\text{sc}}$ ( $\mu\text{A}/\text{cm}^2$ )	$V_{\text{oc}}$ (mV)	FF (%)	$P_{\text{in}}$ ( $\mu\text{W}/\text{cm}^2$ )	$P_{\text{out}}$ ( $\mu\text{W}/\text{cm}^2$ )	PCE (%)
DSC <sup>a</sup>	OSRAM Warm White 930	200 lux	27.2	732.0	0.79	61.3	<b>15.6</b>	25.5
DSC <sup>b</sup>		200 lux	24.8	700.0	0.79	61.3	<b>13.7</b>	22.3
DSC <sup>a</sup>		1000 lux	138.0	797.0	0.80	306.6	<b>88.5</b>	28.9
DSC <sup>b</sup>		1000 lux	137.2	766.0	0.80	306.6	<b>84.1</b>	27.4
flexi GaAs Alta	OSRAM Warm White 827	200 lux	20.1	870.0	0.75	70.6	<b>13.1</b>	18.6
flexi GaAs Alta		1000 lux	99.0	940.0	0.80	354.0	<b>74.5</b>	21.0

Considering that the spectral region in which the DSCs absorb light is limited to the visible part of the solar spectrum, it is expected that their efficiency in the visible region (400 -700 nm) is twice the full spectrum value.<sup>172</sup> Taking into consideration that the indoor light sources emit mostly visible light, a DSC with 11.3 % PCE under full solar illumination, is expected to have an efficiency over 20% in their particular spectrum of operation indoors. When an indoor light source was used, the DSCs outperformed the GaAs solar cells under similar conditions. The illumination intensity of the indoor light sources was varied between 200 and 1000 lux and, in both cases, the power output of DSCs was higher. At 200 lux, the best performing DSC yields a power output of 15.6  $\mu\text{W}/\text{cm}^2$  (average of 19 samples is 13.5  $\mu\text{W}/\text{cm}^2$ ), which is substantially higher than the 13.1  $\mu\text{W}/\text{cm}^2$  obtained for GaAs. At 1000 lux the best DSC gives 88.5  $\mu\text{W}/\text{cm}^2$  (average of 7 samples 80.0  $\mu\text{W}/\text{cm}^2$ ) again clearly above the 74.5  $\mu\text{W}/\text{cm}^2$  produced by GaAs, Table 7-2, Figure 7-9. This translates into a PCE of 28.9% for the DSC operating at 1000 Lux. Low power electronic devices, such as wireless sensor nodes or low power microcontroller units (MCU), typically consume about 100 $\mu\text{W}$  in sleep-

ing mode.<sup>184–186</sup> Roundy and co-workers illustrate that at this average power consumption, a  $1\text{cm}^3$  primary battery ( $0.8\text{ Wh/cm}^3$ ) lasts for about 11 month, before the node goes into idle state. A  $2\text{cm}^2$  sized DSC would therefore be able to render the low power device fully autonomous.<sup>187</sup>

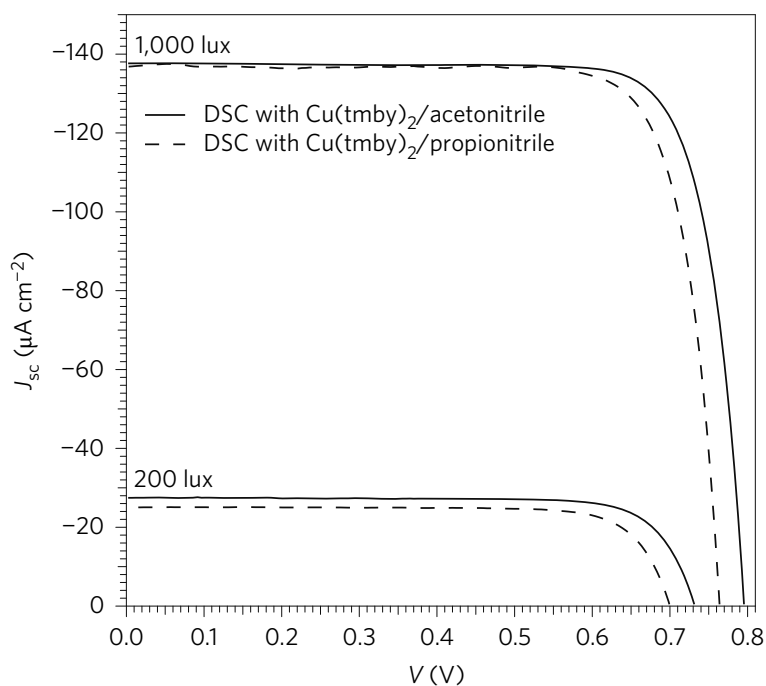


Figure 7-9 Photovoltaic characteristics of co-sensitized DSCs measured under indoor light conditions. J-V curves at 200 lux and 1000 lux of DSCs with the co-sensitized dyes, D35:XY1 (4:1), with  $\text{Cu}(\text{tmby})_2$  acetoneitrile (solid line) and propionitrile (dashed line) based electrolyte

We advance the following rational to explain the outstanding ambient light performance of dye sensitized solar cells employing the combination of the two sensitizers with the  $\text{Cu}(\text{II/I})$  redox electrolyte:

- The co-sensitization of mesoscopic titania scaffolds by the two sensitizers whose absorption spectra are complimentary, extends the light harvesting ability of the device over a wider spectral domain increasing its short circuit photocurrent. In the present case, the D35 absorbs mainly blue and green light while the XY1 covers the yellow and red spectral region.
- The sensitizers are judiciously engineered on the molecular scale, such that their electron acceptor moiety, the cyanoacrylate group, is attached by coordinative bonding to the titanium ions surface of the  $\text{TiO}_2$  while their arylamine donor group is positioned away from the interface at the opposite end of the dye molecule. In the chemical design of the sensitizer structure their lowest molecular orbital (LUMO) is adjusted to match the energy of the conduction band edge of  $\text{TiO}_2$  formed by the  $\text{Ti}(3d)$  orbitals. In this way, the energy loss associated with the interfacial electron injection process is minimized. Optical excitation promotes

electrons from the donor to the acceptor moiety of the sensitizer enhancing their electronic coupling with the Ti(3d)-orbitals at the TiO<sub>2</sub> surface, such that the interfacial electron transfer from the excited sensitizer into the TiO<sub>2</sub> can proceed very rapidly, i.e. in the femto to picosecond time range. By contrast, the long distance between the electron in the TiO<sub>2</sub> and the hole that is localized on the terminal arylamine group of the sensitizer weakens their electronic interactions resulting in time constants for the recombination reaction in the millisecond to second domain.

- The two sensitizers undergo synergistic interactions in the adsorbed state. Thus, the second dye may suppress unfavourable interactions of the first dye with the TiO<sub>2</sub> surface or with itself (dye aggregation). This effect enhances the spectral response of the photocurrent of the first dye.<sup>47</sup>
- The two sensitizers form together a more tightly packed monolayer at the surface than the individual dyes. This blocks the approach of the Cu(II) complex to the surface retarding the unwanted back electron transfer reaction increasing the Voc of the device.
- The close matching of the redox potentials of the sensitizers with that of the Cu(II/I) complexes used as a redox shuttle allows achieving much higher V<sub>oc</sub> values than with the conventional iodide/triiodide redox system.

### 7.3 Conclusions

We introduce a new DSC design combining two judiciously selected sensitizers enabling incident light to be harvested over the whole visible range. We use Cu<sup>(II/I)</sup>(tmby)<sub>2</sub> (tmby = 4,4',6,6'-tetramethyl-2,2'-bipyridine) as a redox relay, which is capable of successfully regenerating both dyes at only 0.1 eV to 0.2 eV driving force. In standard AM 1.5G sunlight the PCE reaches 11.3 % a new record for a copper electrolyte based system. Strikingly, under 1000 lux indoor illumination the PCE of this new DSC design is 28.9 %, resulting in a power output of 88.5 μW/cm<sup>2</sup>. This is sufficient to ascertain autonomous operation of a range of electronic devices in an indoor environment with a reasonable solar cell size. Therefore, our study suggests that DSCs are ideally suited for the ambient light applications. We expect our findings to have a major practical impact, since ambient light energy harvesting to power electronic devices or to extend their battery lifetime will open a wide field of applications in a wide range of systems requiring electric power to ascertain their autonomous operation.

### 7.4 Methods

*Materials.* Acetonitrile and propionitrile (Aber), tert-butanol (Sigma-Aldrich), TiO<sub>2</sub> paste (30 NR-D, Dyesol), LiTFSI (TCI), TBP (TCI), tmby (hetcat) and D35 dye (Dyemaco) were purchased from commercial sources and used as received, unless stated otherwise. TiO<sub>2</sub> paste for scattering film was prepared as previously described.<sup>141</sup> The [Cu<sup>I</sup>(tmby)<sub>2</sub>](TFSI), and [Cu<sup>II</sup>(tmby)<sub>2</sub>](TFSI)Cl and the dye XY1 were synthesized as previously described.<sup>102,178</sup>

*Fabrication of solar cells.* The working electrodes were fabricated as described in Chapter 2.<sup>51,102</sup> The TiO<sub>2</sub> films were immersed in dye solutions in acetonitrile/tert-butanol (v/v, 1/1) for 16 h to

graft the dye molecules onto the TiO<sub>2</sub> surface. The sensitizing solutions contained the organic dyes in the following millimolar (mM) concentrations (a) 0.1 mM D35, (b) 0.1 mM D35 and 0.01 mM XY1 (D35:XY1;10:1), (c) 0.08 mM D35 and 0.02 mM XY1 (4:1), (d) 0.05 mM D35 and 0.05 mM XY1 (1:1), (e) 0.02 mM D35 and 0.08 mM XY1 (1:4), (f) 0.01 mM D35 and 0.1 mM XY1 (1:10), (g) 0.1 mM XY1. We used FTO glass covered with electrochemically deposited PEDOT films as counter electrodes.<sup>100</sup> The dye-coated TiO<sub>2</sub> film and the counter electrode were assembled by using thermoplastic frame (Surlyn, DuPont) heated at 120°C. Electrolyte was injected into the space between the electrodes through a predrilled hole on the counter electrode under vacuum. The electrolyte consisted of a solution of 0.2 M Cu(I) and 0.04 M Cu(II) complexes and 0.1 M LiTFSI as well as 0.6 M TBP in acetonitrile. The hole was sealed by using the polymer hot-melt (Surlyn). The DSCs prepared with TiO<sub>2</sub> area of 2.8 cm<sup>2</sup> were assembled using UV – glue (Three Bond: 3035B).

*Characterization of solar cells.* The characterizations of *J-V* and IPCE of small-area solar cells are described in Chapter 2.<sup>51</sup> The solar cells (without antireflection films) were masked to attain an illuminated active area of 0.158 cm<sup>2</sup>.

Big area solar cells (2.8 cm<sup>2</sup>) were covered with a mask of the same aperture. The low light measurements were performed using an OSRAM Warm White 930 and Philips-Warm White (PL Electronic-C; Holland) discharge tubes for DSCs and OSRAM Warm White 827 lamp for GaAs solar cells. A TES-1334 Luxmeter was used to measure the light intensity. Flexi-GaAs solar cells are from Alta Devices measured at the Gcell-company with configuration: 6 cells in parallel and series (of 8.33 cm<sup>2</sup>) as module (50 cm<sup>2</sup>). The Luxmeter TES-1334 was used to measure the light intensity at the DSC. In summary, 63 small area (3 solar cells per condition for 7 conditions, where each was repeated 3 times) and 15 large area solar cells have been tested. The PCE distribution is within ± 0.5%. Care was taken to scan the *J-V* curve sufficiently slowly so that any hysteresis effect on the maximum power point remained below 2%. Hysteresis was checked by scanning the *J-V* curve in forward and backward direction and comparing the PV metrics obtained for the two scanning directions. Indoor light sources. (The indoor light sources OSRAM Warm White 827 hat 1.77 W/m<sup>2</sup> was used at Gcell for GaAs and OSRAM Warm White 930 hat 1.566 W/m<sup>2</sup> was used at EPFL for DSCs.)

GaAs solar cells: The flexi-GaAs-module is from Alta Devices measured at Gcell-company with the following configuration: 6 cells (of 8.33 cm<sup>2</sup>) as module (50 cm<sup>2</sup>) with parallel and series connections as 2 groups of 3 cells (in parallel) measured in series = 2 cells(2x25 cm<sup>2</sup>) in series.

*UV/Vis spectroscopy.* UV/Vis absorption data was collected by a Perkin-Elmer Lambda 950 spectrophotometer.

*Extracted Charge and Electron Lifetime Measurements.* Electron lifetime measurements were performed as detailed in Chapter 2.<sup>109</sup>

*Transient Absorption Spectra (TAS) and Photoinduced Absorption Spectroscopy (PIA).* The photo-induced kinetics was measured with an Ekspla NT-342 Q-switched Nd:YAG laser using 532 nm as excitation wavelength. The pulse width was 4-5 ns (FWHM) and the repetition rate was 20 Hz. The probe light source was a halogen lamp and probe wavelengths at 780 and 1200 nm were chosen using a monochromator (Omni-λ 150, Oriel). The film was positioned at approximately 45° angle

with respect to the incoming laser pulse, for front illumination. The signal was detected using a photomultiplier tube (R9110, Hamamatsu) in the visible and an InGaAs diode (SM05PD5A, Thorlabs) in the near infrared, then recorded using an oscilloscope (DPO 7014, Tektronix). The radiant output of the laser was attenuated to  $50 \mu\text{J}/\text{cm}^2$  using grey optical density filters. Low light intensity value was deliberately chosen in order to ensure that on average less than one electron was injected per nanoparticle, lifetimes were obtained fitting the data with a monoexponential function (see SI for details, Equation S1). Satisfactory signal-to-noise ratios were typically obtained by averaging over 1000 laser shots.

The PIA spectra of the various cells were recorded over a wavelength range of 500–1160 nm following an (on/off) photo-modulation using a 9 Hz square wave emanating from a blue laser (405 nm). White probe light from a halogen lamp (20 W) was used as an illumination source. The light was focused onto the sample and sent into a monochromator (Gemini, Horiba), and detected using a photodiode connected to a lock-in amplifier (SR830, Stanford Research Systems).



# Conclusion

## Achieved results

In this thesis, we firstly concentrated our efforts to minimize dye regeneration overpotentials in DSCs. In order to achieve this, we used copper redox mediators with bipyridyl ligands holding methyl groups on the 6,6 positions. With these set of ligands, we could satisfy a low reorganization energy requirement between the Cu(I) and Cu(II) transition and thus we showed that a driving force of 0.1eV is enough to sustain an efficient dye regeneration. The open-circuit values over 1.0V were obtainable without compromising the photocurrents.

Meanwhile, we gained deeper understanding on copper species (especially for Cu(II)) in terms of synthesis and the interaction with other electrolyte additives. We could trace that Cu(II) synthesized by the CuCl<sub>2</sub> precursor is not electrochemically identical to Cu(I) species because of the Cl<sup>-</sup> coordination. We proposed different methods to produce neat Cu(II) species, and we could achieve better kinetics at the counter electrode and better mass transport with this neat product. Furthermore, we investigated the effect of base coordination to the Cu(II) complex on the different DSC processes. By employing different bases, we could trace different resistances for the counter electrode and diffusion. In addition, dye regeneration and charge recombination kinetics were influenced with the base additive due to the changes in molecular geometries of the complexes.

Especially in the case of charge recombination process, substantial differences are expected in the absence and presence of bases. According to our DFT analysis, the presence of TBP in the electrolyte medium, results in penta-coordinated complexes and this leads to higher reorganization energies ( $\lambda = 1.23-1.40$  eV). By considering these values, the charge recombination is expected to occur in the Marcus normal regime. On the contrary, without TBP the charge recombination is expected to occur in the Marcus inverted regime. Nevertheless, the recombination with copper redox mediators were found to be lower than the standard cobalt complex.

We demonstrated remarkable power conversion efficiencies with our copper redox mediators and the Y123 dye, both for liquid state (10%) and solid state devices (11%). Also, we showed remarkable PCE values (28.9 %) under ambient lighting (1000lux) by employing co-sensitized TiO<sub>2</sub> films and Cu<sup>(II/I)</sup>(tmby)<sub>2</sub> (tmby = 4,4',6,6'-tetramethyl-2,2'-bipyridine). We believe that these high performances will bring DSC technology one step closer for powering a range of electronic devices including e-Readers, tablets, and IoT-related appliances and accordingly commercialization.

## Future development

In a few recent publications, new record PCE values for DSCs employing Cu<sup>(II/I)</sup>(tmby)<sub>2</sub> were reported. Cao et al<sup>189</sup> achieved PCE values of 13.1% and 32% under air mass 1.5 global 100 mWcm<sup>-2</sup> solar radiation and ambient light (1000 lux), respectively, by employing XY1 and Y123 dye blends. By employing Cu<sup>(II/I)</sup>(tmby)<sub>2</sub> as a HTM, Zhang et al.<sup>190</sup> reported PCE of 11.6% under AM 1.5 G

illumination with the WS-72 dye. These studies reveal that with device optimizations and with different dye alternatives, the PCE values can be increased further in the future.

In order to enhance the PCE values for the DSCs employing copper redox couples, some additional work can be proposed as below:

- By designing new ligand structures, the redox potential of the copper complexes can be tuned in order to sustain dye regeneration with the dyes having more negative HOMO levels.
- Charge injection overpotentials can be reduced either by tuning the LUMO level of sensitizers or by employing different semiconductors or doped TiO<sub>2</sub>. V<sub>OC</sub> values can be further increased in this way.
- Marcus inverted regime for charge recombination, can be achieved experimentally by avoiding the bases in the electrolyte. Advantages/disadvantages of the inverted regime can be investigated in detail.

# Chapter 8 Appendix

## 8.1 Appendix to Chapter 2

### 8.1.1 Methods and computational details

All the calculations have been performed with the G09 suite of programs for quantum chemistry.

The PBE0 hybrid DFT approach has been applied in all the calculations together with SDD ECP-basis set for Cu and TZVP basis set for C, H and N atoms.

The acetonitrile solvent is described by the PCM implicit solvation model with the last parameterization of non-empirical solvation term known as SMD.

Vertical excitation energies are computed with the TD-DFT approach by considering the non-equilibrium PCM model to include the solvent effects.

Ground-state minimum-energy structures have been computed considering the default maximum force and displacement tolerance parameters in Gaussian. Molecular frequencies have been computed within the harmonic oscillator approximation, and the thermochemical data are derived at room temperature (298 K) and considering the most common atom isotopes.

Internal reorganization energies ( $\lambda_{in}$ ) have been computed with a common approach by considering the Cu(I)L<sub>2</sub> and Cu(II)L<sub>2</sub> minimum-energy structures in solution.  $\lambda_{in}$  is evaluated in the gas phase as the energy differences of Cu(I) complexes evaluated at the relaxed geometries that correspond to the initial and final electronic states.

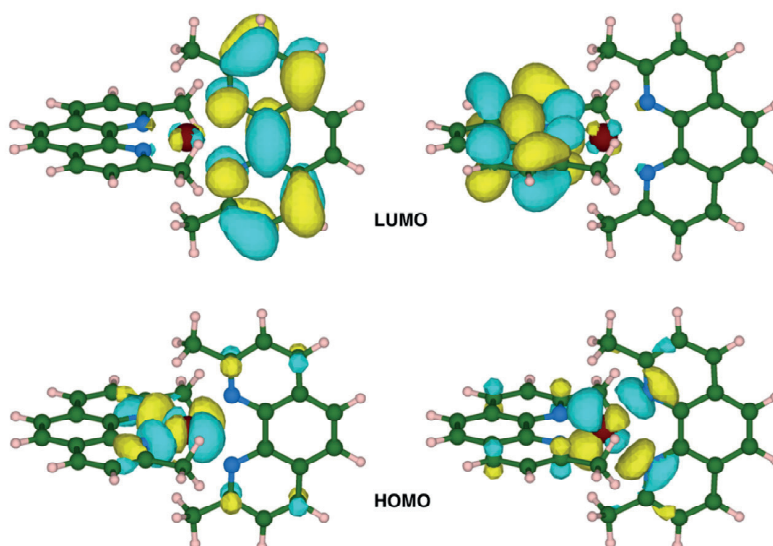


Figure 8-1 Frontier molecular orbitals (HOMO and LUMO) for Cu(I)(dmp)<sub>2</sub>.

Table 8-1 TD-DFT results: first vertical excitation energies ( $\Delta E_{\text{exc}}$ ) and corresponding oscillator strength ( $f$ ) in acetonitrile solution.

	$\Delta E_{\text{exc}}$ (nm)	$f$
$\text{Cu}(\text{dmp})_2^{1+}$	466	0.1996
$\text{Cu}(\text{dmby})_2^{1+}$	474	0.1722
$\text{Cu}(\text{dmp})_2^{1+}$	463	0.1903

Table 8-2 Geometrical features of the minimum-energy structures for  $\text{CuL}_2$  (L=dmp, dmpy, tmby) complexes in acetonitrile solution.

	<i>dmp</i>	<i>dmby</i>	<i>tmby</i>
<b>Cu(I) complexes</b>			
distance Cu-N (Å)	2.074	2.068	2.067
angle N <sub>1</sub> -Cu-N <sub>2</sub> (°)	81.0	80.0	80.0
dihedral N <sub>1</sub> -C <sub>1</sub> -C <sub>2</sub> -N <sub>2</sub> (°)	0.0	2.6	2.0
<b>Cu(II) complexes</b>			
distance Cu-N (Å)	2.041	2.025	2.021
angle N <sub>1</sub> -Cu-N <sub>2</sub> (°)	81.8	81.2	81.3
dihedral N <sub>1</sub> -N <sub>2</sub> -Cu-N <sub>1</sub> ' (°)	0.4	9.0	7.1

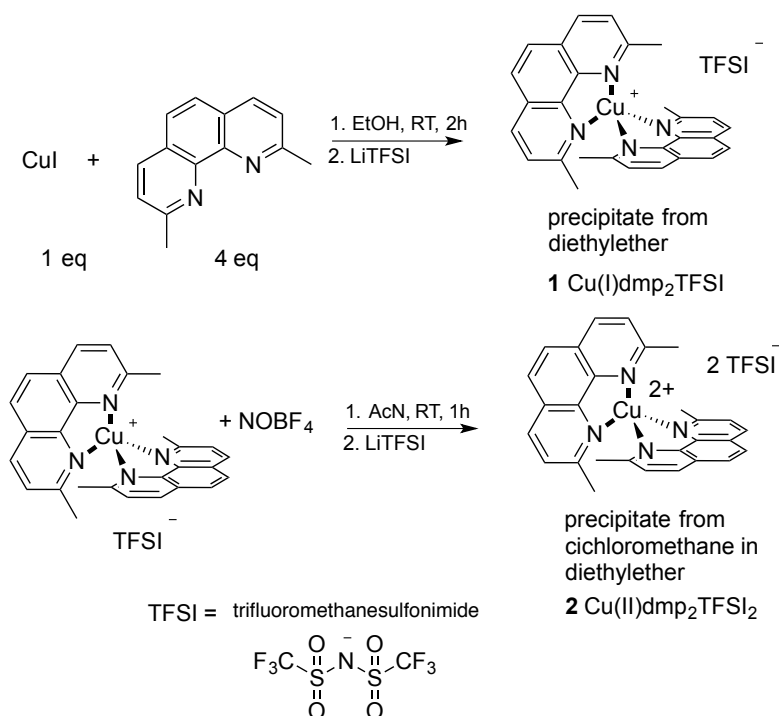
### 8.1.2 Synthesis of copper 2,2'-dimethyl phenanthroline ( $\text{Cu}^{(\text{II})}(\text{dmp})_2\text{TFSI}_{1/2}$ )

$\text{Cu}^{(\text{II})}(\text{dmp})_2\text{TFSI}_{1/2}$  (1,2) Figure 8-2

For  $\text{Cu}(\text{dmp})_2\text{TFSI}$  (1), 1 eq. of CuI (35 mg, 0.175 mmol) was mixed with 4 eq. of Neocuproine hydrate (100 mg, 0.7 mmol) in ethanol, under nitrogen atmosphere, at room temperature for 2 hours. Complex (1) was collected by filtration and washed with water and diethyl ether. The resulted complex (1) was obtained as intense red, crystalline powder. The yield was 90 % (0.16 mmol).

For  $\text{Cu}(\text{dmp})_2\text{TFSI}_2$  (2), Complex (1) (100 mg, 0.13 mmol) was dissolved in acetonitrile. To this solution, 1 equivalent of  $\text{NOBF}_4$  (16 mg, 0.13 mmol) followed by 5 equivalents of LiTFSI (37 mg, 0.65 mmol) were added after 30 min. The solution was further stirred for 2 hours at room temperature and under nitrogen atmosphere. The solvent was removed by rotatory evaporation and the crude redissolved in minimum amount of dichloromethane. Complex (2) was collected by filtration after precipitation from diethylether and washed with diethyl ether. The yield was 72 % (0.09 mmol). The product was a bright violet powder.

$^1\text{H}$  NMR (400 MHz, acetone  $d_6$ ):  $\delta$  8.75 (d,  $J(\text{H-H}) = 8.21$  Hz, 1H), 8.23 (s, 1H), 7.98 (d,  $J(\text{H-H}) = 8.24$  Hz, 1H), 2.52 (s, 3H). MALDI-MS: (1)  $m/z$  (%) 473.132 (90) [ $\text{Cu}(\text{dmp})_2\text{TFSI}]^+$ ; (2)  $m/z$  (%) 479.182 (90) [ $\text{Cu}(\text{dmp})_2\text{TFSI}]^{2+}$

Figure 8-2 Synthetic procedure for  $\text{Cu}^{(\text{I/II})}(\text{dmp})_2\text{TFSI}_{1/2}$ 

### 8.1.3 Synthesis of copper complexes: 6,6'-dimethyl-2,2'-bipyridine ( $\text{Cu}^{(\text{I/II})}(\text{dmby})_2\text{TFSI}_{1/2}$ ) (3,4) and 4,4',6,6'-tetramethyl-2,2'-bipyridine

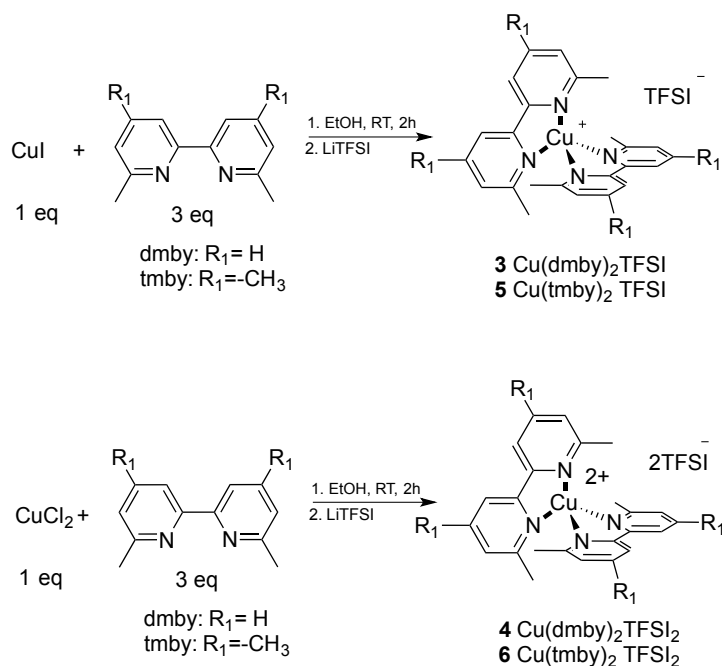
( $\text{Cu}^{(\text{I/II})}(\text{tmby})_2\text{TFSI}_{1/2}$ ) (5,6)  $\text{Cu}^{(\text{I/II})}(\text{dmby})_2\text{TFSI}_{1/2}$  or ( $\text{Cu}^{(\text{I/II})}(\text{tmby})_2\text{TFSI}_{1/2}$ ) (3,5) (Figure 8-3):

For ( $\text{Cu}(\text{dmby})_2\text{TFSI}$ ) and ( $\text{Cu}(\text{tmby})_2\text{TFSI}$ ) (3,5), one equivalent of CuI (35 mg, 0.175 mmol) was mixed with 3 equivalents of 6,6'-dimethyl-2,2'-bipyridine (120 mg, 0.7 mmol) or 4,4',6,6'-tetramethyl-2,2'-bipyridine (150 mg, 0.7 mmol) in 20 ml ethanol, under nitrogen atmosphere, at room temperature for 2 hours. The resulted complex (1) was obtained as intense red, crystalline powder. The product was filtered and redissolved by addition of 5 ml of deionized water followed by an addition of 5 equivalents of LiTFSI (37 mg, 0.65 mmol). The solution was further stirred for 2 hours at room temperature and under nitrogen atmosphere resulting in red precipitation. The complex (3,5) was collected by filtration and washed with water. The yield of the products was 80 % (mol). In both cases product was a bright red powder.

$^1\text{H}$  NMR (400 MHz, acetone  $d_6$ ):  $\delta$  8.75 (d,  $J(\text{H-H}) = 8.21$  Hz, 1H), 8.23 (s, 1H), 7.98 (d,  $J(\text{H-H}) = 8.24$  Hz, 1H), 2.52 (s, 3H). MALDI-MS: (3)  $m/z$  (%) 431.124 (90) ( $[\text{Cu}(\text{dmby})_2\text{TFSI}]^+$ ); (5)  $m/z$  (%) 487.188 (90) ( $[\text{Cu}(\text{tmby})_2\text{TFSI}]^+$ )

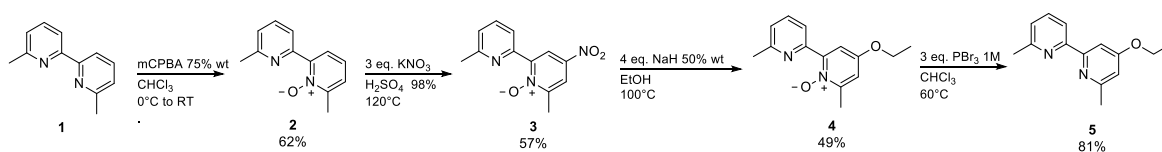
For ( $\text{Cu}(\text{dmby})_2\text{TFSI}_2$ ) (4) or ( $\text{Cu}(\text{tmby})_2\text{TFSI}_2$ ) (6): One equivalent of  $\text{CuCl}_2$  (35 mg, 0.175 mmol) was mixed with 3 equivalents of 6,6'-dimethyl-2,2'-bipyridine (120 mg, 0.7 mmol) or 4,4',6,6'-tetramethyl-2,2'-bipyridine (150 mg, 0.7 mmol) in 20 ml ethanol, under nitrogen atmosphere, at room temperature for 2 hours. The resulted complex (1) was obtained as green powder. The product was filtered and redissolved by addition of 5 ml of deionized water followed by an addition of 5 equivalents of LiTFSI (37 mg, 0.65 mmol). The solution was further stirred for 2 hours at room temperature and under nitrogen atmosphere resulting in green precipitation. The complex (3,5) was collected by filtration and washed with water. The average yield was 70 % (mol). The products were green powders.

$^1\text{H}$  NMR (400 MHz, acetone  $d_6$ ):  $\delta$  8.75 (d,  $J(\text{H-H}) = 8.21$  Hz, 1H), 8.23 (s, 1H), 7.98 (d,  $J(\text{H-H}) = 8.24$  Hz, 1H), 2.52 (s, 3H). MALDI-MS: (4)  $m/z$  (%) 431.129 (90) ( $[\text{Cu}(\text{dmby})_2\text{TFSI}]^{2+}$ ); (6)  $m/z$  (%) 487.197 (90) ( $[\text{Cu}(\text{tmby})_2\text{TFSI}]^{2+}$ )

Figure 8-3 Synthetic procedure for  $\text{Cu}^{(\text{I/II})}(\text{dmby})_2\text{TFSI}_{1/2}$  (3,4) and  $\text{Cu}^{(\text{I/II})}(\text{tmby})_2\text{TFSI}_{1/2}$  (5,6)

## 8.2 Appendix to Chapter 5

### 8.2.1 Synthetic procedures

Figure 8-4 Synthetic procedure of ethoxy-6,6'-dimethyl-2,2'-bipyridine' ligand. Conditions: (i): 1 eq. mCPBA 75% wt,  $\text{CHCl}_3$ ,  $0^\circ\text{C}$  to RT, o.n., 62%; (ii): 3 eq.  $\text{KNO}_3$ ,  $\text{H}_2\text{SO}_4$  98%,  $120^\circ\text{C}$ , o.n., 57%; (iii): 4 eq. NaH 50% wt, EtOH,  $100^\circ\text{C}$ , o.n., 49%; (iv) 3 eq.  $\text{PBr}_3$  1M,  $\text{CHCl}_3$ ,  $60^\circ\text{C}$ , o.n., 81%.

#### Synthesis of 6,6'-dimethyl-[2,2'-bipyridine] 1-oxide (2)

6,6'-dimethyl-2,2'-bipyridine(1) (1.2 g, 6.51 mmol, 1.0 eq.) was dissolved in 5 mL chloroform and cooled down to  $0^\circ\text{C}$  with an ice bath. Then, mCPBA (2.02 g (75% wt), 6.51 mmol, 1.0 eq.) in 15 mL chloroform was added dropwise over 2 hours. Once the addition completed, the ice bath was removed and the reaction mixture allowed to warm up to RT before stirring overnight. After that, chloroform was washed with saturated sodium carbonate (3 x 20 mL) and dried over magnesium sulfate. The product used without further purification for the next step (0.809 g, 62%).

$^1\text{H}$  NMR (400 MHz, Chloroform-*d*)  $\delta$  8.58 (d,  $J = 7.9$  Hz, 1H), 8.00 (dd,  $J = 7.1, 3.0$  Hz, 1H), 7.72 (t,  $J = 7.8$  Hz, 1H), 7.34 – 7.25 (m, 2H), 7.21 (d,  $J = 7.7$  Hz, 1H), 2.64 (s, 3H), 2.61 (s, 3H).

$^{13}\text{C}$  NMR (101 MHz, Chloroform-*d*)  $\delta$  177.41, 158.04, 149.85, 149.73, 147.83, 136.31, 125.63 (d,  $J = 1.7$  Hz), 125.04, 123.61, 122.54, 24.60, 18.46.

Mass Spectrometry (APPI<sup>+</sup>,  $m/z$ ):  $[\text{M}+\text{H}^+]$  calculated: 201.1022 found: 201.1020

### Synthesis of 6,6'-dimethyl-4-nitro-[2,2'-bipyridine] 1-oxide (3)

6,6'-dimethyl-[2,2'-bipyridine] 1-oxide (2) (0.778 g, 3.89 mmol, 1.0 eq.) and potassium nitrate (1.178 g, 11.66 mmol, 3.0 eq.) were charged in a round bottom flask equipped with a condenser. Then, 5 mL Sulfuric acid 98% were added and the mixture stirred until dissolution of the solids. The obtained yellow solution was heated at 120°C over night. The reaction flask was then cooled down to RT, poured over ice and basified with a solution of sodium hydroxide 6 M. The obtained solid was filtered off and dried on the bench. The product was obtained as a beige solid 0.544 g (57 %) and was used without further purification.

$^1\text{H}$  NMR (400 MHz, Chloroform-*d*)  $\delta$  8.98 (d,  $J = 3.2$  Hz, 1H), 8.61 (d,  $J = 7.9$  Hz, 1H), 8.13 (d,  $J = 3.3$  Hz, 1H), 7.77 (t,  $J = 7.8$  Hz, 1H), 7.30 (d,  $J = 7.3$  Hz, 1H), 2.68 (s, 3H), 2.66 (s, 3H).

$^{13}\text{C}$  NMR (101 MHz, Chloroform-*d*)  $\delta$  158.75, 151.65, 147.64, 136.67, 124.72, 123.04, 122.16, 120.08, 118.65, 118.17, 24.60, 18.75.

Mass Spectrometry (APPI<sup>+</sup>,  $m/z$ ):  $[\text{M}+\text{H}^+]$  calculated: 246.0873 found: 246.0872

### Synthesis of 4-ethoxy-6,6'-dimethyl-[2,2'-bipyridine] 1-oxide (4)

Sodium hydride (0.338 g(50% wt), 7.06 mmol, 4.0 eq.) was charged in an over dried schlenk tube under Argon atmosphere. Then, 4 mL anhydrous Ethanol were slowly added under vigorous stirring and was left at RT until Hydrogen evolution stopped. Then, (6,6'-dimethyl-4-nitro-[2,2'-bipyridine] 1-oxide (3) (0.433 g, 1.77 mmol, 1.0 eq.) was added and the beige suspension was heated to 100°C overnight. The reaction mixture was cooled down to RT and diluted with water. The aqueous phase was washed with Chloroform (3x30 mL) and dried over magnesium sulfate. Finally, evaporation of the solvent afforded a green solid as the desired product 0.210 g (49%).

$^1\text{H}$  NMR (400 MHz, Chloroform-*d*)  $\delta$  8.67 (d,  $J = 7.9$  Hz, 1H), 7.71 (t,  $J = 8.1$ , 1H), 7.55 (d,  $J = 3.6$  Hz, 1H), 7.21 (d,  $J = 7.7$  Hz, 1H), 6.85 (d,  $J = 3.6$  Hz, 1H), 4.33 – 4.03 (m, 2H), 2.63 (s, 3H), 2.59 (s, 3H), 1.46 (td,  $J = 7.0, 1.4$  Hz, 3H).

$^{13}\text{C}$  NMR (101 MHz, Chloroform-*d*)  $\delta$  157.90, 155.94, 150.56, 149.78, 148.13, 136.28, 123.67, 122.73, 112.70, 110.69, 64.33, 24.64, 18.84, 14.55.

Mass Spectrometry (ESI<sup>+</sup>,  $m/z$ ):  $[\text{M}+\text{H}^+]$  calculated: 245.1285 found: 245.1285

### Synthesis of 4-ethoxy-6,6'-dimethyl-2,2'-bipyridine (5)

4-ethoxy-6,6'-dimethyl-[2,2'-bipyridine] 1-oxide(4) (0.210 g, 0.86 mmol, 1.0 eq.) was charged in an oven dried round bottom flask brought under Argon and dissolved in 5 mL Chloroform and cooled down to 0°C with an ice bath. Then, Phosphorus tribromide (1.0 M in dichloromethane) (2.58 mL, 2.58 mmol, 3.0 eq.) was added dropwise to the mixture. The reaction was then warmed up to RT and heated at 60°C for 24 hours. After that, the obtained suspension was poured over ice and basified with sodium hydroxyde 6 M to afford the formation of a beige solid, which was removed by vacuum filtration. The remaining filtrate was then washed with Chloroform (3x10 mL) and dried over magnesium sulfate. Evaporation of the solvent afforded the desired product as a beige solid 0.159 g (81 %)

$^1\text{H}$  NMR (400 MHz, Chloroform-*d*)  $\delta$  8.18 (d,  $J = 7.8$  Hz, 1H), 7.78 (d,  $J = 2.3$  Hz, 1H), 7.74 – 7.66 (m, 1H), 7.17 (d,  $J = 7.7$  Hz, 1H), 6.70 (d,  $J = 2.3$  Hz, 1H), 4.21 (qd,  $J = 7.0, 1.9$  Hz, 2H), 2.65 (s, 3H), 2.59 (s, 3H), 1.48 (td,  $J = 7.0, 1.9$  Hz, 3H).

$^{13}\text{C}$  NMR (101 MHz, Chloroform-*d*)  $\delta$  166.25, 159.31, 157.74 (d,  $J = 1.9$  Hz), 155.83, 136.98 (d,  $J = 5.1$  Hz), 123.12, 118.34, 118.18, 109.77, 104.40, 63.46, 24.77, 24.69, 14.63.

Mass Spectrometry (ESI<sup>+</sup>, *m/z*): [M+H<sup>+</sup>] calculated: 229.1330 found: 229.1335

**Synthesis of copper 4-ethoxy-6,6'-dimethyl-2,2'-bipyridine [Cu(eto)<sub>2</sub>][TFSI] (6) and [Cu(eto)<sub>2</sub>][TFSI]<sub>2</sub> (7) (Figure 8-5)**

For [Cu(eto)<sub>2</sub>][TFSI] (6), one equivalent of CuI (27.8 mg, 0.139 mmol) was mixed with 3 equivalents of 4-ethoxy-6,6'-dimethyl-2,2'-bipyridine (95.8 mg, 0.42 mmol) in 20 ml ethanol, under nitrogen atmosphere, at room temperature for 2 hours. The resulted complex was obtained as intense red, crystalline powder. The product was filtered and redissolved by addition of 5 ml of deionized water followed by an addition of 5 equivalents of LiTFSI (200 mg, 0.7 mmol). The solution was further stirred for 2 hours at room temperature and under nitrogen atmosphere resulting in red precipitation. The complex (6) was collected by filtration and washed with water. The yield of the products was 85.6 % (mol).

<sup>1</sup>H NMR (400 MHz, Chloroform-*d*) δ 8.14 (dd, *J* = 8.3, 3.7 Hz, 1H), 8.00 (dt, *J* = 10.9, 5.4 Hz, 1H), 7.64 (s, 1H), 7.44 (dd, *J* = 7.9, 3.6 Hz, 1H), 6.93 (s, 1H), 4.39 – 4.19 (m, 2H), 2.24 (dd, *J* = 21.2, 3.8 Hz, 6H), 1.54 (dt, *J* = 10.8, 5.0 Hz, 3H).

<sup>13</sup>C NMR (101 MHz, Chloroform-*d*) δ 166.70, 158.70, 157.03, 153.16, 151.81, 138.18, 125.71, 119.28, 111.19, 106.59, 64.77, 25.24, 25.09, 14.43.

Mass Spectrometry (ESI<sup>+</sup>, *m/z*): calculated: 519.1821 found: 519.121 [Cu(eto)<sub>2</sub>]<sup>1+</sup>

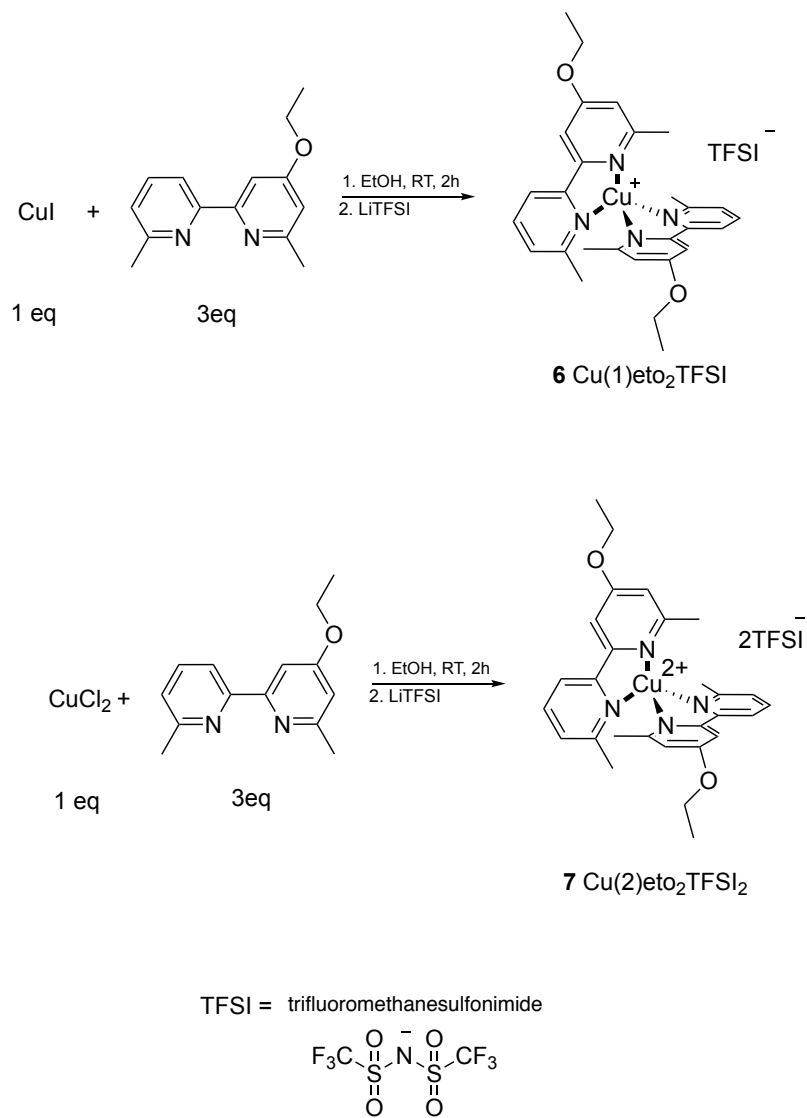
Elemental Analysis: Measured N 8.016 (%);C 44.341 (%);H 4.146 (%);Calculated N 8.75 (%);C 45.02 (%);H 4.03(%)

For [Cu(eto)<sub>2</sub>][TFSI]<sub>2</sub> (7): One equivalent of CuCl<sub>2</sub> (19.6 mg, 0.1 mmol) was mixed with 3 equivalents of 4-ethoxy-6,6'-dimethyl-2,2'-bipyridine (67 mg, 0.3 mmol) in 20 ml ethanol, under nitrogen atmosphere, at room temperature for 2 hours. The resulted complex was obtained as green solution. Addition of 5 ml of deionized water followed by an addition of 5 equivalents of LiTFSI (145 mg, 0.5 mmol). The solution was further stirred for 2 hours at room temperature and under nitrogen atmosphere resulting in green precipitation. The complex (7) was collected by filtration and washed with water. The average yield was 63.4 % (mol). The product was collected as green powder.

Mass Spectrometry (ESI<sup>+</sup>, *m/z*): calculated: 519.1821 found: 519.189 [Cu(eto)<sub>2</sub>]<sup>2+</sup>

Elemental Analysis: Measured N 8.212 (%);C 43.015 (%);H 3.972 (%);Calculated N 7.78(%)C 35.57 (%);H 2.99(%)



Figure 8-5 Synthetic procedure for  $[\text{Cu(eto)}_2][\text{TFSI}]$  and  $[\text{Cu(eto)}_2][\text{TFSI}]_2$

## 8.3 Appendix to chapter 6

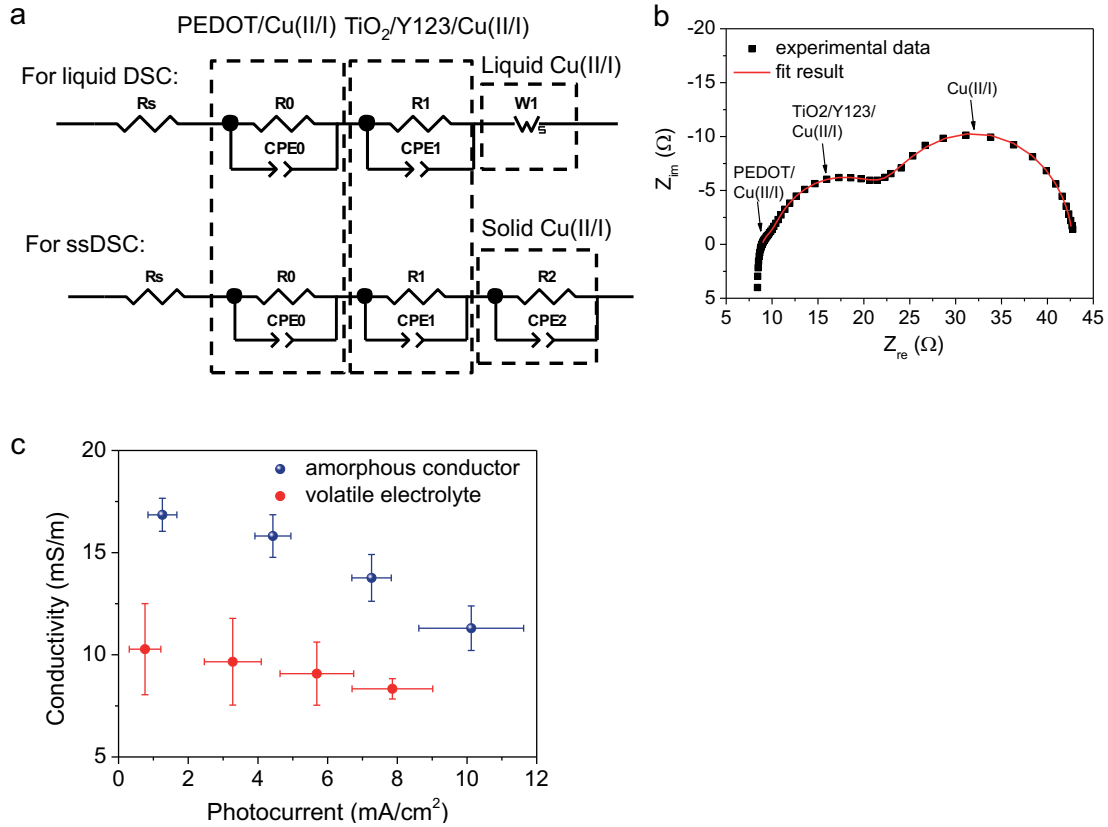


Figure 8-6 (a) Equivalent circuit model to analyze EIS of DSCs based on the volatile electrolyte and the amorphous conductor. At intermediate and higher forward biases, electron transport resistance in TiO<sub>2</sub> is much lower than recombination resistance ( $R_{rec}$ ). A simplified equivalent circuit<sup>2</sup>, where the transmission line element is replaced by a parallel  $R_{rec}C_{\mu}$  circuit, is used to fit the impedance spectra. For liquid DSCs, the equivalent circuit model is composed of a parallel  $R_{rec}C_{\mu}$  in series with an  $RC$  element for the counter electrode and a Warburg diffusion resistance for the ionic transport in the electrolyte. For ssDSCs, we used a similar equivalent circuit model, where a  $R_{hole}C_{hole}$  element replaces the Warburg impedance. (b) A typical spectroscopy of a DSC measured by EIS. The data can be best fitted by using the equivalent circuit models in (a). The arrow indicates frequency-dependent semi-circle (from high to low frequency) corresponding to the interface of PEDOT/Cu(II/I), the interface of TiO<sub>2</sub>/Y123/Cu(II/I), and the Cu(II/I) transport material in DSCs. (c) Photocurrent-dependent conductivity of the amorphous transport and the volatile electrolyte. The solar cells were measured under irradiation intensity of 1,000 W/m<sup>2</sup> provided by a white light-emitting diode (LED). The conductivity was calculated by  $L/(A \times R)$ , where  $L$  (around 9  $\mu\text{m}$ ) is the thickness of the hole conductor or electrolyte between the two FTO glasses,  $A$  (0.286 cm<sup>2</sup>) is the photoactive area of DSCs and  $R$  is resistance obtained by EIS measurements. The average (symbols) and standard deviation (error bars) were calculated from solar cell number between four and six.

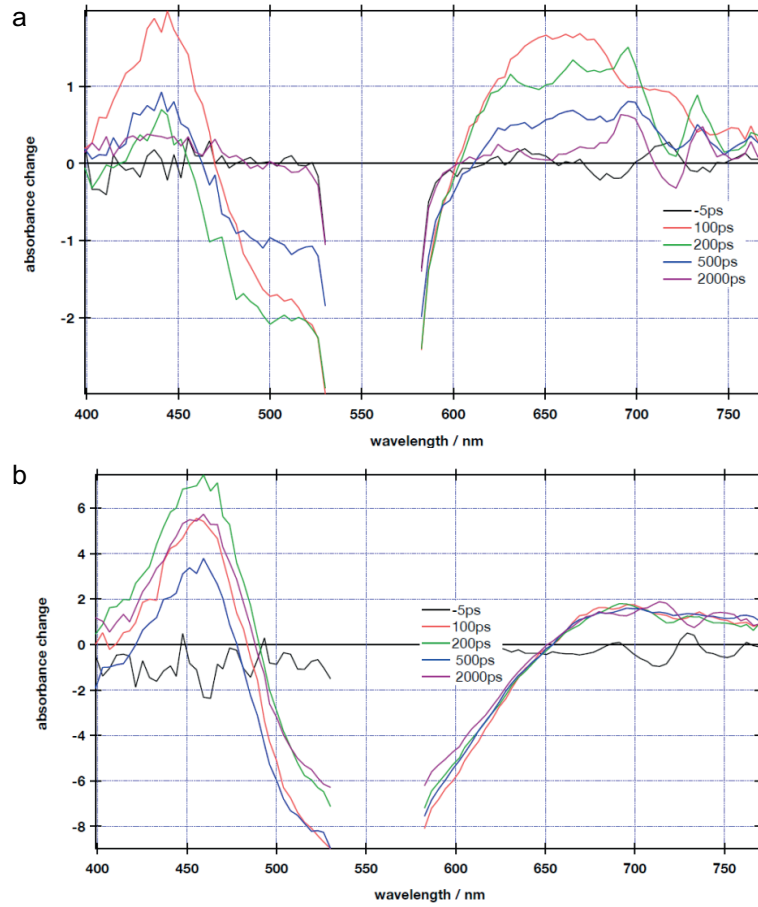


Figure 8-7 Picosecond time resolved transient absorbance of (a) Al<sub>2</sub>O<sub>3</sub>/Y123/inert electrolyte and (b) TiO<sub>2</sub>/Y123/inert electrolyte. The inert electrolyte contains 0.1 M LiTFSI and 0.6 M TBP in acetonitrile.

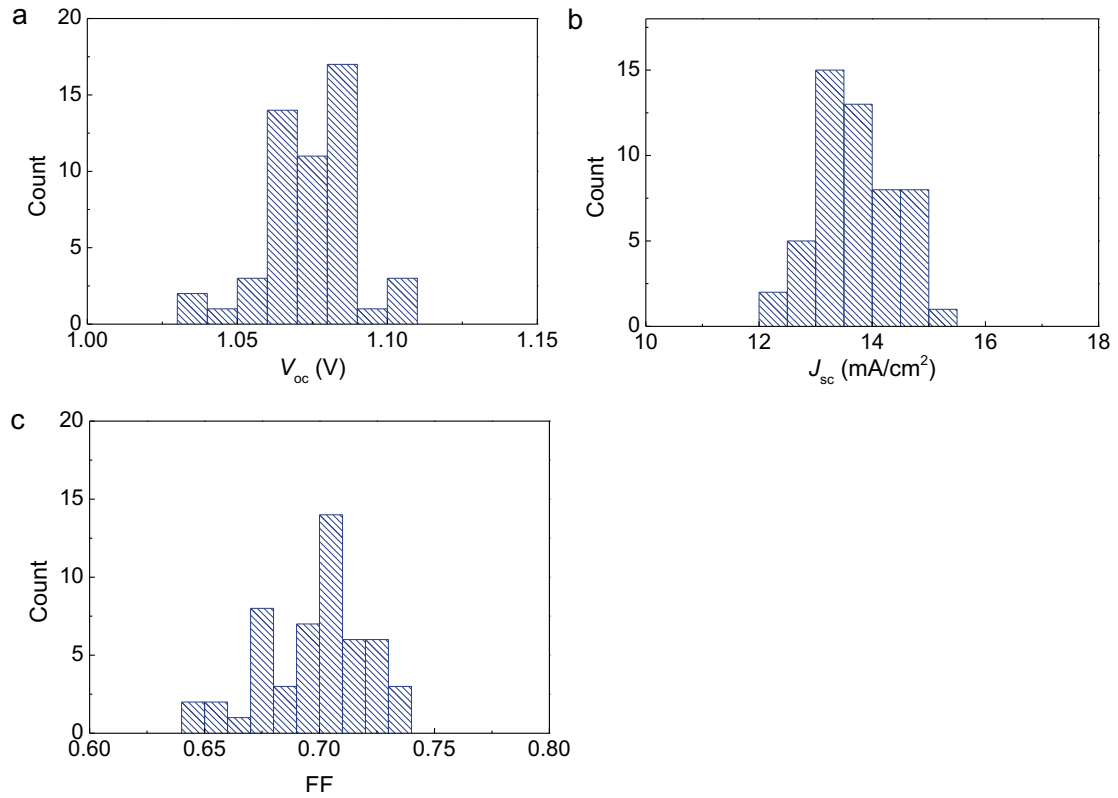


Figure 8-8 Histogram of (a)  $V_{oc}$ , (b)  $J_{sc}$  and (c) FF of ssDSCs based on the Cu(II/I) HTM.

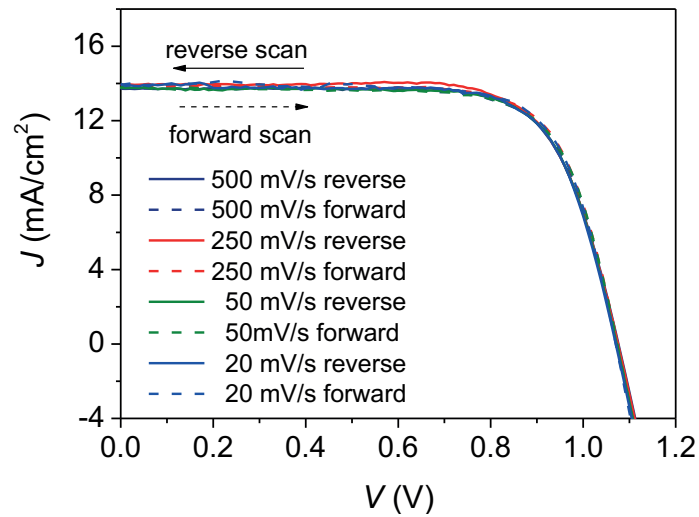


Figure 8-9 Hysteresis test for an efficient ssDSC based on the Cu(II/I) HTM at different scanning rates.

Table 8-3 Photovoltaic parameters of ssDSCs based on Cu(II/I) HTM with different thickness of mesoscopic TiO<sub>2</sub> films. The solar cells were measured under standard AM1.5G conditions.

TiO <sub>2</sub> film thickness (μm)	$J_{sc}$ (mA/cm <sup>2</sup> )	$V_{oc}$ (V)	FF	PCE (%)
2.2 <sup>a</sup>	10.21	1.09	0.72	8.0
3.5 <sup>a</sup>	11.78	1.07	0.71	8.9
6.8 <sup>a</sup>	11.40	1.05	0.64	7.7
3.5+3.0 <sup>b</sup>	13.16	1.07	0.70	9.9

<sup>a</sup>The thickness of transparent mesoscopic TiO<sub>2</sub> films.

<sup>b</sup>The thickness of mesoscopic TiO<sub>2</sub> films composed of 3.5 μm-thick transparent mesoscopic TiO<sub>2</sub> layer + 3.0 μm-thick light scattering TiO<sub>2</sub> layer.



## References

- (1) International Energy Outlook 2017 [https://www.eia.gov/outlooks/ieo/pdf/0484\(2017\).pdf](https://www.eia.gov/outlooks/ieo/pdf/0484(2017).pdf).
- (2) Lewis, N. S.; Nocera, D. G. *Proc. Natl. Acad. Sci.* **2006**, *103* (43), 15729.
- (3) key world energy statistics  
<https://www.iea.org/publications/freepublications/publication/KeyWorld2017.pdf> (accessed Jul 19, 2018).
- (4) Adoption of the Paris Agreement <https://unfccc.int/resource/docs/2015/cop21/eng/l09r01.pdf> (accessed Jul 23, 2018).
- (5) BP Statistical Review of World Energy  
<https://www.bp.com/content/dam/bp/en/corporate/pdf/energy-economics/statistical-review/bp-stats-review-2018-full-report.pdf> (accessed Jul 23, 2018).
- (6) Hagfeldt, A.; Boschloo, G.; Sun, L.; Kloo, L.; Pettersson, H. *Chem. Rev.* **2010**, *110*, 6595.
- (7) 2018 Snapshot of Global Photovoltaic Markets <http://www.iea-pvps.org/index.php?id=92> (accessed Jul 30, 2018).
- (8) World Energy Assessment  
[http://www.undp.org/content/dam/aplaws/publication/en/publications/environment-energy/www-ee-library/sustainable-energy/world-energy-assessment-energy-and-the-challenge-of-sustainability/World Energy Assessment-2000.pdf](http://www.undp.org/content/dam/aplaws/publication/en/publications/environment-energy/www-ee-library/sustainable-energy/world-energy-assessment-energy-and-the-challenge-of-sustainability/World%20Energy%20Assessment-2000.pdf) (accessed Jul 23, 2018).
- (9) Jean, J.; Brown, P. R.; Jaffe, R. L.; Buonassisi, T.; Bulović, V. *Energy Environ. Sci.* **2015**, *8* (4), 1200.
- (10) Becquerel, A.-E. *CR Acad. Sci* **1839**, *9* (145), 1.
- (11) Gurney, R. W.; Mott, N. F. *Proc. R. Soc. London A Math. Phys. Eng. Sci.* **1938**, *164* (917), 151.
- (12) West, W. *Photogr. Sci. Eng.* **1974**, *18* (1), 35.
- (13) Moser, J. *Monatshefte für Chemie und verwandte Teile anderer Wissenschaften* **1887**, *8* (1), 373.
- (14) Namba, S.; Hishiki, Y. *J. Phys. Chem.* **1965**, *69* (3), 774.
- (15) Hauffe, K.; Danzmann, H. J.; Pusch, H.; Range, J.; Volz, H. *J. Electrochem. Soc.* **1970**, *117* (8), 993.
- (16) H., G.; H., T. *Berichte der Bunsengesellschaft für Phys. Chemie* **72** (3), 437.
- (17) H., T.; H., G. *Berichte der Bunsengesellschaft für Phys. Chemie* **73** (3), 251.
- (18) Memming, R. *Prog. Surf. Sci.* **1984**, *17* (1), 7.
- (19) Nelson, R. C. *J. Phys. Chem.* **1965**, *69* (3), 714.
- (20) Tsubomura, H.; Matsumura, M.; Nomura, Y.; Amamiya, T. *Nature* **1976**, *261*, 402.

- 
- (21) Anderson, S.; Constable, E. C.; Dare-Edwards, M. P.; Goodenough, J. B.; Hamnett, A.; Seddon, K. R.; Wright, R. D. *Nature* **1979**, *280*, 571.
- (22) Moser, J.; Graetzel, M. *J. Am. Chem. Soc.* **1984**, *106* (22), 6557.
- (23) O'Regan, B.; Gratzel, M. *Nature* **1991**, *353* (6346), 737.
- (24) Asbury, J. B.; Ellingson, R. J.; Ghosh, H. N.; Ferrere, S.; Nozik, A. J.; Lian, T. *J. Phys. Chem. B* **1999**, *103* (16), 3110.
- (25) Ramakrishna, G.; Jose, D. A.; Kumar, D. K.; Das, A.; Palit, D. K.; Ghosh, H. N. *J. Phys. Chem. B* **2005**, *109* (32), 15445.
- (26) Kuang, D.; Ito, S.; Wenger, B.; Klein, C.; Moser, J.-E.; Humphry-Baker, R.; Zakeeruddin, S. M.; Grätzel, M. *J. Am. Chem. Soc.* **2006**, *128* (12), 4146.
- (27) Benkő, G.; Kallioinen, J.; Korppi-Tommola, J. E. I.; Yartsev, A. P.; Sundström, V. *J. Am. Chem. Soc.* **2002**, *124* (3), 489.
- (28) Koops, S. E.; O'Regan, B. C.; Barnes, P. R. F.; Durrant, J. R. *J. Am. Chem. Soc.* **2009**, *131* (13), 4808.
- (29) Wang, P.; Wenger, B.; Humphry-Baker, R.; Moser, J.-E.; Teuscher, J.; Kantlehner, W.; Mezger, J.; Stoyanov, E. V.; Zakeeruddin, S. M.; Grätzel, M. *J. Am. Chem. Soc.* **2005**, *127* (18), 6850.
- (30) Feldt, S. M.; Wang, G.; Boschloo, G.; Hagfeldt, A. *J. Phys. Chem. C* **2011**, *115* (43), 21500.
- (31) Cao, F.; Oskam, G.; Meyer, G. J.; Searson, P. C. *J. Phys. Chem.* **1996**, *100* (42), 17021.
- (32) Dloczik, L.; Ieperuma, O.; Lauermaun, I.; Peter, L. M.; Ponomarev, E. A.; Redmond, G.; Shaw, N. J.; Uhlendorf, I. *J. Phys. Chem. B* **1997**, *101* (49), 10281.
- (33) Van de Lagemaat, J.; Frank, A. J. *J. Phys. Chem. B* **2000**, *104* (18), 4292.
- (34) Bisquert, J.; Vikhrenko, V. S. *J. Phys. Chem. B* **2004**, *108* (7), 2313.
- (35) Fisher, A. C.; Peter, L. M.; Ponomarev, E. A.; Walker, A. B.; Wijayantha, K. G. U. *J. Phys. Chem. B* **2000**, *104* (5), 949.
- (36) Marcus, R. A. *Annu. Rev. Phys. Chem.* **1964**, *15* (1), 155.
- (37) Marcus, R. A.; Sutin, N. *Biochim. Biophys. Acta - Rev. Bioenerg.* **1985**, *811* (3), 265.
- (38) Marcus, R. A. *Rev. Mod. Phys.* **1993**, *65* (3), 599.
- (39) Yu, Q.; Wang, Y.; Yi, Z.; Zu, N.; Zhang, J.; Zhang, M.; Wang, P. *ACS Nano* **2010**, *4* (10).
- (40) Boschloo, G.; Hagfeldt, A. *Acc. Chem. Res.* **2009**, *42* (11), 1819.
- (41) Gardner, J. M.; Giaimuccio, J. M.; Meyer, G. J. *J. Am. Chem. Soc.* **2008**, *130* (51).
- (42) Rowley, J. G. J. G.; Farnum, B. H. B. H.; Ardo, S.; Meyer, G. J. G. *J. Phys. Chem. Lett.* **2010**, *1* (20), 3132.
- (43) Tian, H.; Sun, L. *J. Mater. Chem.* **2011**, *21* (29), 10592.



- (44) Yu, Z.; Vlachopoulos, N.; Gorlov, M.; Kloo, L.; Yu, Z.; Vlachopoulos, N.; Gorlov, M.; Kloo, L. *Dalt. Trans.* **2011**, *40* (40), 10289.
- (45) Olsen, E.; Hagen, G.; Eric Lindquist, S. *Sol. Energy Mater. Sol. Cells* **2000**, *63* (3), 267.
- (46) Miettunen, K.; Etula, J.; Saukkonen, T.; Jouttijärvi, S.; Halme, J.; Romu, J.; Lund, P. *Prog. Photovoltaics Res. Appl.* **2014**, *23* (8), 1045.
- (47) Miettunen, K.; Halme, J.; Lund, P. *Wiley Interdiscip. Rev. Energy Environ.* **2013**, *2* (1), 104.
- (48) Stergiopoulos, T.; Falaras, P. *Adv. Energy Mater.* **2012**, *2* (6), 616.
- (49) Feldt, S. M.; Gibson, E. A.; Gabrielsson, E.; Sun, L.; Boschloo, G.; Hagfeldt, A. *J. Am. Chem. Soc.* **2010**, *132* (46), 16714.
- (50) Yella, a.; Lee, H.-W.; Tsao, H. N.; Yi, C.; Chandiran, a. K.; Nazeeruddin, M. K.; Diau, E. W.-G.; Yeh, C.-Y.; Zakeeruddin, S. M.; Grätzel, M. *Science (80-. )*. **2011**, *334* (6056), 629.
- (51) Mathew, S.; Yella, A.; Gao, P.; Humphry-baker, R.; Curchod, B. F. E.; Ashari-astani, N.; Tavernelli, I.; Rothlisberger, U.; Nazeeruddin, K.; Gra, M. **2014**, *6* (February).
- (52) Kakiage, K.; Aoyama, Y.; Yano, T.; Oya, K.; Fujisawa, J.; Hanaya, M. *Chem. Commun.* **2015**, *51* (88), 15894.
- (53) Mosconi, E.; Yum, J.-H. J.-H. H.; Kessler, F.; Gómez García, C. J. C. J.; Zuccaccia, C.; Cinti, A.; Nazeeruddin, M. K.; Grätzel, M.; De Angelis, F. *J. Am. Chem. Soc.* **2012**, *134* (47), 19438.
- (54) Yum, J.-H.; Baranoff, E.; Kessler, F.; Moehl, T.; Ahmad, S.; Bessho, T.; Marchioro, A.; Ghadiri, E.; Moser, J.-E.; Yi, C.; Nazeeruddin, M. K.; Grätzel, M. *Nat. Commun.* **2012**, *3*, 631.
- (55) Feldt, S. M.; Lohse, P. W.; Kessler, F.; Nazeeruddin, M. K.; Grätzel, M.; Boschloo, G.; Hagfeldt, A. *Phys. Chem. Chem. Phys.* **2013**, *15* (19), 7087.
- (56) Feldt, S. M.; Cappel, U. B.; Johansson, E. M. J.; Boschloo, G.; Hagfeldt, A. *J. Phys. Chem. C* **2010**, *114* (23), 10551.
- (57) Nelson, J. J.; Amick, T. J.; Elliott, C. M. *J. Phys. Chem. C* **2008**, *112*, 18255.
- (58) Klahr, B. M.; Hamann, T. W. *J. Phys. Chem. C* **2009**, *113* (31), 14040.
- (59) Sapp, S. A.; Elliott, C. M.; Contado, C.; Caramori, S.; Bignozzi, C. A. *J. Am. Chem. Soc.* **2002**, *124* (37), 11215.
- (60) Williams, V. O.; Jeong, N. C.; Prasittichai, C.; Farha, O. K.; Pellin, M. J.; Hupp, J. T. *ACS Nano* **2012**, *6* (7), 6185.
- (61) Jiang, X.; Marinado, T.; Gabrielsson, E.; Hagberg, D. P.; Sun, L.; Hagfeldt, A. *J. Phys. Chem. C* **2010**, *114* (6), 2799.
- (62) Marinado, T.; Nonomura, K.; Nissfolk, J.; Karlsson, M. K.; Hagberg, D. P.; Sun, L.; Mori, S.; Hagfeldt, A. *Langmuir* **2010**, *26* (4), 2592.
- (63) Liu, J.; Zhou, D.; Wang, F.; Fabregat-Santiago, F.; Miralles, S. G.; Jing, X.; Bisquert, J.;

- Wang, P. *J. Phys. Chem. C* **2011**, *115* (29), 14425.
- (64) Tsao, H. N.; Yi, C.; Moehl, T.; Yum, J.; Zakeeruddin, S. M.; Nazeeruddin, M. K.; Grätzel, M. **2011**, 591.
- (65) Gao, J.; Bhagavathi Achari, M.; Kloo, L. *Chem. Commun. (Camb)*. **2014**, *50* (47), 6249.
- (66) Kashif, M. K.; Nippe, M.; Duffy, N. W.; Forsyth, C. M.; Chang, C. J.; Long, J. R.; Spiccia, L.; Bach, U. *Angew. Chemie - Int. Ed.* **2013**, *52* (21), 5527.
- (67) Hathaway, B. J. *Coord. Chem. Rev.* **1981**, *35*, 211.
- (68) Hathaway, B. J.; Billing, D. E. *Coord. Chem. Rev.* **1970**, *5* (2), 143.
- (69) Karlin, K. D.; Yandell, J. K. *Inorg. Chem.* **1984**, *23* (9), 1184.
- (70) Gross, E. L. *Photosynth. Res.* **1993**, *37* (2), 103.
- (71) Burke, P. J.; Henrick, K.; McMillin, D. R. *Inorg. Chem.* **1982**, *21* (5), 1881.
- (72) Rorabacher, D. B. *Chem. Rev.* **2004**, *104* (2), 651.
- (73) Armaroli, N. *Chem. Soc. Rev.* **2001**, *30* (2), 113.
- (74) Alonso-Vante, N.; Nierengarten, J.-F.; Sauvage, J.-P. *J. Chem. Soc. {,} Dalt. Trans.* **1994**, No. 11, 1649.
- (75) Bessho, T.; Constable, E. C.; Graetzel, M.; Hernandez Redondo, A.; Housecroft, C. E.; Kylberg, W.; Nazeeruddin, M. K.; Neuburger, M.; Schaffner, S. *Chem. Commun.* **2008**, No. 32, 3717.
- (76) Housecroft, C. E.; Constable, E. C. *Chem. Soc. Rev.* **2015**, *44* (23).
- (77) Shigeki Hattori; Yuji Wada; Shozo Yanagida; and Shunichi Fukuzumi. *J. Am. Chem. Soc.* **2005**, *127* (26), 9648.
- (78) Pavlishchuk, V. V.; Addison, A. W. *Inorganica Chim. Acta* **2000**, *298* (1), 97.
- (79) Brugnati, M.; Caramori, S.; Cazzanti, S.; Marchini, L.; Argazzi, R.; Bignozzi, C. A.; Chimica, D. **2007**, 2007.
- (80) Bai, Y.; Yu, Q.; Cai, N.; Wang, Y.; Wang, P.; Zhang, M.; Wang, P. *Chem. Commun.* **2011**, *47* (15), 4376.
- (81) Freitag, M.; Giordano, F.; Yang, W.; Pazoki, M.; Hao, Y.; Zietz, B.; Gra, M.; Hagfeldt, A.; Boschloo, G. **2016**.
- (82) Ho, W. L.; Katz, M. J.; Deria, P.; Iii, G. E. C.; Pellin, M. J.; Farha, O. K.; Hupp, J. T. **2016**.
- (83) Fabregat-Santiago, F.; Bisquert, J.; Garcia-Belmonte, G.; Boschloo, G.; Hagfeldt, A. *Sol. Energy Mater. Sol. Cells* **2005**, *87* (1–4), 117.
- (84) Cong, J.; Kinschel, D.; Daniel, Q.; Safdari, M.; Gabrielsson, E.; Chen, H.; Svensson, P. H.; Sun, L.; Kloo, L. *J. Mater. Chem. A* **2016**, *4* (38), 14550.
- (85) Constable, E. C.; Redondo, A. H.; Housecroft, C. E.; Neuburger, M.; Schaffner, S. *Dalt.*

- Trans.* **2009**, No. 33, 6634.
- (86) McCusker, C. E.; Castellano, F. N. *Inorg. Chem.* **2013**, 52 (14), 8114.
- (87) Gothard, N. A.; Mara, M. W.; Huang, J.; Szarko, J. M.; Rolczynski, B.; Lockard, J. V.; Chen, L. X. *J. Phys. Chem. A* **2012**, 116 (9), 1984.
- (88) Buckner, M. T.; McMillin, D. R. *J. Chem. Soc., Chem. Commun.* **1978**, No. 17, 759.
- (89) Freitag, M.; Daniel, Q.; Pazoki, M.; Sveinbjornsson, K.; Zhang, J.; Sun, L.; Hagfeldt, A.; Boschloo, G.; Sveinbjörnsson, K.; Zhang, J.; Sun, L.; Hagfeldt, A.; Boschloo, G. *Energy Environ. Sci.* **2015**, 8 (9), 2634.
- (90) Frisch, M. J.; Trucks, G. W.; Schlegel, H. B.; Scuseria, G. E.; Robb, M. A.; Cheeseman, J. R.; Scalmani, G.; Barone, V.; Mennucci, B.; Petersson, G. A.; others. *Gaussian Inc., Wallingford CT* **2010**.
- (91) Adamo, C.; Barone, V. *J. Chem. Phys.* **1999**, 110 (13).
- (92) Jacopo Tomasi; Benedetta Mennucci; and Roberto Cammi; Tomasi, J.; Mennucci, B.; Cammi, R. *Chem. Rev.* **2005**, 105 (8), 2999.
- (93) Marenich, A. V.; Cramer, C. J.; Truhlar, D. G. *J. Phys. Chem. B* **2009**, 113 (18), 6378.
- (94) Scalmani, G.; Frisch, M. J.; Mennucci, B.; Tomasi, J.; Cammi, R.; Barone, V. *J. Chem. Phys.* **2006**, 124 (9).
- (95) Sun, Z.-Z.; Zheng, K.-M.; Li, Q.; Li, Z.-S. *RSC Adv.* **2014**, 4 (60), 31544.
- (96) Ørnsø, K. B.; Jónsson, E. Ö.; Jacobsen, K. W.; Thygesen, K. S. *J. Phys. Chem. C* **2015**, 119 (23), 12792.
- (97) Cameron, P. J.; Peter, L. M. *J. Phys. Chem. B* **2003**, 107 (51), 14394.
- (98) Cappel, U. B.; Feldt, S. M.; Schoneboom, J.; Hagfeldt, A.; Boschloo, G. *J. Am. Chem. Soc.* **2010**, 132 (26), 9096.
- (99) Ardo, S.; Sun, Y.; Staniszewski, A.; Castellano, F. N.; Meyer, G. J. *J. Am. Chem. Soc.* **2010**, 132 (19), 6696.
- (100) Ellis, H.; Vlachopoulos, N.; Haggman, L.; Perruchot, C.; Jouini, M.; Boschloo, G.; Hagfeldt, A. *Electrochim. Acta* **2013**, 107, 45.
- (101) Kavan, L.; Saygili, Y.; Freitag, M.; Zakeeruddin, S. M. S. M.; Hagfeldt, A.; Grätzel, M. *Electrochim. Acta* **2011**, 56, 194.
- (102) Saygili, Y.; Söderberg, M.; Pellet, N.; Giordano, F.; Cao, Y.; Muñoz-García, A. B.; Zakeeruddin, S. M. S. M.; Vlachopoulos, N.; Pavone, M.; Boschloo, G.; Kavan, L.; Moser, J.-E. J.-E.; Grätzel, M.; Hagfeldt, A.; Freitag, M. *J. Am. Chem. Soc.* **2016**, 138 (45), 15087.
- (103) Freitag, M.; Teuscher, J.; Saygili, Y.; Zhang, X.; Giordano, F.; Liska, P.; Hua, J.; Zakeeruddin, S. M. S. M.; Moser, J.-E. J.-E. E.; Grätzel, M.; Hagfeldt, A. *Nat Phot.* **2017**, 11, 372.
- (104) Cao, Y.; Saygili, Y.; Ummadisingu, A.; Teuscher, J.; Luo, J.; Pellet, N.; Giordano, F.;

- Zakeeruddin, S. M. S. M.; Moser, J.-E. J.-E.; Freitag, M.; Hagfeldt, A.; Grätzel, M. *Nat. Commun.* **2017**, *8*, 15390.
- (105) Kavan, L.; Krysova, H.; Janda, P.; Tarabkova, H.; Saygili, Y.; Freitag, M.; Zakeeruddin, S. M.; Hagfeldt, A.; Grätzel, M. *Electrochim. Acta* **2017**, *251*.
- (106) Kavan, L.; Yum, J.-H.; Graetzel, M. *Electrochim. Acta* **2014**, *128*, 349.
- (107) Kim, J.-Y.; Kim, J. Y.; Lee, D.-K.; Kim, B.; Kim, H.; Ko, M. J. *J. Phys. Chem. C* **2012**, *116* (43), 22759.
- (108) Kang, S. H.; Kim, J.-Y.; Kim, H. S.; Koh, H.-D.; Lee, J.-S.; Sung, Y.-E. *J. Photochem. Photobiol. A Chem.* **2008**, *200* (2), 294.
- (109) Boschloo, G.; Häggman, L.; Hagfeldt, A. *J. Phys. Chem. B* **2006**, *110* (26), 13144.
- (110) Laskova, B.; Moehl, T.; Kavan, L.; Zikalova, M.; Liu, X.; Yella, A.; Comte, P.; Zikal, A.; Nazeeruddin, M. K.; Graetzel, M. *Electrochim. Acta* **2015**, *160*, 10. 296.
- (111) Laskova, B.; Zikalova, M.; Kavan, L.; Chou, A.; Liska, P.; Wei, Z.; Bin, L.; Kubat, P.; Ghadiri, E.; Moser, J. E.; Grätzel, M. *J. Solid State Electrochem.* **2012**, *16* (9), 9. 2993.
- (112) Wu, J.; Lan, Z.; Lin, J.; Huang, M.; Huang, Y.; Fan, L.; Luo, G. *Chem. Rev.* **2015**, *115*, 5, 2136.
- (113) Gorlov, M.; Kloo, L. *Dalton Trans.* **2008**, 2655.
- (114) Kavan, L.; Yum, J.-H.; Grätzel, M. *Nano Lett.* **2011**, *11* (12), 5501.
- (115) Kavan, L.; Liska, P.; Zakeeruddin, S. M.; Grätzel, M. *Electrochim. Acta* **2016**, *195*, 34.
- (116) Carli, S.; Casarin, L.; Syrgiannis, Z.; Boaretto, R.; Benazzi, E.; Caramori, S.; Prato, M.; Bignozzi, C. A. *ACS Appl. Mater. Interfaces* **2016**, *8* (23).
- (117) Blauch, D. N.; Saveant, J. M. *J. Am. Chem. Soc.* **1992**, *114* (9), 3323.
- (118) Barrosse-Antle, L. E.; Bond, A. M.; Compton, R. G.; O'Mahony, A. M.; Rogers, E. I.; Silvester, D. S. *Chem. – An Asian J.* **5** (2), 202.
- (119) Itoh, S.; Noda, K.; Yamane, R.; Kishikawa, N.; Takagi, H. D. *Inorg. Chem.* **2007**, *46* (4), 1419.
- (120) Kavan, L.; Yum, J.-H.; Graetzel, M. *ACS Appl. Mater. Interfaces* **2012**, *4* (12), 6999.
- (121) Bisquert, J.; Fabregat-santiago, F. *J. Phys. Chem. C* **2009**, *113*, 17278–17290.
- (122) Ferdowsi, P.; Saygili, Y.; Zakeeruddin, S. M.; Mokhtari, J.; Grätzel, M.; Hagfeldt, A.; Kavan, L. *Electrochim. Acta* **2018**, *265*, 194.
- (123) Magni, M.; Giannuzzi, R.; Colombo, A.; Cipolla, M. P.; Dragonetti, C.; Caramori, S.; Carli, S.; Grisorio, R.; Suranna, G. P.; Bignozzi, C. A.; Roberto, D.; Manca, M. *Inorg. Chem.* **2016**, *55* (11), 5245.
- (124) Leandri, V.; Daniel, Q.; Chen, H.; Sun, L.; Gardner, J. M.; Kloo, L. *Inorg. Chem.* **2018**, *57* (8), 4556.

- (125) Tian, H.; Gabrielsson, E.; Lohse, P. W.; Vlachopoulos, N.; Kloo, L.; Hagfeldt, A.; Sun, L. *Energy Environ. Sci.* **2012**, 5 (12), 9752.
- (126) Eriksson, S. K.; Josefsson, I.; Ellis, H.; Amat, A.; Pastore, M.; Oscarsson, J.; Lindblad, R.; Eriksson, A. I. K.; Johansson, E. M. J.; Boschloo, G.; Hagfeldt, A.; Fantacci, S.; Odellius, M.; Rensmo, H. *Phys. Chem. Chem. Phys.* **2016**, 18 (1), 252.
- (127) Moehl, T.; Tsao, H. N.; Wu, K.-L.; Hsu, H.-C.; Chi, Y.; Ronca, E.; Angelis, F. De; Nazeeruddin, M. K.; Grätzel, M. *Chem. Mater.* **2013**, 25 (22), 4497.
- (128) Hagberg, D. P.; Edvinsson, T.; Marinado, T.; Boschloo, G.; Hagfeldt, A.; Sun, L. *Chem. Commun.* **2006**, No. 21, 2245.
- (129) Ellis, H.; Schmidt, I.; Hagfeldt, A.; Wittstock, G.; Boschloo, G. *J. Phys. Chem. C* **2015**, 119 (38), 21775.
- (130) Xu, Y.; Schoonen, M. A. A. *Am. Mineral.* **2000**, 85 (3–4), 543 LP.
- (131) Becke, A. D. *J. Chem. Phys.* **1993**, 98 (7), 5648.
- (132) Grimme, S.; Ehrlich, S.; Goerigk, L. *J. Comput. Chem.* 32 (7), 1456.
- (133) Ochterski, J. W. *Thermochemistry in Gaussian*; Gaussian, Inc: Wallingford, CT, 2000.
- (134) Yanai, T.; Tew, D. P.; Handy, N. C. *Chem. Phys. Lett.* **2004**, 393 (1–3), 51.
- (135) Jacquemin, D.; Perpète, E. A.; Scuseria, G. E.; Ciofini, I.; Adamo, C. *J. Chem. Theory Comput.* **2008**, 4 (1), 123.
- (136) Kaupp, M.; v. R. Schleyer, P.; Stoll, H.; Preuss, H. *J. Chem. Phys.* **1991**, 94 (2), 1360.
- (137) Francl, M. M.; Pietro, W. J.; Hehre, W. J.; Binkley, J. S.; Gordon, M. S.; DeFrees, D. J.; Pople, J. A. *J. Chem. Phys.* **1982**, 77 (7), 3654.
- (138) Michaels, H.; Benesperi, I.; Edvinsson, T.; Muñoz-Garcia, A. B.; Pavone, M.; Boschloo, G.; Freitag, M. *Inorganics* **2018**, 6, 53.
- (139) Saliba, M.; Matsui, T.; Domanski, K.; Seo, J.-Y.; Ummadisingu, A.; Zakeeruddin, S. M.; Correa-Baena, J.-P.; Tress, W. R.; Abate, A.; Hagfeldt, A.; Grätzel, M. *Science* **2016**, 354 (6309) 207.
- (140) Saliba, M.; Matsui, T.; Seo, J.-Y.; Domanski, K.; Correa-Baena, J.-P.; Nazeeruddin, M. K.; Zakeeruddin, S. M.; Tress, W.; Abate, A.; Hagfeldt, A.; Grätzel, M. *Energy Environ. Sci.* **2016**, 9 (6), 1989.
- (141) Bach, U.; Lupo, D.; Comte, P.; Moser, J. E.; Weissortel, F.; Salbeck, J.; Spreitzer, H.; Grätzel, M. *Nature* **1998**, 395 (6702), 583.
- (142) Noh, J. H.; Jeon, N. J.; Choi, Y. C.; Nazeeruddin, M. K.; Grätzel, M.; Seok, S. Il. *J. Mater. Chem. A* **2013**, 1 (38), 11842.
- (143) Ding, I.-K.; Tétreault, N.; Brillet, J.; Hardin, B. E.; Smith, E. H.; Rosenthal, S. J.; Sauvage, F.; Grätzel, M.; McGehee, M. D. *Adv. Funct. Mater.* 19 (15), 2431.
- (144) O'Regan, B.; Lenzmann, F.; Muis, R.; Wienke, J. *Chem. Mater.* **2002**, 14 (12), 5023.

- (145) Tennakone, K.; Kumara, G. R. R. A.; Kottegoda, I. R. M.; Wijayantha, K. G. U.; Perera, V. P. S. *J. Phys. D. Appl. Phys.* **1998**, *31* (12), 1492.
- (146) Zhang, J.; Vlachopoulos, N.; Jouini, M.; Johansson, M. B.; Zhang, X.; Nazeeruddin, M. K.; Boschloo, G.; Johansson, E. M. J.; Hagfeldt, A. *Nano Energy* **2016**, *19*, 455.
- (147) Xu, B.; Gabrielsson, E.; Safdari, M.; Cheng, M.; Hua, Y.; Tian, H.; Gardner, J. M.; Kloo, L.; Sun, L. *Adv. Energy Mater.* *5* (10), 1402340.
- (148) Lee, B.; Stoumpos, C. C.; Zhou, N.; Hao, F.; Malliakas, C.; Yeh, C.-Y.; Marks, T. J.; Kanatzidis, M. G.; Chang, R. P. H. *J. Am. Chem. Soc.* **2014**, *136* (43), 15379.
- (149) Kashif, M. K.; Milhuisen, R. A.; Nippe, M.; Hellerstedt, J.; Zee, D. Z.; Duffy, N. W.; Halstead, B.; De Angelis, F.; Fantacci, S.; Fuhrer, M. S.; Chang, C. J.; Cheng, Y.-B.; Long, J. R.; Spiccia, L.; Bach, U. *Adv. Energy Mater.* *6* (24), 1600874.
- (150) Davies, K.; Byers, B. *Inorg. Chem.* **1987**, *26* (22), 3823.
- (151) Eggleston, M. K.; McMillin, D. R.; Koenig, K. S.; Pallenberg, A. J. *Inorg. Chem.* **1997**, *36* (2), 172.
- (152) Snaith, H. J.; Grätzel, M. *Adv. Mater.* *19* (21), 3643.
- (153) Leijtens, T.; Lim, J.; Teuscher, J.; Park, T.; Snaith, H. J. *Adv. Mater.* *25* (23), 3227.
- (154) Dunn, B. C.; Ochrymowycz, L. A.; Rorabacher, D. B. *Inorg. Chem.* **1995**, *34* (7), 1954.
- (155) Hide, J. G. F.; Wang, H. *Synth. Met.* **1997**, *84* (1), 979.
- (156) Koster, L. J. A.; Mihailetschi, V. D.; Xie, H.; Blom, P. W. M. *Appl. Phys. Lett.* **2005**, *87* (20), 203502.
- (157) Parker, W. L.; Crosby, G. A. *J. Phys. Chem.* **1989**, *93* (15), 5692.
- (158) Cunningham, C. T.; Cunningham, K. L. H.; Michalec, J. F.; McMillin, D. R. *Inorg. Chem.* **1999**, *38* (20), 4388.
- (159) Online, V. A.; Iwamura, M.; Takeuchi, S.; Tahara, T. **2014**, 4143.
- (160) Gushurst, A. K. I.; McMillin, D. R.; Dietrich-Buchecker, C. O.; Sauvage, J. P. *Inorg. Chem.* **1989**, *28* (22), 4070.
- (161) Kirchhoff, J. R.; Gamache, R. E.; Blaskie, M. W.; Del Paggio, A. A.; Lengel, R. K.; McMillin, D. R. *Inorg. Chem.* **1983**, *22* (17), 2380.
- (162) Coppens, P.; Sokolow, J.; Trzop, E.; Makal, A.; Chen, Y. *J. Phys. Chem. Lett.* **2013**, *4* (4), 579.
- (163) Antony, M. P.; Moehl, T.; Wielopolski, M.; Moser, J.-E.; Nair, S.; Yu, Y.-J.; Kim, J.-H.; Kay, K.-Y.; Jung, Y.-S.; Yoon, K. B.; Grätzel, C.; Zakeeruddin, S. M.; Grätzel, M. *ChemSusChem* *8* (22), 3859.
- (164) Ghadiri, E.; Zakeeruddin, S. M.; Hagfeldt, A.; Grätzel, M.; Moser, J.-E. *Sci. Rep.* **2016**, *6*, 24465.
- (165) Park, N.-G.; Grätzel, M.; Miyasaka, T.; Zhu, K.; Emery, K. *Nat. Energy* **2016**, *1*, 16152.

- (166) Fraas, L. M.; Partain, L. D. *Solar Cells and Their Applications*; Wiley Series in Microwave and Optical Engineering; Wiley, 2010.
- (167) Kalyanasundaram, K. *Dye-sensitized solar cells*; EPFL Press: Lausanne, 1990.
- (168) Sakamoto, R.; Katagiri, S.; Maeda, H.; Nishimori, Y.; Miyashita, S.; Nishihara, H. *J. Am. Chem. Soc.* **2015**, *137* (2), 734.
- (169) Mathews, I.; King, P. J.; Stafford, F.; Frizzell, R. *IEEE Journal of Photovoltaics*. 2016, pp 230–235.
- (170) Yang, P. C.; Chan, I. M.; Lin, C. H.; Chang, Y. L. *Photovoltaic Specialists Conference (PVSC), 2011 37th IEEE*. 2011, pp 696–698.
- (171) Barber, G. D.; Hoertz, P. G.; Lee, S.-H. A.; Abrams, N. M.; Mikulca, J.; Mallouk, T. E.; Liska, P.; Zakeeruddin, S. M.; Grätzel, M.; Ho-Baillie, A.; Green, M. A. *J. Phys. Chem. Lett.* **2011**, *2* (6), 581.
- (172) Lechêne, B. P.; Cowell, M.; Pierre, A.; Evans, J. W.; Wright, P. K.; Arias, A. C. *Nano Energy* **2016**, *26*, 631.
- (173) Lan, J.-L.; Wei, T.-C.; Feng, S.-P.; Wan, C.-C.; Cao, G. *J. Phys. Chem. C* **2012**, *116* (49), 25727.
- (174) Kroon, J. M.; Bakker, N. J.; Smit, H. J. P.; Liska, P.; Thampi, K. R.; Wang, P.; Zakeeruddin, S. M.; Grätzel, M.; Hinsch, A.; Hore, S.; Würfel, U.; Sastrawan, R.; Durrant, J. R.; Palomares, E.; Pettersson, H.; Gruszecki, T.; Walter, J.; Skupien, K.; Tulloch, G. E. *Prog. Photovoltaics Res. Appl.* **2007**, *15* (1), 1.
- (175) Kontos, A. G.; Stergiopoulos, T.; Likodimos, V.; Milliken, D.; Desilvesto, H.; Tulloch, G.; Falaras, P. *J. Phys. Chem. C* **2013**, *117* (17), 8636.
- (176) Mathews, I.; Kelly, G.; King, P. J.; Frizzell, R. *2014 IEEE 40th Photovoltaic Specialist Conference (PVSC)*. 2014, 510.
- (177) Hagberg, D. P.; Jiang, X.; Gabrielsson, E.; Linder, M.; Marinado, T.; Brinck, T.; Hagfeldt, A.; Sun, L. *J. Mater. Chem.* **2009**, *19* (39), 7232.
- (178) Zhang, X.; Xu, Y.; Giordano, F.; Schreier, M.; Pellet, N.; Hu, Y.; Yi, C.; Robertson, N.; Hua, J.; Zakeeruddin, S. M.; Tian, H.; Grätzel, M. *J. Am. Chem. Soc.* **2016**, *138* (34), 10742.
- (179) *AIP Adv.* **2013**, *3* (7), 72113.
- (180) Rühle, S.; Greenshtein, M.; Chen, S.-G.; Merson, A.; Pizem, H.; Sukenik, C. S.; Cahen, D.; Zaban, A. *J. Phys. Chem. B* **2005**, *109* (40), 18907.
- (181) De Rossi, F.; Pontecorvo, T.; Brown, T. M. *Appl. Energy* **2015**, *156*, 413.
- (182) Reich, N. H.; van Sark, W. G. J. H. M.; Turkenburg, W. C. *Renew. Energy* **2011**, *36* (2), 642.
- (183) Randall, J. F.; Jacot, J. *Renew. Energy* **2003**, *28* (12), 1851.
- (184) Tan, Y. K.; Panda, S. K. *IEEE Transactions on Industrial Electronics*. 2011, pp 4424–4435.
- (185) Borgeson, J.; Schauer, S.; Diewald, H. *Benchmarking MCU power consumption for ultra-*

*low-power applications*; 2012.

- (186) Dolgov, A.; Zane, R.; Popovic, Z. *IEEE Transactions on Circuits and Systems I: Regular Papers*. 2010, pp 1802–1811.
- (187) Roundy, S.; Leland, E. S.; Baker, J.; Carleton, E.; Reilly, E.; Lai, E.; Otis, B.; Rabaey, J. M.; Wright, P. K.; Sundararajan, V. *IEEE Pervasive Computing*. 2005, pp 28–36.
- (188) Ogura R. K.; Nakane S; Morooka M.; Orihashi M.; Suzuki Y.; Noda K. *Appl. Phys. Lett.* **2009**, *94* (7), 73308.
- (189) Cao, Y.; Liu, Y.; Zakeeruddin, S. M.; Hagfeldt, A.; Grätzel, M. *Joule* **2018**.
- (190) Zhang, W.; Wu, Y.; Bahng, H. W.; Cao, Y.; Yi, C.; Saygili, Y.; Luo, J.; Liu, Y.; Kavan, L.; Moser, J. E.; Hagfeldt, A.; Tian, H.; Zakeeruddin, S. M.; Zhu, W.; Gratzel, M. *Energy Environ. Sci.* **2018**.



# Acknowledgements

First of all, I would like to thank to my thesis supervisor Prof. Anders Hagfeldt for giving me the opportunity to become a member of Laboratory of Photomolecular Sciences. I am really glad to have such a chance for studying in this leading group. I appreciate Prof. Anders Hagfeldt, for always being positive and optimistic and giving me freedom for my studies.

In special, I would like to thank Dr. Marina Freitag for all kind of support she provided in terms of science and the difficulties in life. I am happy that I could make use of her knowledge and experience during the time she supervised me.

I thank to my PhD jury committee members Prof. Majed Chergui, Prof. Md-Khaja Nazeeruddin, Prof. Edwin Constable and Prof. Lars Kloo.

I thank to Prof. Michael Graetzel, Dr. Shaik Zakeeruddin, Prof. Ladislav Kavan, Prof. Gerrit Boschloo, Dr. Ana Belen Munoz-Garcia, Dr. Michele Pavone, Dr. Nick Vlachopoulos, Prof. Jacques-E. Moser, Dr. Wolfgang Tress, Dr. Fabrizio Giordano and Dr. Paul Liska for their valuable contributions to my study and all the scientific discussions. I thank to Ms. Heidi Francelet and Ms. Carmen Biagini for their administrative support. I want to thank Marko Stojanovic, Parnian Ferdowsi, Dr. Silver Turren for the nice collaboration on our common work. Apart from these I want to thank to all LSPM and LPI members, I believe that I learned a lot from the past and current group members.

I want to especially thank to my friends and colleagues Dr. Hui-Seon Kim, Dr. Ji-Youn Seo, Natalie Florez Diaz, Dr. Jeannete Kadro and Jessica Flach. They became my closest friends during my life in Lausanne. In any case, I always felt their support with me. All the times I enjoyed to be with them, I really had fun in our trips, hikes, picnics, long and frequent coffee breaks.

Thanks!



# Curriculum Vitae

## YASEMIN SAYGILI

Laboratory of Photomolecular Sciences (LSPM)

Ecole Polytechnique Fédérale De Lausanne

*e-mail:* yaseminsaygili@gmail.com

## EDUCATION AND RESEARCH EXPERIENCES

### PhD Candidate

Ecole Polytechnique Fédérale de Lausanne  
Laboratory of Photomolecular Sciences

2015-cont

### *R&D Engineer at 'Gate Electronics'*

2014

### Master's Degree in Chemical Engineering

Middle East Technical University, Ankara, Turkey

2011-2013

### *Project Assistant: "Development of a 3 KW PEM Fuel Cell"*

between UNIDO-ICHET and METU, Ankara, Turkey

2011-2013

### *Project Assistant: "Development of composite membranes and electrocatalysts for PEM fuel cells and identification of long term performance" between METU and TÜBİTAK*

2011- 2012

### Bachelor's Degree in Chemical Engineering

Middle East Technical University, Ankara, Turkey

2005-2010

*Intern:* BOTAŞ Yapracık- Natural Gas Operations Unit, Ankara, Turkey

August 2009

*Intern:* Onay Painting Plant, Ankara, Turkey

August 2008

## RESEARCH SUMMARY

*PhD Thesis Topic: Development of novel redox mediators for Dye-sensitized solar cell applications.* Thesis Supervisor: Prof.Dr.Anders Hagfeldt

*Design and Synthesis of Copper Redox Mediators  
Fabrication and characterization of Dye-sensitized solar cells*

*Master Thesis Topic: Modelling and Control of a Fuel Cell System: Modelling and Control of a Fuel Cell System* Thesis Supervisors: Prof. Dr. Serkan Kincal and Prof. Dr. Inci Eroglu.

## CERTIFICATE AND AWARDS

Poster Prize at International Conference Asia-Pacific Hybrid and Organic Photovoltaics (2017), May 21-24, Lausanne, Switzerland.

Certificate of Attendance to 13th International Conference on Clean Energy, June 8-12 2014, Istanbul, Turkey.

Certificate of International Summer School on PEM Fuel Cells Applications and Integration, July 2011, İzmir, Turkey.

NanoBiotech 2014-1st International NanobioTechnology Symposium, August 27-29,2014, Köyceğiz, Turkey.

International Workshop on Detection of Pathogenic Microorganisms: Probes, Platforms and Detectors, (Oral Presentation: Laser and Radiofrequency in Medical Applications), August 29-30, 2014, Köyceğiz, Turkey.

## PUBLICATIONS

- (1) **Saygili, Y.**; Stojanovic, M.; Michaels, H.; Tiepelt, J.; Teuscher, J.; Massaro, A.; Pavone, M.; Giordano, F.; Zakeeruddin, S. M.; Boschloo, G.; Moser, J.-E.; Grätzel, M.; Muñoz-García, A. B.; Hagfeldt, A.; Freitag, M. *ACS Appl. Energy Mater* **2018**, 1(9), 4950-4962.
- (2) Liu, Y.; Cao, Y.; Zhang, W.; Stojanovic, M.; Dar, M. I.; Péchy, P.; **Saygili, Y.**; Hagfeldt, A.; Zakeeruddin, S. M.; Grätzel, M. *Angew. Chemie* **2018**. DOI:10.1002/ange.201808609
- (3) Ferdowsi, P.; **Saygili, Y.**; Zhang, W.; Edvinson, T.; Kavan, L.; Mokhtari, J.; Zakeeruddin, S. M.; Grätzel, M.; Hagfeldt, A. *ChemSusChem* **2018**, 11 (2).
- (4) Zhang, W.; Wu, Y.; Bahng, H. W.; Cao, Y.; Yi, C.; **Saygili, Y.**; Luo, J.; Liu, Y.; Kavan, L.; Moser, J. E.; Hagfeldt, A.; Tian, H.; Zakeeruddin, S. M.; Zhu, W.; Grätzel, M. *Energy Environ. Sci.* **2018**.
- (5) Ferdowsi, P.\*; **Saygili, Y.\***; Zakeeruddin, S. M.; Mokhtari, J.; Grätzel, M.; Hagfeldt, A.; Kavan, L. *Electrochim. Acta* **2018**, 265, 194. (\* shared first co-authors)
- (6) **Saygili, Y.\***; Turren-Cruz\*, S.-H.; Olthof, S.; Saes, B. W. H.; Pehlivan, I. B.; Saliba, M.; Meerholz, K.; Edvinsson, T.; Zakeeruddin, S. M.; Grätzel, M.; Correa-Baena, J.-P.; Hagfeldt, A.; Freitag, M.; Tress, W. *ChemPhysChem* **2018**. (\* shared first co-authors)
- (7) Seo, J.-Y.; Uchida, R.; Kim, H.-S.; **Saygili, Y.**; Luo, J.; Moore, C.; Kerrod, J.; Wagstaff, A.; Eklund, M.; McIntyre, R.; Pellet, N.; Zakeeruddin, S. M.; Hagfeldt, A.; Grätzel, M. *Adv. Funct. Mater.* **2018**, 1705763.
- (8) Kavan, L.; Krysova, H.; Janda, P.; Tarabkova, H.; **Saygili, Y.**; Freitag, M.; Zakeeruddin, S. M.; Hagfeldt, A.; Grätzel, M. *Electrochim. Acta* **2017**, 251.
- (9) Cao, Y.\*; **Saygili, Y.\***; Ummadisingu, A.; Teuscher, J.; Luo, J.; Pellet, N.; Giordano, F.; Zakeeruddin, S. M. S. M.; Moser, J.-E. J.-E.; Freitag, M.; Hagfeldt, A.; Grätzel, M. *Nat. Commun.* **2017**, 8, 15390. (\* shared first co-authors)
- (10) Freitag, M.; Teuscher, J.; **Saygili, Y.**; Zhang, X.; Giordano, F.; Liska, P.; Hua, J.; Zakeeruddin, S. M.; Moser, J.-E.; Grätzel, M.; Hagfeldt, A. *Nat. Photonics* **2017**, 11 (6).
- (11) Kavan, L.; **Saygili, Y.**; Freitag, M.; Zakeeruddin, S. M. S. M.; Hagfeldt, A.; Grätzel, M. *Electrochim. Acta*, **2017**, 227.
- (12) Hao, Y.; Yang, W.; Zhang, L.; Jiang, R.; Mijangos, E.; **Saygili, Y.**; Hammarström, L.; Hagfeldt, A.; Boschloo, G. *Nat. Commun.* **2016**, 7, 13934.
- (13) Hao, Y.; **Saygili, Y.**; Cong, J.; Eriksson, A.; Yang, W.; Zhang, J.; Polanski, E.; Nonomura, K.; Zakeeruddin, S. M. S. M.; Grätzel, M.; Hagfeldt, A.; Boschloo, G. *ACS Appl. Mater. Interfaces* **2016**, 8 (48), 32797.
- (14) **Saygili, Y.**; Söderberg, M.; Pellet, N.; Giordano, F.; Cao, Y.; Muñoz-García, A. B.; Zakeeruddin, S. M. S. M.; Vlachopoulos, N.; Pavone, M.; Boschloo, G.; Kavan, L.; Moser, J.-E. J.-E.; Grätzel, M.; Hagfeldt, A.; Freitag, M. *J. Am. Chem. Soc.* **2016**, 138 (45), 15087.
- (15) **Saygili, Y.**; Kincal, S.; Eroglu, I.; Saygili, Y.; Kincal, S.; Eroglu, I. *Int. J. Hydrogen Energy* **2015**, 40 (24), 7886.
- (16) **Saygili, Y.**; Eroglu, I.; Kincal, S. *Int. J. Hydrogen Energy* **2015**, 40 (1), 615.

## CONFERENCE PROCEEDINGS

Copper Bipyridyl Redox Mediators for Dye-Sensitized Solar Cells with High Photovoltage - Poster Presentation at Dyenamo DSSC Conference, October 16-17, Uppsala, Sweden.

Copper Bipyridyl Redox Mediators for Dye-Sensitized Solar Cells with High Photovoltage - Poster Presentation at International Conference of Hybrid and Organic Photovoltaics (2017), May 21-24, Lausanne, Switzerland.

Copper Redox Mediators for Dye-Sensitized Solar Cells with High Photovoltage - Oral Presentation at International Conference Asia-Pacific Hybrid and Organic Photovoltaics (2017), February 3-4, Yokohama, Japan.

3 kW PEMFC Piping and Instrumentation Diagram Development and Modeling for Process Control Purposes- Oral Presentation at International Conference on Clean Energy (ICCE) 2014, June 8-12, Istanbul.

